A MODEL BASED FRAMEWORK FOR FAULT DIAGNOSIS AND PROGNOSIS OF DYNAMICAL SYSTEMS WITH AN APPLICATION TO HELICOPTER TRANSMISSIONS

A Thesis
Presented to
The Academic Faculty

By

Romano Patrick-Aldaco

In Partial Fulfillment
Of the Requirements for the Degree
Doctor of Philosophy in
Electrical and Computer Engineering

Georgia Institute of Technology

August 2007

A MODEL BASED FRAMEWORK FOR FAULT DIAGNOSIS AND PROGNOSIS OF DYNAMICAL SYSTEMS WITH AN APPLICATION TO HELICOPTER TRANSMISSIONS

Approved by:

Dr. George J. Vachtsevanos, Advisor
School of Electrical and Computer Engineering

Dr. Aldo A. Ferri, Co-advisor
School of Mechanical Engineering

Dr. Thomas G. Habetler
School of Electrical and Computer Engineering

Dr. George Kardomateas
School of Aerospace Engineering

Dr. Jennifer E. Michaels
School of Electrical and Computer Engineering

Dr. Thomas E. Michaels
School of Electrical and Computer Engineering

Dr. David G. Taylor
School of Electrical and Computer Engineering

Date Approved: June 21, 2007

To Jesus Christ,

source of all my inspiration and abilities,

and to my wife and our parents

ACKNOWLEDGMENTS

The author wishes to thank Dr. George Vachtsevanos, advisor of this work, not only for the technical guidance in the realization of this thesis, but also for the genuine care and supervision of all the academic and professional activities involved with the attainment of the doctoral degree. His support and example have always gone beyond academics. They will now last a lifetime.

Most sincere thanks also go to Dr. Aldo Ferri, co-advisor of this thesis, for the many enlightening discussions, the instruction and coaching in several aspects of Mechanical Engineering, his unrestricted availability and amicable disposition, and his wise guiding and supportive comments throughout the entire realization of this work, especially in the final stages.

Gratitude is also expressed to the dissertation committee members, Dr. David Taylor, Dr. Thomas Habetler, and Dr. Thomas Michaels. The interest and stance of Dr. Thomas Michaels concerning this work, as well as that of Dr. Jennifer Michaels, are especially valued.

The author wishes to express his appreciation to faculty and personnel of the School of Electrical and Computer Engineering of Georgia Tech, especially to Dr. David Hertling, Dr. Bonnie Heck Ferri, and Ms. Marilou Mycko, who enabled the initiation, conclusion, and persistence in all the procedures involved with attaining the doctoral degree.

Support for completing the doctoral degree was provided by a scholarship from the Mexican National Council of Science and Technology (CONACYT), and is most gratefully appreciated.

Appreciation is also expressed to the Goizueta Foundation Scholarship Program at Georgia Tech for their support, and to Mr. Jorge Breton, the program manager, for his kindness and friendship.

The author also wishes to thank Dr. Raul Fernandez and Dr. Frank Lewis of the University of Texas at Arlington, both of whom prepared the author and encouraged his interest for pursuing a doctoral degree and attending Georgia Tech.

Esteem is expressed to all the members and friends of the Intelligent Control Systems Laboratory of Georgia Tech engaged in simultaneous projects with this research, especially to Mr. Gary O'Neill, Dr. Biqing (Becky) Wu, Dr. Panagiotis Sparis, Dr. George Georgoulas, Abhinav, Bhaskar, Dr. Otis Smart, Taimoor, Jackie, Matt, Lauren, Manzar and Ms. Sharon Lawrence. Particular gratitude is expressed for the help and collaborative work of Marcos Orchard and Dr. Bin (Ben) Zhang.

The support and collaboration of DARPA, Northrop Grumman Corp., Sikorsky Corp., Impact Technologies LLC, and NAVAIR is acknowledged and appreciated, especially the collaborative efforts of the following people involved with these institutions: Mr. Steve Engel, Mr. Mark Davis, Mr. William Hardman, Mr. Glen

Sahrmann, Mr. Greg Kacprzynski, Mr. Mike Koelemay, Mr. David Muench and Mr. Joel Berg.

The author wishes to express appreciation to old friends who have paved the way to reaching this stage in his life, including friends and professors at Universidad Panamericana in Guadalajara, Mexico, most particularly to Ing. Luis Felipe Guerrero, M.S.I.E.

Last, but not least, the author wishes to express not only the deepest gratefulness to the unconditional support of his family, but a deep and immense love. Special expression of these feelings is extended to his loving wife, who endured the demands of the doctoral program along with her husband and turned them into an enjoyable adventure. This expression goes also to the author's mother "Chiquita", his father "Johnny", his grandmother "Abue", his uncle Marco Aldaco and aunts "Chilin" and Gabriela, and to his mother-in-law Anita, and his father-in-law Enrique. Although the present thesis is written by one man in the span of months, it is wondrous how many people, more than are listed here, have influenced and truly participated in putting together all that was needed for so many years. Such is the way of the social world we live in. Such is the path that God gives us an opportunity to traverse, and upon which Him so gently guides us. Thus, the greatest thanks are given to Him. May all the glory and honor be unto our Lord for all eternity.

TABLE OF CONTENTS

ACKNOWLEDGMENTS ..... **iv**

LIST OF TABLES ..... **xi**

LIST OF FIGURES ..... **xii**

LIST OF SYMBOLS ..... **xx**

SUMMARY ..... **xxvii**

1. INTRODUCTION **1**

1.1. Outline **1**

1.2. Overview and Objective of this Thesis **2**

1.3. Approach and Validation **4**

1.4. Principal Contributions **7**

1.5. Organization of the thesis **8**

2. HISTORICAL BACKGROUND **11**

2.1. The Importance of Diagnostics and Prognostics of Engineering Systems **11**

2.2. Diagnostics of Engineering Systems **14**

2.2.1. Background 14
2.2.2. Classification of approaches to performing engineering system diagnostics 14
2.2.3. Model-based diagnostics 19

2.3. Prognostics of Engineering Systems **21**

2.3.1. Background 21
2.3.2. Classification of approaches to performing engineering system prognostics 22
2.3.3. Model-based prognostics 23

2.4. Diagnostics and Prognostics Today **31**

3. THE HELICOPTER TRANSMISSION PROBLEM IN FOCUS **33**

3.1. Description and Importance of the Problem **33**

3.1.1. Discovery and assessment of the problem 33
3.1.2. Problem significance 35
3.1.3. Vibration is key for diagnosis 36
3.1.4. A chance to validate prognostic efforts 38
3.1.5. Selection of this problem for research 39

3.2. Experimental Support for Studying the Helicopter Transmission 39

3.3. Main Transmission Gearbox of the Helicopter..... 42

3.3.1. Planetary gearboxes....42
3.3.2. Vibration of planetary gearboxes....44

3.3.2.1. McFadden and Smith's planetary gear vibration insights....45
3.3.2.2. Keller and Grabill's equation....49
3.3.2.3. Planetary gearbox vibration as a sum of similar but delayed signals....53
3.3.2.4. Characterization of the vibration of an ideal planetary gearbox and definition of the types of sidebands....55

3.4. A Vibration Model for Planetary Gearboxes with Planet-gear shifts..... 59

3.4.1. Effect of the shift of a planet gear....60
3.4.2. Other effects due to the number of planet gears....67
3.4.3. Sensitivity of the vibration to planet-gear shifting....69
3.4.4. Effects of large shift angles....71
3.4.5. Model validation....73

3.4.5.1. Validation through experiments with specific crack lengths (first set of experimental data)....74
3.4.5.2. Validation through experiments with a growing crack (second set of experimental data)....79

3.4.6. Remarks about the vibration model....87

4. A MODEL-BASED DIAGNOSIS ARCHITECTURE 89

4.1. Objectives 89

4.2. A Generic Diagnostics Methodology for a Class of Dynamic Mechanical Systems..... 90

4.2.1. Adapting a model for its use in diagnostics....90

4.2.1.1. The experiment case....92
4.2.1.2. The fault case....93
4.2.1.3. Analysis of damage-sensitive subsystems or components....94
4.2.1.4. Simulations with the plant model....94
4.2.1.5. Use of the proposed simulation architecture in model-based diagnosis....95

4.2.2. A reverse engineering approach to model-based diagnostics....96

5. DIAGNOSIS OF THE HELICOPTER TRANSMISSION 99

5.1. Special considerations of the planetary gear vibration model..... 99

5.1.1. Considering the shift of multiple planet gears....100
5.1.2. The importance of the frequency response coefficients....103

5.2. Adaptation of the planetary gear vibration model for its use in diagnostics..... 104

5.2.1. The planetary gearbox vibration model as the diagnostic model....105
5.2.2. Frequency response analysis for determining the fault-insensitive parameters....105
5.2.3. Finite element analysis for determining the fault-sensitive parameters....105
5.2.4. Calibration of the simulation....106

5.3. Determination of the fault-insensitive parameters 106

5.3.1. Relating experimental data to the vibration model 107
5.3.2. A system of non-linear equations characterizing the frequency response of a planetary gearbox 110
5.3.3. Fault insensitive parameters of the helicopter planetary gearbox 113

5.4. Determination of the fault-sensitive parameters 122

5.4.1. Computer model of the planetary carrier plate and the major forces acting on it 123
5.4.2. Modeling the fracture in the planetary carrier plate 129
5.4.3. Deformation analysis and interpretation 132

5.5. Proposed condition indicators (features) for diagnosing the planetary gearbox through vibration 136

5.5.1. Background in the condition assessment of the helicopter planetary gearbox 136
5.5.2. Consideration of the sideband magnitude variability and noise at different frequencies 140
5.5.3. Suggested condition indicators 145

5.5.3.1. Suggested condition indicator 1: relative sideband index 146
5.5.3.2. Suggested condition indicator 2: sized relative harmonic sideband index 146
5.5.3.3. General form of suggested relative metrics 147
5.5.3.4. Definition of N_p-sideband groups and basic group metrics 148
5.5.3.5. Condition indicators 3 and 4: relative size of sidebands in an N_p-sideband group 150
5.5.3.6. Condition indicators 5 and 6: group averaging of relative sideband sizes 151
5.5.3.7. Condition indicator enhancement: harmonic averaging of relative condition indicators 152

5.6. Noise calibration for the simulations of gearbox vibration 153

5.6.1. Justification of the need for noise calibration 153

5.6.1.1. Explanation of the procedure followed to show the importance of noise calibration 153
5.6.1.2. Example 1, using non-dominant sidebands 156
5.6.1.3. Example 2, using non-dominant sidebands 158
5.6.1.4. Example 3, using feature values 159

5.6.2. Two variants of a possible technique for calibrating the noise levels 160

5.6.2.1. Noise-calibration variant 1 162
5.6.2.2. Noise-calibration variant 2 165

5.7. Validation and performance of the vibration model 167

5.8. Application of the reverse engineering technique for identifying a crack in the helicopter transmission 177

6. A MODEL-BASED PROGNOSIS ARCHITECTURE 181

6.1. Objectives 181

6.2. A generic approach to model-based prognosis for a class of dynamic mechanical systems 182

6.3. The damage progression model 186

6.3.1. Initial conditions for the prognostic model: the integration with diagnostics 189
6.3.2. The loading profile 190
6.3.3. The fault-insensitive parameters or states 192
6.3.4. The fault-sensitive parameters or states 193
6.3.5. The damage progression model 196

7. PROGNOSIS OF THE HELICOPTER TRANSMISSION 197

7.1. Model-based prognosis of the helicopter transmission fault 198

7.2. Damage progression model of the planetary carrier crack 200

7.2.1. Initial conditions: the starting crack length 201
7.2.2. Loading profile 202
7.2.3. The fault-insensitive parameters 205
7.2.4. The fault-sensitive parameters 206
7.2.5. The crack growth model 206

7.3. The crack growth equation used 208

7.3.1. The perspective of linear elastic fracture mechanics 208
7.3.2. Geometric crack-tip stress intensity factors 210
7.3.3. The limiting cases of plane stress and plane strain 211
7.3.4. Paris Law and Elber's crack closure model 212

7.4. Determination of the static crack-tip stress intensity factors through FEA 217

7.4.1. Preliminary considerations 217
7.4.2. Determination of the static crack-tip stress intensity factors as a function of crack length and shape 217
7.4.3. Determination of crack-tip stress intensity factors as a function of applied load (torque) 222

7.5. Application of the loading profile in the crack growth model 223

7.5.1. Preliminary considerations 223
7.5.2. Plasticity-induced crack closure 224
7.5.3. Effective crack-tip stress intensity range 226
7.5.4. Application of variable-amplitude loading 228

7.5.4.1. GAG cycles varying the load from 20% to 120% of nominal engine torque 229
7.5.4.2. GAG cycles varying the load from 20% to 93% of nominal engine torque 232
7.5.4.3. Application of load cycles 232

7.6. Simulation of damage progression and model validation 238

8. CONCLUSIONS AND FUTURE WORK 241

REFERENCES 245

LIST OF TABLES

Table 2.1. Comparative table of approaches to maintenance of engineering systems 13

Table 3.1. Sources of experimental data for the validations and results presented in this thesis 41

Table 3.2. Sideband suppression pattern of a planetary gearbox with $N_p = 3$ and $N_t = 134$. Clear cells marked with "0" correspond to sidebands that become suppressed. Sidebands, each of whose frequency can be evaluated as $(m \cdot N_t + n) \cdot f^s$, subsist only when $(m \cdot N_t + n) / N_p$ is an integer 49

Table 5.1. Sideband suppression pattern of a planetary gearbox with $N_p = 5$ and $N_t = 228$. Clear cells marked with "0" correspond to sidebands that become suppressed. Compare to Table 3.2 109

Table 5.2. Pattern of sideband locations for the planetary gearbox of the helicopter transmission gearbox in focus. The pattern shows the values of n at which sidebands are dominant or apparent near tooth meshing harmonics. Five tooth meshing harmonics are listed (m = 1 to 5) 109

Table 5.3. Characteristics of the finite element model of the planetary carrier plate 124

Table 5.4. Static shift angles, in degrees, of planet gears at 100% of nominal engine torque (54,000 lb·ft) caused by the presence of different cracks on the planetary carrier plate. The crack is located on the root of the mounting post of planet gear number 1. Angles are measured with respect to the planet gear positions of the unforced plate 134

Table 5.5. Characteristics of the examples used to show that adding noise to the gearbox vibration model improves the replication of vibration characteristics of experimental data 155

Table 7.1. Crack-tip stress intensity factors obtained from ANSYS. The simulations were run using the same half-lengths in the inboard and outboard sides of the crack, i.e., inboard length = outboard length = (total length / 2) 222

Table 7.2. Summary of assumed loading profile parameters for the crack growth experiment with the helicopter transmission planetary carrier plate 237

LIST OF FIGURES

Figure 1.1. Scheme of organization of the thesis 9

Figure 2.1. Comparison of situations where the physics-based approach or the data-driven approach are appropriate. Adapted from Inman et al. (2005), p. 6 18

Figure 2.2. An overview of the general approach to performing model-based fault detection, the fundamental aspect of model-based diagnostics 19

Figure 2.3. Parameter estimation procedure 20

Figure 2.4. Residual evaluation procedure 20

Figure 2.5. Hierarchical classification of approaches to prognostics. Reproduced from Byington et al. (2002) 23

Figure 2.6. Finite element computer model of a mechanical component. The design has been divided into finite elements thorough a process known as *meshing* 26

Figure 2.7. Illustration of some of the functions of nodes in a finite element model 27

Figure 3.1. Mechanical components of the helicopter transmission of focus in this thesis 34

Figure 3.2. Planetary gear carrier plate of a UH-60A Blackhawk helicopter. Photographs reproduced from Sahrmann (2004) 35

Figure 3.3. Top view of helicopter transmission gearbox assembly. Reproduced from Keller and Grabill (2003) 42

Figure 3.4. Representation of a planetary gear system with 5 planet gears 44

Figure 3.5. Representation of a planetary gear with vibration sensor fixed on the annulus gear 46

Figure 3.6. Vibration signature of the main rotor gearbox of a "Sea King" helicopter, used by McFadden and Smith to illustrate their findings. Adapted from McFadden and Smith (1985) 47

Figure 3.7. Simulated spectrum representation of vibrations generated by a planetary gear 48

Figure 3.8. Magnitude spectrum of non-epicyclic tooth meshing vibration as seen from a fixed point on the planetary carrier 51

Figure 3.9. Representation of the intensity of the meshing vibration signal of a single planet gear in translation as perceived on a fixed point (vibration sensor) over the annulus gear 51

Figure 3.10. Magnitude spectrum of the modulation signal caused by the translation motion of a planet gear 52

Figure 3.11. Vibration spectrum of a single planet gear 56

Figure 3.12. Sidebands of equally spaced planetary gearbox with $N_p = 3$ and $N_t = 134$ 59

Figure 3.13. Angular shift of planet gear number 3 in a system with $N_p = 3$ 60

Figure 3.14. Effect of angular planet-gear shift on the phase of a planet gear's sidebands 62

Figure 3.15. Sideband phase change $\Delta\varphi_{p,m,n}$ of the dominant sideband ($n = 0$) as a function of the geometric angular shift δ_p of a planet gear for different tooth meshing harmonics 64

Figure 3.16. Phasor representation of the formation of planetary system sidebands through addition of individual planet-gear sidebands 65

Figure 3.17. Effect of single-planet-gear shift in the magnitude of dominant (or apparent) and non-dominant sidebands for a system with three planet gears and unity single-planet sideband magnitudes 66

Figure 3.18. Comparison of sidebands in the spectra of an equally spaced planetary gearbox and a gearbox with planetary shifting 67

Figure 3.19. Effect of single-planet-gear shift on the formation of dominant and apparent sidebands 68

Figure 3.20. Effect of single-planet-gear shift on the formation of non-dominant sidebands 69

Figure 3.21. Illustration of the case when dominance of sidebands can switch from a sideband to an adjacent sideband 73

Figure 3.22. Vibration spectrum for test cell gearboxes with $N_p = 5$ planet gears and $N_t = 228$ teeth in the annulus gear. One of the gearboxes had a 3.25-inch crack on the root of a mounting post of one of the planet gears in the planetary carrier plate. Engine torque is 20% of the nominal 76

Figure 3.23. Vibration spectrum for test cell gearboxes at 30% engine torque 77

Figure 3.24. Vibration spectrum for test cell gearboxes at 50% engine torque 77

Figure 3.25. Vibration spectrum for test cell gearboxes at 70% engine torque 77

Figure 3.26. Vibration spectrum for test cell gearboxes at 90% engine torque 78

Figure 3.27. Vibration spectrum for test cell gearboxes at 100% engine torque 78

Figure 3.28. Vibration spectrum for on-aircraft gearboxes with $N_p = 5$ planet gears and $N_t = 228$ teeth in the annulus gear. Engine torque is 20% of the nominal 79

Figure 3.29. Vibration spectrum for on-aircraft gearboxes at 30% engine torque 79

Figure 3.30. Representation of vibration snapshots taken for the crack growth experiment of a seeded crack in a planetary carrier plate 81

Figure 3.31. Categorization of planetary gear spectrum sidebands for a planetary gearbox with $N_p = 5$ planet gears 82

Figure 3.32. Progression of sideband magnitudes for frequency components as a function of crack length at 20% of nominal engine torque 84

Figure 3.33. Progression of sideband magnitudes for frequency components as a function of crack length at 40% of nominal engine torque. 85

Figure 3.34. Progression of sideband magnitudes for frequency components as a function of crack length for 100% of nominal engine torque up to about 3.3 inches and 93% engine torque thereafter 86

Figure 4.1. Suggested architecture for performing model-based simulation of systems with a static fault 90

Figure 4.2. Approach suggested for performing fault identification. Compare to the general approach followed in fault detection, shown in Figure 2.2. 96

Figure 4.3. Reverse engineering approach to fault identification through residual evaluation. This technique shows the application of the approach suggested in Figure 4.2 to the procedure followed in Figure 2.4. 97

Figure 5.1. Representation of the path of transmission of power from the engines through the planetary gear transmission to the main rotor blades of the helicopter 101

Figure 5.2. Representation of the major forces acting on the planetary carrier plate of the planetary gearbox of the helicopter transmission during operation 102

Figure 5.3. Application of the technique of Figure 4.1 to the problem of simulating the vibration of a faulted helicopter transmission 104

Figure 5.4. Representation of the $\alpha_n\beta_m$ factors describing the amplitude of different frequency components in the vibration signature of the helicopter's planetary gearbox 107

Figure 5.5. Procedure followed for characterizing sidebands in experimental vibration data of a planetary gearbox using the vibration model 108

Figure 5.6. Procedure for estimating the fault-insensitive α and β parameters of a planetary gearbox using experimental vibration data 111

Figure 5.7. Weighting function utilized to approximate the frequency response parameters α_n and β_m in the planetary gearbox vibration experiments. This weighting function is applied as defined by Equation 5.5 114

Figure 5.8. Results of the characterization of the α_n and β_m parameters of a healthy planetary gearbox transmission operating in a test cell at 20% of nominal torque 116

Figure 5.9. Results of the characterization of the α_n and β_m parameters of a healthy planetary gearbox transmission operating in a test cell at 50% of nominal torque 117

Figure 5.10. Results of the characterization of the α_n and β_m parameters of a healthy planetary gearbox transmission operating in a test cell at 100% of nominal torque 118

Figure 5.11. Results of the characterization of the α_n and β_m parameters of a planetary gearbox transmission with a small crack (1.34 inches), but assumed to be healthy, operating in a test cell at 20% of nominal torque 119

Figure 5.12. Results of the characterization of the α_n and β_m parameters of a planetary gearbox transmission with a small crack (1.34 inches), but assumed to be healthy, operating in a test cell at 40% of nominal torque 120

Figure 5.13. Results of the characterization of the α_n and β_m parameters of a planetary gearbox transmission with a small crack (1.34 inches), but assumed to be healthy, operating in a test cell at 100% of nominal torque 121

Figure 5.14. Three-dimensional computer model of the planetary carrier plate as used for deformation analysis 123

Figure 5.15. Representation of the forces acting on the gear teeth of the planetary gears 126

Figure 5.16. Representation of the application of loads and constraints to the planetary carrier plate in the finite element model 127

Figure 5.17. Definition of the axes of deflection at individual planetary gear mounting posts..... 127

Figure 5.18. Representation of the gear mesh clearance of a planet gear..... 128

Figure 5.19. View of the finer mesh used in regions near the simulated crack plane of the planetary carrier plate model 129

Figure 5.20. Views of a crack design in the finite element model of the planetary carrier plate 130

Figure 5.21. Procedure for simulating the presence of a crack in a finite element model 130

Figure 5.22. View of open crack in the finite element model of the planetary carrier plate, corresponding to the design of Figure 5.20 131

Figure 5.23. Illustration showing example results of the FEA analysis of the deformation experienced by the planetary carrier plate exhibiting a crack more than 7 inches long..... 132

Figure 5.24. Illustration of the deflection experienced by different regions of the planet gear mounting posts of the planetary carrier plate..... 133

Figure 5.25. Nodes on the planet gear mounting posts of the carrier plate model are used to approximate the geometric center of the planet gears and estimate the planet-gear shift angles caused by deformation of the plate 133

Figure 5.26. Graph of the static shift angles, in degrees, of planet gears at 100% of nominal engine torque (54,000 lb·ft) as a function of the length of a crack present on the planetary carrier plate..... 135

Figure 5.27. Graph of the static shift angles, in degrees, of the planet gear whose mounting post has a crack on the planetary carrier plate. Shift angles are plotted as a function of crack length and percent of nominal engine torque..... 136

Figure 5.28. Evaluation of vibration-based SI and SLF condition indicators for five different helicopters. Helicopter number 1 is known to have a crack in the planetary carrier plate of about 3.5 inches in length..... 140

Figure 5.29. Illustration of the effect of continuous small angular shifts in multiple planet gears 142

Figure 5.30. Effect of noise and variability levels on the sidebands at different frequency regions..... 145

Figure 5.31. Effect of single-planet-gear shift on basic sideband magnitude metrics. The planet-gear shifts considered are "small", i.e., $\Delta\varphi < \pi$ for all cases shown (Compare to Figure 3.17)..... 148

Figure 5.32. Definition of N_p-sideband groups..... 149

Figure 5.33. Illustration of the difference in the levels of non-dominant sidebands between a noiseless model and experimental data. Model parameters were extracted from a different system than the one providing the experimental data shown..... 157

Figure 5.34. Illustration of the difference in the levels of non-dominant sidebands between a noiseless model and experimental data. Model parameters were extracted from the same system than the one providing the experimental data shown..... 158

Figure 5.35. Illustration of the effect of noise in the feature values calculated from simulated vibration signals of the helicopter planetary gearbox..... 159

Figure 5.36. Illustration of the procedure followed to perform calibration of the noise levels in modeled gearbox vibration sidebands..... 164

Figure 5.37. Results of noise calibration using the calibration procedure variant number 1 at 40% of nominal engine torque..... 165

Figure 5.38. Results of noise calibration using the calibration procedure variant number 2 at 100% of nominal engine torque..... 167

Figure 5.39. Results of noise calibration using the calibration procedure variant number 2 at 40% of nominal engine torque..... 167

Figure 5.40. Comparison of feature values extracted from the helicopter transmission vibration and features extracted from the vibration produced by simulations with the planetary gear vibration model. The model uses the noise-calibration procedure variant number 1. Torque is 100%..... 170

Figure 5.41. Comparison of feature values extracted from the helicopter transmission vibration and features extracted from the vibration produced by simulations with the planetary gear vibration model. The model uses the noise-calibration procedure variant number 1. Torque is 40%..... 171

Figure 5.42. Comparison of values for the feature of Figure 5.40 in its harmonically averaged form..... 172

Figure 5.43. Comparison of values for the feature of Figure 5.41 in its harmonically averaged form..... 172

Figure 5.44. Comparison of feature values extracted from the helicopter transmission vibration and features extracted from the vibration produced by simulations with the planetary gear vibration model. The model uses the noise-calibration procedure variant number 2. Torque is 100% 173

Figure 5.45. Comparison of feature values extracted from the helicopter transmission vibration and features extracted from the vibration produced by simulations with the planetary gear vibration model. The model uses the noise-calibration procedure variant number 2. Torque is 40% 174

Figure 5.46. Comparison of values for the feature of Figure 5.44 in its harmonically averaged form 175

Figure 5.47. Comparison of values for the feature of Figure 5.45 in its harmonically averaged form 175

Figure 5.48. Application of the "reverse engineering" approach for performing model-based fault diagnostics with the helicopter transmission problem 178

Figure 5.49. Illustration of the procedure followed to match experimental feature values to model feature data to perform crack length identification 179

Figure 5.50. Example vibratory feature value data as a function of crack length for experimental data and model data 180

Figure 6.1. A generic approach to model-based prognostics 182

Figure 6.2. Suggested architecture for performing model-based simulation of systems with a dynamic fault 188

Figure 6.3. Illustration of how different loading profiles can be selected for simulating the progression of damage in a system 191

Figure 6.4. The on-line and off-line approaches to the dynamic determination of parameters and states of a prognostic model 195

Figure 7.1. Application of the technique of Figure 6.1 for performing model-based prognostics to the helicopter transmission problem 199

Figure 7.2. Application of the technique of Figure 6.2 for performing model-based simulation of the damage progression in the planetary carrier plate 201

Figure 7.3. Definition of the crack length and the inboard and outboard directions of crack growth on the planetary carrier plate 202

Figure 7.4. Illustration of the application of ground-air-ground (GAG) cycles in the operation of the helicopter transmission during the crack progression experiment 203

Figure 7.5. Approximate pattern of individual GAG cycles used in the crack progression experiments 204

Figure 7.6. Assumed composite loading of the planetary gearbox 205

Figure 7.7. Crack growth model used in the helicopter transmission problem 207

Figure 7.8. Basic geometric definitions in fracture studies 209

Figure 7.9. Fatigue-crack-propagation data for Ti-6Al-4V titanium alloy. Relationship to the values of the constants *C* and *m* of Paris Law is illustrated. Adapted from Rice et al. (2003) 214

Figure 7.10. Illustration of constant-amplitude load cycles at different mean levels of the stress intensity. Reproduced from Sanford (2003), p. 292 215

Figure 7.11. Collapsing of the side of a finite element to be used for modeling and simulating crack tip stresses and displacements 218

Figure 7.12. Illustration of how crack-tip stress intensity factors can be determined for different lengths and locations along the crack front 219

Figure 7.13. Three-dimensional computer model of the planetary carrier plate as used for crack-tip stress studies 220

Figure 7.14. Details on the finite element modeling of crack tips 221

Figure 7.15. Illustration of the stresses appearing in the material around the crack tip in the wake of plasticity-induced crack closure. Reproduced from Anderson (1995), p. 540 225

Figure 7.16. Definition of the effective crack-tip stress intensity range. Reproduced from Anderson (1995), p. 521 227

Figure 7.17. Illustration of the crack closure threshold for GAG cycles 1 through 320 231

Figure 7.18. Example of simplified rainflow cycle counting. Reproduced from ASTM (2005) 233

Figure 7.19. Instrumentation for measuring the progression in length of a crack and certain localized strains on the root of a planet gear mounting post of a planetary carrier plate with a seeded fracture. Reproduced from Vachtsevanos et al. (2006) 239

Figure 7.20. Comparison of crack growth model of the planetary carrier plate and experimental crack growth data 240

LIST OF SYMBOLS

1. Remarks about the nomenclature followed

The application aspect of the present work spans multiple engineering disciplines, the most notable of which are vibration and signal analysis, and fracture mechanics. Each discipline utilizes particular symbols to describe physical or mathematical parameters of importance. However, some of the symbols used to represent different parameters are the same across different disciplines, even if the parameters are completely unrelated. Such is the case, for example, of the Greek-alphabet letter σ, which is generally recognized to represent the *standard deviation* in Statistics and signal analysis, and the *stress* in Mechanical Engineering.

Although it would have been possible to assign different symbols to different parameters to avoid confusion within this document, it was decided not to proceed thus. The approach has been to maintain the standard use of symbols followed by each concerning discipline, even if the symbols are reused. Confusion is averted by focusing in individual chapters. Thus, all symbols used within each chapter have been ensured to maintain one definition only. Chapters 3 through 5 will follow the symbol definitions concerning analysis of vibration. Chapter 5 additionally uses unambiguous symbols to represent vibration-based condition indicators. Chapters 6 and 7 will follow the symbol definitions concerning fracture analysis. The symbol definitions for each of these areas of concern are listed, separately, below.

2. Symbols used in the analysis of vibration of gearboxes[1] – Chapters 3 through 5

α_n Amplitude of component n in the frequency representation of the intensity curve of the meshing vibration signal of a single planet gear in translation as perceived on a fixed point over the annulus gear; note that $\alpha_n = \alpha_{-n}$ for all values of n

β_m Amplitude of harmonic component m in the non-epicyclic tooth meshing vibration signal of a pair of gears as measured from a fixed point

δ_p Angular shift of planet gear number p in a planetary gearbox, as measured with respect to its corresponding θ_p; a gearbox with equally spaced planet gears would have $\delta_p = 0$ for all p

$\Delta\varphi_{p,m,n}$ Change in the phase angle $\varphi_{p,m,n}$ in sideband (m, n) resulting from an angular shift δ_p in planet gear number p of a planetary gearbox

η A normally distributed random variable with mean μ and variance σ^2

η_m A normally distributed random variable with zero-mean (μ=0) and variance σ_m^2

$\eta_{m,n}$ A random variable with mean $\mu_{m,n}$ and variance $\sigma_{m,n}^2$

θ_p Angular position of planet gear number p over the planetary carrier in a planetary gearbox

μ Mean of a normal probability distribution

$\mu_{m,n}$ Mean of random variable $\eta_{m,n}$. $\mu_{m,n}$ is approximately equal to the mean value of $SB_{m,n}$ in a particular set of experimental gearbox vibration data that is affected by the presence of noise

π The mathematical constant describing the ratio of a circle's perimeter to its diameter

σ^2 Variance of a normal probability distribution

[1] When referring to certain aspects of gearbox vibration, the present work sometimes refers and expands on the ideas presented by McFadden and Smith (1985) and by Keller and Grabill (2003). Their respective works used different notations for certain physical magnitudes that were, however, common between them. For those magnitudes that are of concern in this thesis, not to suggest a third notation system and considering that the work of Keller and Grabill is more recent, the notation used by Keller and Grabill is given preference, although not always strictly followed. Deviations from their notation system are expressly identified in footnotes.

σ_m^2 Variance of the random variable η_m. σ_m^2 is the variance that is added to a series of sidebands $SB_{m,n}$, for $n = -N$ to N, in the spectrum of simulated gearbox vibration to approximate the behavior of the corresponding series of $SB_{m,n}$ in a particular set of experimental gearbox vibration data that is affected by the presence of noise. The behavior approximated is that shown by the evaluation of vibration-based condition indicators

$\sigma_{m,n}^2$ Variance of random variable $\eta_{m,n}$. $\sigma_{m,n}^2$ is the variance that is added to sideband $SB_{m,n}$ in the spectrum of simulated gearbox vibration to approximate the behavior the corresponding $SB_{m,n}$ in a particular set of experimental gearbox vibration data that is affected by the presence of noise. The behavior approximated is that shown by the evaluation of vibration-based condition indicators. $\sigma_{m,n}^2$ is approximately equal to the variance of $SB_{m,n}$ in the experimental gearbox vibration

$\Phi_{m,n}$ Phase angle of sideband (m, n) in the spectrum of the planetary gearbox (vibration of all planet gears combined)

$\vec{\Phi}_{m,n}$ Phasor (vector quantity representation) of sideband (m, n) in the spectrum of the planetary gearbox (vibration of all planet gears combined)

$\Phi_{m,n}^{\text{equal-spc}}$ The value of $\Phi_{m,n}$ in a planetary gearbox with equally spaced planet gears

$\Phi_{m,n}^{\text{shifted}}$ The value of $\Phi_{m,n}$ in a planetary gearbox with unequally spaced planet gears

$\varphi_{p,m,n}$ Phase angle of sideband (m, n) in the spectrum of planet gear number p

$\vec{\varphi}_{p,m,n}$ Phasor (vector quantity representation) of sideband (m, n) in the spectrum of planet gear number p

$\varphi_{p,m,n}^{\text{equal-spc}}$ The value of $\varphi_{p,m,n}$ in a planetary gearbox with equally spaced planet gears

$\varphi_{p,m,n}^{\text{shifted}}$ The value of $\varphi_{p,m,n}$ in a planetary gearbox where planet gear number p has shifted away from the equally spaced angular position

c Constant factor for characterizing the amplitude of sidebands; $c = N_p/2$ for sidebands with n=0; $c = N_p/4$ for sidebands with $n \neq 0$

e_i Individual "error" terms used in the implementation of least squares optimization

d Value of n for which sideband $(m, n = d)$ is dominant[2] (see section 3.4.4)

f Frequency

f^s Planetary carrier plate rotation frequency (f_c for McFadden and Smith)

[2] Keller and Grabill refer to this parameter as n_{dominant}. For simplicity, d is used instead within this thesis.

G	Index for N_p-Sideband Groups (see section 5.5)
i	Index for error and weight terms in the implementation of least squares optimization
K	Total number of elements in an indexed series
k	Discrete, integer index; this symbol is used in generalizations
M	Total number of harmonics of the tooth meshing frequency to consider in vibration analyses
m	Index for harmonics of the tooth meshing frequency; $m = 1, 2, \ldots, M$
(m, n)	Identifier pair for specific sidebands (frequency components) in the vibration of a planetary gearbox; (m, n) refers to the sideband located at frequency $f = (m \cdot N_t + n) \cdot f^s$
N	Total number of multiples of the carrier rotation frequency to consider in vibration analyses
n	Index for multiples of the carrier plate rotation frequency[3]; $n = -N, \ldots, -1, 0, 1, \ldots, N$ [4]
N_p	Total number of planet gears in a planetary gearbox (referred to as N by McFadden and Smith)
N_t	Number of teeth in the annulus gear of a planetary gearbox (Z_a for McFadden and Smith)
p	Index for the number of planet gears present in a specific geometry of a planetary gear arrangement[5]
$SB_{m,n}$	Half amplitude of the frequency component located at frequency $f = (m \cdot N_t + n) \cdot f^s$, i.e., of sideband (m, n), in the vibration signal of a planetary gearbox. Note that $SB_{m,n} = \lvert \vec{\Phi}_{m,n} \rvert$
$SB_{m,n}^{\text{experim}}$	The mean value of $SB_{m,n}$ in experimental vibration that is affected by noise

[3] Keller and Grabill refer to this parameter as an "index of shaft harmonics". This term may be somewhat misleading because, strictly speaking, we are not studying vibrations of the shaft (i.e., we are not considering its fundamental vibration frequency and harmonics). Rather, following in the steps of McFadden, we are concerned with the **modulation effect** caused by the rotation of the planet gears around the sun gear at the angular speed (frequency) of the planetary carrier plate. This modulating signal can be decomposed in the frequency domain to generate **indexed coefficients** (in n) that, although being multiples of the carrier plate or "shaft" rotation frequency, are in cases like this not typically referred to as harmonics, but as **frequency** or **spectral components** instead. McFadden referred to these as "nth sidebands."

[4] McFadden and Smith defined n as an integer number. Keller and Grabill used it as a nonnegative integer in their equations, so that in their paper we see two terms whenever n is referenced, one for $+n$ and one for $-n$. In this thesis, McFadden's definition is followed to avoid this duplication.

[5] Keller and Grabill refer to this parameter as n_p. To avoid a sub-sub-index notation necessary in some equations, the single letter p is used in this thesis.

$SB_{m,n}^{\text{noiseless}}$	The value of $SB_{m,n}$ in a simulated vibration signal before simulated noise is added
$SB_{m,n}^{\text{noisy}}$	The value of $SB_{m,n}$ in a simulated vibration signal after simulated noise is added
T_p	Time it takes for planet gear number p to reach the closest point to a vibration sensor mounted on the annulus gear of a planetary gearbox (see section 3.3.2.3)
t	Time
w_i	Weights for the individual error terms used in the implementation of least squares optimization
X	Number of adjacent sideband groups taken in averaging operations for condition indicator evaluations (see section 5.5.3)
x	Any discrete-time signal
x_k	Individual discrete-time samples of signal x, indexed in k.
y	Vibration signal of a planetary gearbox in continuous time
y_p	Vibration signal generated individually by planet gear number p in a planetary gearbox in continuous time

3. Vibration-based condition indicators (vibratory features) – Chapter 5

avgND	Average size of non-dominant sidebands
BrelSG	Basic relative size of sidebands in an N_p-sideband group
BrelSX	Group averaging of BrelSG
HA	Harmonic averaging operation; can be applied to any relative feature. The HA operation is specified as a sub-index; for example relSX_{HA} is the harmonic averaging of the relSX feature
relHSI	Size-X relative harmonic sideband index
relSG	Compensated relative size of sidebands in an N_p-sideband group
relSI	Relative sideband index
relSX	Group averaging of relSG
SI	Sideband index
SLF	Sideband level factor

4. Symbols used in fracture analysis – Chapters 6 and 7

α	Newman's crack closure model constraint factor
ΔK	Crack-tip stress intensity range
ΔK_{eff}	Effective crack-tip stress intensity range
$\Delta K_{eff,\text{ torque cycle}}$	Effective crack-tip stress intensity range for a full cycle of torque applied to a helicopter transmission
$\Delta K_{eff,n}$	Effective crack-tip stress intensity range for a cycle of load described within a series n of similar cycles applied to a helicopter transmission
θ	Angular coordinate in a polar coordinate system
π	The mathematical constant describing the ratio of a circle's perimeter to its diameter
σ	Directional stress in a specific spatial location near a crack tip; the parameter is either used generally or direction is made clear by the context of use; the direction be any of the x, y, or z directions of a normal stress, or the xy, yz, or zx directions of a shear stress
σ_{op}	Crack-opening stress
σ_y	Newman's closure model flow stress
A_n	Amplitude of load cycles in a particular series of cyclic loads. The series is identified by the sub-index n
a	Crack length
C	Fatigue crack growth coefficient
f	Function
K	Geometric crack-tip stress intensity factor
K_{Load}	Instantaneous value of K for a particular application of a static load. The value of the load, referenced by the sub-index, is in percent of the nominal engine torque of the helicopter
$K_{\max}$	Maximum value of K within an individual fatigue load cycle
K_{mean}	Mean value of K within an individual fatigue load cycle
$K_{\min}$	Minimum value of K within an individual fatigue load cycle
K_{op}	Instantaneous value of K within a load cycle when $\sigma = \sigma_{op}$
$K_{p\varepsilon}$	Value of K for a particular case assuming plane-strain conditions
$K_{p\sigma}$	Value of K for a particular case assuming plane-stress conditions
m	Fatigue crack growth exponent
N	Index for the number of load cycles applied causing fatigue of a material

n	Index for a particular series of cyclic loads applied to the helicopter transmission. All series described by a particular n have cycles that are comparable in some way
r	Radial coordinate in a polar coordinate system
R	Stress intensity ratio; $R = K_{\min} / K_{\max}$
S	Instantaneous load
$S^{\%}$	Normalized load
$S_{\max}$	Maximum value of a cyclic load
$S^{\%}_{\max}$	Normalized value of maximum cyclic load
$S^{\%}_{\text{mean, }eff}$	Normalized mean effective load
$S_{\min}$	Minimum value of a cyclic load
$S^{\%}_{\min}$	Normalized value of minimum cyclic load
S_{op}	Instantaneous value of the load S at which K_{op} exists
$S^{\%}_{op}$	Normalized value of S_{op}
U	Elber's effective stress correction factor; $\Delta K_{eff} = U \cdot \Delta K$
x	Distance on the horizontal (x) axis

SUMMARY

This thesis presents a framework for integrating models, simulation, and experimental data to diagnose incipient failure modes and prognosticate the remaining useful life of critical components, with an application to the main transmission of a helicopter. Although the helicopter example is used to illustrate the methodology presented, by appropriately adapting modules, the architecture can be applied to a variety of similar engineering systems. Models of the kind referenced are commonly referred to in the literature as *physical* or *physics-based* models. Such models utilize a mathematical description of some of the natural laws that govern system behaviors.

In recent years, a paradigm shift has been introduced in the way critical systems are maintained and operated to ensure their safety, availability and reliability. The technology base is focusing on technologies to monitor, process on-line real-time data, and detect and predict the remaining useful life of failing components or subsystems. The military and industrial sectors are recognizing the importance of such condition-based maintenance (CBM) or prognostic and health management (PHM) technologies, and are actively pursuing their development and implementation.

The present work addresses a significant component of CBM or PHM. An attempt is made to (1) detect and identify a fault before an engineering system is brought to failure, and (2) provide information about how much time the system can operate safely before it fails. This work provides a way to integrate these two activities by relying on models of the system's behavior.

The methodology presented considers separately the aspects of diagnosis and prognosis, but a similar generic framework is proposed for both. However, for diagnosis, a fault is viewed as a static event, whereas prognosis considers its future dynamics. The methodology is tested and validated through comparison of results with experimental data obtained from helicopters in operation, and from a test cell employing a prototypical helicopter gearbox. Two kinds of experiments have been used. The first one retrieved vibration data from several healthy and faulted aircraft transmissions in operation. The second is a seeded-fault damage-progression test providing vibration data and ground truth data of increasing crack lengths. Both kinds of experiments collected vibration data through a number of accelerometers mounted on the frame of the transmission gearbox.

The applied architecture consists of modules with key elements such as the modeling of vibration signatures, extraction of descriptive vibratory features, finite element analysis of a gearbox component, and characterization of fracture progression.

Contributions of the thesis include: (1) generic model-based fault diagnosis and failure prognosis methodologies, readily applicable to a dynamic large-scale mechanical system; (2) the characterization of the vibration signals of a class of complex rotary systems through model-based techniques; (3) a “reverse engineering” approach for fault identification using simulated vibration data; (4) the utilization of models of a faulted planetary gear transmission to classify descriptive system parameters as fault-sensitive or fault-insensitive; and (5) guidelines for the integration of the model-based diagnosis and prognosis architectures into prognostic algorithms aimed at determining the remaining useful life of failing components.

1. INTRODUCTION

1.1. Outline

This thesis presents a framework for integrating models, simulation, and experimental data to diagnose incipient failure modes and prognosticate the remaining useful life of critical components, with an application to the main transmission of a helicopter. Although the helicopter example is used to illustrate the methodology presented, by appropriately adapting modules, the architecture can be applied to a variety of similar engineering systems. Models of the kind referenced primarily are commonly referred to in the literature as *physical* or *physics-based* models. Such models utilize a mathematical description of some of the natural laws that govern system behaviors.

This research addresses a significant component of condition-based maintenance (CBM) or prognostic and health management (PHM) technologies, focusing on technologies to monitor, process on-line real-time data, and detect and predict the remaining useful life of failing components or subsystems.

The methodology presented considers separately the aspects of diagnosis and prognosis, but a similar generic framework is proposed for both. An important difference between the two, however, is that, for diagnosis, a fault is viewed as a static event, whereas prognosis considers its future dynamics. The methodology is tested and validated through comparison of results to data from experiments carried out on helicopters in operation and a test cell employing a prototypical helicopter gearbox. Two

kinds of experiments have been used. The first kind retrieved vibration data from several healthy and faulted aircraft transmissions in operation. The second kind is a seeded-fault damage-progression test providing gearbox vibration data and ground truth data of increasing crack lengths. For both kinds of experiments, vibration data were collected through a number of accelerometers mounted on the frame of the transmission gearbox.

The applied architecture consists of modules with the following key elements:

- Vibration signature analysis and extraction of descriptive vibratory features,
- Vibration signature characterization and modeling under both healthy and faulted conditions,
- Finite Element Analysis of a gearbox component under varying operating conditions to determine the effect of different extents of damage, and
- Characterization of fracture progression.

1.2. Overview and Objective of this Thesis

Mechanisms, machines and all kinds of devices on which engineering systems depend can fail *unexpectedly*. This places the lives of innumerable human beings, scientific progress and the efforts of industry and government to provide goods, services and safety in constant peril. Thus, we have an interest in *preventing* the occurrence of *failure* in an engineering system.

In recent years, a paradigm shift has been introduced in the way critical systems are maintained and operated to ensure their safety, availability and reliability. The technology base is focusing on technologies to monitor, process on-line real-time data, and detect and predict the remaining useful life of failing components or subsystems. The military and industrial sectors are recognizing the importance of such condition-based maintenance (CBM) or prognostic and health management (PHM) technologies, and are actively pursuing their development and implementation.

The present work falls within the arena of predictive maintenance, addressing a significant component of CBM or PHM, where an attempt is made to (1) detect and identify a fault before an engineering system is brought to failure and (2) provide information about how much time a system can operate before it fails. There are multiple ways of approaching these two areas of concern, and in fact, they can be considered separately and independently of each other. However, this work provides a way to integrate these two activities by relying on models of a system's behaviors.

The objective of the present work is to present a framework for integrating models, simulation, and experimental data to diagnose incipient failure modes and prognosticate the remaining useful life of critical components, with an application to the main transmission of a helicopter. Although the helicopter example is used to illustrate the methodology, by appropriately adapting modules, the architecture can be applied to a variety of similar engineering systems.

1.3. Approach and Validation

Mathematical models and descriptions of engineering systems and particular system behaviors are typically available even before a system is built; think, for example, of those needed in the design stage. While it is advantageous to thus have models readily available, it must be noted that models are largely used to reproduce the expected behavior of certain variables in a system under *normal* operation, i.e., without faults of any kind. However, to perform diagnosis and prognosis, models that represent the operation of a system at *fault* are needed. Furthermore, mathematical models most commonly address narrow characteristics or specific variables of engineering subsystems, and not the functional interaction of these as a whole in a complex machine or device. A diagnosis or prognosis will likely address this interaction and the effects of a fault or damage.

Realizing a model-based, health-management architecture for a complex engineering system can be a daunting task. There are many aspects to consider, the most obvious of which may be the choice and complexity of the models themselves, which may depend on analyses from a wide variety of engineering disciplines. There are also issues like determining how best to use the data from the models, how to validate them under a wide variety of operating and fault conditions, how to deal with uncertainties in results and parameters, etc. If this were not enough of a challenge, there is still the problem of integrating solutions to all of these concerns into a procedure that provides reliable information about the conditions of a system in operation.

The present work establishes methods to facilitate the overcoming of some of these difficulties, and its foundation is the proposition of modular considerations of the problems of designing model-based diagnosis and prognosis architectures. Thus, in a manner typically followed within the engineering realm of *systems and controls*, the approach of this work has been to identify distinct "building blocks" or *functional modules* that may be used as part of a diagnostic or prognostic operation in a variety of engineering systems. These modules have been deliberately defined to address specific challenges in designing model-based architectures, some like those mentioned above.

The modular approach is in line with the intent to adopt a so-called *system of systems* approach for the present research. Better expressed, this research follows a *system of subsystems approach*. The subsystems in question are many, and include, for example, the diagnostic and prognostic subsystems, the inner components of each of these two (like the physics-based models, the model adaptation routines, the data acquisition devices, the data preprocessing algorithms, etc.) or the operation regimes or assumption sets. Results from the system of systems approach are evident throughout this thesis. It is possible to identify the definition of blocks with particular functionality in different sections, as well as the interconnections of these blocks to perform more and more complex tasks.

The identification of individual functional and analysis modules has also made it possible to perform relatively independent work in the fields of engineering that must be addressed to analyze a system like the helicopter transmission that is being considered, including fracture mechanics, finite element analysis, signal processing, system

identification, and mechanics and vibration of geared systems, among others. The two major modules of the architecture are the diagnostic and prognostic modules. These two modules are comprised of other sub-modules with the following key functions:

- Vibration signature analysis and extraction of descriptive vibratory features in standard fashion, including the use of techniques for preprocessing and interpreting mechanical vibration signals (like time-synchronous averaging and frequency component analysis).

- Vibration signature characterization and modeling, with foundations on developments by experts in the field of mechanical vibrations of geared systems, including the analysis of vibration components, the effects of frequency modulation caused by the rotary motion, and the determination of vibration changes induced by the appearance of a fault. This modeling effort also incorporates system-specific parameters and effects (e.g., frequency response, noise, etc.).

- Finite Element Analysis (FEA), utilizing the widely-known ANSYS software package, of the system geometry under varying operating conditions to determine the mechanical effect caused by different extents of damage, including deformation patterns of the gearbox and structural stress distributions, especially at critical locations like fracture fronts.

- Use of an empirical model and considerations for characterizing crack growth, based on developments in the field of Fracture Mechanics, including adaptations of the

famous Paris' law of crack growth, load cycle shape considerations and plasticity-induced crack closure.

Validation of this research is obtained by applying the techniques and procedures developed for simulating and detecting a crack within the helicopter transmission, and for characterizing and predicting the growth of this crack. These results are produced using model-based diagnostic and prognostic architectures, and are compared to the results obtained from experiments carried out on helicopters in operation and a test cell employing a prototypical helicopter gearbox. Two kinds of experiments have been used in the comparison. The first kind retrieved vibration data from several healthy and faulted aircraft transmissions in operation. The second kind is a seeded-fault damage-progression test providing gearbox vibration data and ground truth data of increasing crack lengths. For both kinds of experiments, vibration data were collected through a number of accelerometers mounted on the frame of the transmission gearbox.

1.4. Principal Contributions

The principal contributions of this work include:

- Generic model-based fault diagnosis and failure prognosis methodologies, readily applicable to a dynamic large-scale mechanical system,

- Characterization of the vibration signals of a class of complex rotary systems through model-based techniques to provide a better understanding of certain physics-of-failure mechanisms and arrive at descriptive fault features or condition indicators,

- A "reverse engineering" approach for fault identification using simulated vibration data and fault features or condition indicators,

- Utilization of models of a faulted planetary gear transmission to classify descriptive system parameters either as fault-sensitive or fault-insensitive, and

- Guidelines for the integration of the model-based diagnosis and prognosis architectures into prognostic algorithms aimed at determining the remaining useful life of failing components.

1.5. Organization of the thesis

There are four major parts to this thesis, each represented as a row of blocks in Figure 1.1. The first part, comprised of Chapters 1 through 3, covers historical aspects and background material, including a description of the helicopter transmission problem in focus throughout the thesis.

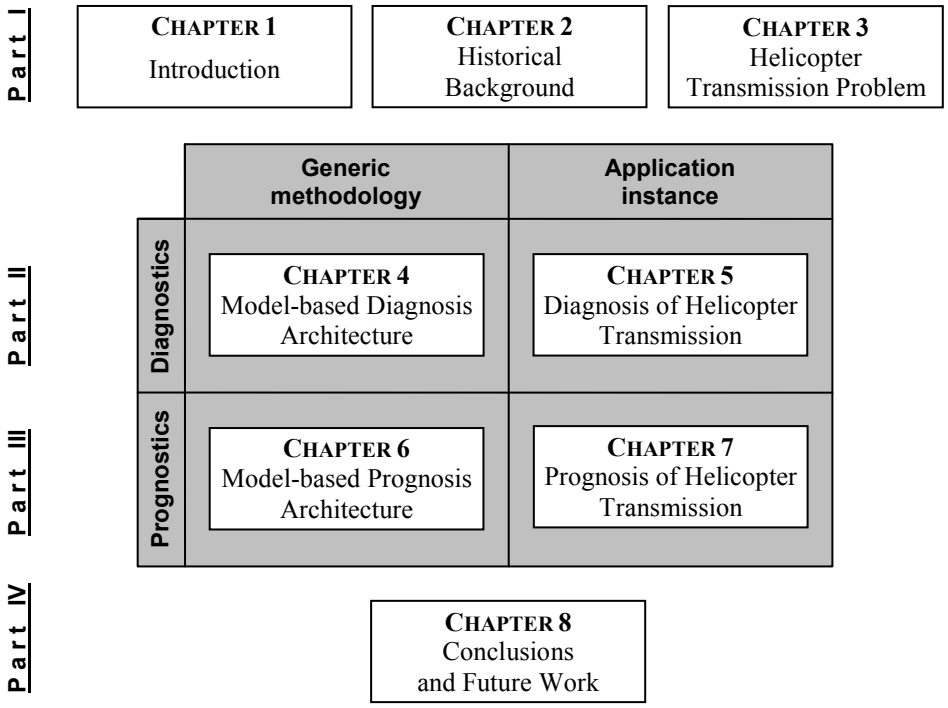

Figure 1.1. Scheme of organization of the thesis

The second part of the thesis is made up of Chapters 4 and 5, and it covers the aspect of fault diagnosis. Chapter 4, in particular, presents a generic methodology for designing and implementing model-based diagnostic architectures. The methodology is presented in a modular fashion with the intent of making it applicable to various engineering systems. On the other hand, Chapter 5 shows how the architecture can be applied to the problem of diagnosing the fault in the helicopter transmission described in Chapter 3.

The third part of the thesis, comprised of Chapters 6 and 7, is the prognostic counterpart of the diagnostic second part. Chapter 6 addresses a generic methodology for designing and implementing model-based prognostic architectures. The methodology has been deliberately set up in a way that is, as much as possible, analogous to the diagnostic

methodology presented in Chapter 4. Aside from the obvious aspects, one of the main differences between the two methodologies is the consideration of a fault as a static versus a dynamic event. Chapter 7 shows how the prognostic architecture can be applied to characterize the progression of damage in the helicopter transmission.

The last part of the thesis, in Chapter 8, presents conclusions and possible future work in developing and implementing model-based fault diagnosis and failure prognosis architectures of dynamic systems.

2. HISTORICAL BACKGROUND

2.1. The Importance of Diagnostics and Prognostics of Engineering Systems

Interest in diagnosing and prognosticating faults in engineering systems is as old as engineering systems themselves (Gertler, 1998, p.1). Designers and users alike have an interest in preventing the occurrence of *failure* of a mechanism, a machine or any kind of device. To this end, several approaches can be taken, the most obvious of which is to stop the system whenever an *anomaly* is *observed*, i.e., a *fault* is *detected* as a difference in the performance of the system from its *normal behavior*. The alternative approaches consider a variety of situations. For example, what happens when an operator cannot sense or detect the fault? Or, what should be done if it were desired to keep a machine running while the damage is not yet critical? In many situations, making the correct diagnosis is a life or death decision, like when an aircraft in flight undergoes damage.

The potential benefits offered by a successful implementation of a system for diagnosis and prognosis in engineering is well expressed in a quote transcribed by Vosilla (2006) from Joseph Garone, a program director for Northrop Grumman Corp.: "Just imagine that you can anticipate major structural failures in an aircraft or other structure before they happen. Or that you can schedule maintenance according to the usage and stresses imposed on an aircraft, instead of at fixed intervals." Garone places emphasis on avoiding maintenance operations at fixed, regular intervals because, as will be seen below, such standard practice is costly. The implications of achieving scheduled maintenance based on the usage and needs of an aircraft, he concludes, "would save

operators significant amounts of money and ensure greater availability of aircraft." This quote is relevant because Northrop Grumman Corp. is a premier contractor to the U.S. Department of Defense.

Attempting to detect a fault before it becomes a failure is a prerequisite to the elimination of *corrective maintenance*. We want to bring the maintenance operations *forward in time*, i.e., before the system fails and needs repair. In this sense, we have two generally recognized options: apply *preventive maintenance* or *predictive maintenance*. Preventive maintenance, or PM, typically refers to performing *regular*, *scheduled* operations that keep the system running reliably. Federal Standard 1037C (1996) indicates that, within the span of these operations, we find the tasks of inspecting, testing or adjusting of equipment, and the replacing or repairing of worn or wearing components. Predictive maintenance, or PdM, on the other hand, attempts to defer maintenance operations until they are required. Although sometimes there is confusion between the two strategies, it is more generally acknowledged that PM is concerned with preventing a failure *blindly*, i.e., without knowing if a fault exists or not, whereas PdM endeavors to detect faults before action is taken.

Table 2.1. Comparative table of approaches to maintenance of engineering systems

Type of Maintenance	Approach	Actions taken	Comparative Associated Costs*	Safety and Reliability
Corrective (CM)	Fault never detected. Failure occurs	Repair	High	None
Preventive (PM)	Fault presence unknown	Regular Inspection and replacement of components	Medium	Medium to High (Inspection can fail)
Predictive (PdM)	Incipient fault detection	Maintenance deferred until actually needed	Low	High when proven

** of maintenance*

Table 2.1 suggests that, when taking into consideration the costs of maintenance and the safety and reliability of the different approaches to engineering system maintenance, the approach of predictive maintenance is preferable. Because each of these strategies works by considering a different time span with respect to the occurrence of faults and failures, Jarrell et al. (2002) have even suggested that there is yet another way of dealing with maintenance. The approach suggested by them, dubbed "proactive operation and maintenance," although similar to predictive maintenance in many aspects, also considers the time range *before* a fault is detected.

The present work falls within the realm of predictive maintenance and more specifically within such in-vogue efforts known as condition based maintenance (CBM) and prognostics and health management (PHM), which are techniques that utilize automated strategies for detecting a fault and provide ways of extending the operational time (known as *uptime*) of damaged engineering systems. This extension in time can be offered because, in most cases, it is possible to continue to operate a system *safely* even if a fault has been detected, at least for a limited amount of time. Diagnostics and prognostics engineering belong within the arena of CBM and PHM.

2.2. Diagnostics of Engineering Systems

2.2.1. Background

Diagnosing an engineering system involves three activities. First, a fault must be deemed to exist through *fault detection* techniques. Second, the fault is located through a process known as *fault isolation*. The concern of many industrial diagnostic systems focuses on these two activities exclusively, so that their practice has become known as "fault detection and isolation", or FDI (Chen and Patton, 1999). The third and final activity, known as *fault identification*, assesses the severity of the fault, either qualitatively or quantitatively (Patton et al., 2000). The process of fault identification is of paramount importance for the research presented in this thesis. The books by Gertler (1998), and Chen and Patton (1999) provide an extensive review of the history and progress of research in the area of diagnostics engineering.

2.2.2. Classification of approaches to performing engineering system diagnostics

There are several ways of classifying approaches to the problem of diagnosing an engineering system. Farrar, Lieven, and Bement (Inman et al., 2005, chapter 1, pp. 4-5), for example, suggest that health assessment operations can be classified as either online or offline, depending on whether they are performed while a system is in operation or not, respectively.

Another way of classifying diagnostic techniques depends on whether the diagnosis assessment is based on deterministic information (e.g., one obtained from a

model) or on stochastic information (e.g., historical, statistical data). The first of these two has been termed a "white box" approach, while the second has been called a "black box" approach. Park et al. (2003) even suggest that a combination of these two techniques might be referred to as a "gray box" approach.

We can think of existing solutions to the problems of performing diagnostics and prognostics as belonging to one (or perhaps even both) of two types: *data-driven* –also called *model-free*– techniques and *model-based* techniques, although other classifications exist. Data-driven techniques include, for example, signal processing algorithms and knowledge-based methodologies. Model-based techniques more commonly involve the description of a system through mathematical models of the physical laws governing its behavior. Both types of techniques are described and compared below.

Data-driven techniques rely on comparative assessments of the status of a system under testing with other known occurrences. For as long as the behavior of the system under testing remains similar to that of a previously known, healthy configuration, the former is deemed to be healthy. When the measured behavior deviates from this reference, a fault is detected, and a comparison with the conditions previously observed in analogous faulted systems can take place. Under the appropriate conditions, this new comparison hast the potential to isolate and identify the fault efficiently. Thus, the ability of data-driven techniques to perform the task of diagnosis is given by the *training* of a classification algorithm.

The training algorithms used by data-driven decision processes are highly automated tasks for which extensive literature exists. Intelligent algorithms in support of this duty abound, and implementation is generally a straightforward and proven activity. Even more appealing is the fact that the data-driven effort typically avoids the need to understand the underlying physical mechanisms that describe the behavior of a system; diagnostics are performed regardless of the causes of a fault. Furthermore, data-driven algorithms can continue to "learn" as they operate, ideally making their assessments more reliable with each fault detection attempt.

However, we must note that data-driven techniques can be ineffective when dealing with measurements that deviate from the references available in the training "library," whether there is damage or not. If the behavior of a system is for some reason dissimilar to all the past observations from healthy and faulted cases that were available at the time of training, there may be no telling what the data-driven algorithm is going to decide. If this is a recurring situation, or if some change has made the deviations permanent, the algorithm can continue to misinterpret the system status until retraining is performed. Changes like this might be likened to "under-training", since the new situations must be added to the training library. In the other hand, there also exists a danger of "over-training", which occurs when all of the training data is similar and the algorithms adjust too finely to specific details of the data that are more of a coincidence than have a causal relationship with the fault. Thus, over-training, which is more properly termed *overfitting*, has the opposite effect of what training intends; instead of making data-driven classification algorithms more effective, it makes them less "prepared" to

deal with changes in data sets. Designers of data-driven algorithms must always take care of balancing the algorithm implementations so neither under- or over-training take place.

In contrast, the model-based approach is generally more robust in the sense that it can sort out new or unforeseen situations more easily, since this technique can incorporate and replicate, per its mathematical models, a wider range of behaviors, even if previously unobserved in actual systems. If the state of a system deviates from expected operational ranges, model-based techniques can continue to work by updating physical parameters that describe the new situation. Because of this ability, model-based techniques can also dispense with the use of the extensive training and historical information required by the data-driven approach, and is less prone to the kind of difficulties introduced by under- or over-training.

Yet, setting up an accurate model that describes the physics-of-failure mechanisms (i.e., a physics-based model) requires so much effort and expertise, that many simplifying assumptions have to be made, which degrade the model's reliability or applicability to the real situation. This effort is typically beyond that required by data-driven techniques. All the observed occurrences of a fault in past instances become useless to the modeling effort if the physics behind such behavior are not well understood. A comparison between the applicability of the data-driven and the model-driven approaches is given graphically in Figure 2.1.

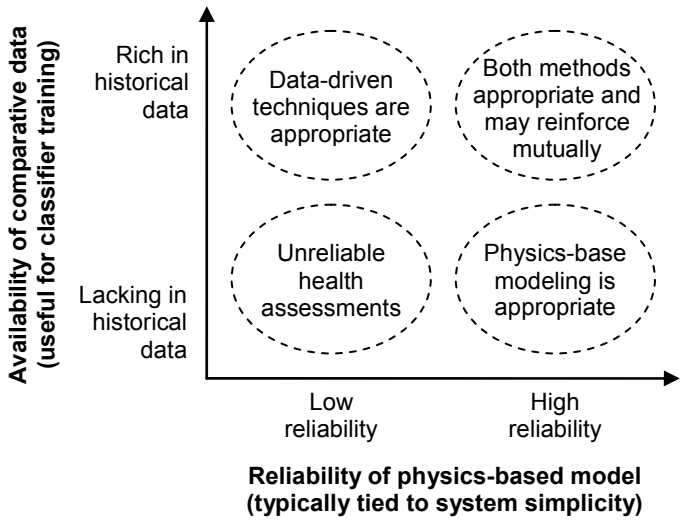

Figure 2.1. Comparison of situations where the physics-based approach or the data-driven approach are appropriate. Adapted from Inman et al. (2005), p. 6

Designers adept at the model-based approach almost invariably find themselves at a crossroads when defining models; either simplicity or accuracy has to be given priority at the expense of the other. Choosing a course that maximizes accuracy may always be desired, but the limited availability of the resources it requires (time and energy; computational or analytical effort; simulation hardware and software; training and expertise), tends to favor the path of simplicity. Thus, when enough resources are available, the quest for accuracy will normally lead to a more complex model.

It is worthwhile to note that, although the classification of model-based vs. data-driven approaches refers here to diagnostics, it can also apply to prognostics, as confirmed by Farrar, Lieven and Bement (Inman et al., 2005, chapter 1, pp. 4-5).

2.2.3. Model-based diagnostics

The focus of this thesis is exclusively on quantitative techniques for performing model-based fault diagnoses of engineering systems, although qualitative techniques exist (Yang, 2004). Quantitative engineering diagnosis techniques (Gertler, 1998, p. 6; Park and Zak, 2003) operate by comparing a particular measurement from a plant with an expected value. When there is a difference, the plant is declared to be at fault. The comparison is typically performed using one of two techniques, *parameter estimation* or *residual evaluation*, as represented in Figure 2.2. These techniques are explained below. For now, notice in the figure that a two-stage process is typically followed: attribute calculation (i.e., the residual or the parameter) followed by decision-making. Such two-stage process was originally suggested by Chow and Willsky (1980).

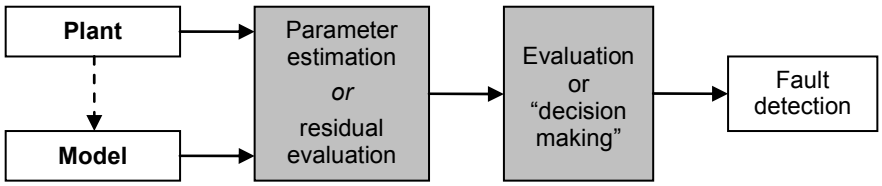

Figure 2.2. An overview of the general approach to performing model-based fault detection, the fundamental aspect of model-based diagnostics. The dotted-line arrow represents the idea that observations from the plant may be used to update the model before a diagnosis is pronounced, although this is not always desired

Although the "model" block of Figure 2.2 can refer to a mathematical description of a system, this need not be so. As suggested in a famous publication by Willsky (1976), this model can be any realization that replicates certain behaviors (i.e., variables, signals or any other measurable activity) of an engineering system; it may be, for example, a

computer simulation tying different processes, even if described without equations; it may be linear or non-linear; it may be deterministic or stochastic, etc. The approach of parameter estimation for performing model-based diagnostics is represented in Figure 2.3. A *system identification* model is updated with observations from the plant to try to determine some internal parameters of the plant's process and ensure that they remain within specified bounds, or else a fault may be declared.

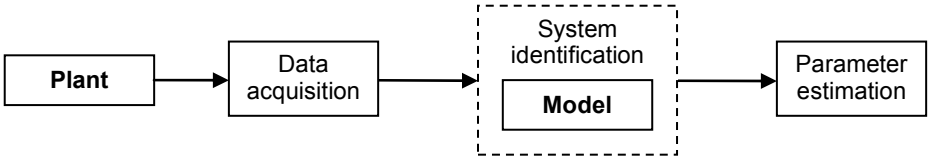

Figure 2.3. Parameter estimation procedure

The approach of residual evaluation is depicted in Figure 2.4. Signals acquired from the plant or from model simulations are used to calculate *features* (also known as *condition indicators*), which are quantities that describe some condition of the system and do not necessarily have a clear physical meaning. When residual evaluation is used, a large difference (i.e., the residual) between comparable measures (i.e., the features) of the model and the plant can be regarded as indicative of a fault condition.

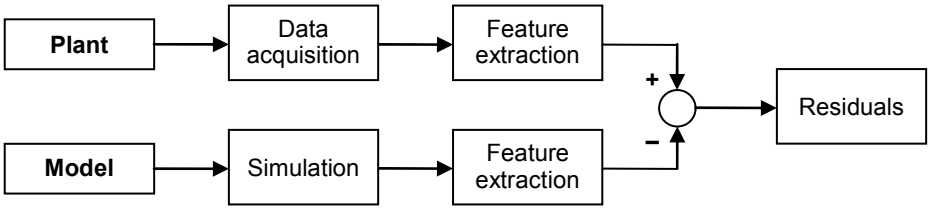

Figure 2.4. Residual evaluation procedure

Hybrids of the approaches of parameter estimation and residual evaluation may be built, but, in any case, the model is intended to replicate some behaviors of the plant. This can be a very cumbersome task, especially when considering that (1) selecting the most appropriate measurements from which to generate residuals or estimate parameters can involve choosing among thousands or even millions of possibilities, and that (2) some models require information from multidisciplinary engineering analyses. The subject of measurement selection has drawn considerable attention, and in its own right has become a particular area of study for which extensive literature exists, commonly referred to as *sensor location and selection*, or SLS. Zhang (2005) and Padula and Kincaid (1999), for example, have reviewed some techniques and literature on the subject. SLS is beyond the scope of this thesis. However, the use of multidisciplinary engineering techniques is of great concern to the present work, and is regarded when fitting throughout this document.

2.3. Prognostics of Engineering Systems

2.3.1. Background

In general, prognostic systems are expected to provide predictive information about the remaining useful life (RUL) or time-to-failure (TTF) of a deteriorating machine or machine component. Because a prognosis is thus inherently uncertain, in addition to this indication, a prognosis call should also offer some representation of the amount of uncertainty in the prediction, as will be seen in section 2.2.3.

Some prognostic systems provide RUL estimates based on *a priori* knowledge of life expectancy and, possibly, of expected usage patterns. This approach to prediction

does not involve damage monitoring. Another kind of prognostic is performed only after a fault is detected and damage is evaluated, i.e., it is based on a diagnosis, and thus requires system status monitoring. Byington et al. (2002) refer to these two kinds of performing prognostics as *vertical* and *horizontal*, respectively. This thesis focuses on prognostic systems that require anteceding diagnostic activities, i.e., using the horizontal approach, although certain aspects of the thesis can be applied to systems that do not require diagnostic updates.

At present, damage-progression prognosis is an intense area of study (see, for example, Inman et al., 2005, chapter 1; Byington and Stoelting, 2004; Hess, 2002; and Mathur et al., 2001). An effective prognostic system is expected to provide considerable benefits in the costs, reliability, and safety of engineering systems. Multiple organizations have expressed strong interest and provided support in this area of research, including those related to the aircraft and other industries (e.g., the Aging Aircraft program of the Federal Aviation Administration), the government and the military, and regulation institutions (e.g., the International Standards Organization, ISO).

2.3.2. Classification of approaches to performing engineering system prognostics

Developing prognostic systems has been attempted from a few varying perspectives. For example, Byington et al. (2002) suggest that there are three major classifications to approaching the problem: use experience, trending models, or physics-based modeling. Each of these techniques offers its own advantages. Such classification is represented in Figure 2.5.

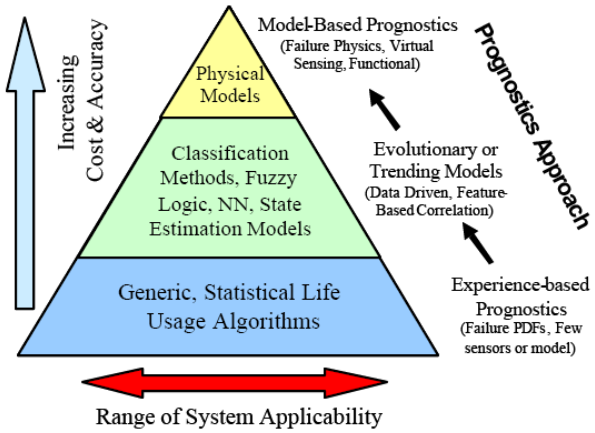

Figure 2.5. Hierarchical classification of approaches to prognostics. Reproduced from Byington et al. (2002)

Another classification is proposed by Jaw and Wang (2004), noting that prognostic systems can perform health assessment tasks online (i.e., while the analyzed system is in operation and providing recent data), offline (using stored information that was retrieved in past operation of the system), or via a combination of the two.

Regardless of the classification, it seems that most attempts to perform prognosis start by executing diagnosis (see, for example, Byington and Stoelting, 2004; Luo et al., 2003; and Kacprzynski et al., 2004). Then, some sort of technique, whether empirical or analytical, is used to characterize the future progression of damage and predict when, as a function of time or usage, a fault will reach a condition of concern.

2.3.3. Model-based prognostics

Mathur et al. (2001) propose that model-based diagnostic and prognostic systems can use one of four modeling paradigms. The first one, based on *physical models*, references the natural laws that govern the system behavior. The second one analyzes the

probability of failure of individual components separately and combines them to determine the probability of failure of the parent system, thus generating *reliability models* whose information is useful to establish periodic maintenance schedules. The third class, consisting of *machine learning models,* uses historical data and training techniques to provide comparison-based estimations of the present and future status of a system. The fourth modeling paradigm uses artificial intelligence with *dependency models* to attempt to establish cause-and-effect relationships in the behavior of a system.

Sometimes, even combinations of these four approaches (i.e., *hybrid techniques*) are developed, like the technique proposed by Garga et al. (2001), which combines machine learning and dependency models.

The use of physical models, often referred to in the literature as a "*physics-based modeling*" approach, is the focus of this thesis, although parts of the methodology presented are applicable to the other types of models as well.

Prognosticating damage evolution is, in general, a very demanding problem. Farrar, Lieven, and Bement (Inman et al., 2005, chapter 1, pp. 1-12) identify the system prognostic problem as a "grand challenge" requiring a multidisciplinary approach. In a non-exhaustive list, they mention that the following engineering disciplines are involved in prognostics: engineering mechanics, reliability engineering, electrical engineering, computer science, information science, material science, statistics, and mathematics.

When performing engineering prognostics, the response of a system to varying operating conditions and to structural changes induced by the fault need to be considered. Thus, fault progression models are typically complex and require much expertise to be set up. Unfortunately, sufficient expertise is not always available, and experimentation is sometimes necessary to validate the models. This experimentation is often carried out through a process widely known as *seeded fault testing* (see, for example, Hess and Hardman, 2002; Bilosova, 2002; and Swanson, 2001). This process uses specimens with damage deliberately caused by designers, as opposed to faults originating during normal operation of a system.

Sometimes simple models can be set up for analyzing the effects of either varying operating conditions or fault-induced structural changes. However, combining both of these effects in practical applications requires more than analytical equations. Advanced numerical solutions or computer simulation may be required. This is true, for example, when modeling the growth of cracks in mechanical components from considerations of fracture mechanics. One of several techniques able to predict crack growth rates and directions is the use of computer simulations performing *finite element analysis* (FEA).

FEA is a methodology that serves to study the behavior of systems in many engineering disciplines, including Thermal Engineering, Fluid Mechanics, Electromagnetism and Mechanics of Materials, among others. The method derives its name from the idea that a complex system or structure can be analyzed by dividing it into small parts called *elements*, each of which is fully defined in its geometry and/or properties, i.e., is discrete and *finite* (as opposed to infinitesimal), as represented in Figure

2.6. Elements can be more easily studied than the complete structure they are a part of, and each can be considered as a continuous structural member (Rao, 1990). The finite element method converts a continuous medium into systems of algebraic or ordinary differential equations. To solve a finite element problem, the method calls for a search of simultaneous solutions to the reaction problem of the elements caused by applied loads or disturbances (i.e., forces, fields, heat, etc.), constraints (like those of motion, position, temperature, etc.) and the interaction of adjacent elements. Elements interact through their connections, defined by means of *nodes*, as illustrated in Figure 2.7. The problem is set up so that the numerical solution converges iteratively towards the behavior of the total structure, with better approximations provided by larger numbers of elements.

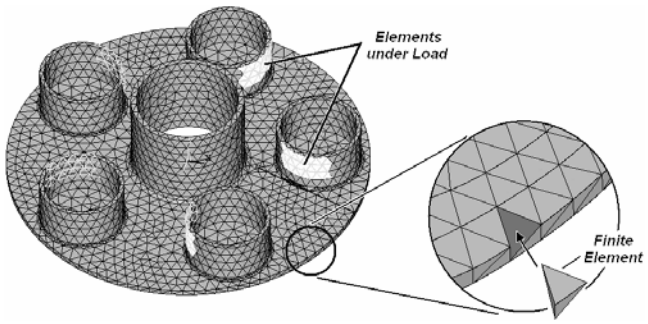

Figure 2.6. Finite element computer model of a mechanical component. The design has been divided into finite elements thorough a process known as *meshing*

Introduction of the finite element method is generally attributed to Courant (1943), who was then studying the vibration of systems. Important steps in the development of the method are later taken by Turner et al. (1956) and Clough (1960) leading to a formal establishment of the method in a book by Strang and Fix (1973).

Through the years, the Finite Element Method has been successfully applied to a wide variety of problems, and at present literature on the subject is abundant.

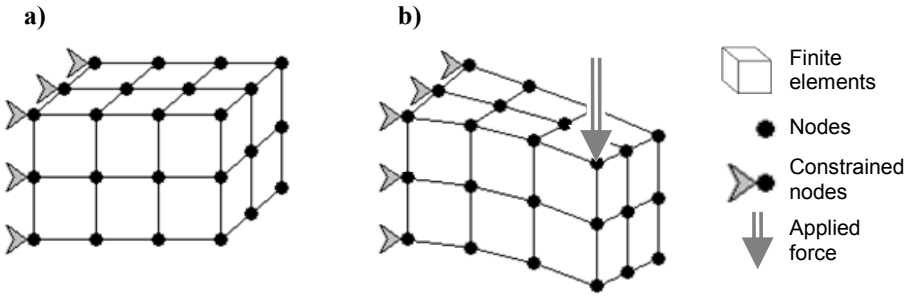

Figure 2.7. Illustration of some of the functions of nodes in a finite element model. a) The elements of a simple design are connected by nodes, some of which are in this case constrained from motion and some of which may be recipient of forces. b) The effect of applying a force on a node affects the entire structure through elements and nodes, but constrained nodes remain fixed

Finite element models allow a designer to analyze the static or dynamic response of a system to the application of loads or the presence of disturbances. In the case of structural studies, a model for FEA can be as simple as a single truss experiencing a point load or as complex as a complete engine with moving parts. Today's software tools based on FEA are usually available for very specific engineering disciplines or else they are very large and complex program packages useful in a wide range of applications. For the first case, we find programs like FASTRAN (Newman, 1992) and FRANC3D (Cornell Fracture Group, 2003), which rely on results from finite element studies to simulate mechanical fracture growth. For the other case, we find powerful packages like ANSYS and ABAQUS.

FEA simulations can be applied to many different situations to approximate the behavior of systems when operating conditions vary or when faults appear and progress. Thus, the utility of FEAs in diagnostics and prognostics is that they offer the potential to determine the way in which a condition of the system changes when a fault or anomaly is introduced.

The successful solutions to certain kinds of problems might tempt us to think that computer simulations (including, but not limited to FEA techniques), when applied to the fault progression problem, are in general the panacea of machine health prognostics. However, we have to take into account the following caveats:

1) The models and solution techniques used in computer simulations are numerical approximations to real physical behaviors and not all problems generate satisfactory solutions, either because not all actual conditions are properly modeled or because the physics of the problem are not entirely understood. For example, certain crack growth and corrosion mechanisms are yet to be adequately explained and characterized.

2) Rough model approximations are often accepted because of the considerable effort and amount of data required to set up certain computer simulations, and because of the extensive running time of the simulations. Validation of the simulation's results and correction of deviations from the real system's behavior must be thus executed with other tools, among which we may even find "expert's judgment".

3) Computer simulations require significant computing power and resources, making real-time application of these techniques impossible or, at the very least, impractical in many situations. It may be possible, nevertheless, to use a collection (database) of results from previously executed simulations (prepared off-line) as a baseline for diagnosis and prognosis studies.

4) Computer simulation results provide information for variables that may not be directly observable (i.e., measurable) in the system (e.g., a crack in a rotating component). We need other tools (like physics-based models) to map these variables to real-world sensor measurements and produce usable information out of the simulation results.

5) System parameters and initial state conditions are not necessarily known with sufficient accuracy. Only approximations or estimates are available, hence making the simulation results inherently uncertain.

6) To realize a prognosis of RUL, information about the future operating conditions is necessary. Because most physics-based models are deterministic, the accuracy of a prognosis is severely affected by the accuracy of information about the future operation conditions. This situation has led in many cases to the preferred use of a worst-case assumption that limits the effectiveness of the ability to extend component life through prognostics.

Points number (5) and (6) in the list above have provided the motivation to attempt to implement *adaptation mechanisms* for the models. These mechanisms allow a model to improve its system replication tasks by analyzing and correcting for differences between its estimates and the actual behavior observed in the system. Jaw (1999), for example, has used an artificial neural network to improve the results of a physics-based damage-progression model related to a condition of the rotating blades of a turbine engine. Going a step further, Vachtsevanos and Wang (2001) have used a dynamic wavelet neural network to assess also the performance of different prognostic routines. In a different approach, Kacprzynski et al. (2002) have proposed a technique for using diagnostic information to adapt physics-based prognostic models.

The same two points of the list also justify the specification of confidence intervals when attempting to make a prognosis and RUL assessments in general, because the prognostic can vary depending on the certainty of our estimates of the parameters (including system geometry or configuration, material properties, etc.), the initial state, and the future operating conditions. Analyzing the issue of confidence bound determination and specification has spawned a detailed research area, as evidenced in work done by Barlas et al. (2003), Vachtsevanos (2003), Khiripet (2001), Roemer et al. (2001), and Engel et al. (2000). Consider, for example, the case of the future operating conditions. These are typically either unknown (e.g., in an aircraft) or expectedly bounded (e.g., in a motor under constant load). In either case, the exact loads cannot be determined as a function of future time, although they can be estimated to some degree, sometimes roughly and sometimes accurately. Computer simulation is hence a tool whose

results need to be properly interpreted and even adjusted to provide realistic information about the expected development of faults.

Notwithstanding these drawbacks, and given the fact that computer simulation is considered one of the most accurate and powerful techniques for performing system behavior studies, it is clear that this tool remains promising for providing a reliable diagnosis of the health of an engineering system and an accurate prognosis of its RUL after a fault is identified.

2.4. Diagnostics and Prognostics Today

It has been suggested that the discipline of engineering diagnostics has been studied for quite some time now yielding reliable techniques for fault detection, isolation and identification. At present, there is considerable and widespread interest in advancing the related discipline of prognostics engineering to such levels of success. However, this has proven to be a challenging problem. The primary motivation to advance prognostics engineering and provide the engineering community with reliable CBM and PHM methods and techniques is the desire to avoid the unexpected failure of systems, because such failures can be extremely costly both economically and in terms of human lives. For example, imagine the breakage of a critical gear or bearing in a complex machine operating at high speed. The fracture may lead to a "chain reaction" that damages multiple components of the machine, rendering it inoperable and even perhaps more costly to repair than replace. The cost may not just involve the loss of the machine, but the loss of productivity as well. Alternatively, imagine an aircraft in flight experiencing

the failure of an engine component, or tearing of the fuselage… many lives can be at stake. There is a multiplicity of application domains for CBM and PHM techniques. Take for example the efforts in realizing engine health monitoring (EHM) for the next-generation aircraft known as the Joint Strike Fighter (JSF) described by Powrie and Fisher (1999) as a critical component of a prognostics and health management (PHM) program that is expected "to reduce direct costs such as hardware, labor, fuel, and logistics," and increase safety. Jaw (2004) lists as other important applications the cases of rockets and aircraft engines. This list of examples could go on for many pages.

The interest in integration of diagnostics and prognostics in CBM and PHM systems concerns the multiple approaches to carrying out the task of predicting the RUL of systems in operation, some of which have already been described earlier. The focus of the research presented in this document, however, is on model-based techniques. Larsen and Christodoulou (2004) suggest that efforts of this kind are expected to provide "dramatic improvements in the accuracy of predictions of the future health and capability" of structures or their components. They also identify the aspect of materials damage prognosis as requiring the union of non-intrusive state awareness and physics-based models, similarly to what is pursued by the research presented in this thesis: a combination of (1) a diagnostic system that relies on data acquisition with (2) a model-based prognostic system. Even though they present many challenges, it is clear from the preceding sections that diagnostic and prognostic efforts relying on physics-based modeling are among the more promising for implementing effective engineering health management systems.

3. THE HELICOPTER TRANSMISSION PROBLEM IN FOCUS

3.1. Description and Importance of the Problem

3.1.1. Discovery and assessment of the problem

In May of 2002 the U.S. Army grounded almost a thousand of its helicopters after an unexpected and unexplained mechanical fault had been detected in one of them (Strass, 2002). Instruments of a UH-60A "Black Hawk" helicopter indicated, while in flight, that there was low oil pressure in the main mechanical transmission system of the aircraft. Once the aircraft was on the ground, the maintenance crew in charge of checking the lubrication pump and flow system discovered the presence of metal chips in the sump of the transmission gearbox. These chips were hindering adequate oil flow, thus causing the instrumentation alarm. Obviously, the presence of these metal shavings was indicative of damage to mechanical parts, and a teardown of the transmission was carried out for further investigation.

This investigation found that the *planetary gear carrier plate* –or "*carrier plate*" for short– of the main rotor transmission of the helicopter had developed a crack, which had gone undetected by the gearbox warning instrumentation system. The carrier plate is a critical component of the *planetary gear* transmission system that is used to transmit mechanical power from the engines to the main rotor blades of the helicopter. Some components of the planetary gear transmission are shown in Figure 3.1 (planetary gear systems are described in more detail in section 3.3).

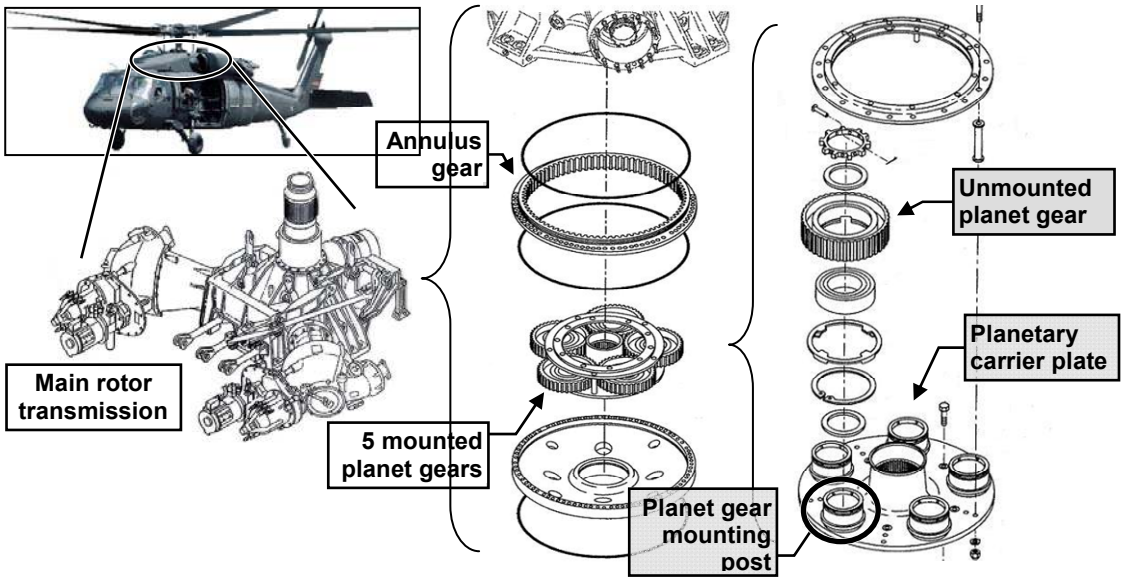

Figure 3.1. Mechanical components of the helicopter transmission of focus in this thesis

It was determined that the metal shavings were not coming from the planetary carrier plate, but rather from certain alignment shims belonging to the gearbox. However, it was still deemed that the cause for the destruction of the shims was excessive vibration and stressing of the gearbox, which was in fact due to the crack in the plate.

Later on, a similar crack was found in another U.S. Army "Black Hawk" helicopter and in a U.S. Navy "Seahawk" helicopter. Because the damaged part is a critical component of the aircraft, there is concern that, if unchecked, it may lead to the loss of the machine and the lives of people on board. Thus, its appearance in multiple aircraft has become an issue of great concern to the U.S. military and companies involved in the design and maintenance of these machines, including Sikorsky Aircraft (the principal manufacturer) and Northrop Grumman (providing avionics and other kinds of

support). Even the Defense Advanced Research Projects Agency (DARPA) has sponsored research projects treating this issue, including a portion of the present work.

The crack, illustrated in Figure 3.2, developed on the root of one of the five *planet gear mounting posts* of the planetary carrier plate, which is a region of high stress. Sahrmann (2004) carried out a comprehensive analysis of the crack origin and growth characteristics on the damaged part, while Keller and Grabill (2003), Wu et al. (2004), Hines et al. (2005), and Blunt and Keller (2006), among others, have attempted to provide early detection techniques based on vibration changes.

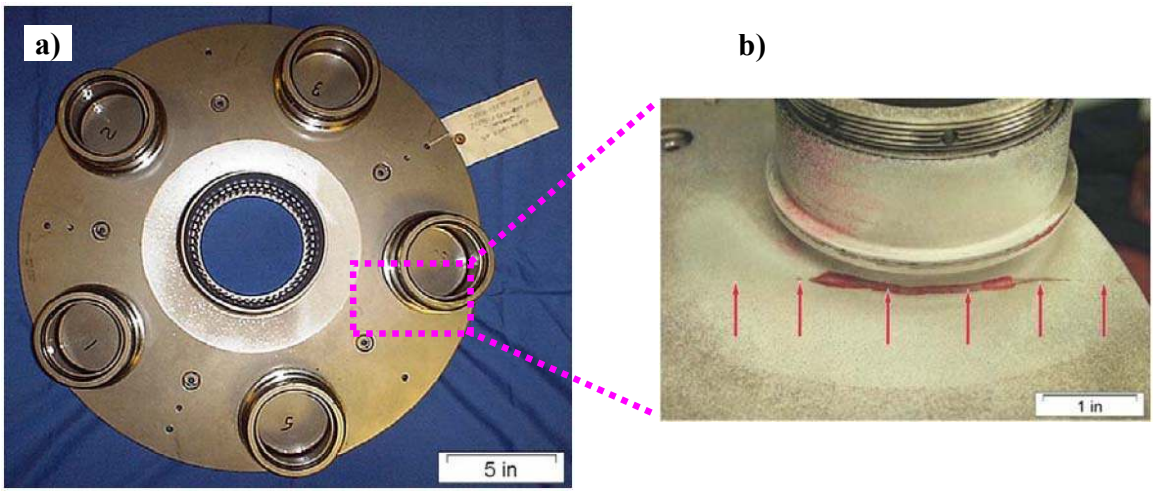

Figure 3.2. Planetary gear carrier plate of a UH-60A Blackhawk helicopter; a) Top view of a healthy plate; b) View of Crack on one of the posts; the crack path is indicated by the arrows. Photographs reproduced from Sahrmann (2004)

3.1.2. Problem significance

The recurring problem of damage in the planetary carrier plate of helicopter transmissions is important because thousands of helicopters with a potential to develop

the cracking problem described above operate today around the world. Variants of the Black Hawk helicopter model are in service not only in the U.S. military but in civilian use and the military of foreign governments as well. One of these variants even serves to transport the President of the United States as one of the famed "Marine One" helicopters. An attempt to replace the failure-prone component would involve not only the redesign of an expensive and complicated part, but would also require a considerable amount of maintenance labor, which would be nearly impossible to carry out economically with so many aircraft in service.

Diagnosing and prognosticating the carrier-plate cracking fault in helicopters without the need to disassemble the transmission has become an important aspect of a multi-million dollar program sponsored by DARPA charged with developing a structural integrity prognosis system (SIPS). The goal of this system, Vosilla (2003) reports, "is to provide military commanders with data and quantitative performance predictors they can use to manage, deploy, and use individual combat systems to the limit of their capability." The reach of this program goes beyond the banner application of the helicopter transmission problem, which has been used, along with other applications, to evaluate the feasibility of the program goals, as reported by Vosilla (2006).

3.1.3. Vibration is key for diagnosis

It is highly desirable to detect the crack in the helicopter transmission through vibration data because such a data acquisition arrangement is reliable, economical and non-invasive. Vibration sensors are easy to install and maintain because they can be

mounted on the frame of the gearbox, precluding the need to modify or disassemble the transmission for installation and service. Furthermore, vibration sensors and instrumentation are already available in many of these aircraft, and measurements can be made while an aircraft is operating, so that a crack might be detected even in flight, possibly offering a pilot the ability to make critical decisions over an incipient fault or based upon the severity of developing damage. Thus, the applications of focus in this thesis are detecting the planetary carrier crack in its early stages of development by analyzing changes in the vibration caused by the operation of the gearbox, and characterizing the crack growth rate.

It is worthwhile to note that the vibration analysis of concern in this thesis for diagnosing the helicopter transmissions is related to the operation of the gears in the planetary gearbox. These vibrations are generated by the motion of gears and gear components and, particularly, by the contact or clash of gear teeth (i.e., the *gear meshing* action). This kind of vibration analysis is opposed to approaches that focus on other physical aspects like the natural frequency and resonances of a structure (for example, Giurgiutiu, 2002; and Gelman and Gorpinich 2000) or the changing patterns of sound waves around certain geometries (for example, Michaels and Michaels, 2005; and Mi et al., 2006).

It should also be noted that focus on this thesis is on the vibration changes caused by the appearance of a crack on the planetary carrier plate of the helicopter transmission. This is different from diagnostic efforts involving the gears or gear teeth, which is in many respects a simpler problem. Samuel (2003) provides a review of techniques to

diagnose gears in helicopter transmissions and describes a novel technique to separate and analyze the vibration patterns of individual gear teeth, thus offering the ability to detect and localize tooth faults.

3.1.4. A chance to validate prognostic efforts

As discussed in chapter 2, model-based prognosis is an area of research with much promise but young in its stage of development. Some of the obstacles for its advancement are the limited availability of data to validate research efforts, the complexity of the systems and their corresponding models, the required multidisciplinary expertise, and the need for many kinds of resources. The helicopter transmission problem is exceptionally well suited for prognosis research because it is being supported and researched by the government and many institutions simultaneously, and provides means to circumvent all of the obstacles mentioned. The wide interest in this problem has brought together many experts and professionals with the willingness to cooperate and produce results in a manner that may have never been done before. The research in this thesis is a part and product of these efforts, and has been helped and supported by many people and institutions. Furthermore, and of particular importance for the aspect of prognosis, experiments have been carried out to characterize the progression of the crack in the planetary gear plate. This characterization enables the validation of many aspects of model-based techniques, which in turn may set the foundation for developing integral, health-management architectures with state-of-the-art technologies.

3.1.5. Selection of this problem for research

The helicopter transmission problem has been chosen as the focus of the research for this thesis principally because of the following reasons:

1. The problem is of importance to save human lives and can be considered as involving a prototypical mechanism. Some results, techniques, and methods derived from the studies carried out with this system may be widely applicable.

2. There is interest by industry and government in this application, so there is adequate support and experimental data. The present research effort has been given access to such data.

3. The problem is complex enough to merit detailed research and provides an excellent opportunity to test and validate modern diagnostic and prognostic techniques. It also offers the opportunity to be modeled with considerations based on the physics of the system.

3.2. Experimental Support for Studying the Helicopter Transmission

Experimental research on the planetary carrier plate fault described in section 3.1, includes experiments involving the U.S. Army Aviation Engineering Directorate, Aeromechanics Division (see Keller and Grabill, 2003), the U.S. Army Research

Laboratory (see Sahrmann, 2004), and the Helicopter Transmission Test Facility of the U.S. Naval Air Systems Command at Patuxent River, Maryland (see McInerny et al., 2003). Different kinds of tests have been performed, but, throughout this thesis, we will be referring to two sets of experiments for which gearbox vibration data was acquired from the main-rotor transmissions used in some Sikorsky-brand helicopters with potential to develop the problem.

The first set of experiments involved the acquisition of vibration signals from planetary transmissions either with a 3.25-inch crack in the carrier plate (shown earlier in Figure 3.2b) or with a "healthy" plate (i.e., without any crack). Furthermore, the cracked plate was used in a test cell for some experiments and in an actual aircraft for some others. Similarly, vibrations from transmissions using healthy plates were acquired both from the same test cell and from operational helicopters. The test cell is a set up that uses actual aircraft engines to power the transmission components in an effort to replicate the on-board behavior of the mechanical components tested. We will be referring to this set of experiments as "experiments with specific crack lengths".

The second set of experiments was carried out in the test cell exclusively. It involved the use of a single planetary carrier plate with a seeded crack. The objective of the experiments was to observe the change in vibration signals as the crack experienced growth caused by the operational loads of the functioning planetary gear transmission. Initially, a notch was carved on the carrier plate through electrical discharge machining (EDM). Then, high stress cycles were applied to the plate with a custom-made machine to turn the notch from a fault seed into an actual crack of 1.34 inches in length. The

vibration experiments were run in the test cell starting with this crack length. The crack reached the outer edge of the circumference of the plate at a total length of about 4.8 inches. From this point on the crack grew towards the inside of the plate, the plate experienced greater deformations, and vibration data showed increased variability (i.e., as if noise had increased). These experiments were run until the total length of the crack was beyond 8 inches. We will be referring to this set of experiments as "experiments with a growing crack".

Table 3.1. Sources of experimental data for the validations and results presented in this thesis

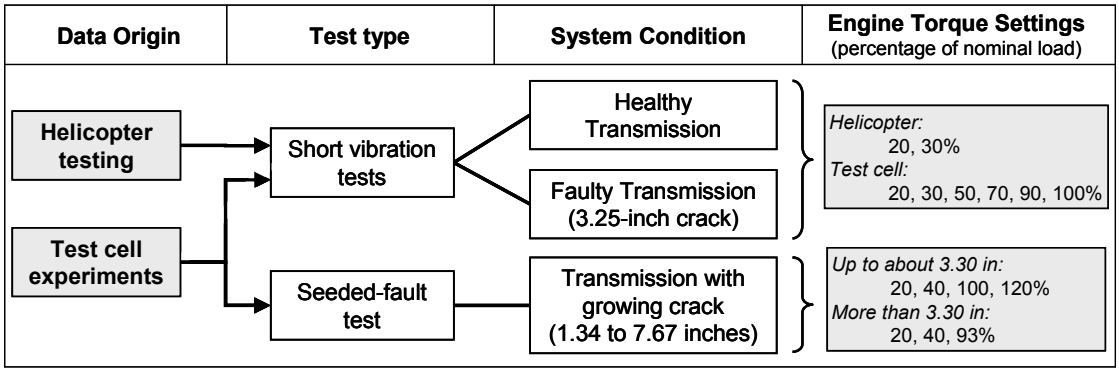

The two sets of experiments described above are summarized in Table 3.1. The vibration data generated by the experiments was acquired from the systems by means of a number of accelerometers mounted on the frame of the transmission. Although data for several accelerometers was available, focus in this thesis is placed on those installed near the annulus gear of the planetary gearbox, since the analysis of this research is based upon this assumption (see section 3.3.2). Furthermore, since results from all the accelerometers near the annulus gear were similar, for reasons of brevity, results

presented in this thesis refer only to a selected subset of these accelerometers. Examples of accelerometers mounted near the annulus gear are positions 5 and 6 of those illustrated in Figure 3.3.

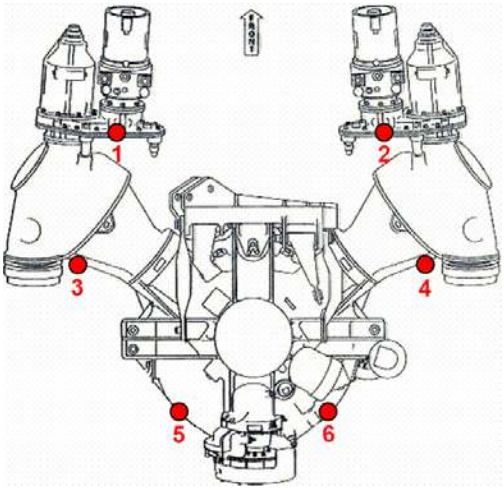

Figure 3.3. Top view of helicopter transmission gearbox assembly. The image highlights examples of possible locations for mounting vibration-measuring accelerometers; the locations of focus for this thesis are similar to locations 5 and 6 in the image. Reproduced from Keller and Grabill (2003)

3.3. Main Transmission Gearbox of the Helicopter

3.3.1. Planetary gearboxes

Planetary gear arrangements are used extensively in aircraft and other systems that require mechanic transmissions with specifications of high power per unit-weight and good speed and torque ratios within a limited volume. These geared transmissions belong to the "epicyclic"[6] kind because some of the gears in the arrangement move around other gears. In a planetary gear arrangement the axis of rotation of each of several

[6] Epicyclic gears are known as such because their axis of rotation in turn rotates about another gear, thus introducing a "translational" rotary motion component, which is in addition to the "rotational" motion.

epicyclic gears, each of which is known as a *planet gear*, in turn rotates about another gear, known as *sun gear*, thus introducing a "translational" rotary motion component, which is in addition to the "rotational" motion of each planet gear. To be able to complete the translational cycles while remaining spaced among each other planet gears are mounted on a rotating planetary *carrier plate*. During operation, the teeth of the planet gears mesh with those of the sun gear and, simultaneously, with those of the *annulus* or *ring gear*.

The axis of rotation of the carrier plate, the sun gear and the annulus gear are aligned, but their rotational speeds are always different, which is what makes a planetary gearbox useful as a transmission. Planetary gearboxes are designed to transmit power from any one of these three components to any other while keeping the third fixed. The gear ratio of the transmission depends not only on the number of teeth of the gears, but also upon the choice of the stationary component. The ability to change the gear ratio by fixing a different one of the three components is exploited in systems where it is useful to have varying gear ratios, like in the automatic transmissions of automobiles. For the helicopter transmission of our focus, which has $N_p = 5$ planet gears, the annulus gear is always fixed. This configuration is represented in Figure 3.4.

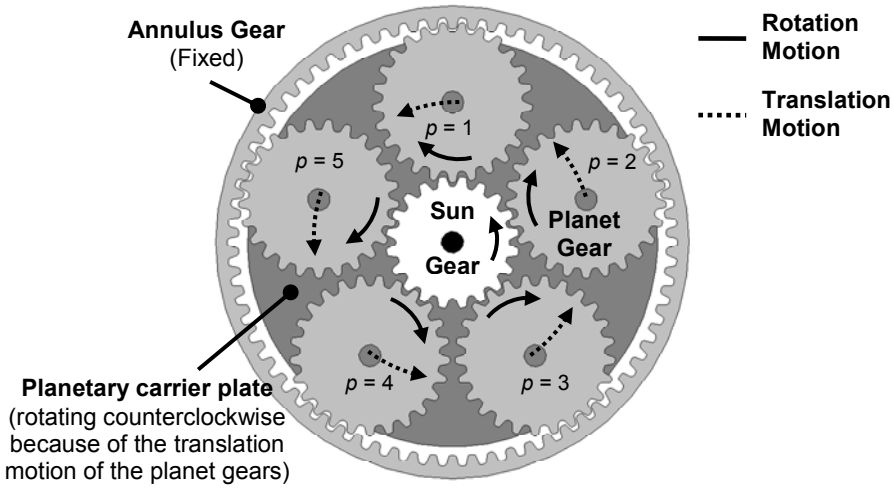

Figure 3.4. Representation of a planetary gear system with 5 planet gears (p = 1 to 5). Arrows represent the directions of motion of the gears

3.3.2. Vibration of planetary gearboxes

As discussed in section 3.1, the use of vibration signals is an appealing way to monitor the condition of a planetary gearbox. To use vibration for such purpose, however, calls for the understanding of the vibratory characteristics of this kind of mechanism, especially if model-based condition monitoring is to be involved.

The particular vibration characteristics of planetary gear transmissions have been studied by several researchers. The span of these efforts ranges, for example, from such classic work of Botman and his co-workers (see Botman, 1975; Toda and Botman 1979; and Botman, 1980) to the more recent research of Kahraman and his co-workers (see Kahraman, 1994a, 1994b and 2001; Bodas and Kahraman, 2004; and Yuksel and Kahraman, 2004). Parker and his co-workers have very notably advanced the state of the art in the subject (see, for a brief example of their ample research, Lin and Parker, 1999 and 2000; Parker and Lin, 2004; and Ambarisha and Parker, 2006) by developing elastic

models of planetary gears. Some effects of unequal planet gear spacing studied by Lin and Parker (2002) and the influence of planet gear phasing examined by Parker (2000) are closely related to the model presented here. These latter references, however, place emphasis on using unequal phasing as a means of reducing vibration levels in planetary gear transmissions.

Planetary gearboxes have particular vibration characteristics because of the interaction of the individual vibrations generated by each one of the planet gears as they move with rotation axis fixed on the planetary carrier plate, about the sun gear and along the annulus gear. In non-epicyclic gearing systems, one can typically expect to see vibration components in frequencies that are multiples of the number of teeth in the gears, i.e., harmonics of the *tooth meshing frequency*. This frequency characterizes the rate at which successive teeth come in contact as the gears rotate. However, because of the interaction and motion of the planet gears, it is possible that these exact harmonic frequencies become faint or even disappear in planetary transmissions. Ideas initially proposed by McFadden and Smith (1985) and advanced by Keller and Grabill (2003) explain the suppression of tooth meshing harmonics.

3.3.2.1. McFadden and Smith's planetary gear vibration insights

Consider a planetary gearbox operating in a fixed-annulus-gear configuration[7] whose vibrations are measured at a fixed point in the annulus gear, as illustrated in Figure 3.5. McFadden and Smith (1985) found that harmonics of the tooth meshing frequency

[7] Visualizing the annulus gear as fixed is useful in the analysis, although this may not be the case. A necessary condition, however, is that the vibration must be measured at a fixed point with respect to the annulus gear.

and the modulation effect described below generate "regions" where the vibration spectrum of an epicyclic gear system, as measured from a point fixed with respect to the annulus gear, shows multiple frequency components. As will be seen below, these components, known as *sidebands*, appear as a harmonically spaced series.

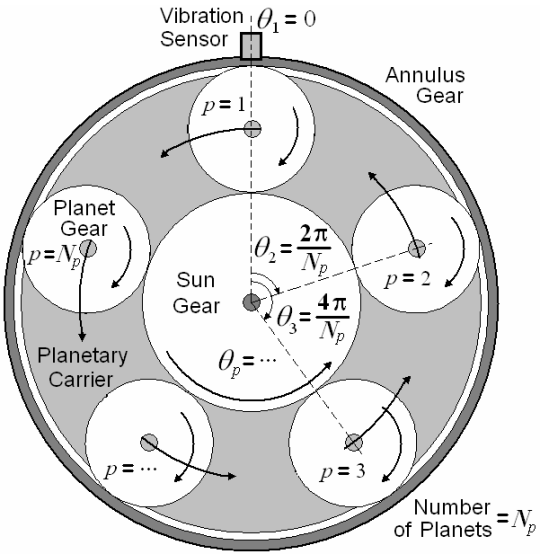

Figure 3.5. Representation of a planetary gear system with vibration sensor fixed on the annulus gear. Arrows represent direction of motion. θ_p is the angle (measured clockwise) from the sensor to the axis of rotation of planet gear number p

The work of McFadden and Smith explains at which frequencies such sidebands will be observed, and typical evidence of sidebands is shown in Figure 3.6. However, the amplitude of the sidebands cannot be determined from their study. Furthermore, their work is based on the assumption that all planet gears are equally spaced along the circumference of the planetary carrier plate.

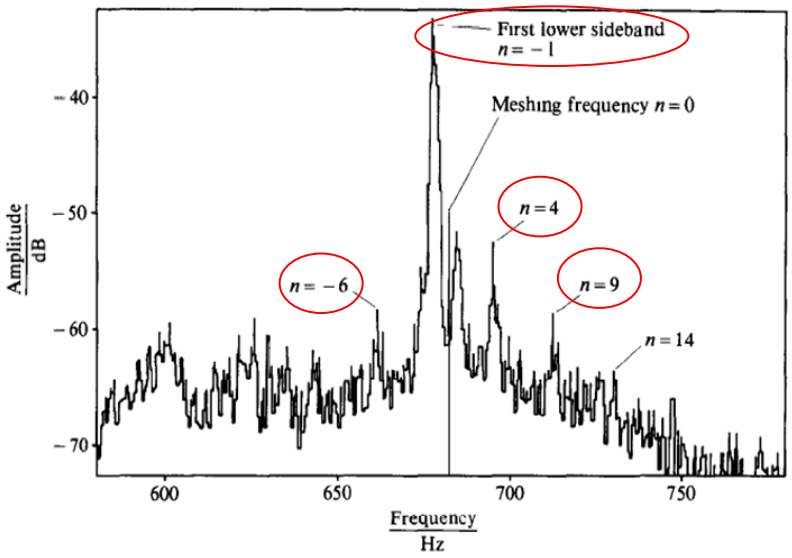

Figure 3.6. Vibration signature of the main rotor gearbox of a "Sea King" helicopter, used by McFadden and Smith to illustrate their findings. Adapted from McFadden and Smith (1985)

The vibration regions considered by McFadden and Smith are centered at integer multiples (i.e., harmonics) of the tooth meshing frequency, which is quantified as $N_t \cdot f^s$ with N_t being the number of teeth in the annulus gear and f^s the planetary carrier ("shaft") rotation frequency (denoted as f_c by McFadden and Smith.)

In general, although these vibration regions appear to be centered at $m \cdot N_t \cdot f^s$, where m is an index designating the harmonic number, the pattern of sidebands may not be symmetric about this value, as illustrated in Figure 3.7. These patterns form because of the interaction of two effects: the addition of the de-phased vibrations of the planet gears and the modulation of these vibrations effected by the translation of the planet gears about the sun gear and (more importantly) along the annulus gear.

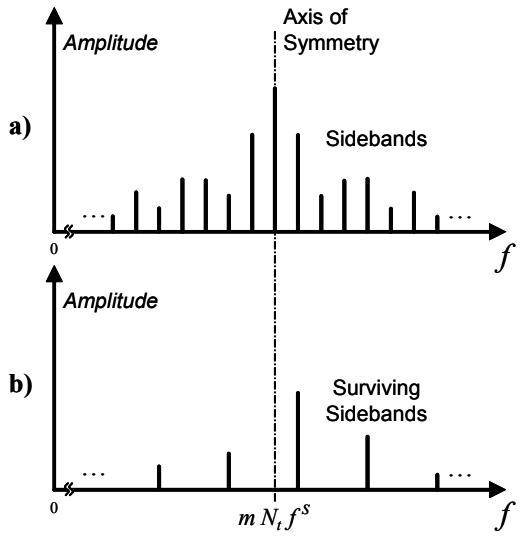

Figure 3.7. Simulated spectrum representation of vibrations generated by a planetary gear. (a) Symmetrical vibration caused by a single planet gear. (b) Asymmetrical sidebands of the combined vibration of all the planet gears

The vibrations individually generated by each one of the planet gears combine and experience interference. Some components interfere destructively, and thus we observe that certain frequency components that otherwise would be present as sidebands in the vibration spectrum of individual planet gears, can altogether disappear in the overall system's vibration. This elimination of frequencies has an explainable pattern that gives rise to the observed asymmetry of the sidebands, as illustrated in Figure 3.7b.

According to McFadden and Smith's model, in the vibration signal of individual planet gears –i.e., before the interference effect described above occurs–, sidebands can exist only at frequencies that are $m \cdot N_t + n$ multiples of the planetary carrier frequency f^s, where n is an index designating multiples of the carrier rotation frequency. The frequency components of individual planet gears (and their corresponding sidebands) have comparable amplitudes, but can differ in phase. The difference in phase causes that, in an

ideal, equally spaced planetary gear system, the individual planet-gear components whose $m \cdot N_t + n$ frequency factor is not also divisible by the number of planet gears N_p in the system, combine with phase shifts that null the vibration component in the gearbox vibration –i.e., after interference occurs–. McNames (2002) has confirmed that sidebands whose $m \cdot N_t + n$ factor is not a multiple of N_p will be suppressed.

Take for example the same case considered by McFadden and Smith of a compressor drive planetary gearbox. Table 3.2 lists which frequency components (sidebands) will and will not be suppressed. The table is similar to the one presented by McFadden and Smith, but is here expanded to show more harmonics.

Table 3.2. Sideband suppression pattern of a planetary gearbox with $N_p = 3$ and $N_t = 134$. Clear cells marked with "0" correspond to sidebands that become suppressed. Sidebands, each of whose frequency can be evaluated as $(m \cdot N_t + n) \cdot f^s$, subsist only when $(m \cdot N_t + n) / N_p$ is an integer

n	*m = 1*	*m = 2*	*m = 3*
-3	0	0	**1**
-2	**1**	0	0
-1	0	**1**	0
0	0	0	**1**
1	**1**	0	0
2	0	**1**	0
3	0	0	**1**

3.3.2.2. Keller and Grabill's equation

McFadden and Smith's analysis addresses the issue of sideband suppression. However, it does not go into considering the amplitude of the unsuppressed sidebands. For the experimental results of their paper (McFadden and Smith, 1985), they indicated that it was "not possible to predict the relative amplitudes of the surviving components

because these are determined by the pattern of [the frequency response coefficients of the modulating signal], which is not known."

Using McFadden and Smith's model, Keller and Grabill (2003) suggested an expression to represent the vibration signals of the system. In addition, their expression explicitly considers the effect of the frequency response coefficients of (1) the tooth meshing signal along with its harmonics, and (2) the modulating signal generated by the planetary carrier rotation (i.e., the planet gears' translation motion). Before discussing the actual equation suggested by Keller and Grabill, let us consider its underlying theory.

The tooth meshing vibration signal of a single planet gear, as seen from a fixed point in the planetary carrier, is generated by the engaging of teeth of this gear with the teeth of both the sun gear and the annulus gear. It is assumed that all the teeth behave similarly and thus that their vibration components have uniform amplitude. Because the speed at which teeth come in contact is proportional to the angular velocity of the planetary carrier, the meshing vibration is a multiple of the rotational frequency of the latter and is given by $N_t \cdot f^s$. This signal, whose amplitude is defined as β_1, is expected to show harmonics, with amplitudes of β_2 for the second, β_3 for the third and so on. Figure 3.8 illustrates a simulated spectrum of this vibration.

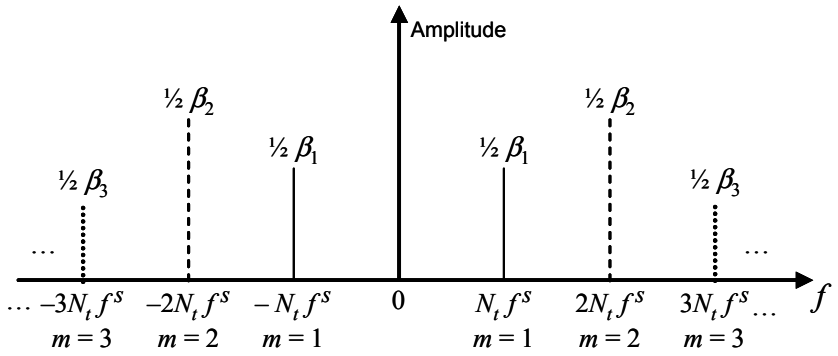

Figure 3.8. Magnitude spectrum of non-epicyclic tooth meshing vibration as seen from a fixed point on the planetary carrier

As the planet gears move in translation over the planetary carrier around the sun gear and along the annulus gear, a static observer located on the annulus gear would see the planet gears approaching from one side and retreating towards the opposite. As McFadden explained, when a planet gear is the closest, the observer would sense its meshing vibration the loudest; at the farthest, this vibration would be weaker. Figure 3.9 represents how the intensity of the signal varies as a single planet gear rotates.

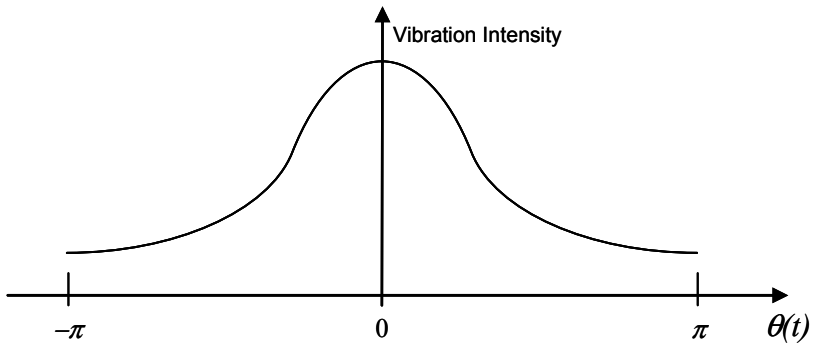

Figure 3.9. Representation of the intensity of the meshing vibration signal of a single planet gear in translation as perceived on a fixed point (vibration sensor) over the annulus gear. Horizontal axis represents the varying angular position of the planet gear as time passes

To the observer, the regular change in position of the planet gears and the subsequent change in intensity of their respective vibration signals modulate the overall meshing vibration. Figure 3.10 represents the spectrum of the modulating signal, showing the Fourier Transform coefficients of the curve of Figure 3.9. The coefficients are represented with indices of the letter α. Note that each α_n shows at both $n=k$ and $n=-k$ for any integer k. Also note that, in agreement with customary spectrum representation, α's have a constant coefficient of ½, with the exception of α_0, whose coefficient is 1.

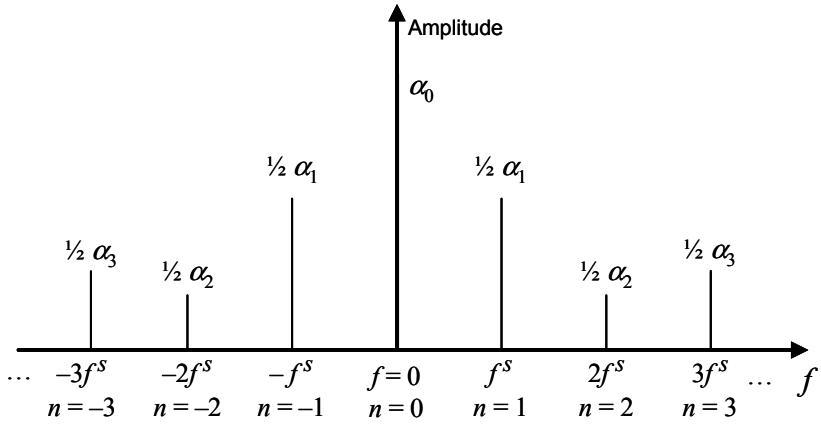

Figure 3.10. Magnitude spectrum of the modulation signal caused by the translation motion of a planet gear

When a planet gear moves, the signals represented in Figure 3.8 and Figure 3.10 combine in modulation. Recognizing the influence of the α_n and β_m coefficients of each of the signals involved in the modulation process, Keller and Grabill showed that the expected vibration signal of a planetary gearbox can be expressed as

$$y(t) = \frac{1}{2}\sum_{p=1}^{N_P}\sum_{m=1}^{M}\sum_{n=-N}^{N}\alpha_n\beta_m \sin(2\pi(m\cdot N_t + n)f^s t + \varphi_{p,m,n}), \tag{3.1}$$

where M is the and N are, respectively, the total number of harmonics of the tooth meshing frequency and of multiples of the carrier rotation frequency to consider in a given vibration analysis (ideally, M and N have values equal to infinity, but in practice only finite values are considered). $\varphi_{p,m,n}$ is a phase angle dependent upon the geometric position of the planet gears and is evaluated as

$$\varphi_{p,m,n} = (m \cdot N_t + n)\theta_p \,. \tag{3.2}$$

As suggested by the summation over p, the overall vibration of the planetary gear system is formed by the addition of the vibrations generated by the individual planet gears. In the ideal case, where the planet gears are identical, their vibrations would also be identical. Hence, the vibration perceived at the sensor would be the combination of N_p similar signals, equal in shape (amplitude) but differing in place of origin (phase). This difference in the signals is generated by the planet gear positions, as substantiated below.

3.3.2.3. Planetary gearbox vibration as a sum of similar but delayed signals

Define T_p as the time it takes for planet gear p to reach the sensor within one revolution of the planetary carrier. Because the planetary carrier plate has a rotational frequency of f^s, and because planet gear p is located at θ_p at the instant where time $t = 0$, we have that

$$\theta_p = 2\pi f^s T_p \,. \tag{3.3}$$

The modulation of the signals represented earlier in Figure 3.8 and Figure 3.10 produces vibration signatures of individual planet gears that can be described as a sum of sinusoids given by

$$y_p(t) = \frac{1}{2}\sum_{m=1}^{M}\sum_{n=-N}^{N}\alpha_n\beta_m \sin(2\pi(m \cdot N_t + n) f^s t + \varphi_{p,m,n}), \tag{3.4}$$

where $y_p(t)$ is the vibration signal of any one planet gear, numbered p. Substituting Equation 3.2 we can rewrite this as

$$y_p(t) = \frac{1}{2}\sum_{m=1}^{M}\sum_{n=-N}^{N}\alpha_n\beta_m \sin(2\pi(m \cdot N_t + n) f^s t + (m \cdot N_t + n)\theta_p). \tag{3.5}$$

Substituting (5) and regrouping we obtain that

$$y_p(t) = \frac{1}{2}\sum_{m=1}^{M}\sum_{n=-N}^{N}\alpha_n\beta_m \sin(2\pi(m \cdot N_t + n) f^s (t + T_p)). \tag{3.6}$$

Next, since we assumed that the first planet gear is aligned with the sensor at t = 0, yielding $\theta_1 = T_1 = 0$, and because of the $t + T_p$ factor in Equation 3.6, the vibration of any planet gear may be expressed as a delayed version of the first planet gear's vibration, i.e.,

$$y_p(t) = y_1(t - T_p). \tag{3.7}$$

Hence, in the ideal case where all planet gears and all teeth contacts behave similarly, if the planet gears are equally spaced, the overall planetary system vibration is the sum of N_p delayed copies of one planet gear's vibration signal, which can be expressed as

$$y(t) = \sum_{p=1}^{N_P} y_1(t - T_p) . \tag{3.8}$$

If the system is not equally spaced but the vibrations of the individual planet gears still have similar shapes, the overall vibration of the system is a combination of these similar signals, each with its respective T_p delay. This form of delayed addition has led researchers to search for ways to separate the vibration of the individual planet gears. Several of these techniques are referenced and described by Samuel (2003).

3.3.2.4. Characterization of the vibration of an ideal planetary gearbox and definition of the types of sidebands

We can now analyze the vibration spectrum of a planetary gear system with equally spaced planet gears using the definition of Keller and Grabill for α_m and β_m considered in section 3.3.2.2. After the signals represented in Figure 3.8 and Figure 3.10 have combined in modulation, the spectrum for the vibration of a single planet gear will be as shown in Figure 3.11. Note the effect on the constant coefficients, which, because of the product of coefficients caused by modulation, become either ½ or ¼ for all sidebands.

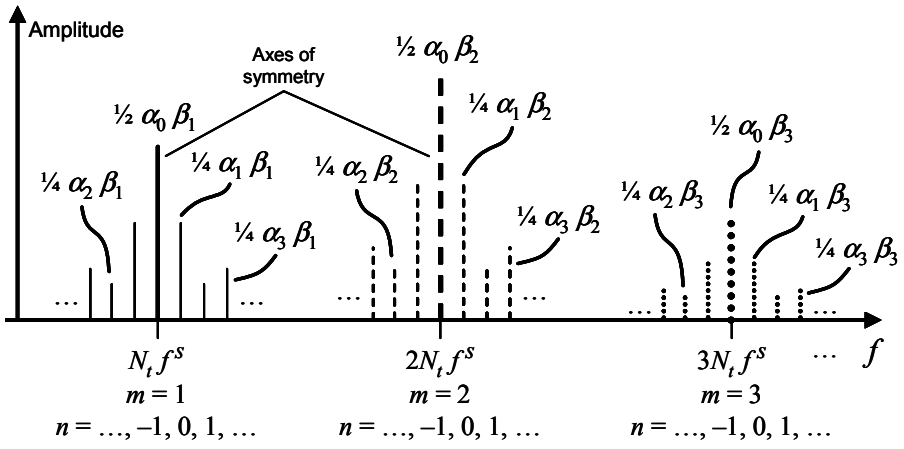

Figure 3.11. Vibration spectrum of a single planet gear. Only right-hand side of the spectrum is shown

As described in section 3.3.2.1, sidebands can only be found at $m \cdot N_t + n$ multiples of the planetary carrier frequency f^s. Hence, we can refer to individual sidebands by their particular $m \cdot N_t + n$ numbers, which are always integers, as Keller and Grabill have done[8]. We can also identify sidebands by the pair (m, n).

The phase of each sideband shown in Figure 3.11, as found by McFadden and Smith, depends on the geometrical angular position of the planet gear in the planetary carrier. The phase of sideband $m \cdot N_t + n$ is equal to $\theta \cdot (m \cdot N_t + n)$, where θ is the *initial* angular position of the planet gear under consideration about the axis of rotation of the planetary carrier, and taking zero angle at the sensor, by "initial" meaning the time instant at which the system's vibrations start to be measured.

To generalize this claim, consider again Figure 3.5. Suppose planet gear number 1 is aligned with the vibration sensor when the system's vibrations start to be measured. In

[8] Keller and Grabill refer to this number as the *order* of a sideband.

this case, planet gear number p (for any p=1 to N_p) has an initial angular position of $2\pi\cdot(p-1)/N_p$ with respect to the axis of the planetary carrier and taking zero angle at the sensor. Then, for an equally spaced system, the phase angle of sideband $m\cdot N_t + n$ in the spectrum of planet gear p is

$$\varphi_{p,m,n}^{\text{equal-spc}} = (m \cdot N_t + n)\theta_p , \tag{3.9}$$

where $\theta_p = 2\pi \dfrac{p-1}{N_p}$. In accord with McFadden and Smith's findings, the phase angles of corresponding sidebands across different planet gears are for some frequencies in phase with the rest, and for the rest out of phase. Clearly, because of Equation 3.9, only when $m\cdot N_t + n = k\cdot N_p$ for any integer k are the sidebands of all the planet gears in phase. Thus, when the vibrations generated by the different planet gears in the system combine, vibrations from the sidebands that are in phase add constructively.

If the planet gears are evenly spaced along the circumference of the planetary carrier, then, whenever $m\cdot N_t + n \neq k\cdot N_p$ for any integer k, the phase angles of the sidebands are also evenly spaced from 0 to 2π. Thus, when the vibrations generated by the different planet gears in the gear system combine, vibrations from the sidebands that are out-of-phase add destructively, as McFadden and Smith found, and can in fact altogether become zero.

When the sidebands add constructively, because this addition involves as many sidebands as the gearbox has planet gears, the sidebands that are located over axes of symmetry (i.e., at frequencies equal to harmonics of the tooth meshing frequency,

quantified as $m \cdot N_t \cdot f^s$) will produce an overall system sideband with half-amplitude equal to

$$\frac{N_p}{2}\alpha_0\beta_m, \quad \text{for sidebands with } n = 0. \tag{3.10}$$

The sidebands that are not in the axes of symmetry will generate a system sideband with a half-amplitude of

$$\frac{N_p}{4}\alpha_n\beta_m, \quad \text{for sidebands with } n \neq 0. \tag{3.11}$$

Equations 3.10 and 3.11 agree with the recognition by McNames (2002) that the overall system's sidebands would be an N_p scaling of the individual planet gears' sidebands.

Take again McFadden and Smith's compressor drive gearbox as an example (refer to Table 3.2). Suppose that Figure 3.11 represents the spectrum of one planet gear of such system. Since there are $N_p = 3$ planet gears, and because the number of teeth $N_t = 134$ generates the sideband suppression pattern previously shown in Table 3.2, we could expect to see a gearbox spectrum as shown in Figure 3.12. The spectrum of the graph represents the case of an ideal system, where all the planet gears are evenly spaced along the planetary carrier's circumference.

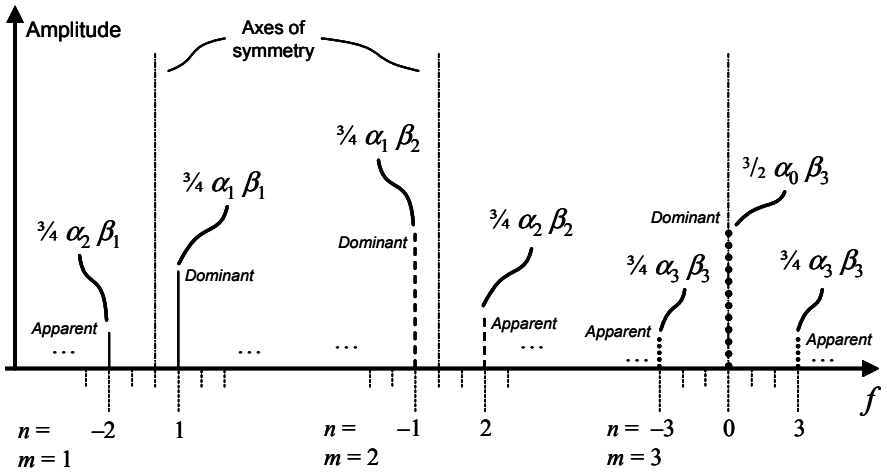

Figure 3.12. Sidebands of equally spaced planetary gearbox with $N_p = 3$ and $N_t = 134$

Keller and Grabill referred to the surviving sidebands with two different names. For each group of sidebands with the same value of *m*, there is one *dominant* sideband, which is the one closest to the axis of symmetry. The other surviving sidebands in the group are called *apparent* sidebands[9]. This naming convention is used in Figure 3.12, and is followed throughout this thesis. The suppressed sidebands, which are not visible in the ideal case discussed, are important for the present study, and hence they will be referred to as *non-dominant* sidebands. Regardless of this naming convention, sidebands will also be identified by their *m* and *n* numbers.

3.4. A Vibration Model for Planetary Gearboxes with Planet-gear shifts

Relating sideband changes to the amount of relative shift between the planet gears can be of interest for detecting faults in planetary gear systems. Take for example the

[9] McNames calls all surviving sidebands "dominant." McFadden calls one sideband "dominant", the others just "surviving".

problem described in section 3.1. A crack near the root of one of the planet gear mounting posts of the planetary carrier plate would reduce the stiffness of this component, leading to abnormal deformation that in turn causes non-uniform shifting of the planet gears. Hence, the angular shifts will vary with the length of the crack.

3.4.1. Effect of the shift of a planet gear

Sections 3.3.2.1 through 3.3.2.4 assumed that planet gears were evenly spaced along the circumference of the planetary carrier plate, with geometric angles given by $\theta_p = 2\pi \frac{p-1}{N_p}$. Consider now the case when one planet gear has shifted with respect to its corresponding θ_p angle by a specific amount, namely δ_p. This condition is illustrated in Figure 3.13.

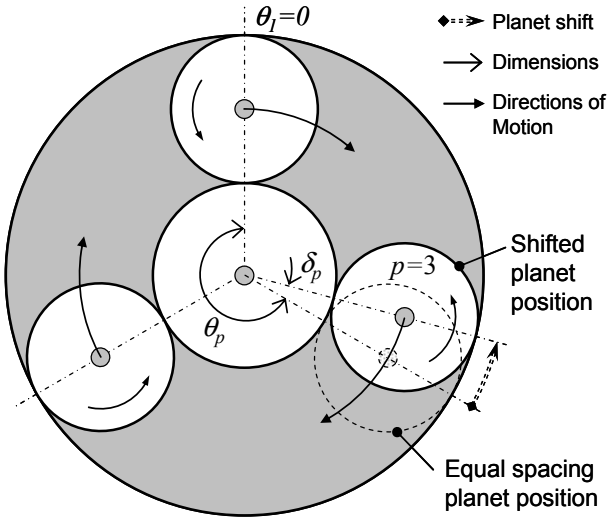

Figure 3.13. Angular shift of planet gear number 3 in a system with $N_p = 3$

We discussed in section 3.3.2.4 that the phase of the sidebands generated by the meshing of single planet gears are $m \cdot N_t + n$ scalings of the geometric angular position of the corresponding planet gears. Because the phases of the sidebands thus depend on the geometric position of the planet gears, once a planet gear has shifted from its corresponding θ_p position to a new $\theta_p + \delta_p$ angle, the phases of its sidebands also change. This is verified by substituting the new angle in Equation 3.9 to obtain that

$$\varphi_{p,m,n}^{\text{shifted}} = (\theta_p + \delta_p) \cdot (m \cdot N_t + n). \tag{3.12}$$

By rearranging this result, we find that the phases of the sidebands of a shifted planet gear $\varphi_{p,m,n}^{\text{shifted}}$ are equal to the phase of the equally spaced planet gear position (i.e., without the shift) plus a quantifiable phase change, i.e.,

$$\varphi_{p,m,n}^{\text{shifted}} = \theta_p \cdot (m \cdot N_t + n) + \delta_p \cdot (m \cdot N_t + n) = \varphi_{p,m,n}^{\text{equal-spc}} + \Delta\varphi_{p,m,n}, \tag{3.13}$$

where $\varphi_{p,m,n}^{\text{equal-spc}}$ is obtained from Equation 3.9, and

$$\Delta\varphi_{p,m,n} = \delta_p \cdot (m \cdot N_t + n) \tag{3.14}$$

is the sideband phase change effected by the planet-gear shift. In conclusion, when a planet gear shifts, the phase of each of its corresponding sidebands changes by an $m \cdot N_t + n$ proportion of that shift. Following McFadden and Smith's approach, the idea is illustrated in Figure 3.14 using phasor representation.

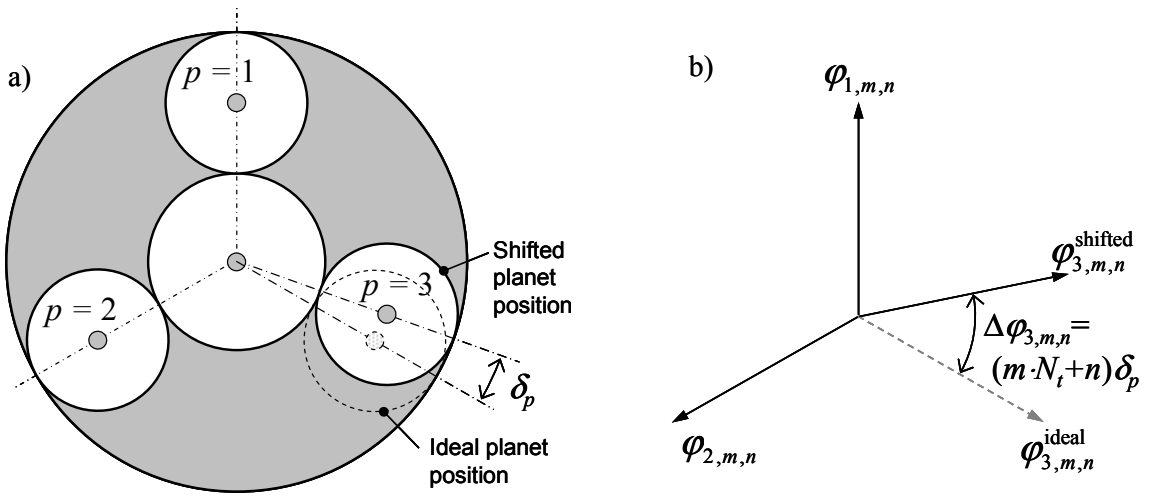

Figure 3.14. Effect of angular planet-gear shift on the phase of a planet gear's sidebands; a) representation of a shift in planet gear number 3 of a three-planet-gear system; b) Phasor representation of the corresponding effect in the phases of the sidebands of each planet gear; the φ's represent angles of the phasors. *Note*: δ_p is not to scale in a) and b)

Expectedly, sidebands generated by systems with a shifted planet gear that experience phase changes of $\Delta\varphi_{p,m,n} = 2\pi \cdot k$ for any integer k are equivalent to the sidebands of a system without planet-gear shifts (i.e., equally spaced), since a phase change of multiples of 2π return a $\varphi^{\text{shifted}}_{p,m,n}$ phasor angle to its equal-spacing position. We might be tempted to think that it is thus possible for all evidence of a gear shift to disappear when a shift angle causes $\Delta\varphi_{p,m,n} = 2\pi \cdot k$. However, by substituting $\Delta\varphi_{p,m,n} = 2\pi \cdot k$ in Equation 3.14, we find that only the sidebands whose $m \cdot N_t + n = \dfrac{2\pi \cdot k}{\delta_p}$ will return to the equally spaced position and eliminate any evidence of shifting. The equality condition $m \cdot N_t + n = \dfrac{2\pi \cdot k}{\delta_p}$ is rarely met among all the (m, n)

sidebands corresponding to a planet gear. Thus, in general, we can expect most of the sidebands of a shifted planet gear to be affected, and show evidence, of an angular shift.

Consider now the changes experienced by the sidebands in relation to the amount of angular shift of a planet gear. From the discussion above, we know that we can expect to see the effect of a planet-gear shift on a specific $m \cdot N_t + n$ sideband disappear whenever $\delta_p = \frac{2\pi \cdot k}{m \cdot N_t + n}$ for any integer k. Conversely, because the effect of the shift on the sideband's phase has to increase as $\Delta\varphi_{p,m,n}$ moves away from multiples of 2π, the effect will be maximum when $\delta_p = \frac{\pi \cdot k}{m \cdot N_t + n}$. In practice, because the value of n is typically small when compared to $m \cdot N_t$, and because sideband analyses are typically done in the regions where n is close to 0, we may be able to use the following two approximations within the group of sidebands of a specific m^{th} harmonic region:

$$\text{For the } m^{\text{th}} \text{ harmonic, if } \begin{cases} \delta_p \approx \dfrac{2\pi \cdot k}{m \cdot N_t}, & \text{then planet shift effect is negligible} \\ \delta_p \approx \dfrac{\pi \cdot k}{m \cdot N_t}, & \text{then planet shift effect is maximum} \end{cases} \quad (3.15)$$

for any integer k. This behavior is demonstrated graphically in Figure 3.15.

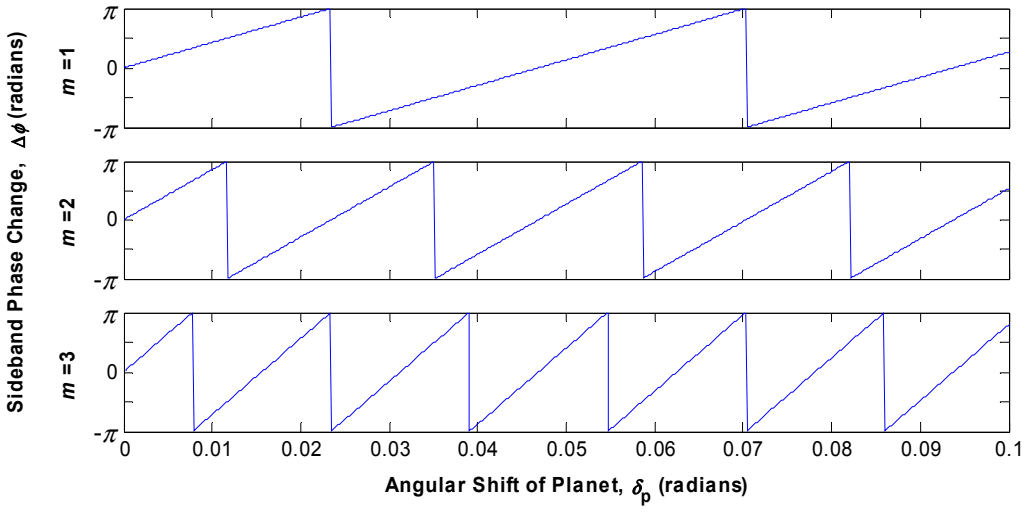

Figure 3.15. Sideband phase change $\Delta\varphi_{p,m,n}$ of the dominant sideband (n = 0) as a function of the geometric angular shift δ_p of a planet gear for different tooth meshing harmonics. System represented has N_p=3 and N_t=134

Note in Equation 3.14 that, because typically a large number scales the planet-gear shift angle, even small shifts can noticeably affect the sidebands of a planetary gear system, especially in higher harmonics, where m is larger. For example, in a system with N_t=134, the dominant sideband (n=0) of the third tooth meshing harmonic (m=3) can experience a full phase reversal (phase change of $\Delta\varphi_{p,3,0} = \pi$) with a planet-gear shift of only about 0.45 degrees (0.008 radians).

Also note that, with respect to the first tooth meshing harmonic (m=1), phase changes are twice as fast on the second tooth meshing harmonic (m=2), three times as fast on the third (m=3), and so on. This fact suggests that the effect of small planet-gear shifts may be more perceptible at higher tooth meshing harmonics. However, other factors must be considered, as discussed later, in section 3.4.3.

As was discussed in section 3.3.2.4, when the vibrations of the individual planet gears combine to form the overall planetary system vibration signal, an equally spaced system would experience suppression of all non-dominant sidebands, i.e., those whose $m \cdot N_t + n \neq k \cdot N_p$. However, this does not entirely hold true for a system with planet-gear shifts. As is represented in Figure 3.16, when a planet gear shifts, the formation of sidebands in the overall system's spectrum is affected. Depending on the magnitude of the planet-gear shift angle it is most likely that the dominant and apparent sidebands will see their magnitude reduced by some amount with respect to that of the equally spaced case; simultaneously, non-dominant sidebands will not be completely suppressed.

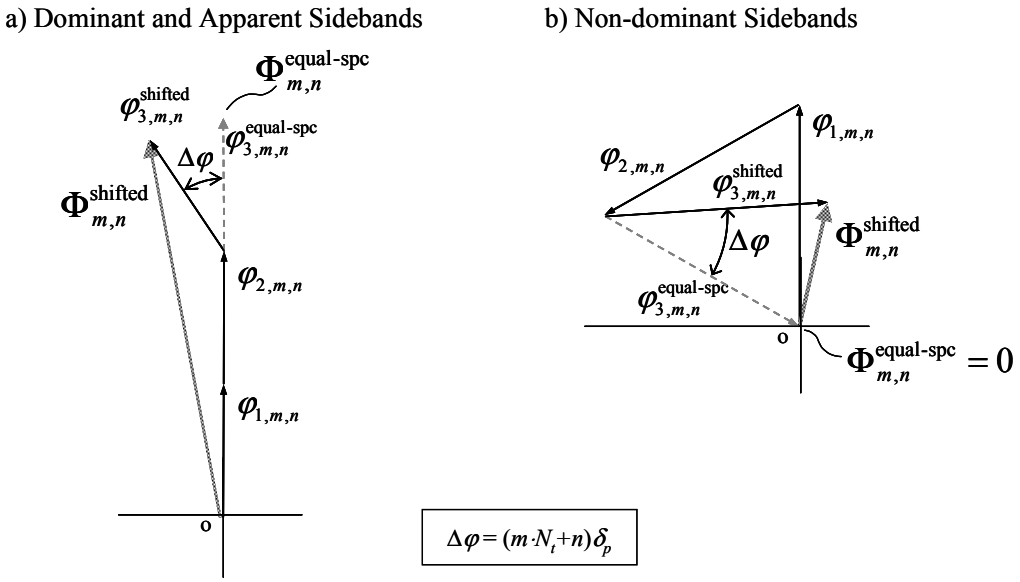

Figure 3.16. Phasor representation of the formation of planetary system sidebands through addition of individual planet-gear sidebands; a) dominant and apparent sidebands, $m \cdot N_t + n = k \cdot N_p$; b) non-dominant sidebands, $m \cdot N_t + n \neq k \cdot N_p$. The φ's and Φ's are used to represent, respectively, the angles of individual planet gear phasors and of overall system phasors

The drop in magnitude of the dominant and apparent sidebands and the corresponding rise of the non-dominant sidebands, all caused by planet-gear shifting, is illustrated in Figure 3.17 as a function of the change of phase on a single-planet-gear sideband, $\Delta\varphi$. Figure 3.18 shows what changes would be observed in the spectrum of a gearbox with a particular planet-gear shift. Notice in this graph that the effect tends to be more perceptible on the regions of higher harmonics, where the planetary shift angle is scaled by a larger amount.

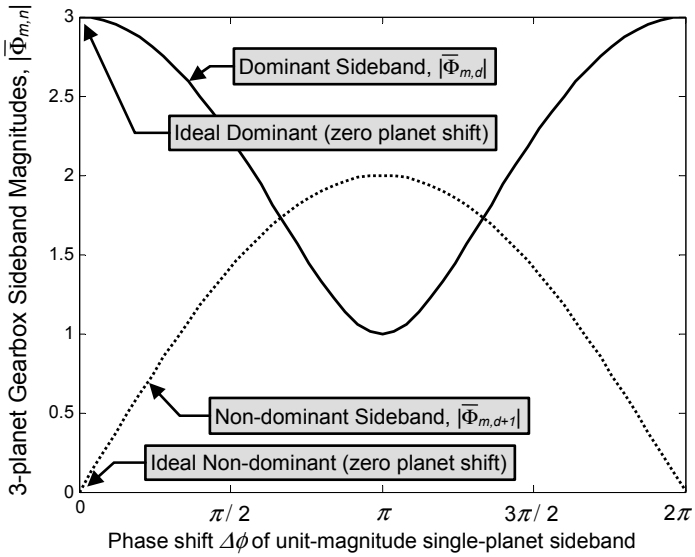

Figure 3.17. Effect of single-planet-gear shift in the magnitude of dominant (or apparent) and non-dominant sidebands for a system with three planet gears and unity single-planet sideband magnitudes. Ordinate axis is scaled to the magnitude of a single planet gear's contribution

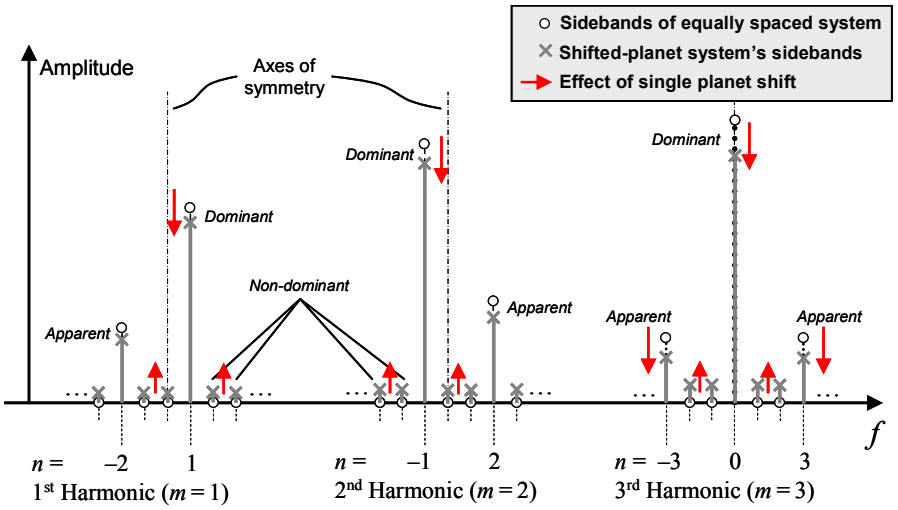

Figure 3.18. Comparison of sidebands in the spectra of an equally spaced planetary gearbox and a gearbox with planetary shifting. When planet-gear shifting occurs, dominant and apparent sideband magnitudes are expected to decrease while non-dominant sidebands are expected to increase with respect to the equally spaced case

3.4.2. Other effects due to the number of planet gears

Figure 3.19 shows in more detail how dominant and apparent sidebands are formed by the addition of single-planet-gear sidebands when one planet gear shifts for the cases of systems with $N_p = 3$ planet gears and with $N_p = 5$ planet gears. The illustration also shows the theoretical ranges for the overall system sidebands when the last planet gear ($p = N_p$) shifts. It is worthwhile to note that both the magnitude $\left|\vec{\Phi}_{m,n}\right|$ and phase ($\angle\vec{\Phi}_{m,n} = \Phi_{m,n}$) of the system sidebands change with the planet-gear shift. However, the change in magnitude is relatively smaller as the number of planet gears increases.

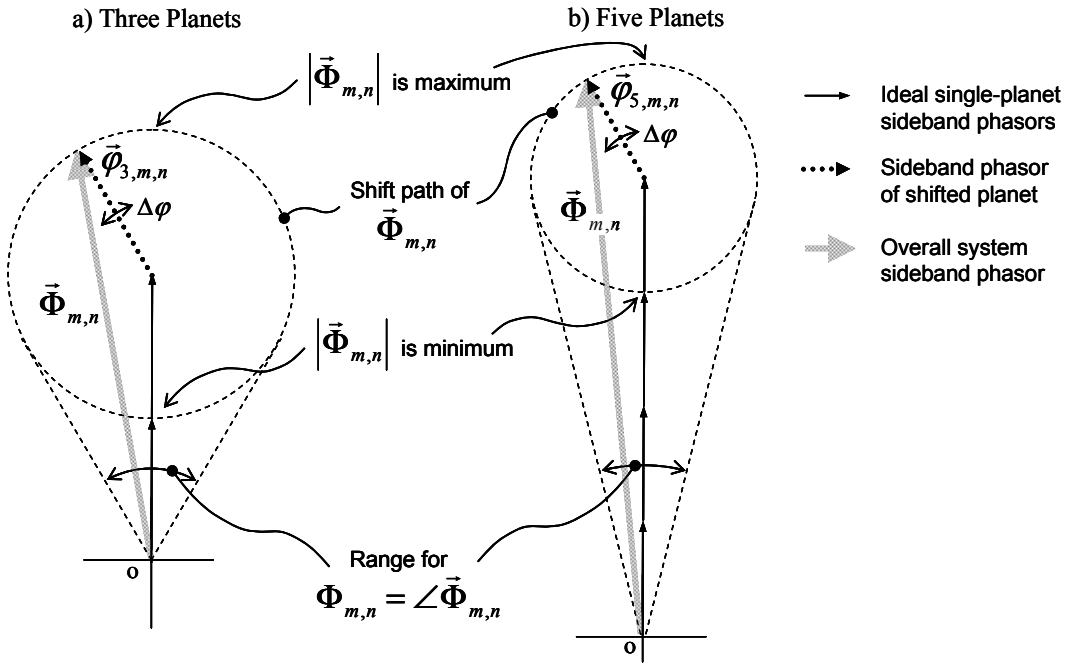

Figure 3.19. Effect of single-planet-gear shift on the formation of dominant and apparent sidebands; a) system with 3 planet gears; b) system with 5 planet gears. The φ's and Φ's are used to represent, respectively, planet gear and system phasors (i.e., vector quantities)

For example, the minimum of the system's sideband magnitude in the system with three planet gears equals the magnitude of one single-planet-gear sideband, suggesting a maximum change of 2/3 of the magnitude of the equally spaced case. The minimum magnitude when there are five planet gears equals the sum of 3 single-planet-gear sidebands, corresponding to a maximum variation of only 2/5 of the magnitude of the sideband of the equally spaced system.

Effects of the number of planet gears over the magnitude and phase of the non-dominant overall system sidebands are shown in Figure 3.20.

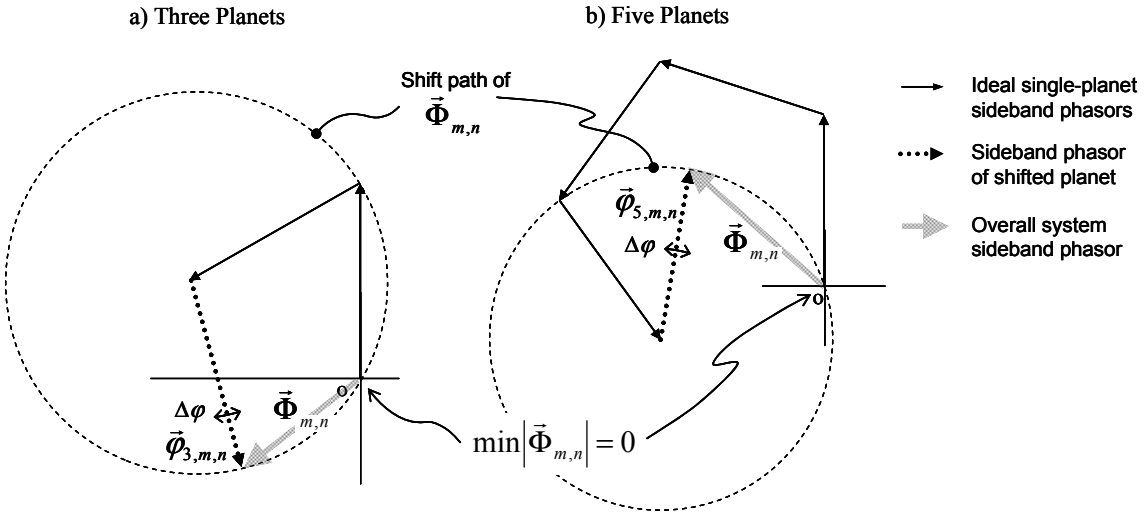

Figure 3.20. Effect of single-planet-gear shift on the formation of non-dominant sidebands; a) system with 3 planet gears; b) system with 5 planet gears. The φ's and Φ's are used to represent, respectively, planet gear and system phasors (i.e., vector quantities)

3.4.3. Sensitivity of the vibration to planet-gear shifting

The preceding discussion and the results of Equation 3.15 already suggest what can be formally determined to be the sensitivity of the phase of sidebands to angular shifts. When the spectrum of a single planet gear is considered, it should be expected that the amplitude of the sidebands is insensitive to angular shifts. Yet, the phase of the sidebands changes proportionally to both the amount of angular shift and the sideband number. This is immediately verified by differentiating Equation 3.13 with respect to the angular shift of a planet gear to obtain that

$$\frac{d\varphi_{p,m,n}^{\text{shifted}}}{d\delta_p} = \frac{\Delta\varphi_{p,m,n}}{\delta_p} = m \cdot N_t + n \,. \tag{3.16}$$

This result suggests once again that sidebands located at increasingly higher frequencies (i.e., for the most part at larger harmonics, or greater *m* values, and for the least at higher *n* values) show an increased phase change when small planet-gear shifts occur. The finding is important because it might provide a guide to selecting frequency bands for planet-gear shift detection, as will be discussed below.

The sensitivity of the overall system's vibration is a different matter, however. In this case, both the amplitude and the phase angle of the system's sidebands are affected by the angular shift of any one planet gear because of the interference of the individual planet gears' vibrations.

Evaluating the sensitivity of the overall system's sidebands can be done analytically via vector operations by representing the sidebands as vector quantities, or phasors, in a fashion similar to that of McFadden and Smith's work. However, this task is overlooked in the present research. Nevertheless, the following points will be made about the sensitivity of the overall system's vibration:

1) The overall system's sensitivity may be better expressed as a vector result (with phase sensitivity and magnitude sensitivity). In addition, the sensitivity might have to be evaluated as a partial derivative of the overall system with respect to the angular shift of a single planet gear; i.e., when more than one planet gear shifts, sensitivity can be evaluated on a gear-by-gear basis.

2) The combined effect of multiple planet-gear shifts can be complex, chiefly because the single-planet-gear phasors, as was shown in Figure 3.16, combine in a different manner at each spectral frequency. Thus, each one of the overall system's sidebands, each of which is located at its own $m \cdot N_t + n$ value, is formed by the combination of individual planet gear sidebands with their own $m \cdot N_t + n$ sensitivity to the particular δ_p shift angle corresponding to their planet gear.

3) Even though the sensitivity of the phase of a single-planet-gear sideband is for the most part proportional to the harmonic number m at which it is located, as suggested by Equation 3.9, the sensitivity of the overall system's sidebands may not be in any way comparable to this amount.

4) As mentioned earlier, even small planet-gear shifts can cause considerable changes in the system sidebands. Hence, even manufacturing tolerances (for the planet gears' angular positions) can cause differences in the sideband signature of otherwise similar systems.

3.4.4. Effects of large shift angles

One of the effects of large angular shifts of planet gears is that dominance of sidebands may change from one sideband to the next, especially in systems with 4 planet gears or less, per the analysis of the effect of the number of planet gears, above. By dominance here, it is meant that the "tallest" sideband (i.e., with the largest amplitude) is no longer at a position where $m \cdot N_t + n$ is an integer multiple of N_p. When one planet gear

shifts relatively to the others, dominance of sidebands can change at each group of N_p adjacent sidebands. However, whether dominance changes or not depends on the planet-gear shift angle δ_p and the relative change in amplitude of the specific sidebands involved, all adjacent, since each sideband experiences a particular $\Delta\varphi_{p,m,n}$.

Suppose for example that in the equally spaced case with no planet-gear shifting some particular (m, n) sideband with $n = d$ is dominant. The sideband may be formed in fashion similar to that illustrated by Figure 3.16a, regardless of the number of planet gears in the system. For this case, the adjacent sideband, identifiable by (m, d + 1), would be non-dominant, and would be formed in a manner similar to the representation of Figure 3.16b. If δ_p is large enough, it may happen that the respective $\Delta\varphi$ values of each of these two sidebands causes the magnitude of the phasors to change considerably, up to a point where the (m, d) sideband becomes "shorter" than the (m, d + 1) sideband, thus showing an effect of "dominance shift". The situation is illustrated in Figure 3.21.

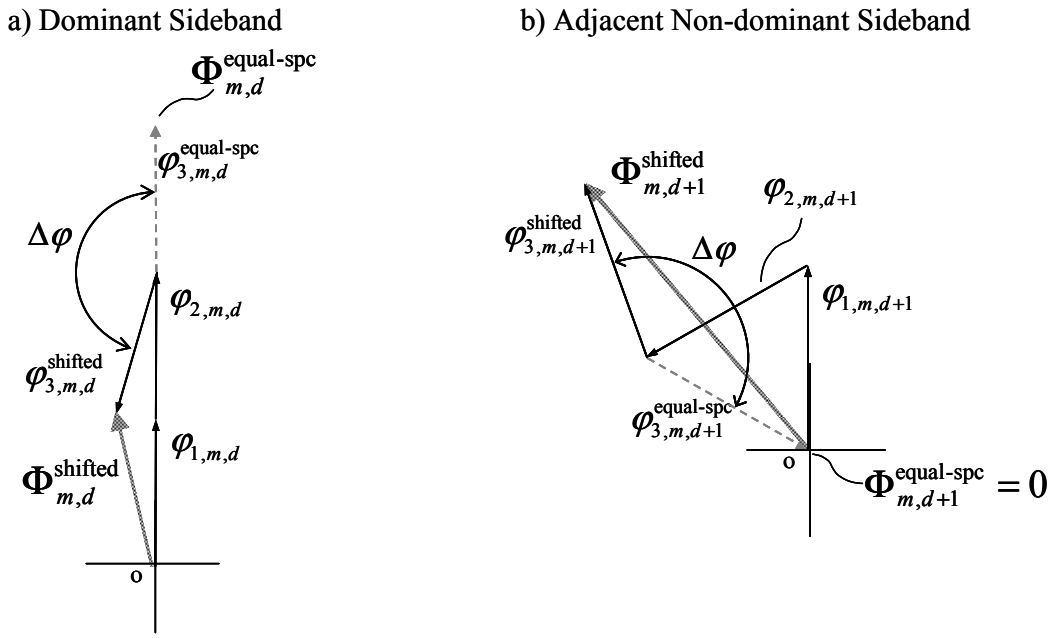

Figure 3.21. Illustration of the case when dominance of sidebands can switch from a sideband to an adjacent sideband. a) What appeared to be a dominant sideband on an equally spaced system can become a "short" sideband on the system with a planet-gear shift. b) The adjacent non-dominant sideband becomes longer than the "short" sideband in the system with the planet-gear shift, thus giving the impression of a dominance shift

Even though it is possible to observe this dominance shift effect in systems with planet-gear shifts, it is improbable at a specific frequency. Nevertheless, since there are so many sidebands, it is very likely that in a real system with 4 planet gears or less, apart from noise-induced or other variability effects, some sideband groups will show this effect.

3.4.5. Model validation

Vibration data from the experiments described in section 3.2 is used to validate the vibration model for planetary gearboxes with planet-gear shifting developed above. Time synchronous averaging (TSA) was applied to the vibration signals of the

accelerometers to normalize the frequency units with respect to the carrier rotation speed. The procedure is in line with techniques used by Keller and Grabill (2003), Wu et al. (2004) and Hines et al. (2005). Descriptions of the TSA technique can be found in Vachtsevanos et al. (2006) and Samuel (2003).

As was listed earlier in Table 3.1 (see section 3.2), vibration signals were acquired in all cases at various engine torque settings. Different toque settings produce different amounts of deformation on the planetary carrier plate, leading to varying degrees of planet-gear shifting. Nevertheless, the strains near the planet gear mounting post root, where the crack is located, vary linearly with torque (see Sahrmann, 2004). Thus, we would expect the gearbox to experience larger planet-gear shift angles at increased torques.

3.4.5.1. Validation through experiments with specific crack lengths (first set of experimental data)

Tests with specific crack lengths were carried out for two different cases, each of which required different a different planetary carrier plate. One of the carrier plates was cracked and the other was healthy (i.e., without a crack). Because of the possible variations between the two system-setups, if would be unfair trying to compare vibratory signatures of the two systems without making proper adjustments. The adjustments are necessary because each system tested can have a different frequency response. In other words, the values for α_m and β_m considered in sections 3.3.2.2 and 3.3.2.4 can vary among experiments and produce different signature scales. To correct for this variation, results

are here presented with frequency components normalized. The normalization is done with respect to the magnitude of the dominant frequencies (i.e., all sideband magnitudes divided by the magnitude of dominant sideband located at $f = m \cdot N_t \cdot f^s$).

For this first set of experiments, the gearbox was run at a desired engine torque setting and allowed to stabilize for some time before vibration data was acquired. Results presented here use data from the sensor referred to as "Port Ring" by Blunt and Keller (2006). The graphs in Figure 3.22 through Figure 3.29 show how most non-dominant sidebands in the system where a 3.25-inch crack is present (i.e., where there is a planet-gear shift) rise above those in the system with a healthy carrier plate (i.e., without abnormal planet-gear shifts). Sidebands that do not behave this way may exhibit the discrepancy because of noise or other signal variability effects, but the mean value of the non-dominant sidebands seen in the picture is represented by a horizontal line to show the overall effect.

The graphs report on data from the test cell gearbox and from on-board actual helicopters. Observe, furthermore, that the dominant and apparent sidebands (located at frequencies that are multiples of 5 and plotted over the vertical, dotted grid lines) tend to decrease in magnitude when the carrier plate experiences crack-induced planet-gear shifting, although they sometimes show a discrepancy too. Note however, that, when the torque applied to the planetary carrier is low and thus the planet-gear shift angles are not as large, the shifting effect does not show clearly in the sideband magnitudes of the vibration spectrum. Such situation, which may be caused by noise or other signal variations overwhelming the sideband magnitudes, can be seen in the third harmonic

region plot of Figure 3.22 and Figure 3.23, where the engine torque values are only 20% and 30%, respectively, for test cell data. Signal variability levels have been observed to be larger in the experimental data used at higher frequencies, and this would explain why higher harmonic regions, such as the third, sometimes show the discrepancy. There, the mean value line of the non-dominant sideband magnitudes for the cracked carrier plate is below that of the healthy plate. Nevertheless, at 30% engine torque, the effect is reduced, and this is in line with the possibility that planet-gear shift angles become larger. This discrepancy effect does not appear in aircraft data at 20% torque (Figure 3.28), but it does slightly at 30% (Figure 3.29).

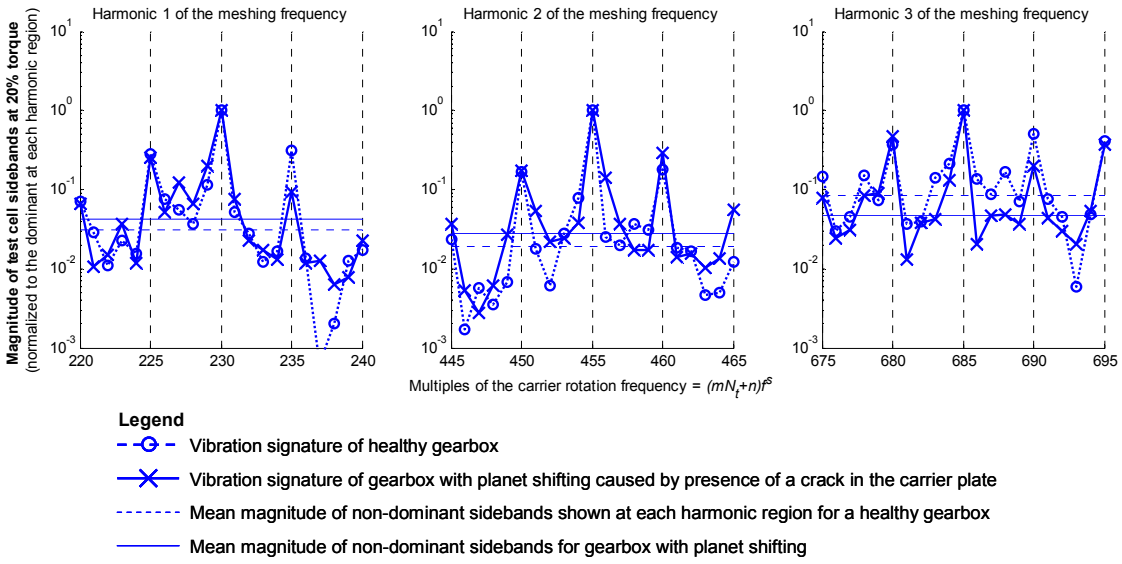

Figure 3.22. Vibration spectrum for test cell gearboxes with $N_p = 5$ planet gears and $N_t = 228$ teeth in the annulus gear. One of the gearboxes had a 3.25-inch crack on the root of a mounting post of one of the planet gears in the planetary carrier plate, leading to abnormal planet-gear shifting; the other gearbox was in normal operating conditions. Planet-gear shifting is here expected to be low because stresses on the planetary carrier plate, caused by an operational engine torque of only 20% of the nominal, were also relatively low

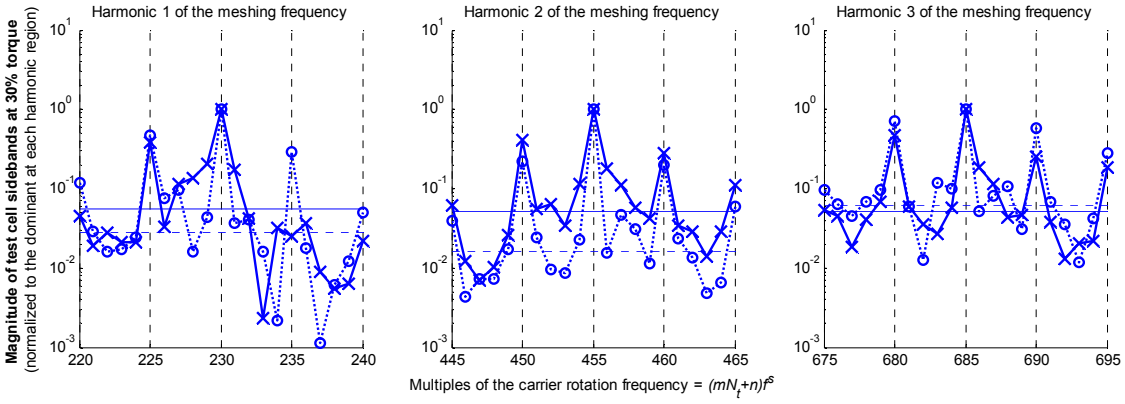

Figure 3.23. Vibration spectrum for test cell gearboxes at 30% engine torque.
Data legend is same as in Figure 3.22

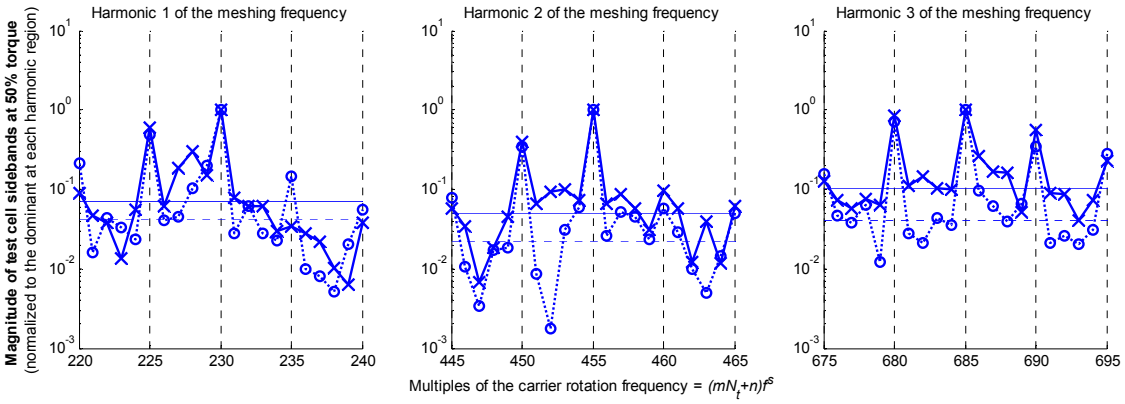

Figure 3.24. Vibration spectrum for test cell gearboxes at 50% engine torque.
Data legend is same as in Figure 3.22

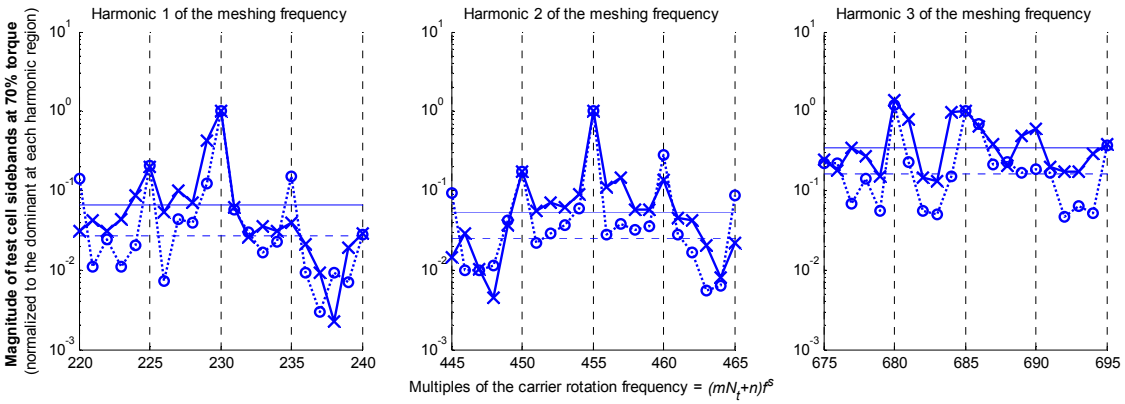

Figure 3.25. Vibration spectrum for test cell gearboxes at 70% engine torque.
Data legend is same as in Figure 3.22

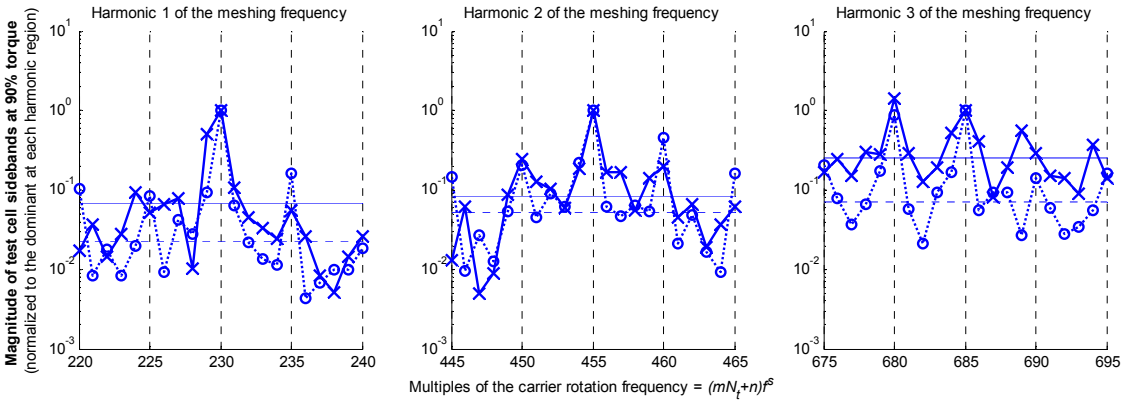

Figure 3.26. Vibration spectrum for test cell gearboxes at 90% engine torque.
Data legend is same as in Figure 3.22

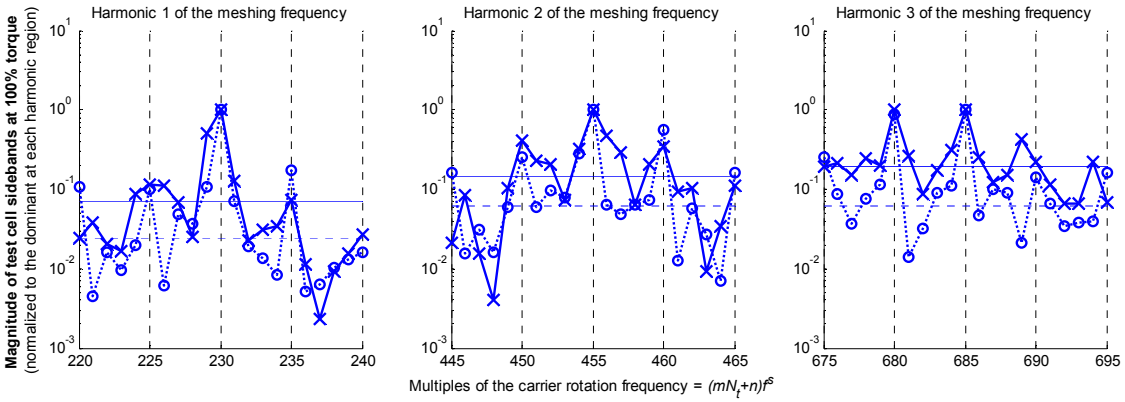

Figure 3.27. Vibration spectrum for test cell gearboxes at 100% engine torque.
Data legend is shown in Figure 3.22

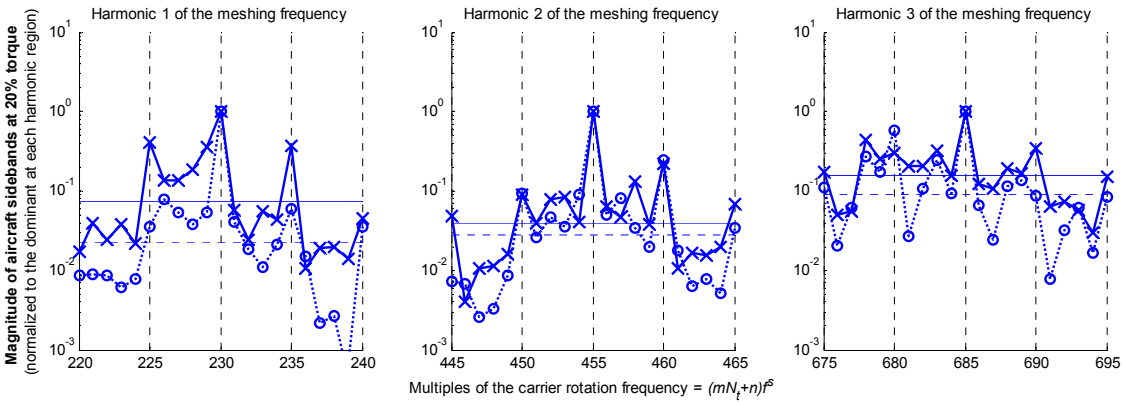

Figure 3.28. Vibration spectrum for on-aircraft gearboxes with $N_p = 5$ planet gears and $N_t = 228$ teeth in the annulus gear. The vibration data used for this figure was acquired from actual helicopters in operation. One gearbox had a 3.25-inch crack in the planetary carrier plate, leading to abnormal planet-gear shifting; the other gearbox was in normal operating conditions. Engine torque is 20% of the nominal. Data legend is same as in Figure 3.22

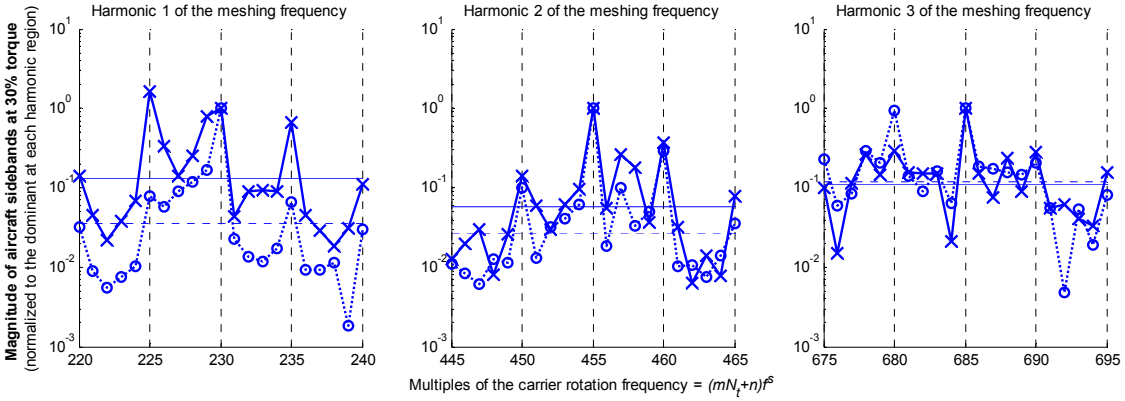

Figure 3.29. Vibration spectrum for on-aircraft gearboxes at 30% engine torque. Data legend is same as in Figure 3.22

3.4.5.2. Validation through experiments with a growing crack (second set of experimental data)

Unlike the first set of experimental data used above, vibration for the second set of experimental data was acquired entirely from a single gearbox. The frequency response of the system was found to vary throughout the test as the crack grew, especially

at larger crack lengths. Hence, results presented below are once again with frequency components normalized with respect to the magnitude of the dominant frequencies (i.e., all sideband magnitudes divided by the magnitude of dominant sideband located at $f = m \cdot N_t \cdot f^s$).

The experiment applied load cycles by varying the engine torque continuously to make the crack grow. These cycles were designed by the technical leaders of the experiment to resemble a helicopter taking off the ground, hovering for some time and then landing, in what is called a ground-air-ground (GAG) cycle. A GAG cycle is comprised of a succession of increasing and decreasing engine torques. Vibration data "snapshots" were acquired at each GAG cycle for specific torque settings. Each snapshot corresponded to the time it took for the planetary carrier plate to complete about 21 to 22 full revolutions. Crack length measurements were obtained throughout the experiment with the use of specialized instrumentation (i.e., crack length gages) to measure discrete increments in the crack size. Each discrete crack length measurement obtained is referred to as a "ground truth" point. By interpolating the ground truth crack lengths with respect to the GAG cycle numbers, it is possible to assign specific crack lengths to the vibration snapshots. More details on the GAG cycles are provided in section 7.2.2, and on the crack length measurements in section 7.6.

The experiment was run for more than 1000 GAG cycles, but provided vibration data usable by the present study only up to GAG cycle number 999. Inside this region, crack growth rates ranged from about 53 to 327 GAG cycles per inch, with an average of about 210.1 GAG cycles per inch, except near the region where the crack reached the

outer edge of the circumference of the plate (crack length of about 4.8 inches), time at which the crack growth rate shot up. Results presented here use data from a sensor similar to the "Port Ring" sensor of the first set of experimental data and identified as "VMEP2" by researchers and technicians involved with the experiment (see Vachtsevanos et al., 2006).

Figure 3.30 gives an idea on how it is possible to observe vibration changes throughout the experiment for specific crack lengths and at specific engine torque settings. Time-synchronous vibration spectra (refer to section 3.4.5) for 10 adjacent GAG cycles are averaged at each crack length shown in the graph.

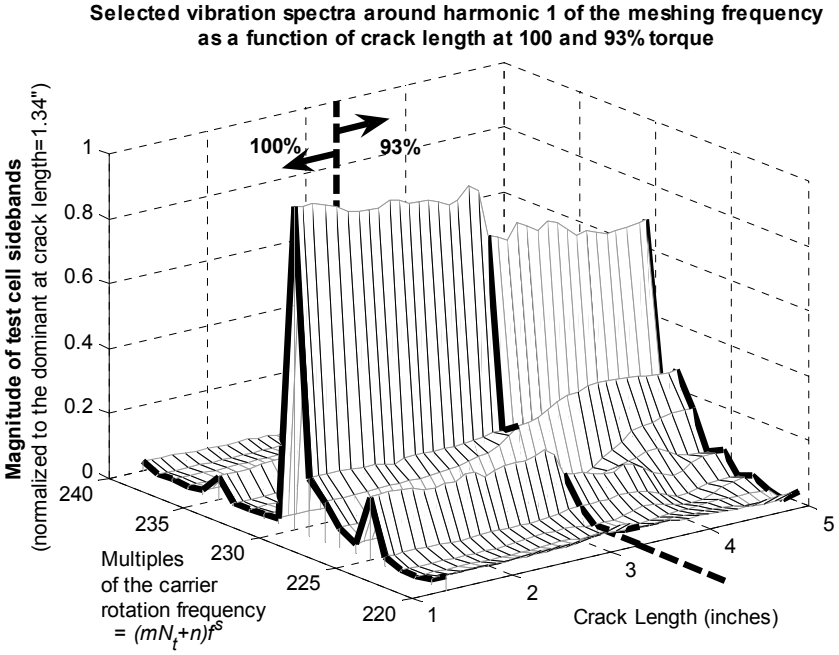

Figure 3.30. Representation of vibration snapshots taken for the crack growth experiment of a seeded crack in a planetary carrier plate. The vibration spectra shown at each crack length correspond to the frequency components near the first meshing harmonic at either 100% or 93% engine torque settings

For reasons of clarity, results for the behavior of sidebands are presented after classifying sidebands in one of three categories: (1) dominant and apparent sidebands, (2) non-dominant sidebands adjacent to dominant or apparent sidebands, and (3) non-dominant sidebands not adjacent to dominant or apparent sidebands. This categorization is represented in Figure 3.31. According to the theory set forth in section 3.4.1, category 1 sidebands are expected to decrease as the crack in the planetary carrier plate grows and planet-gear shifting increases. In contrast, the non-dominant sidebands of categories 2 and 3 are expected to increase.

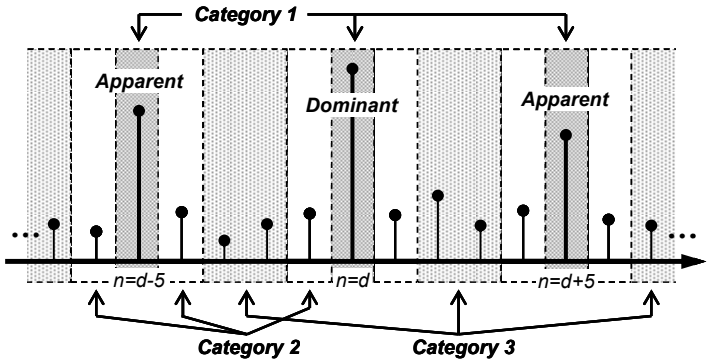

Figure 3.31. Categorization of planetary gear spectrum sidebands for a planetary gearbox with $N_p = 5$ planet gears. Category 1 includes dominant and apparent sidebands. Category 2 includes non-dominant sidebands immediately adjacent to dominant or apparent sidebands. Category 3 includes non-dominant sidebands away from dominant or apparent sidebands

The graphs of Figure 3.32 through Figure 3.34 show the progression in magnitude, for different engine torque settings, of the categorized sidebands as the crack grew in the seeded crack experiment. For reasons of clarity, results presented show only certain crack lengths and not all available data. To better show the trend in the sideband magnitudes, spectrum determination was done after utilizing time-synchronous averaging

for 21 or 22 revolutions (depending on data availability) of the planetary carrier plate at each GAG cycle, and then averaging the sideband magnitudes of 50 successive GAG cycles at each crack length depicted. The intent is to mitigate variations likely caused by noise or other effects. The 50 GAG cycles averaged for the results shown correspond to variations in the crack length of about 0.24 inches in average and are never more than one inch. It can be seen that, in general, the results presented show the expected trends in sideband magnitudes for the different categories. Note however that, once again, the trend is less clear at low engine torques. Furthermore, it appears that, as the crack increases, the magnitudes of non-dominant sidebands of category 2 do not decrease as quickly as those of category 3 do. This effect may be caused by frequency leakage from the sidebands in category 1 to those in category 2.

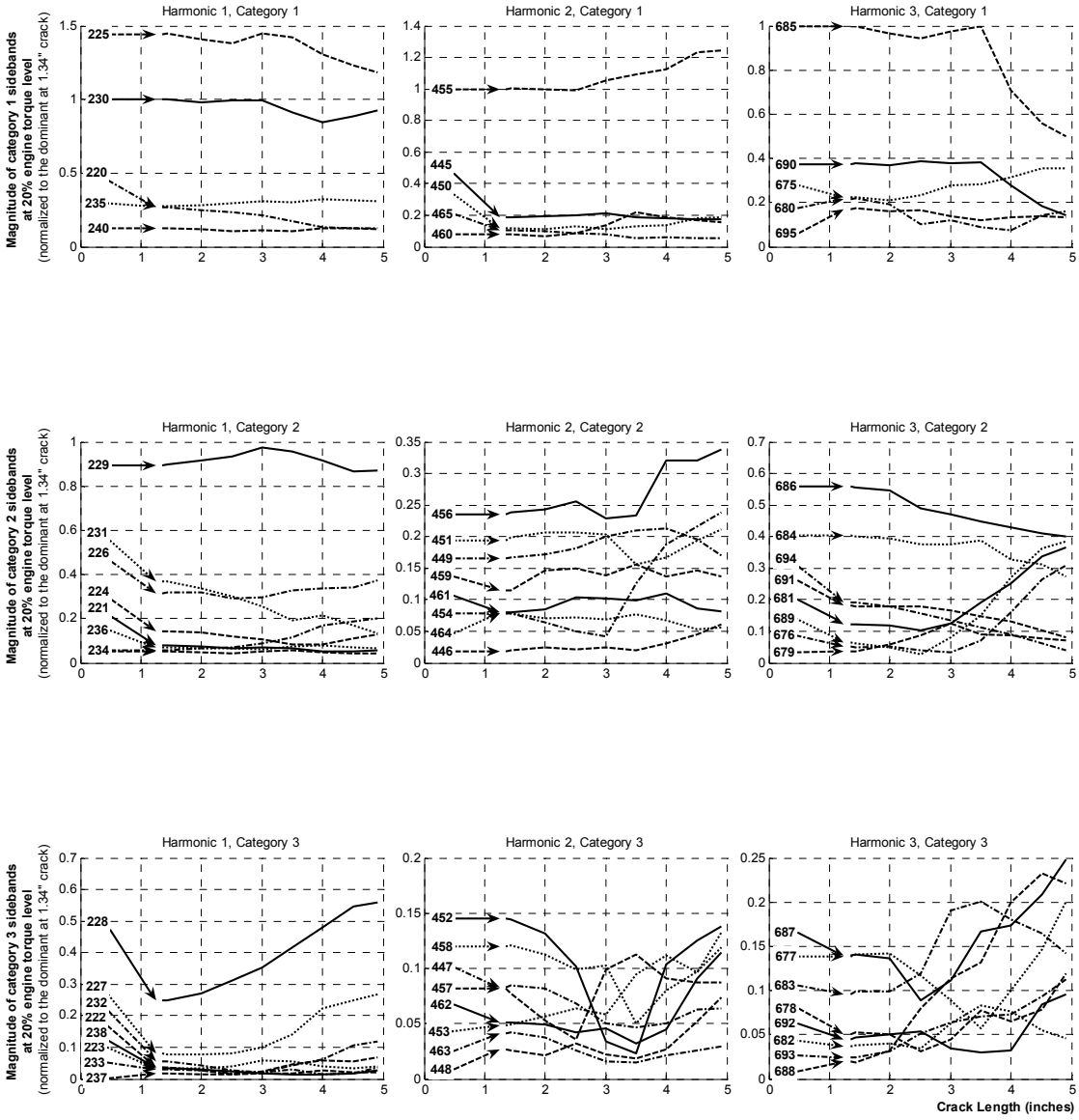

Figure 3.32. Progression of sideband magnitudes for frequency components as a function of crack length at 20% of nominal engine torque. Arrows indicate the frequency values corresponding to each sideband depicted. This frequency is in multiples of the planetary carrier plate rotation frequency, i.e., $f = (m \cdot N_t + n) f^s$

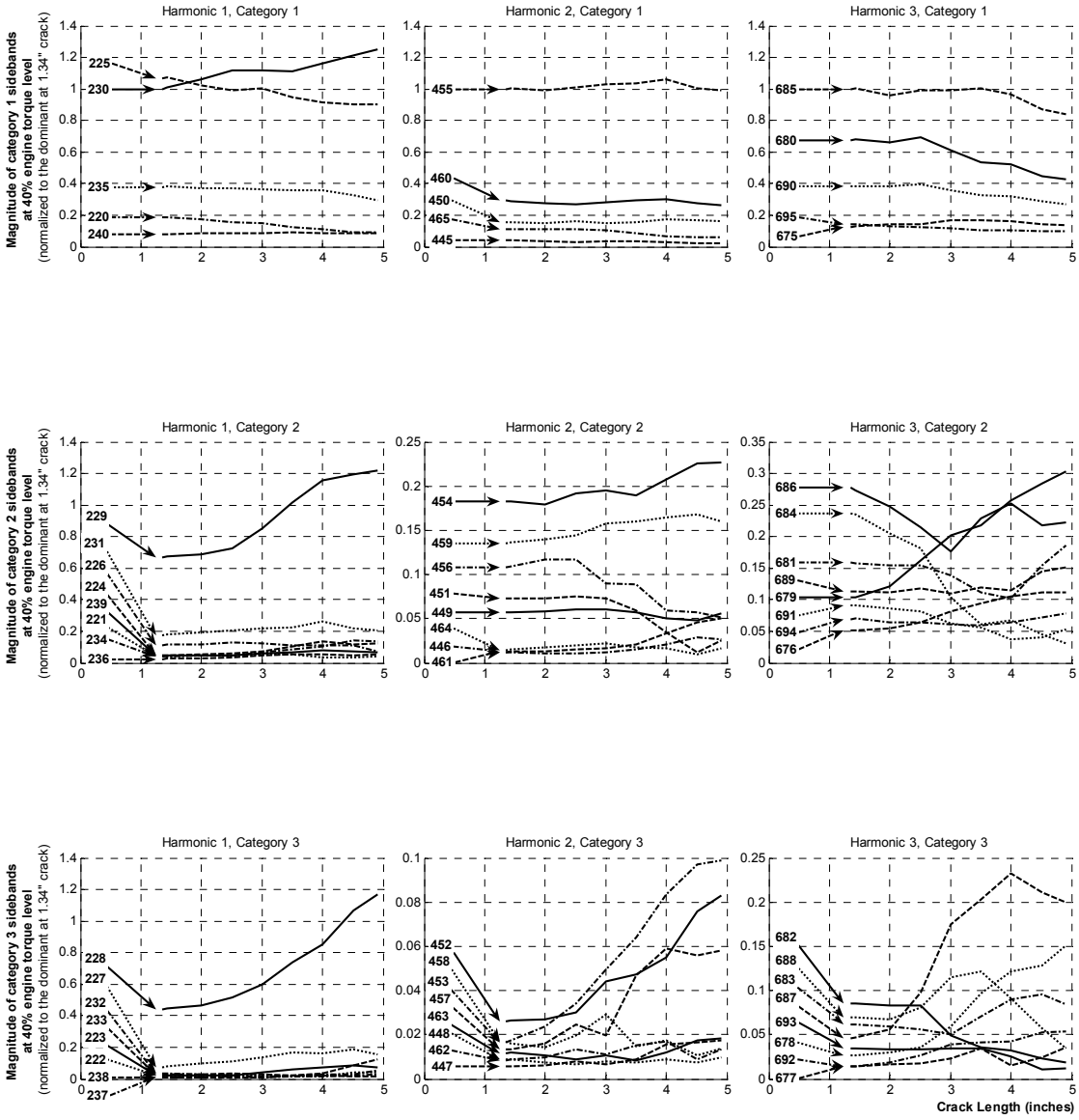

Figure 3.33. Progression of sideband magnitudes for frequency components as a function of crack length at 40% of nominal engine torque. Arrows indicate the frequency values corresponding to each sideband depicted. This frequency is in multiples of the planetary carrier plate rotation frequency, i.e., $f = (m \cdot N_t + n) f^s$

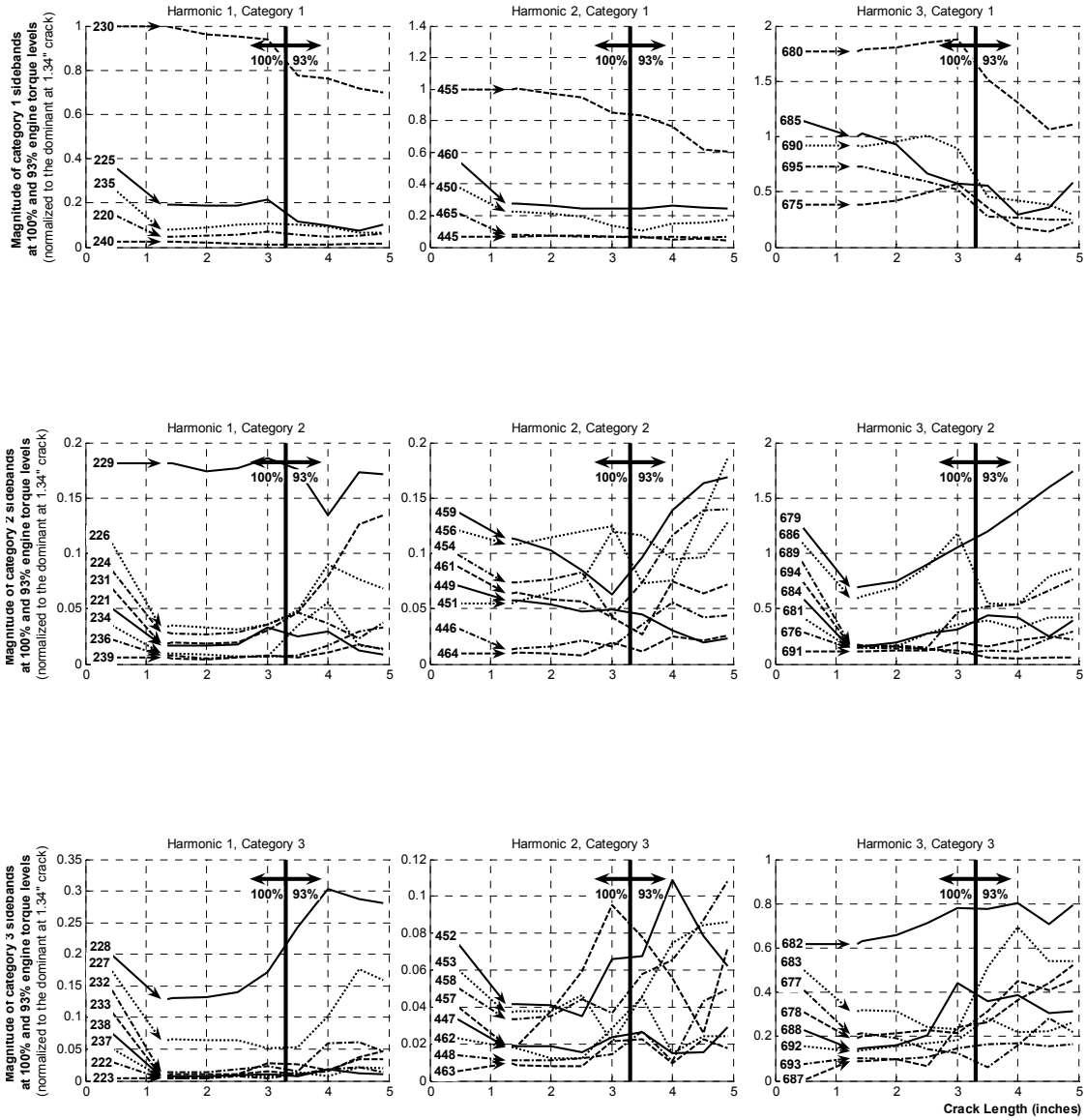

Figure 3.34. Progression of sideband magnitudes for frequency components as a function of crack length for 100% of nominal engine torque up to about 3.3 inches and 93% engine torque thereafter. Arrows indicate the frequency values corresponding to each sideband depicted. This frequency is in multiples of the planetary carrier plate rotation frequency, i.e., $f = (m \cdot N_t + n) f^s$

3.4.6. Remarks about the vibration model

The vibration model presented in section 3.4.1 characterizes analytically certain trends in specific frequency components of the vibration signature of a planetary gearbox occurring when planet gears shift and become unevenly spaced. More specifically, the model ties the increase or decrease in magnitude of sidebands of a gearbox's vibration spectrum at specific frequencies to planet-gear shifts. The model also shows that the rate of this increase or decrease is related to both the angle of the shift and the frequency of the sidebands.

It is important to note that all planet gears are expected to shift during normal operation of a planetary gear transmission because of elasticity, especially that of the planetary carrier. When a system operates normally, angular-symmetric design provides for the shifting to be approximately equal on all planet gears. However, some anomaly in the system, like a fault in the system's geometry, can cause excessive and uneven shifting of the planet gears. Such was the case in focus on the characterizations presented.

The values of α_n and β_m are important parameters in the description of the frequency response of a planetary gearbox. However, these parameters were not directly available from the experimental data used to validate the model in section 3.4.5. Hence, to be able to present results that could be compared across experiments or across data taken at different times in the same experiment, experimental spectra had to be normalized with respect to the dominant sideband at each harmonic region of the tooth meshing frequency.

The need for this normalization is explained by McFadden and Smith (1985) when they express that "*it is not possible to predict the relative amplitudes of the surviving components* [in the vibration spectrum of a planetary gearbox] *because these are determined by the pattern of* [the vibration intensity function of Figure 3.9], *which is not known*." This claim highlights the importance of determining the values of α_n and β_m to characterize the vibration of a planetary gear system. Without these values, we do not have a direct way of relating the vibration components of experimental vibration data to the sideband behaviors studied analytically in section 3.4.1.

The values of α_n and β_m are, in practice, difficult to measure. Nevertheless, it is possible to use numeric techniques to approximate their values from the spectrum of a specific planetary gearbox, as section 5.3 will show. However, to complicate further any efforts in trying to determine the noiseless frequency response of a planetary gearbox, we have that the frequency response of the vibration sensor can disrupt the relation between the measured spectrum and the values of the $\alpha_n\beta_m$ factors characteristic to a particular system. In addition to the $\alpha_n\beta_m$ factor describing the magnitude of the sidebands in the vibration spectrum, there may be an additional γ factor produced by the frequency response of the sensor, such that each frequency component would be described by a quantity such as $\alpha_n\beta_m\gamma_f$. This consideration was overlooked in the analysis presented, just as it may be possible to neglect it in practical applications as long as the frequency response of the vibration sensor remains fairly smooth and constant.

4. A MODEL-BASED DIAGNOSIS ARCHITECTURE

4.1. Objectives

The goal of this chapter is to suggest a methodology for designing a model-based diagnostic architecture that can (1) establish the foundation for performing model-based diagnosis in a class of dynamic systems, (2) be easily integrated with the model-based prognostic architecture of chapter 6, and (3) be applied to diagnose a crack in the planetary carrier plate of a helicopter transmission such as the one described in section 3.1.

The diagnostic architecture suggested in the present chapter integrates modeling, simulation, and experimental data. The class of dynamic systems to which it can be applied will fit the assumptions and descriptions set forth in section 4.2. Focus is placed on models that characterize the physics-of-failure mechanisms of faulted systems. Models of this kind are commonly referred to as *physics-based models* in the engineering diagnostics literature. However, the methodology suggested might be applicable to other kinds of models by appropriately adapting its constituent modules. The architecture is immediately applicable to diagnose particular mechanical rotary systems, such as the helicopter transmission. Such application, discussed in detail in chapter 5, will validate and demonstrate the use of the methodology suggested in the present chapter.

4.2. A Generic Diagnostics Methodology for a Class of Dynamic Mechanical Systems

4.2.1. Adapting a model for its use in diagnostics

A model to be used for realizing model-based diagnostics must provide the ability to simulate an engineering system under varying types of faults and varying amounts of damage, because, as covered in section 2.2.1, comprehensive fault diagnostics involve not just the aspect of *fault detection*, but *fault isolation* and *fault identification* as well. Effort has thus been invested in designing a diagnostic architecture that can use a so-called physics-based model to simulate the changing behavior of a system with a developing fault. Figure 4.1 shows the architecture developed. Note that it is *generally applicable to many kinds of systems*.

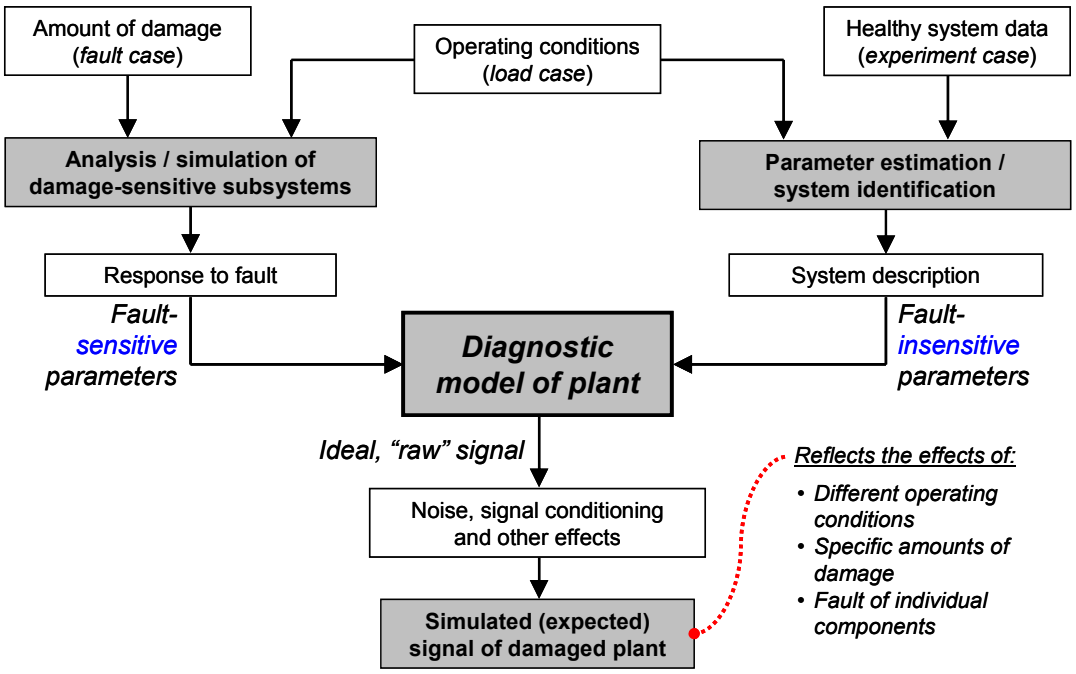

Figure 4.1. Suggested architecture for performing model-based simulation of systems with a static fault

Any model can be cast in the form of a function, with inputs, outputs, variables and parameters. Physics-based models are functions referencing and relating variables and parameters having physical significance, i.e., that can be associated with physical laws governing the behavior of the system that is modeled, like the laws of motion, mechanics, electromagnetism, etc.

To be able to use a physics-based model to replicate the behavior of a system experiencing a fault, we need to apply values that are indicative of the presence of the fault to some of the variables and parameters. This is the reason why it is fitting to classify these according to whether they are sensitive to the fault or not, as proposed by Figure 4.1. This classification will allow the study of the effect of a fault to focus on significant components of the model while simultaneously isolating them to facilitate their consideration.

The most basic underlying assumption in the methodology proposed here is that the model can replicate the behavior of the system under the fault. As discussed in section 1.3, models are often available for operational engineering systems, but it is more difficult to ensure that they truly reflect the changing behavior of a system when a fault is present. If the model were not ready to do this, then it must be modified to allow it to simulate the fault conditions. In many occasions, system models based in physical behaviors should have this ability, but in the design stage of an engineering system, the model is reduced or simplified to simulate the normal operating conditions that designers wish to study. Such is the case, for example, of the planetary gear vibration characterization proposed by McFadden and Smith (1985) and studied in section 3.3.2.1.

The model was established to describe the vibration signature of a planetary gear system working normally. Parker (2000) also developed a similar model from a different perspective, but precisely with the intent to aid in the design of planetary gear systems and provide a means to reduce the vibration.

Another assumption in this development is that the parameters describing the system have been correctly classified into fault-sensitive or fault-insensitive. This may not be simple, however. It is further assumed that it is possible to study the response of the fault-sensitive parameters to a fault, and that the fault-insensitive parameters either are known or can be determined experimentally.

The approach proposed in Figure 4.1 integrates the use of a model with experimental data for simulation, and provides the ability to consider different operating conditions. This simulation architecture can be applied by following the steps described in sections 4.2.1.1 through 4.2.1.5, below.

4.2.1.1. The experiment case

Experimental data are used to approximate all the *fault-insensitive parameters* describing the system. Of course, experimental data are used only when the values of these parameters are not readily known quantities like invariant material properties or physical constants. This step is included considering that we want to calibrate a model that requires the values of parameters that are specific to a particular system realization or arrangement. The determination of the fault-insensitive parameters is done through any

reliable technique for parameter estimation or system identification. These parameters should be determined for particular cases of experimental data that were obtained at known operating conditions of interest. These known operating conditions, given by the application of a particular *loading case*, are represented in the diagram of Figure 4.1 in the center-top block. Because the parameters to be determined are supposed to be insensitive to the fault, it should not matter whether the plant from which the experimental data were retrieved was at fault or not. However, if some of the parameters are sensitive to the fault to some extent but for reasons of simplicity were assumed insensitive[10], then it is up to the diagnostic system designer to choose whether it would be better to use experimental data from a system with or without a fault. The decision would be made after considering which of the two instances (with or without a fault) reflects the most adequate values of the parameters chosen as "fault-insensitive". Data from one of these particular *experimental cases* enter the methodology on the upper-right corner of the diagram of Figure 4.1.

4.2.1.2. The fault case

To use the model for simulating the behavior of the plant under a fault with a particular degree of development, one must quantify this development as a specific *amount of damage* in the system. The exact amount of damage is used to describe the size of a particular fault, i.e., it is a specific *fault case*, and is entered in the diagnostic algorithm of Figure 4.1 through the top-left corner.

[10] This would be done if the effect of a fault is negligible in such parameters

4.2.1.3. Analysis of damage-sensitive subsystems or components

In this step, the operating conditions (load case) and the amount of damage (fault case) are used to analyze the response of *different components or subsystems* of the plant to the presence of the specific fault size considered. The objective of this analysis is to determine the values of *fault-sensitive parameters* describing the system for the model. Such an analysis is particular to the plant, and may require support from a variety of engineering disciplines. For example, in the case of the helicopter transmission problem considered in this thesis, the plant model for diagnosis is a vibration model of the planetary gearbox. The model, described in section 3.4, requires information about the angular shift of the planet gears. Determining the angular shifts requires analyzing the deformation of the planetary carrier plate. In this case, the angular shifts are the fault-sensitive parameters of interest that the plant model at the center of Figure 4.1 requires.

4.2.1.4. Simulations with the plant model

Once the fault-insensitive and fault-sensitive parameters have been determined, the parameters are input to the plant model at the center of Figure 4.1. The model is used to simulate the behavior of the plant for a specific fault case in individual components or subsystems and under a particular load case. It is possible to run simulations for particular faults and loads because the parameters were determined also for particular faults and loads. The simulation will produce a signal, or the values of a set of system variables, replicating those from the plant under similar conditions. However, in the real world, the corresponding values of this signal or set of variables are observed (i.e., measured) in the plant after they have been affected by different events, including noise,

sensor response characteristics, signal processing, etc. Thus, the signals or variables obtained from the model should be treated or modified in a similar manner to ensure that the simulation truly replicates the plant and allow for fair comparisons between the model and plant. Calibration of the model-based diagnostic architecture is hence due here. Take for example the case of noise. If we know that the signal the plant produces is distorted by extraneous signals that can be characterized with a statistical distribution, the same distribution may be added to the model signal to have it approximate better the behavior of the plant. Omitting the calibration or signal conditioning step described has the potential to invalidate any comparisons between simulation results and plant measurements.

4.2.1.5. Use of the proposed simulation architecture in model-based diagnosis

The architecture of Figure 4.1 is used to simulate the behavior of a plant for a specific fault case in individual components or subsystems and under a particular load case. The simulation produces a signal or values that replicate those of the plant when operating under such conditions. However, the plant may not be operating under such conditions. It is the intent of a diagnostic effort to determine the conditions of the plant, and the simulation does not directly provide information about this. To arrive at a diagnosis of the plant, the signal or values resulting from the model simulations must still be interpreted and compared to those coming from the plant. This task is discussed in section 4.2.2.

4.2.2. A reverse engineering approach to model-based diagnostics

Section 2.2.3 discussed the approach that is generally followed to perform model-based *fault detection*. Since the approach refers to fault detection, it is useful for determining whether a fault exists or not in a plant. This detection approach was depicted earlier in Figure 2.2. We are here interested, however, in assessing the size of the fault or the severity of damage as well, i.e., we want to perform *fault identification* in addition to fault detection. A modification of the detection approach is proposed here to allow for the task of fault identification. The technique is similar, but an iterative step is added, as shown in Figure 4.2, below. The idea is to use the model repetitively with different amounts of damage to generate a series of residuals or parameter estimates. The process stops when the evaluation block decides that a residual or parameter estimate has an "adequate" value. At that point, the fault size used in the model to generate the residual or parameter estimate is deemed to approximate the fault size present in the plant. By "adequate value", different things are meant when using parameter estimation or residual generation. In the case of parameter estimation, an adequate value would be that of a parameter remaining within previously specified bounds (see section 2.2.3). For residual generation, the adequate value approaches zero.

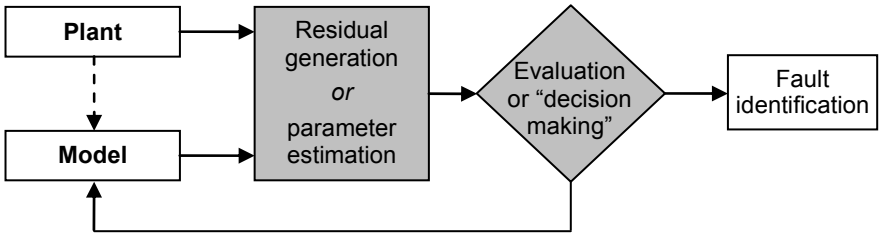

Figure 4.2. Approach suggested for performing fault identification. Compare to the general approach followed in fault detection, shown in Figure 2.2.

Let us consider how this approach can be applied with the residual evaluation procedure described earlier in section 2.2.3 and illustrated by Figure 2.4. Consider Figure 4.3. The unknown amount of damage present in the plant is assessed by running repeated trials with different amounts of damage in the model. The trial with an amount of damage in the model that minimizes the absolute value of the residual is taken to be the amount of damage present in the plant.

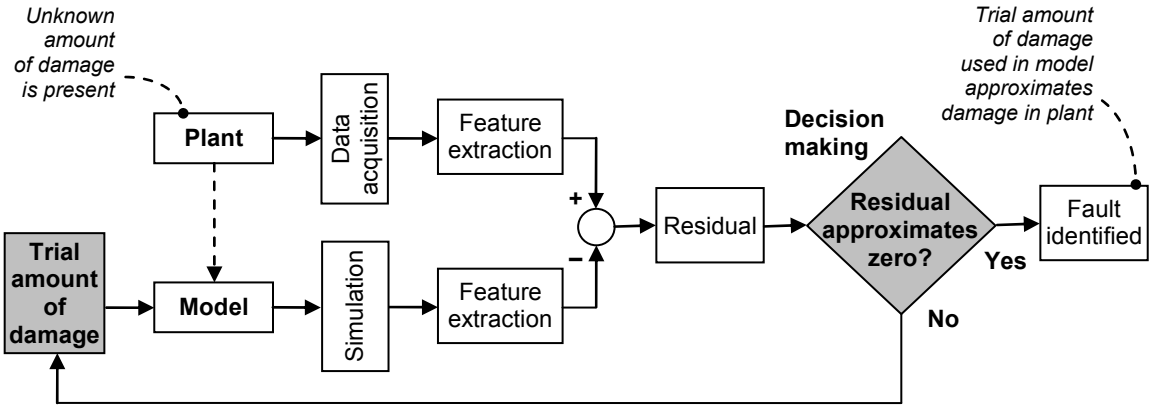

Figure 4.3. Reverse engineering approach to fault identification through residual evaluation. This technique shows the application of the approach suggested in Figure 4.2 to the procedure followed in Figure 2.4.

This approach to modeling makes it possible to use feature extraction techniques to diagnose a specific size of fault in the plant by searching for a correspondence of the behaviors observed in the plant among the behaviors of several simulation trials. The simulation trials represent varying degrees of damage, and the one that exhibits the closest correspondence is taken to be the one representing the size of the fault in the plant. Thus, this "searching" technique can be likened to a *reverse engineering process* of fault identification.

In summary, for this technique to work, the model must be able to replicate the behaviors that the plant would exhibit under different amounts of damage and specific operating conditions. To this end, the simulation architecture proposed in section 4.2.1 and represented in Figure 4.1 can be used.

5. DIAGNOSIS OF THE HELICOPTER TRANSMISSION

In this chapter, we diagnose the helicopter transmission problem described in section 3.1. We want to achieve this by using *model-based diagnostics* and applying the architecture and methodologies proposed in section 4.2. Our diagnostic signal is *vibration data* retrieved from a planetary gearbox in operation. Within this chapter, we also validate the model-based diagnostic architecture by comparing simulation results to experimental data obtained from helicopter transmissions exhibiting cracks.

To implement the diagnostic architecture, we need to characterize changes in the vibration signal of the planetary gearbox caused by the presence of the crack on the planetary carrier plate. To this end, we can apply the model proposed in section 3.4. We also need to classify the model parameters as either *fault-sensitive* or *fault-insensitive*. The next step in the use of the diagnostic architecture is to establish adequate *feature extraction* routines by selecting vibration features that can adequately characterize the fault in the gearbox. This information can be used to assess the length of a crack using the reverse engineering methodology proposed in section 4.2.2.

5.1. Special considerations of the planetary gear vibration model

Section 3.4.5 used experimental vibration data to validate the analytic predictions about the frequencies at which sidebands will increase or decrease in magnitude. The experimental data were not useful, however, to validate directly the analytic

characterization of the rate of the increase or decrease of the sideband magnitudes. There are two reasons for this inability:

1) The analytic studies of section 3.4.1 through section 3.4.4 considered the shifting of a single planet gear, whereas the abnormal deformations of the planetary carrier plate, attributable to the crack, produced uneven shifting of the planet gears.

2) The values of α_n and β_m, which are important parameters in the description of the frequency response of a planetary gearbox, were not directly available from the experimental data.

These two points are important if the model is to be used for replicating the behavior of a planetary gear transmission, and hence are addressed individually below.

5.1.1. Considering the shift of multiple planet gears

The planetary gearbox transmits power coming from the engines to the main rotor blades. The power is input to the planetary gearbox through the sun gear, then transmitted to the planet gears, and is output by the planetary carrier plate and delivered to the main rotor shaft that drives the rotor blades. The ring gear is stationary and thus does not transmit any power. See Figure 5.1.

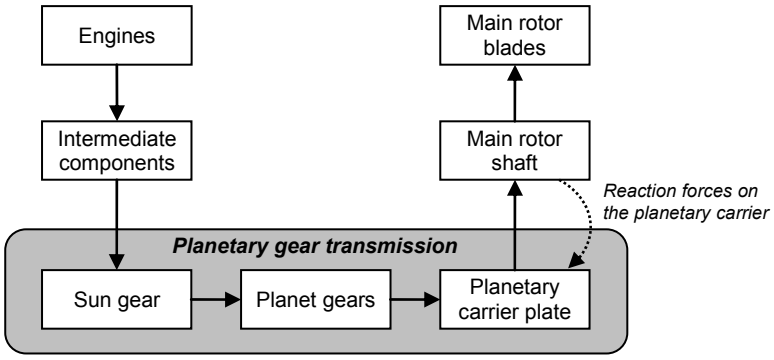

Figure 5.1. Representation of the path of transmission of power from the engines through the planetary gear transmission to the main rotor blades of the helicopter. Solid arrows represent the action forces applied by one component on the next. The dotted-line arrow represents the reaction forces acting on the planetary carrier plate

As in any structural member of a mechanism, loads in the planetary carrier plate can be classified as either *action* or *reaction* forces. The action forces are generated by the input of power, and, at the carrier plate, they are applied through the posts where the planetary gears are mounted. The reaction forces are generated by the component receiving the power output, and, at the carrier plate, they are applied through the internal splines of the plate, to which the main rotor shaft is attached. See Figure 5.2.

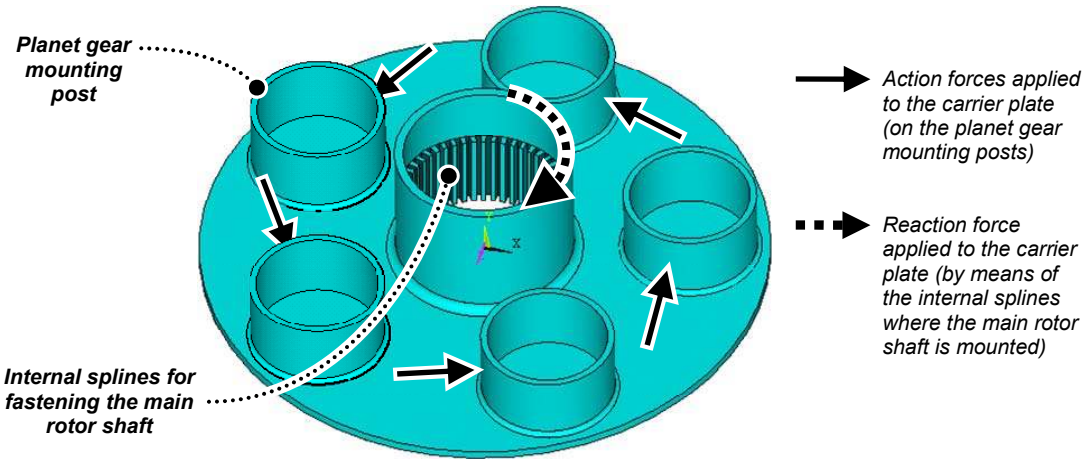

Figure 5.2. Representation of the major forces acting on the planetary carrier plate of the planetary gearbox of the helicopter transmission during operation

When the planetary gearbox is operating without faults, the carrier plate will respond to the action and reaction forces with localized deflections. If the loads in each of the five planet gears are all equal and the rotor shaft remains aligned with the axis of the planetary gearbox, the angular symmetry of the carrier plate will ensure that the deflections of the five mounting posts are also angularly symmetric, i.e., the five posts will deflect comparably.

A crack on the root of a planet gear mounting post of the planetary carrier plate will reduce the stiffness of that post. It should be clear that this reduction in stiffness will increase the deflection of the post when load is applied to the carrier plate. What is not so clear is the effect of the crack on this one post on the deflections of the other posts.

According to the vibration model presented in section 3.4, the angular shift of the planet gears drives changes in the vibration patterns of the planetary gearbox. To be able to use this vibration model in the characterization of the effect of the crack on the

planetary carrier plate, we need information about the deformation patterns of the plate and the corresponding angular shifting of all the planet gears.

5.1.2. The importance of the frequency response coefficients

As explained in section 3.4.6, to characterize adequately the vibration of a planetary gear system we need information about its frequency response. In practice, this can be done by approximating the values of a sufficient number of the α_n and β_m parameters of the planetary gear vibration model.

To approximate these parameters for a particular gearbox we can use the vibration model itself. Note that we are not trying to fit a model to the plant and then validate the model by its approximation to the plant. This would nullify the validation process. The suggestion here is to obtain descriptive parameters using experimental data of a gearbox under normal operating conditions. It is then assumed that these parameters remain constant when the gearbox operates with a fault, and only then is the model used to characterize the changes that should be observed under the fault. Why do we not estimate the parameters from experimental data representative of the fault conditions? There are two reasons. First, if we were to determine the parameters from the fault conditions we cannot use the model to characterize those fault conditions. Once again, we either characterize the model with the experiment or the experiment with the model, but not both things at the same time. Second, the vibration model characterizes the values of a series of parameters (α_n and β_m for a series of n and m) in a system of non-linear equations. As will be seen below, the complexity of the system of equations becomes

reduced in the healthy configuration, where many of the equations cancel out, so it is simpler to determine the parameters from a healthy configuration.

5.2. Adaptation of the planetary gear vibration model for its use in diagnostics

Figure 5.3 shows how the architecture described in section 4.2.1 (Figure 4.1) can be applied to the particular case of diagnosing the crack in the planetary carrier plate. Each of the four shaded blocks of the process shown in Figure 5.3 corresponds to a specific task that will now be addressed.

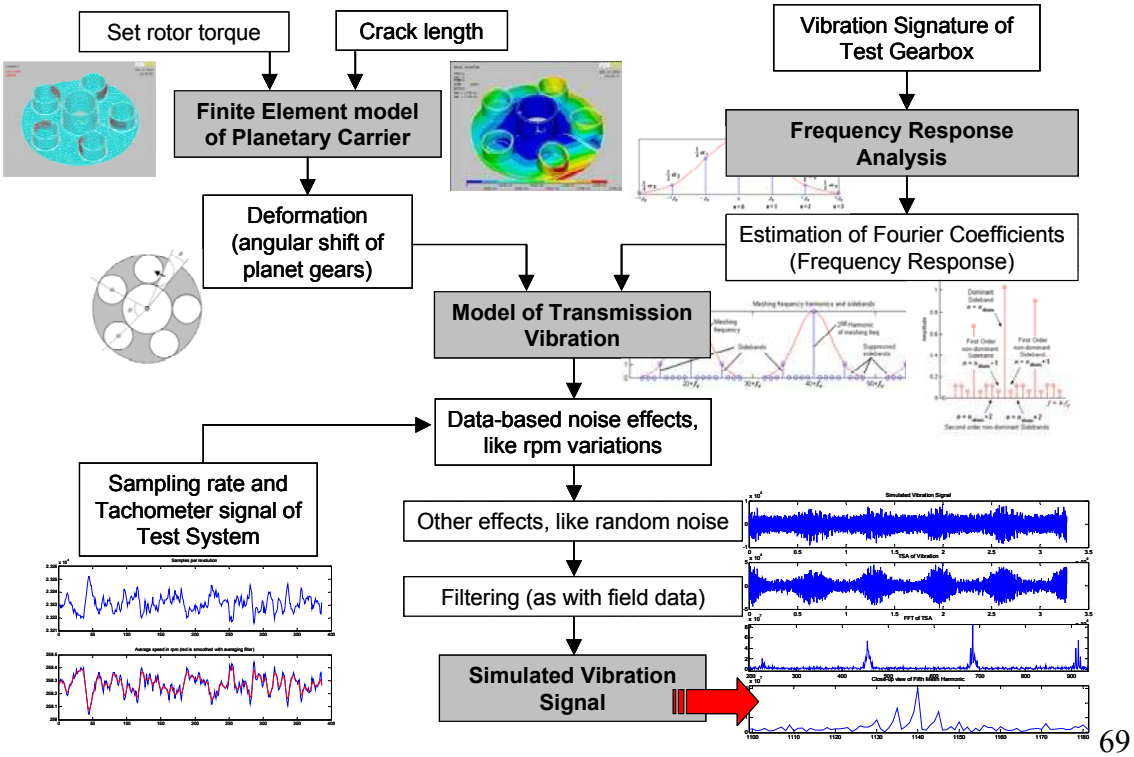

Figure 5.3. Application of the technique of Figure 4.1 to the problem of simulating the vibration of a faulted helicopter transmission

5.2.1. The planetary gearbox vibration model as the diagnostic model

The block located at the center, "model of transmission vibration", refers to the use of the planetary gear vibration model (discussed in section 3.4) for simulating expected changes in the vibration of the gearbox at different operating conditions with different crack sizes.

5.2.2. Frequency response analysis for determining the fault-insensitive parameters

The block located near the top-right corner of Figure 5.3, "frequency response analysis", corresponds to the determination of the fault insensitive-parameters of the planetary gearbox that the model needs. The fault-insensitive parameters are the frequency response coefficients α_n and β_m, and their determination is done by attempting to solve a system of non-linear equations that utilize input from experimental data.

5.2.3. Finite element analysis for determining the fault-sensitive parameters

The block located near the top-left corner of Figure 5.3, "finite element model of planetary carrier", corresponds to the determination of the fault sensitive-parameters of the planetary gearbox that the model needs. The fault-sensitive parameters are the planet-gear shift angles, and their determination is done by analyzing the static deformation of the planetary carrier plate when a crack is present. Finite element analysis is used to characterize the deformation patterns and approximate the amount of angular shift of the planet gears at various levels of torque load.

5.2.4. Calibration of the simulation

The block located at the center-bottom of Figure 5.3, represents the simulated vibration signal that the model of the planetary transmission vibration can generate by incorporating the results of the frequency response analysis and of the finite element model. We want to ensure that this simulated vibration signal is similar in certain characteristics to the vibration observed in the planetary gearbox for a particular crack length and under specific operating conditions. To this end, we need to calibrate the generation of simulated signals to replicate effects altering the experimental signals, like noise. Performing simulations with different crack lengths will enable us to use the reverse engineering technique of section 4.2.2 for diagnosing a helicopter transmission gearbox.

5.3. Determination of the fault-insensitive parameters

In this section, we are interested in determining the frequency response coefficients α_n and β_m that describe vibration characteristics of a planetary gearbox in a manner consistent with the model presented in section 3.4. The actual value of these parameters in a measured vibration signal is affected by many system-specific factors, among which are the gearbox frequency response, frequency response of the vibration sensor, transmission path of the vibrations (i.e., sensor location), operational conditions, vibration of other components, etc., so that attempting to analytically estimate them would be extremely difficult. Nevertheless, we can use a numeric technique to try to approximate them from experimental data.

5.3.1. Relating experimental data to the vibration model

The vibration model proposed in section 3.4 offers a description of the vibration components of an ideal (i.e., noiseless) planetary gear system. For a system with 5 planet gears, such as the helicopter transmission considered, such description involves a series of $\alpha_n\beta_m$ factors like those exemplified in Figure 5.4. When the spectrum represented is obtained from actual experimental vibration of a planetary carrier, the sideband amplitudes will also reveal the presence of noise in the signal.

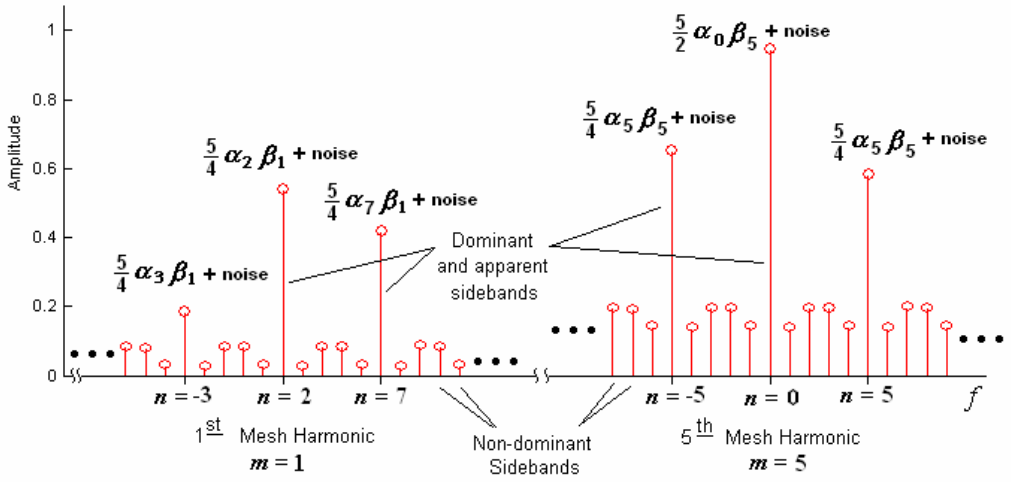

Figure 5.4. Representation of the $\alpha_n\beta_m$ factors describing the amplitude of different frequency components in the vibration signature of the helicopter's planetary gearbox

The model characterizes the amplitude of non-dominant sidebands as being zero for an ideal planetary gearbox with equally spaced planet gears. Hence, through the model, we can attribute all non-dominant sidebands found in the experimental vibration of a gearbox with equally spaced planet gears as being pure noise. This technique for

using the model to characterize sidebands in the experimental vibration is illustrated in Figure 5.5.

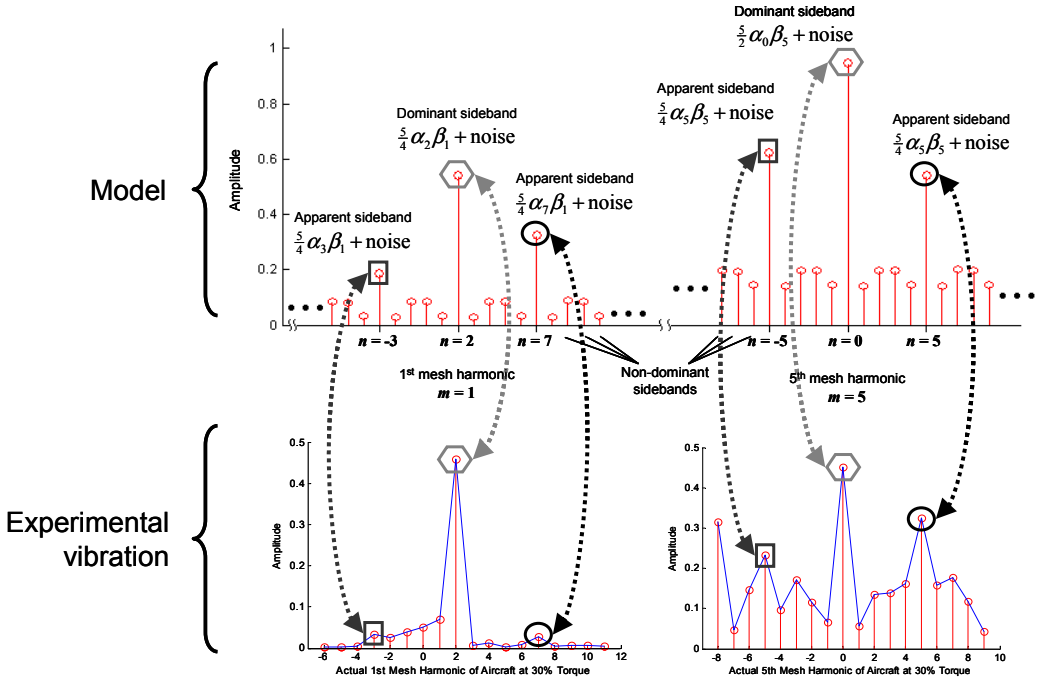

Figure 5.5. Procedure followed for characterizing sidebands in experimental vibration data of a planetary gearbox using the vibration model

The locations of specific α_n and β_m parameters in the vibration characterization offered by the model have a discernible pattern. This pattern is explained by McFadden and Smith (see section 3.3.2.1), who pinpoint the locations where sidebands have theoretical non-zero amplitude. This is shown in Table 5.1. Recall that the exact location (i.e., frequency) of a specific (m, n) sideband is given by $f = (m \cdot N_t + n) \cdot f^s$.

Table 5.1. Sideband suppression pattern of a planetary gearbox with $N_p = 5$ and $N_t = 228$. Clear cells marked with "0" correspond to sidebands that become suppressed. Compare to Table 3.2

n	*m = 1*	*m = 2*	*m = 3*	*m = 4*	*m = 5*
-5	0	0	0	0	**1**
-4	0	0	**1**	0	0
-3	**1**	0	0	0	0
-2	0	0	0	**1**	0
-1	0	**1**	0	0	0
0	0	0	0	0	**1**
1	0	0	**1**	0	0
2	**1**	0	0	0	0
3	0	0	0	**1**	0
4	0	**1**	0	0	0
5	0	0	0	0	**1**

Once the unsuppressed sidebands have been located, we can proceed to establish the pattern of appearance of dominant and apparent sidebands, i.e., determine the values of n at which sidebands are dominant or apparent near each tooth meshing harmonic m. For the planetary gear transmission with N_p=5 planet gears and N_t=228 teeth in the annulus gear, the pattern is as shown in Table 5.2.

Table 5.2. Pattern of sideband locations for the planetary gearbox of the helicopter transmission gearbox in focus. The pattern shows the values of n at which sidebands are dominant or apparent near tooth meshing harmonics. Five tooth meshing harmonics are listed (m = 1 to 5)

Harmonic number	Values of *n*						
m= 1	…	-8	-3	2	7	12	…
m= 2	…	-11	-6	-1	4	9	…
m= 3	…	-9	-4	1	6	11	…
m= 4	…	-12	-7	-2	3	8	…
m= 5	…	-10	-5	0	5	10	…

5.3.2. A system of non-linear equations characterizing the frequency response of a planetary gearbox

Using the pattern of Table 5.2 and equations 3.10 and 3.11 of section 3.3.2.4 we can characterize the sideband amplitudes in the vibration of the helicopter gearbox. Each (m, n) pair corresponding to a cell in the table can be substituted in one of the two equations to describe the amplitude of the sideband located at frequency given by $(m \cdot N_t + n) \cdot f^s$ in experimental vibration data. Thus, we characterize the sideband amplitudes of experimental vibration data according to the relation

$$\frac{N_p}{2}\alpha_0\beta_m + \text{noise} = \begin{pmatrix} \text{Half amplitude of} \\ \text{frequency component at} \\ f = m \cdot N_t \cdot f^s \end{pmatrix}, \quad \text{for sidebands with } n = 0, \qquad (5.1)$$

or with the relation

$$\frac{N_p}{4}\alpha_n\beta_m + \text{noise} = \begin{pmatrix} \text{Half amplitude of} \\ \text{frequency component at} \\ f = (m \cdot N_t + n) \cdot f^s \end{pmatrix}, \quad \text{for sidebands with } n \neq 0. \qquad (5.2)$$

Using these relations, we can proceed to estimate the values of individual α_n and β_m parameters. We do this by noticing that we can build a system of nonlinear equations considering each cell of Table 5.2 separately. Take for example the case of the sideband at m=1 and n=–8 for our planetary gearbox with N_p=5 and N_t=228. To simplify the notation let us define $SB_{m,n}$ as the symbol representing the half amplitude of the frequency component located at frequency $f = (m \cdot N_t + n) \cdot f^s$. Using equation 5.1 and recalling that, by definition, $\alpha_n = \alpha_{-n}$ we obtain

$$\frac{5}{4}\alpha_8\beta_1 + \text{noise} = SB_{1,-8}\,, \tag{5.3}$$

where $SB_{1,-8}$ represents the half-amplitude of the sideband at $f = 220{\cdot}f^s$. The inclusion of the sign of n in the subscripts of the SB symbol is important because although $\alpha_n = \alpha_{-n}$, the asymmetry of the sidebands causes $SB_{m,n} \neq SB_{m,-n}$ for most cases.

The system of equations is non-linear because of the $\alpha_n\beta_m$ factors. Under the definition suggested, the system of equations has an infinite number of solutions because the system is *underconstrained* by having one different unknown "noise" term per each equation. Nevertheless, we can still approximate the plant parameters with a valid solution to the system of equations, as represented in Figure 5.6. We want to find a solution that is representative of the system, and one possible way to do this is by minimizing a function constructed with the noise terms. This *objective function* can be defined as a kind of mean squared error. This approach to solving the problem assumes that the noise amplitude is relatively small and searches for a solution that minimizes the noise terms in the equations.

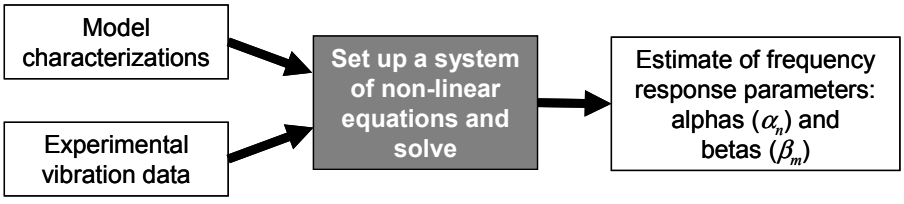

Figure 5.6. Procedure for estimating the fault-insensitive α and β parameters of a planetary gearbox using experimental vibration data

Under this consideration the optimization problem is set up in general for a planetary gearbox as a *least squares optimization* problem with

$$\begin{aligned} &\text{Objective function :} \\ &\quad \text{minimize } \sum_i e_i^{\,2} \\ &\text{Subject to :} \\ &\quad \left\{ c \cdot \alpha_n \cdot \beta_m - SB_{m,n} = e_i \right\} \text{for one } (m,n) \text{ pair corresponding to each } i \end{aligned} \quad , \qquad (5.4)$$

where c is a constant that is either $c = N_p/2$ for sidebands with n=0 or $c = N_p/4$ for sidebands with $n \neq 0$, the e_i terms represent the noise present at each sideband, and the total number of i values taken is the number of sidebands we wish to characterize.

In the implementation of this algorithm, the designer might want to add weights to the "error" terms depending on the confidence that he has on the accuracy of different frequency components of the vibration spectrum of a given planetary gearbox. In this case, individual w_i weights for frequency components can be included in the optimization problem, such that the objective function of Equation 5.4 becomes

$$\text{minimize } \sum_i (w_i e_i)^2 \,. \qquad (5.5)$$

The application of the optimization problem to the helicopter planetary gearbox with N_p=5 planet gears can be done by using the cells in Table 5.2 and substituting in Equation 5.4. Each cell corresponds to a value of i. The problem setup is:

Objective function :

$$\text{minimize } \sum_{i=1}^{25} e_i^{\,2}$$

Subject to :

$$\left\{\begin{array}{c} \frac{5}{4}\alpha_8\beta_1 - SB_{1,-8} = e_1 \\ \frac{5}{4}\alpha_3\beta_1 - SB_{1,-3} = e_2 \\ \vdots \\ \frac{5}{4}\alpha_7\beta_4 - SB_{4,-7} = e_{17} \\ \vdots \\ \frac{5}{2}\alpha_0\beta_5 - SB_{5,0} = e_{23} \\ \frac{5}{4}\alpha_5\beta_5 - SB_{5,5} = e_{24} \\ \frac{5}{4}\alpha_{10}\beta_5 - SB_{5,10} = e_{25} \end{array}\right\}. \tag{5.6}$$

As suggested before, the α and β parameters are a measure of the frequency response of the overall system, from the gears to the casing to the sensor. Since the frequency response is dependent upon sensor response, mechanical configuration, and operating conditions, α and β parameters should be estimated for different sensors, mechanical configurations, and operating conditions. The two mechanical configurations of interest for our helicopter transmission are the test cell setup and the aircraft setup of the transmission. The operating conditions of interest are the varying engine torque levels applied to the transmission. The estimated values of α and β corresponding to the different sensors, mechanical configurations, and operating conditions can be used by the model to replicate the vibration signature more closely in each case.

5.3.3. Fault insensitive parameters of the helicopter planetary gearbox

We now proceed to estimate the frequency response parameters α_n and β_m of our helicopter planetary gearbox using the techniques described in sections 5.3.1 and 5.3.2.

To solve the non-linear equations described in section 5.3.2 by least squares optimization we use Equation 5.6 with the modification to the objective function proposed by Equation 5.5. The values of the weights are here calculated from the weighting function shown in Figure 5.7. This function was selected empirically, taking into consideration observed waning patterns of the sidebands in experimental vibration data. Observe that the weighting function is defined with respect to values of *n*, and is hence invariant across harmonics of the tooth meshing frequency *m*.

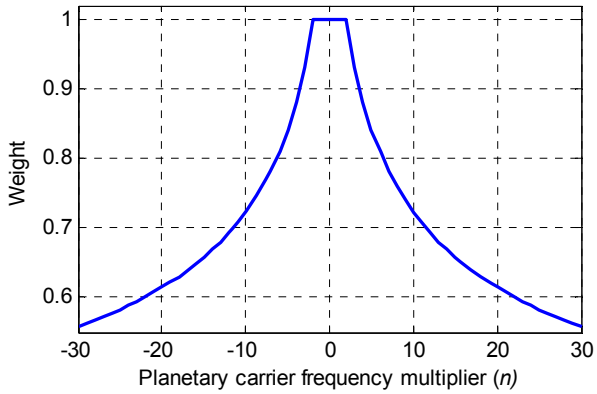

Figure 5.7. Weighting function utilized to approximate the frequency response parameters α_n and β_m in the planetary gearbox vibration experiments. This weighting function is applied as defined by Equation 5.5

As stated earlier, the optimization problem can be solved for different sensors and different values of the operating torque of the gearbox. Figure 5.8 through Figure 5.13 present results obtained by solving the optimization problem for values of *n* ranging from -15 to 15 and for values of *m* ranging from 1 to 6. To be meaningful, results presented illustrate the factors $c \cdot \alpha_m \cdot \beta_n$ on top of the corresponding sidebands of experimental vibration data. Results presented in the graphs use data from the sensor referred to as

"Port Ring" by Blunt and Keller (2006). Figure 5.8 through Figure 5.10 use the same experimental vibration data of section 3.4.5, but only the healthy gearbox (i.e., without the planetary carrier crack) is here considered; thus, these figures use data from the experiments with a specific crack length. In contrast, Figure 5.11 through Figure 5.13 use data from the experiments with a growing crack, but only the initial crack length (1.34 inches) is here considered. For this latter case, we are assuming that the crack is small enough to allow considering the carrier plate as if healthy. These results are later implemented to diagnose the condition of the gearbox using the model-based technique proposed in this thesis (see section 5.6).

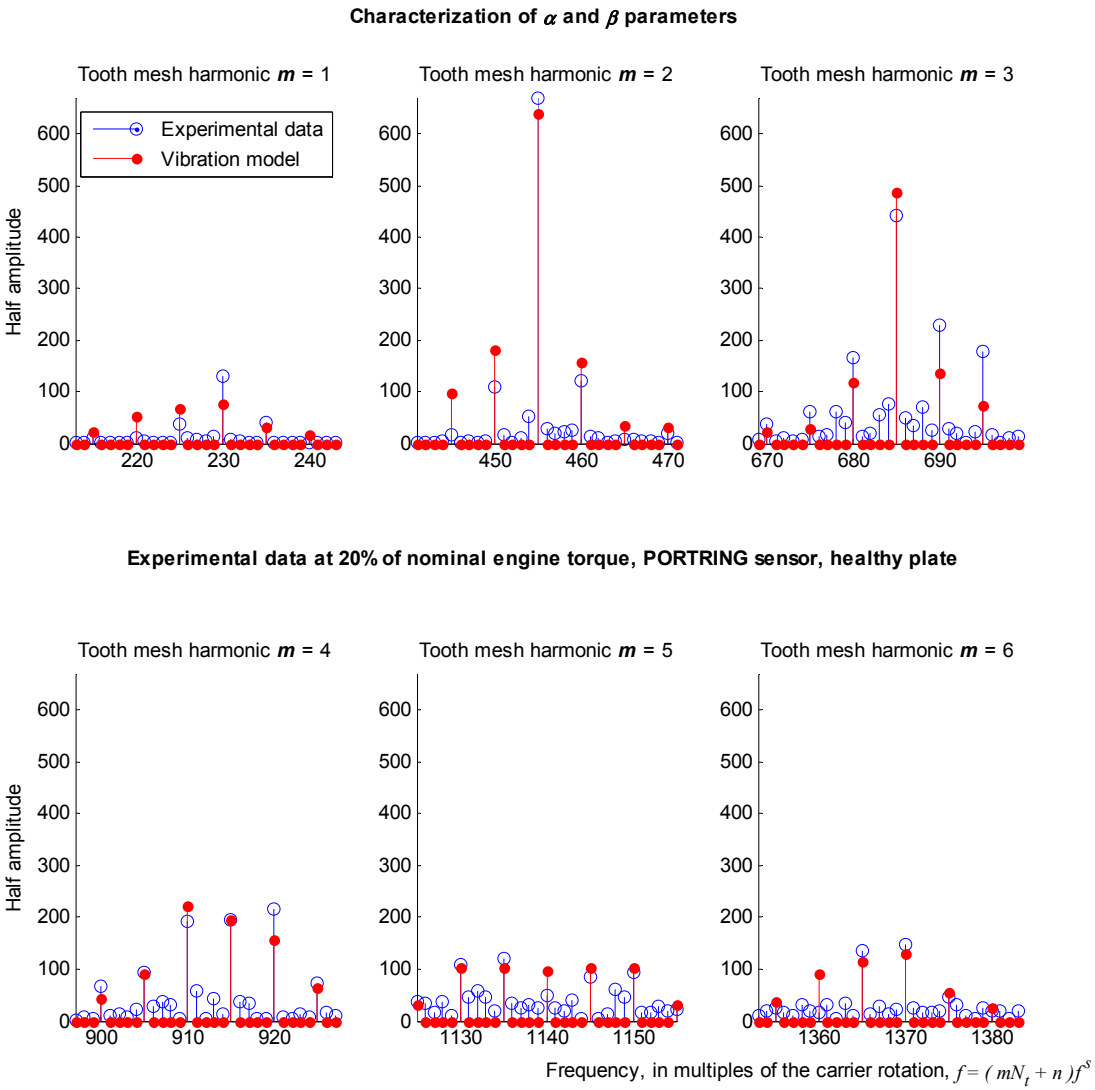

Figure 5.8. Results of the characterization of the α_n and β_m parameters of a healthy planetary gearbox transmission operating in a test cell at 20% of nominal torque

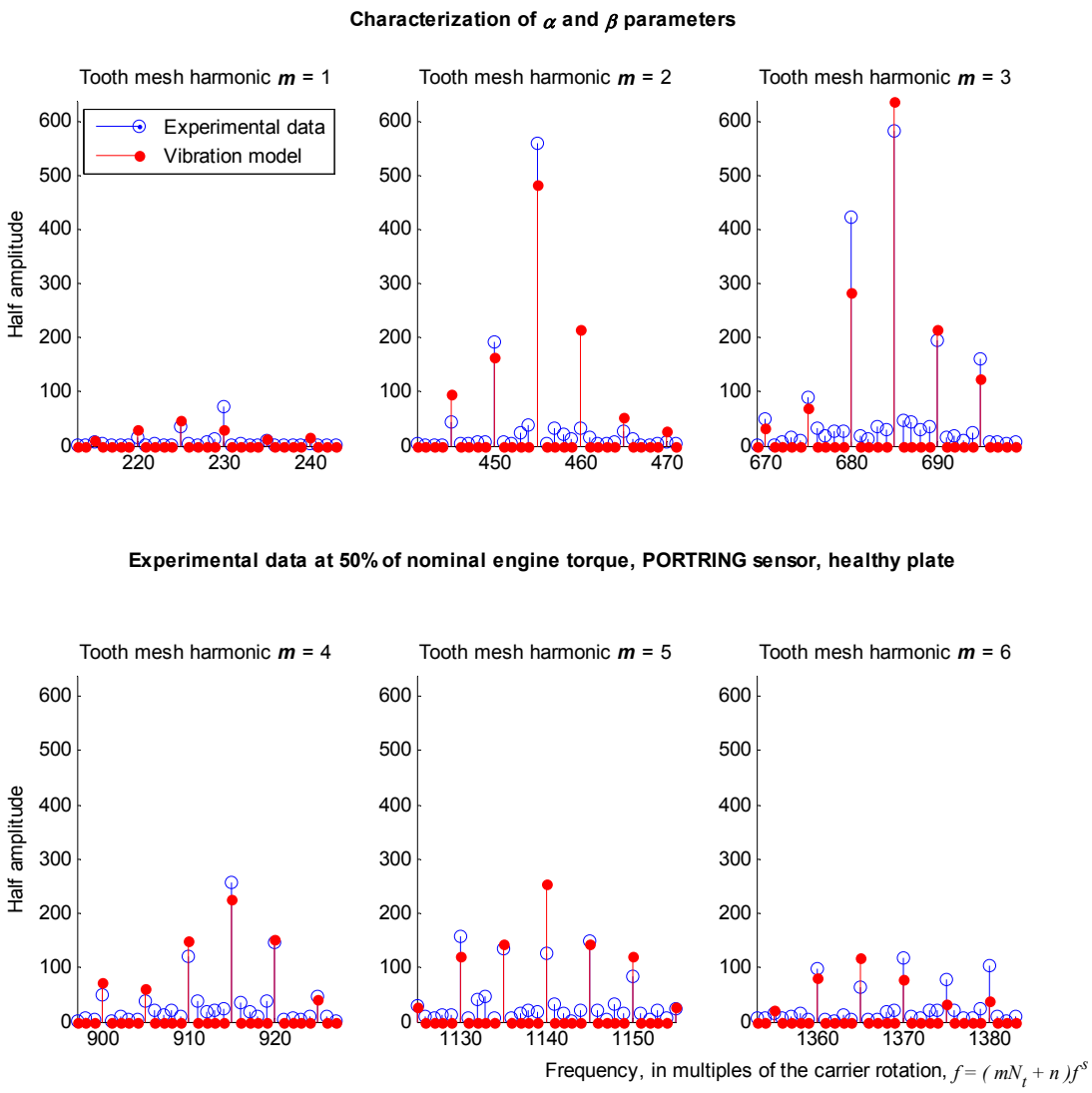

Figure 5.9. Results of the characterization of the α_n and β_m parameters of a healthy planetary gearbox transmission operating in a test cell at 50% of nominal torque

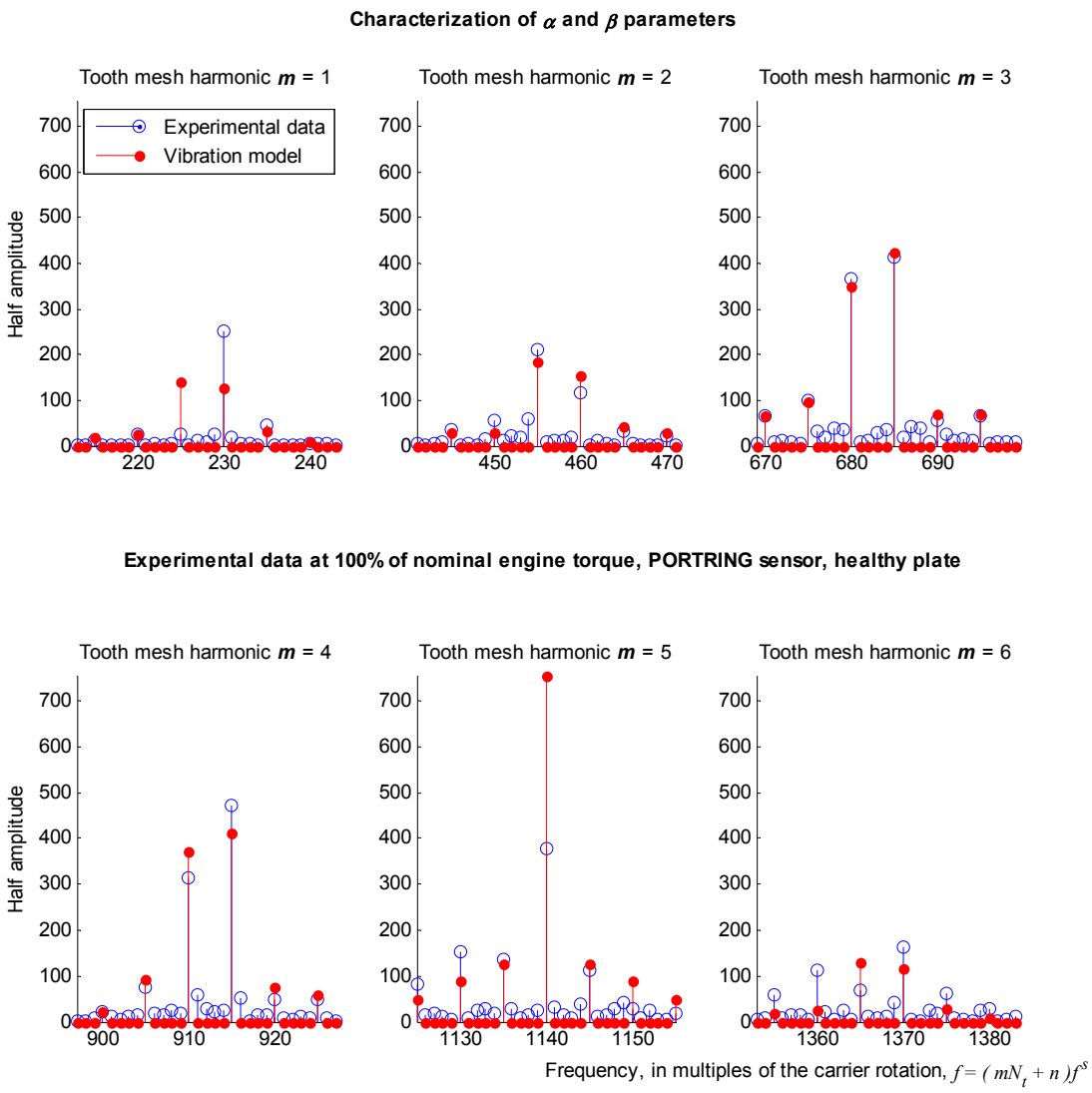

Figure 5.10. Results of the characterization of the α_n and β_m parameters of a healthy planetary gearbox transmission operating in a test cell at 100% of nominal torque

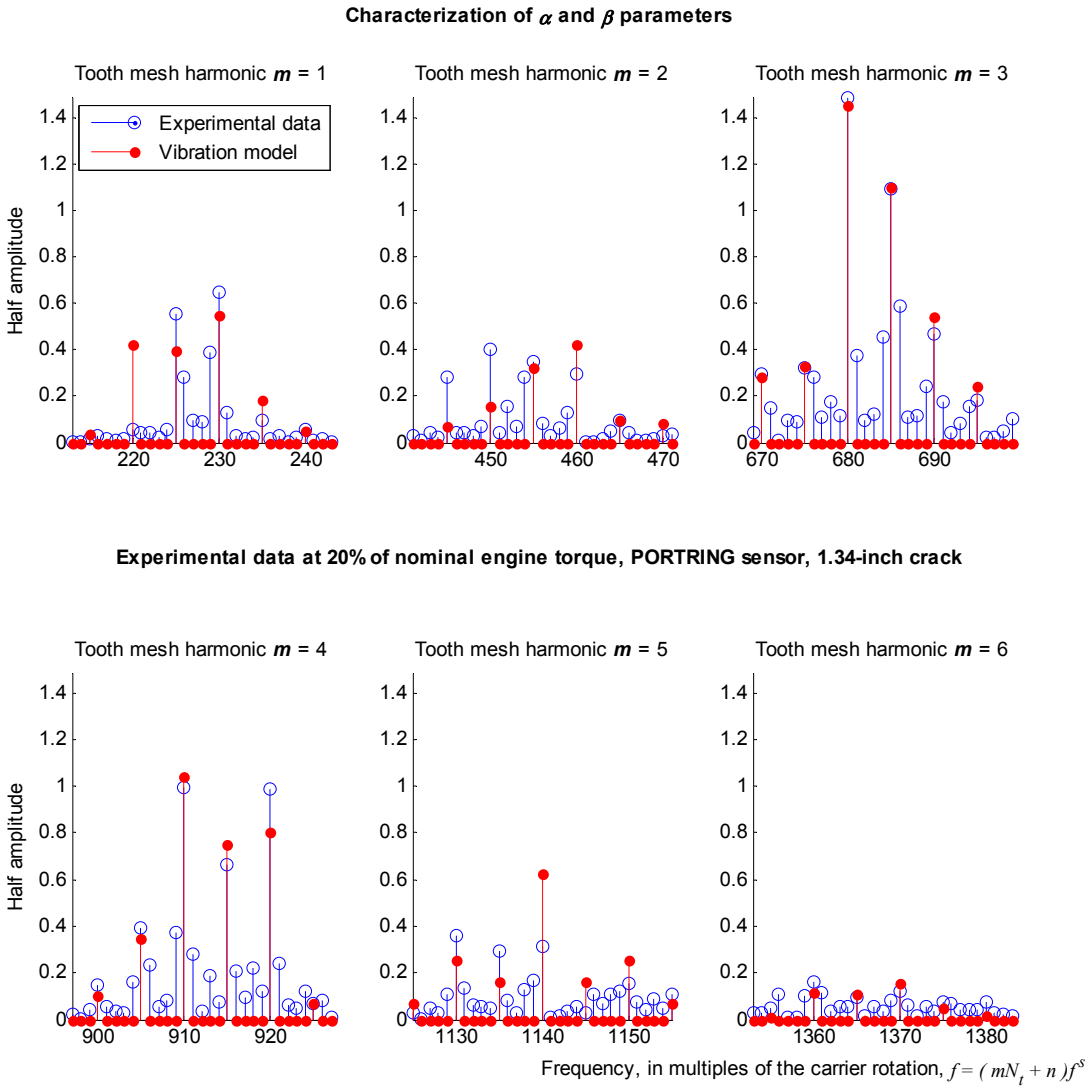

Figure 5.11. Results of the characterization of the α_n and β_m parameters of a planetary gearbox transmission with a small crack (1.34 inches), but assumed to be healthy, operating in a test cell at 20% of nominal torque

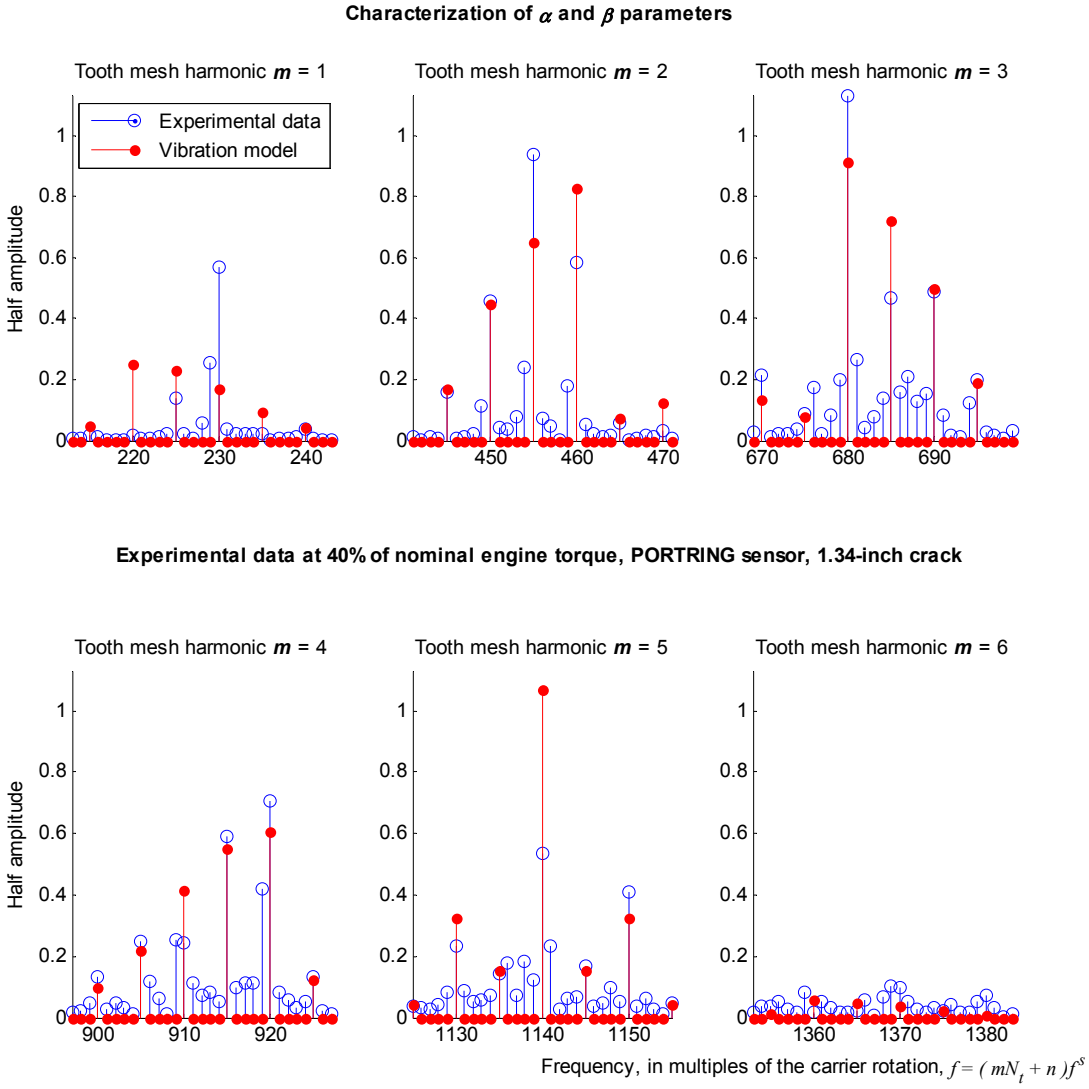

Figure 5.12. Results of the characterization of the α_n and β_m parameters of a planetary gearbox transmission with a small crack (1.34 inches), but assumed to be healthy, operating in a test cell at 40% of nominal torque

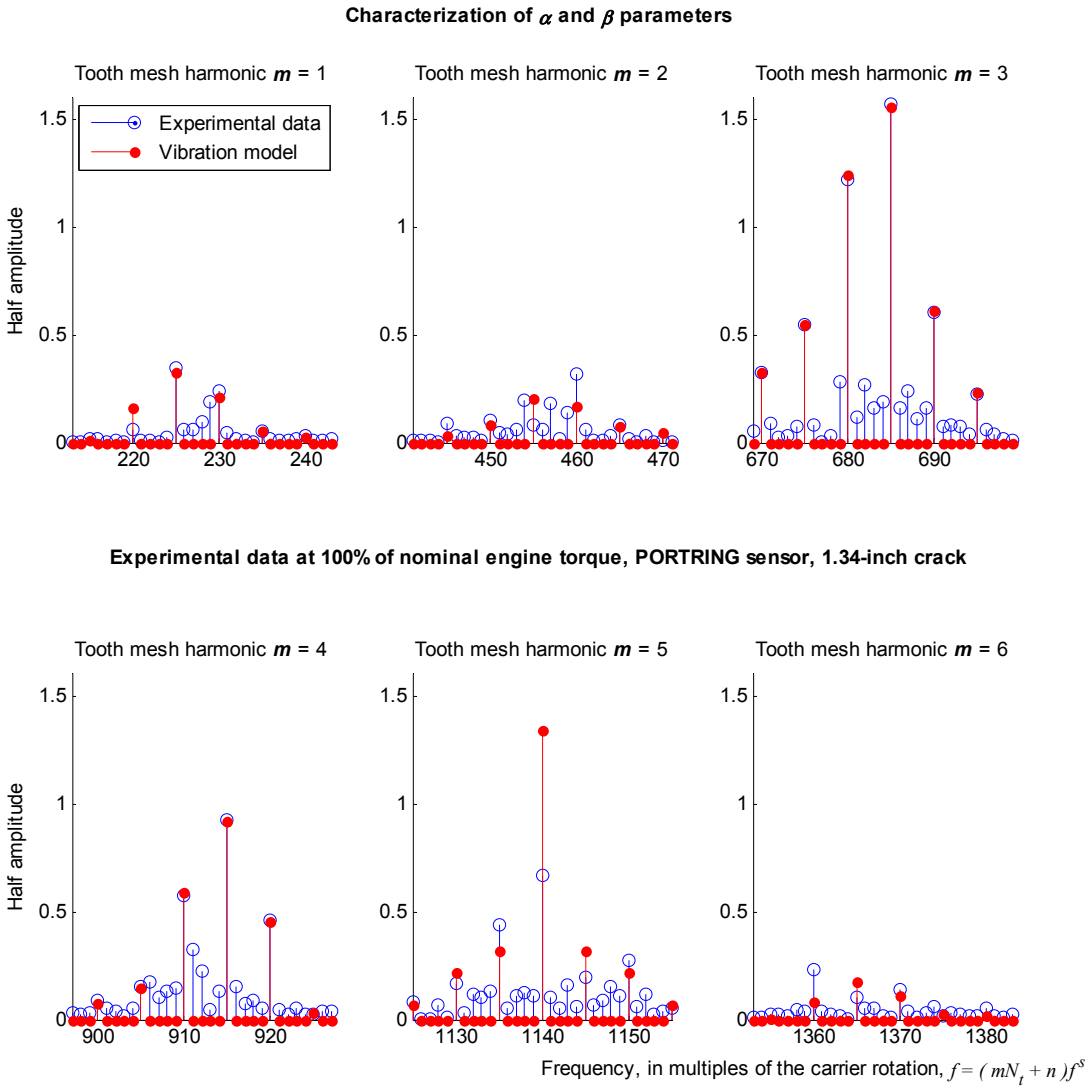

Figure 5.13. Results of the characterization of the α_n and β_m parameters of a planetary gearbox transmission with a small crack (1.34 inches), but assumed to be healthy, operating in a test cell at 100% of nominal torque

5.4. Determination of the fault-sensitive parameters

In this section, we are interested in approximating the shift angles of the planet gears caused by deformations of the planetary carrier plate of the helicopter planetary gearbox while in operation. The angular positions of the planet gears are important parameters in the vibration model proposed in section 3.4. These angular positions are expected to change when a crack is present in the planetary carrier plate, which in turn affects the vibration patterns of the gearbox. The change in these vibration patterns enables us to use vibration signals as a means for diagnosing a gearbox with the crack.

Finite element analysis (FEA) can be used to analyze the deformation of the planetary carrier plate (see section 2.3.3). The deformation patterns should be converted into specific shift angles for each planet gear. To this end, the results presented in this thesis used the FEA software package known as ANSYS (for a useful reference, see Moaveni, 2003). ANSYS was used to determine the planet-gear shift angles resulting from specific crack lengths at different operating torque values of the gearbox.

A three-dimensional model of the planetary carrier plate is built in the program. This model approximates the most relevant geometric features of the part. Forces acting on the part, as described in section 5.1.1, are applied in the simulation to resemble the loads experienced during operation of the gearbox. The FEA simulation produces results giving specific deflection measurements throughout the plate. Results corresponding to regions on the planet gear mounting posts are post-processed to approximate the angular shift of the planet gears.

5.4.1. Computer model of the planetary carrier plate and the major forces acting on it

Figure 5.14 shows the design of the planetary carrier plate used in ANSYS for the deformation study.

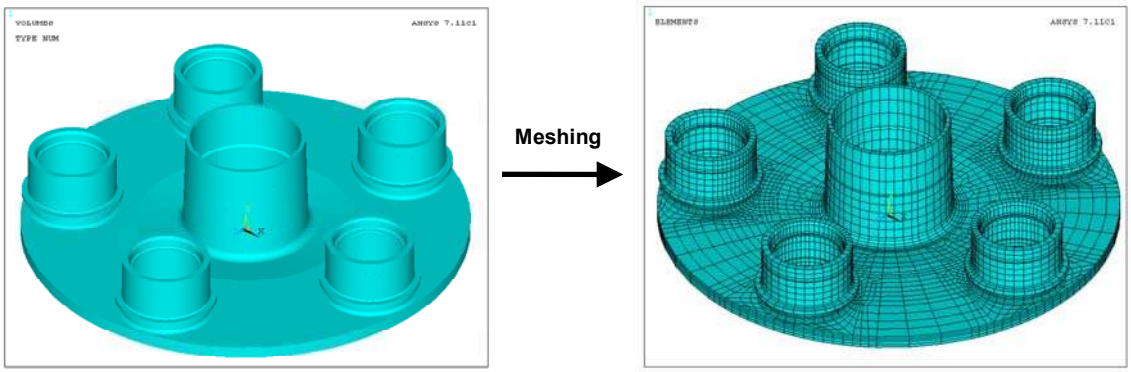

Figure 5.14. Three-dimensional computer model of the planetary carrier plate as used for deformation analysis. The solid model (left) is divided into a mesh of finite elements (right) to be used in finite element analysis of its deformation patterns

After the model is meshed, forces and constraints must be applied to specific finite elements to simulate the operating conditions of the planetary carrier plate. The interaction of these forces and constrains will produce the deformation. Table 5.3 lists some technical characteristics of the ANSYS model of the planetary carrier plate.

Table 5.3. Characteristics of the finite element model of the planetary carrier plate

Material properties	
Type of material	Titanium alloy, Ti-6Al-4V
Density	0.17 lb/in^3
Elastic (Young's) modulus	16,000 ksi
Poisson's ratio	0.33
ANSYS finite element model	
Model without a crack	
Element count	19,185
Node count	101,265
Constraints on nodes (all DOF's)	2,700
Surface loads on elements	20
Models with a crack	
Element count*	25,000 to 29,000 (aprox.)
Node count*	110,000 to 116,000 (aprox.)
Constraints on nodes (all DOF's)	2,700
Surface loads on elements	20
Types of elements	
Away from the crack region	SOLID 95 hexahedrons (manual meshing)
Near the crack region	SOLID 95 tetrahedrons (automated meshing)
Crack tips (fracture stress analyses only)	SOLID 95 prisms (collapsed elements)

** depends on the length of the crack modeled*

Two main groups of forces act on a planetary carrier plate when operating. The first group derives from the action of the planet gears and acts on the planet gear mounting posts of the carrier plate. The second group derives from the reaction of the helicopter's main rotor shaft to which the carrier plate is attached, and to which the carrier plate transmits power. This reaction acts on the central shaft bore of the carrier plate. The deformation patterns of the carrier plate are studied under a *static* consideration of these forces. Although forces acting on the carrier plate are actually dynamic, it is possible to use a static approximation because we are interested in characterizing the deformations of the plate when operating at steady torques. When a steady torque is present, the large majority of the stress experienced by the plate is also

steady (Sahrmann, 2004). Thus, we expect the large majority of the deformation experienced by the plate to be caused by the static component of the stresses.

The static analysis requires that one of the two sets of forces described be applied as a constraint to motion. In the analysis presented in this work, the reaction of the main rotor shaft of the helicopter against the carrier plate is selected as the constraint. The constraint in the finite element model is applied to the shaft bore of the planetary carrier plate, near the location of the splines, because the reaction of the shaft acts there (refer to Figure 5.2). The constraint sets to zero all degrees of freedom at specific contact locations.

After setting the motion constraint in the model, forces are applied to each of the planet gear mounting posts of the carrier plate. The application of these forces is explained next.

Operation of the planetary gearbox causes the planet gears to experience forces similar to those represented in Figure 5.15. We can calculate the magnitude of the resultant force generated by the addition of the two forces represented in the illustration from consideration of the actual helicopter engine power and the radial distances (i.e., conversion of power to torque to force).

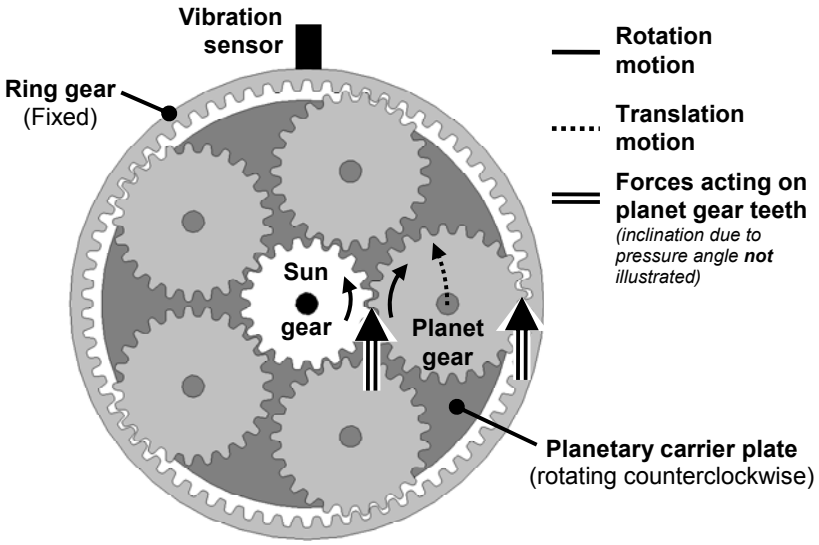

Figure 5.15. Representation of the forces acting on the gear teeth of the planetary gears

Because the forces under consideration act on the teeth of the planet gears, they are transmitted to the planetary carrier plate in a distributed fashion through the gear and the rotary couplings (i.e., the bearings and other mechanical components). Therefore, we apply the resultant force as a distributed (i.e., *area*) force, not a point (or line) force on the planet gear mounting posts of the carrier plate. Thus, the resultant force applied to each of the mounting posts is a *pressure load*. To facilitate modeling, the pressure is applied uniformly, but on the surface of a limited number of elements. The situation is represented in Figure 5.16.

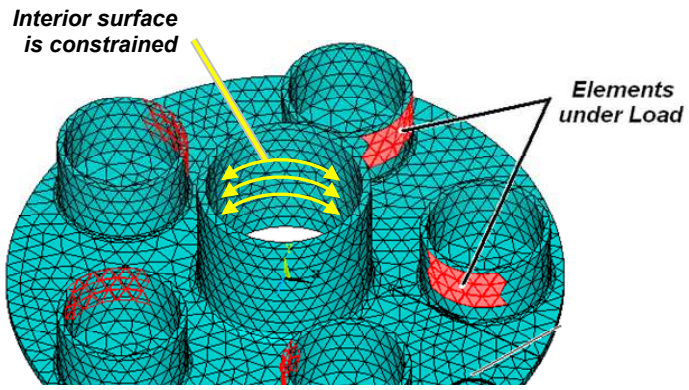

Figure 5.16. Representation of the application of loads and constraints to the planetary carrier plate in the finite element model

The spatial deformations of faulted and healthy carrier plates under different loading levels were analyzed using this model. Figure 5.17 shows how axes have been conveniently defined on each planet-gear mounting post to study deflections. Results from the simulations carried out with the model have been validated by comparing stresses on the mounting-post roots to those determined by Sahrmann (2004). Further validation is provided by the crack growth studies of chapter 7.

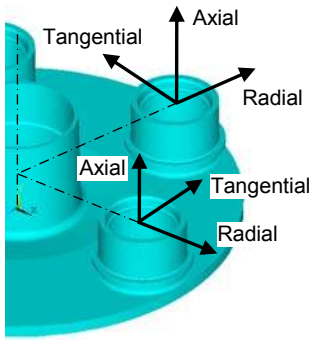

Figure 5.17. Definition of the axes of deflection at individual planetary gear mounting posts

According to the simulation results, deformations in the *axial* direction are the largest. However, the vibration model of section 3.4 is a *gear meshing description* and concerns deviations in *teeth contact timing*. The deflection that affects teeth contact timing the most is in the *tangential* direction. Axial deflection will not modify teeth contact timing in any amount deserving consideration. *Radial* deflection can affect teeth contact timing due to the profile of the teeth, but this variation is small and hence assumed to be negligible.

No constraints are applied to the planet-gear mounting posts. The tangential direction is clearly forced by the application of load already, and no other force or constraint is applied in that axis. Even though excessive deformation could possibly close the *gear mesh clearance* shown in Figure 5.18 and cause contact constraints, it is assumed that the clearance is large enough to prevent this from occurring in either of the tangential or radial directions. In the axial direction, the planet gear mounting posts have no constraints because the gears used in the transmission are spur gears, which are unhindered to slide over this axis.

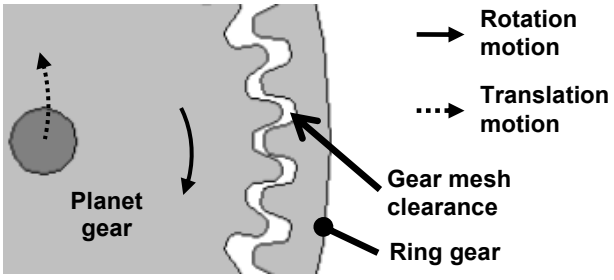

Figure 5.18. Representation of the gear-mesh clearance of a planet gear. It must be noted that the image illustrates the concept of gear mesh clearance used only, and is not representative of the gear teeth shapes or contact patterns

5.4.2. Modeling the fracture in the planetary carrier plate

The first step in modeling the fracture on the root of a planet-gear mounting post of the carrier plate is to define a crack plane. The crack plane is a reference plane that slices the plate model near the post with the crack, as shown in Figure 5.19. A finer mesh is used in this region to maintain precision of the results under the high stresses and strains caused by the crack, and to allow for the modeling of more precise crack shapes. Finite elements around the crack plane are allowed to have faces lying on, but never crossing, the plane.

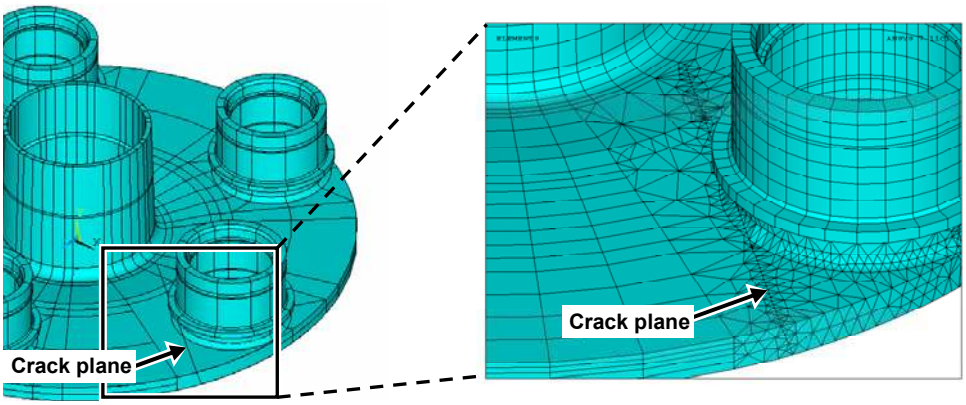

Figure 5.19. View of the finer mesh used in regions near the simulated crack plane of the planetary carrier plate model

A similar condition is applied along the crack front once a particular crack shape is designed: element edges can lie along the crack front but never cross it. These characteristics of the fracture model are represented in Figure 5.20.

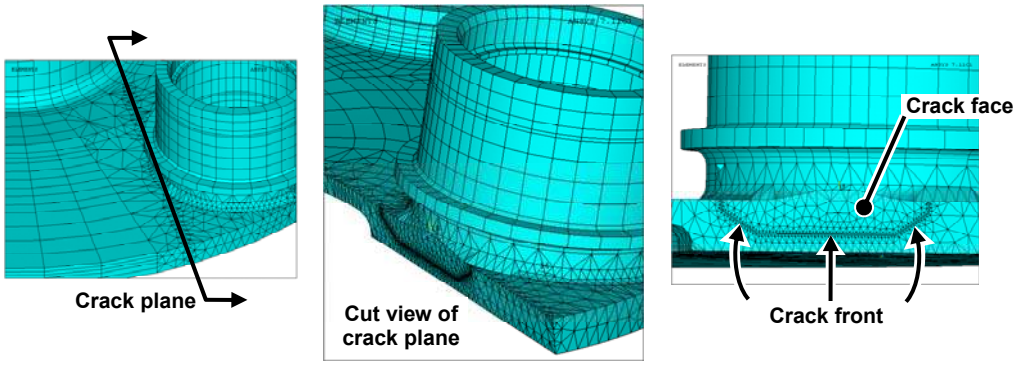

Figure 5.20. Views of a crack design in the finite element model of the planetary carrier plate

To complete the design of the fracture, all the elements sharing nodes inside the crack faces, but on opposite sides of the crack plane, must be separated to allow the crack to open when load is applied to the plate. To achieve this, nodes meeting these conditions are duplicated and the elements on one side of the crack plane that were sharing the original nodes are assigned the duplicate nodes instead. The procedure is illustrated in Figure 5.21.

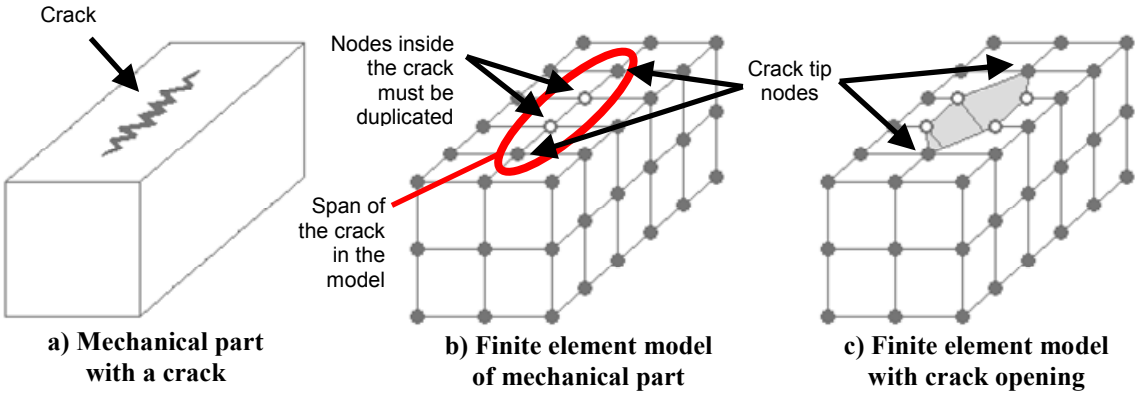

Figure 5.21. Procedure for simulating the presence of a crack in a finite element model

The model is run under the assumption that the crack only opens and does not close or cause finite element interference. This is a reasonable assumption for the geometry and loading configuration under consideration. The deformation results show that, for the static deformation analyses carried out, the crack clearly takes on an open shape and no element interferences occur. Thus, no provisions are taken to handle element interferences in the finite element model.

The finite element simulation delivers results describing the displacements experienced by the nodes, as illustrated in Figure 5.22 and Figure 5.23. These displacements can be used to approximate the shift of the planet gears as described in the following section.

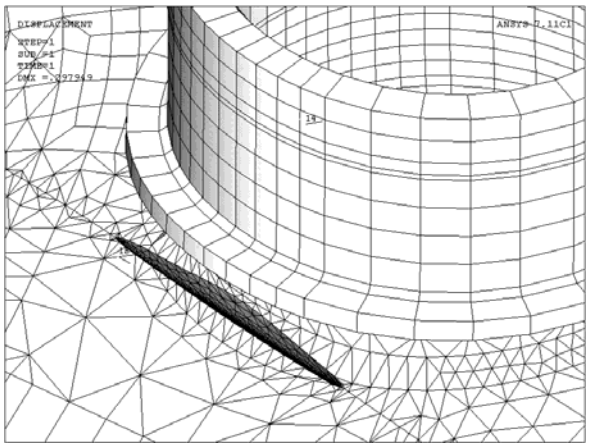

Figure 5.22. View of open crack in the finite element model of the planetary carrier plate, corresponding to the design of Figure 5.20. Deformation results shown here have been enlarged 15 times their actual values to enhance the illustration

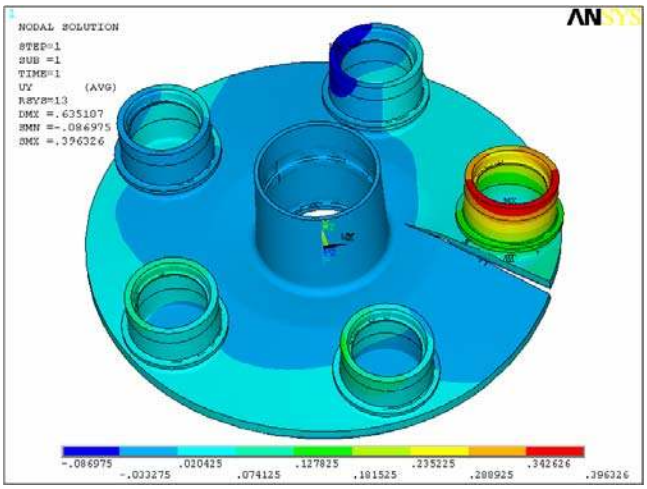

Figure 5.23. Illustration showing example results of the FEA analysis of the deformation experienced by the planetary carrier plate exhibiting a crack more than 7 inches long. Colors represent different amounts of angular deformation over the plane of the plate. Deflection shown has been enlarged to enhance the illustration

5.4.3. Deformation analysis and interpretation

The FEA model provides deflection results for individual nodes in the design. We can process information about nodes located on the planet gear mounting posts to approximate the deflection experienced by the planet gears. Nodes located near the rim of the mounting posts experience larger deflections than nodes near the base of the carrier plate. It was decided to consider the nodes around the circumference of the posts, near the middle of the total height of the posts to measure the deflections. Figure 5.24 illustrates this.

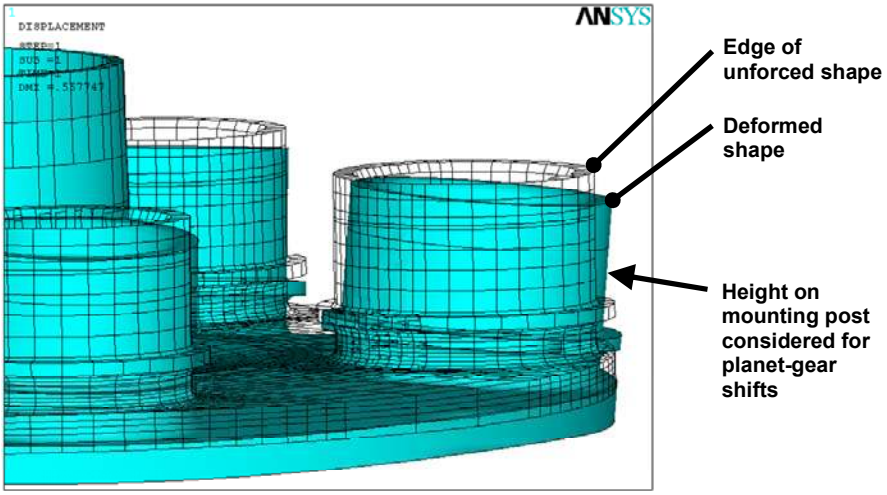

Figure 5.24. Illustration of the deflection experienced by different regions of the planet gear mounting posts of the planetary carrier plate. To measure the deflection as a single value that represents the angular shift of a planet gear that is mounted on a deflected post, the deflection of the post at about the middle of its total height is considered

A geometric center of the nodes chosen is calculated for both the unforced part and the deformed shape. These centers are calculated for each of the five planet gear posts, and are ultimately used to measure the angular shift of the planet gears at each mounting post on the plane of the carrier plate. This is illustrated in Figure 5.25.

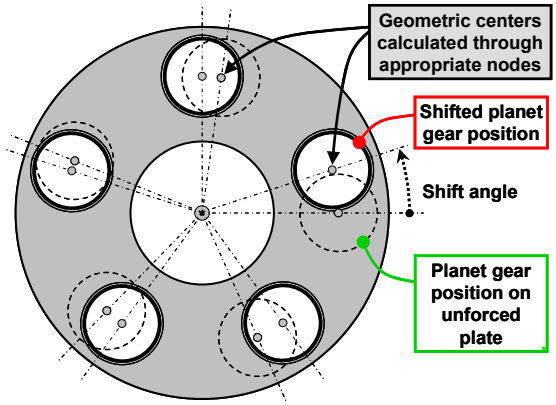

Figure 5.25. Nodes on the planet gear mounting posts of the carrier plate model are used to approximate the geometric center of the planet gears and estimate the planet-gear shift angles caused by deformation of the plate

Table 5.4 reports on the results obtained through simulations. Post mounting numbering is successive in the direction opposite to the rotation of the carrier plate (i.e., numbering is clockwise), in correspondence with the numbering of planet gears defined earlier in Figure 3.4, and taking post number 1 as the post where the fracture is present. Figure 5.26 presents the results of Table 5.4 graphically.

Table 5.4. Static shift angles, in degrees, of planet gears at 100% of nominal engine torque (54,000 lb·ft) caused by the presence of different cracks on the planetary carrier plate. The crack is located on the root of the mounting post of planet gear number 1. Angles are measured with respect to the planet gear positions of the unforced plate

		Planet gear / mounting post numbers				
		1	**2**	**3**	**4**	**5**
Crack Length (inches)	**0.00**	0.22	0.22	0.22	0.22	0.22
	1.34	0.23	0.22	0.23	0.22	0.21
	1.95	0.25	0.22	0.23	0.22	0.21
	2.48	0.27	0.22	0.23	0.22	0.20
	3.02	0.30	0.22	0.23	0.21	0.19
	3.54	0.36	0.23	0.24	0.21	0.17
	4.07	0.39	0.23	0.25	0.21	0.16
	4.57	0.42	0.23	0.25	0.21	0.15
	5.39	0.53	0.23	0.27	0.19	0.12
	6.21	0.68	0.23	0.30	0.18	0.08
	6.47	0.74	0.23	0.31	0.17	0.06
	6.73	0.83	0.23	0.32	0.17	0.04
	7.07	1.38	0.34	0.38	0.08	0.01
	7.38	1.45	0.35	0.39	0.08	0.01

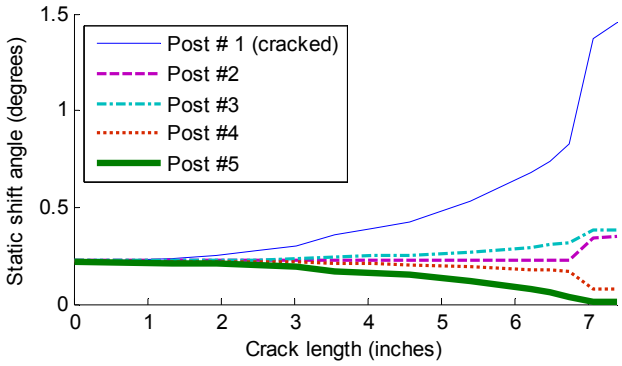

Figure 5.26. Graph of the static shift angles, in degrees, of planet gears at 100% of nominal engine torque (54,000 lb·ft) as a function of the length of a crack present on the planetary carrier plate. The crack is located on the root of the planet gear mounting post identified as number 1. Angles are measured with respect to the planet gear positions of the unforced plate

It was found through FEA simulations of the carrier plate that, although the shift angles do not vary linearly with respect to changes in the crack length, they vary linearly with respect to different values of the torque applied. This is visible in the graph of Figure 5.27, which uses post number 1 as an example.

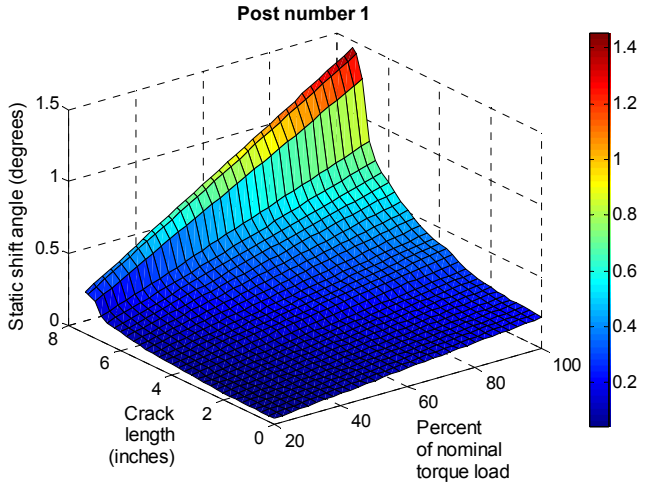

Figure 5.27. Graph of the static shift angles, in degrees, of the planet gear whose mounting post has a crack on the planetary carrier plate. Shift angles are plotted as a function of crack length and percent of nominal engine torque (54,000 lb·ft). Notice that the shift angles have a linear relation with respect to the torque. Angles are measured with respect to the planet gear position of the unforced plate

5.5. Proposed condition indicators (features) for diagnosing the planetary gearbox through vibration

5.5.1. Background in the condition assessment of the helicopter planetary gearbox

For many years, there has been considerable interest in detecting and diagnosing defects in gear train systems based on vibratory sensory outputs. Examples include such *condition indicators* as the figures of merit (FM0 and FM4) presented by Stewart (1977), the energy ratio presented by Swansson (1980), the sideband level factor (SLF) presented by Favaloro (1985), or the sideband index (SI) presented by Szczepanik (1989), all of which are still in use today. Most of the work in gear train diagnostics has been for stationary gear trains; however, some of it has specifically considered planetary train systems. Consider, for example, a recent paper by Chaari, et al. (2006) where the effects of gear teeth defects in the dynamics of a planetary gear system are investigated.

The difference in the way vibration signals are generated between the non-epicyclic and the epicyclic geared transmission systems prevents certain vibration-based standard condition indicators of the former –which is more typical– from working on the latter. Condition indicators of this kind are hence useless for diagnosing planetary gear transmissions. Using the characterization offered by McFadden and Smith (1985) of the epicyclic system's vibration (i.e., the asymmetry effect), Keller and Grabill (2003) tried to adapt some standard non-epicyclic condition indicators to circumvent this inadequacy. The treatment that they followed offers the corresponding epicyclic version of the indicators, all of which keep in use the same underlying functioning theory and specific system parameters or signal measures as their original non-epicyclic counterparts. Unfortunately, as Keller and Grabill have reported, most of the adapted indicators did not seem to work as well as their unmodified non-epicyclic predecessors.

Furthermore, although useful for detecting a fault or evaluating damage progression in a specific system, many of these condition indicators, whether unmodified or adapted, are not always suitable for making comparisons across systems because their numeric values sometimes depend on (1) measurement subsystem, (2) system-specific, or even (3) setup-specific characteristics,[11] in addition to (4) changes in operating conditions (like load). Take for example the case of the sideband index (SI) and the sideband level factor (SLF) condition indicators, both of which Keller and Grabill reported to be the only measures, among those analyzed by them, that could single out

[11] By each of these three types of characteristics, the following is meant: (1) Measurement subsystem characteristics are those related to the vibration data acquisition system, like sensor type, or converter gain and offset; (2) System-specific characteristics are those physical parameters that vary from one geometry or system design to another, e.g. number of planet gears, number of teeth, pitch diameters, etc.; (3) Setup-specific characteristics refer to physical parameters that change between otherwise geometrically identical systems which are installed at different locations or as part of different machines.

the planetary carrier plate crack in the helicopter transmission of our focus, and only under controlled experimental conditions.[12] Because we will be referring constantly to the magnitude of specific sidebands in the vibration frequency spectrum of the planetary gear transmission, let us define $SB_{m,n}$ as the symbol that represents the half amplitude of the frequency component located at frequency $f = (m \cdot N_t + n) \cdot f^s$, i.e., of sideband ($m$, n), in the vibration signal of a planetary gearbox. In this manner, following the notation used in section 3.4,

$$SB_{m,n} = \left| \vec{\Phi}_{m,n} \right| . \tag{5.7}$$

Following this nomenclature, and deviating here from that used by Keller and Grabill[13], the two condition indicators described above can be defined as

$$\mathrm{SI} = \frac{SB_{1,d-1} + SB_{1,d+1}}{2}, \tag{5.8}$$

and

$$\mathrm{SLF} = \frac{SB_{1,d-1} + SB_{1,d+1}}{\mathrm{RMS}} . \tag{5.9}$$

In the two equations above, $n = d$ corresponds to the dominant sideband at the first tooth meshing harmonic (m = 1), so that only the two non-dominant sidebands adjacent to the dominant are used in the calculations. Note that under this definition, the

[12] These experimental conditions correspond to "test cell data," identified as such both in Keller and Grabill's publication (2003) and in this thesis, and are as opposed to data measured onboard an actual aircraft.

[13] Keller and Grabill used the symbol RMC –standing for *regular meshing components*– to refer to the dominant and apparent sidebands. Because we are interested in considering the non-dominant sidebands as well, which under their definition are not regular meshing components, the proposed differing nomenclature is used.

calculations are done only on the first tooth meshing harmonic, although, by varying the first subscript of each $SB_{m,n}$, they could be evaluated at different harmonics. RMS stands for the *root mean square* of the vibration signal, i.e.,

$$\text{RMS} = \sqrt{\frac{\sum_{k=1}^{K} x_k^{\,2}}{K}}, \tag{5.10}$$

where x is a discrete-time vibration signal described by of a total of K individual x_k samples.

Also, be aware that extracting reliable values for the sideband magnitudes involves the application of a suitable preprocessing filtering technique on the "raw" vibration data, like time synchronous average, or TSA (see section 3.4.5).

The SI and SLF condition indicators are functions of numerical quantities –the sideband magnitudes and the RMS– that vary from one system to another. This variation occurs because the quantities are tied to the amplitude of the vibration signal components, which, in addition to noise, depend on the value of parameters like transducer sensitivity, converter gain and even system frequency response, among others. Hence, condition indicators exhibiting this dependency may be inappropriate for making comparative assessments of the status of two or more systems. The graphs of Figure 5.28 show the high variability that the SI and SLF indicators display. The results shown in the graphs have been extracted from the same data used by Keller and Grabill in their work, although with the addition of an extra set of data obtained from yet a fourth aircraft in

proper operating (i.e., "healthy") conditions[14]. The comparison of interest here regards all the data points for the healthy aircrafts (i.e., numbers 2 through 5). Note that, for all cases shown, the range of variability among data sets for comparable operating conditions (20 or 30% of nominal engine torque) is greater than their corresponding mean across all healthy helicopters.

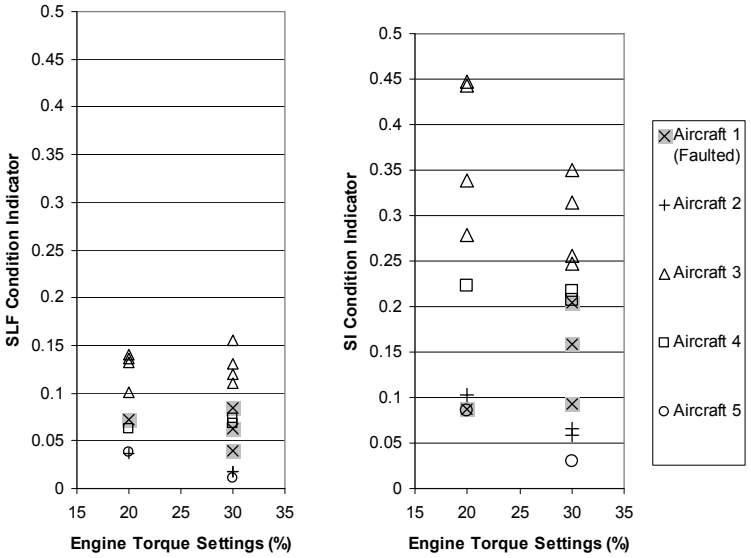

Figure 5.28. Evaluation of vibration-based SI and SLF condition indicators for five different helicopters. Helicopter number 1 is known to have a crack in the planetary carrier plate of about 3.5 inches in length

5.5.2. Consideration of the sideband magnitude variability and noise at different frequencies

The data points shown in Figure 5.28 have illustrated that a significant amount of noise or variability may be present in the vibration signals acquired from operating

[14] Keller and Grabill presented results for one faulted aircraft and three healthy aircraft.

planetary transmission systems. Experimental data from our transmission problem show that sideband magnitudes have large variability. It is worthwhile to consider how the noise and variability affect the construction of the overall system sidebands at different frequency ranges. We assume here that the sideband magnitude variability is generated by unmodeled dynamics, primarily the dynamic deflections of the planet gears' axes of rotation, which is caused by loading of the transmission. These deflections in turn dynamically affect the vibration signature of the system, i.e., the sideband magnitudes. We also assume that noise can be present in the vibration signals because of many known or unknown factors, like resonances, frequency response of the sensors, vibration signal reflections and refractions, transmission path effects, surface roughness and rubbing of the gear teeth, aerodynamic loads on an aircraft, etc.

Even if healthy, when a planetary gear transmission is operating, we can expect the elasticity of the planet gears' axes of rotation to cause, continuously, a small variability in the planet gear angles. As mentioned earlier, this can be caused by the tooth meshing action of the planet gears, among other causes. These slight excursions of the planet gear angles in turn affect the phase of the single-planet-gear sidebands corresponding to each planet gear. Although the phase changes are different at each sideband and at each planet gear, the corresponding sidebands across planet gears are likely to be affected in comparable magnitudes, since the system geometry is angularly symmetric (i.e., all the planet gears have angular excursions within the same orders of magnitude).

However, this effect has a varying outcome on the overall system sidebands, depending on whether the sidebands formed are dominant, apparent or non-dominant. The effect is illustrated in Figure 5.29. The shaded areas in the illustration represent the expected variation of the sideband magnitudes. This variation can be perceived as noise in the spectrum analysis of the system's sidebands, and its effects can be observed in all systems, whether healthy or with a fault condition. This kind of variability is not necessarily indicative of an anomaly, and depends on the load imposed on the planetary gear system, because the load affects the angular excursions of the planet gears.

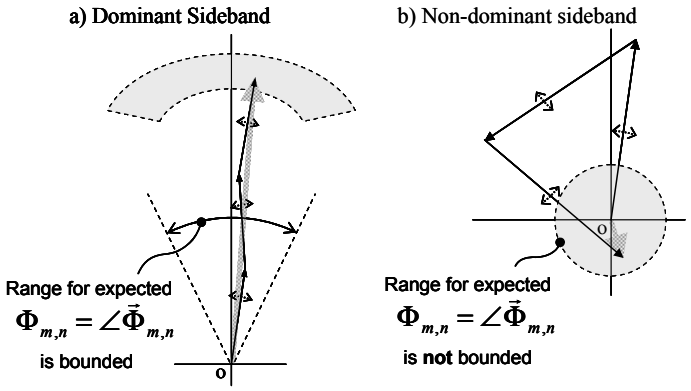

Figure 5.29. Illustration of the effect of continuous small angular shifts in multiple planet gears; a) interaction of single-planet-gear sidebands to form a dominant (or apparent) sideband; small deflections of each planet gear generate an area range for expected values of the sideband; b) corresponding situation for a non-dominant sideband

Figure 5.29 suggests that, when a planet-gear shift is small or when the system is healthy, the *dominant* and *apparent* sidebands can be expected to have an average magnitude close to the value that the sideband would have if the sideband magnitude variability were reduced or eliminated. In the figure, this means that the average

magnitude of the dominant sideband would probably be near the middle of the shaded area.

On the other hand, since the magnitude of the sidebands cannot be negative by definition, averaging the time-changing magnitude of a *non-dominant* sideband will yield a non-zero value. This is in opposition to the behavior of the dominant and apparent sidebands described in the preceding paragraph. If we were able to reduce or eliminate the sideband magnitude variability, we would see that a non-dominant sideband would tend to approach an average magnitude of zero. However, while the variability is present, the average magnitude of the non-dominant sideband *will not approach zero*. This behavior suggests that the average magnitude of the non-dominant sidebands in a healthy system will approximate the average of the noise and variability effects at the specific frequency of each non-dominant sideband.

The observation above is important because it suggests that non-dominant sidebands can be easily overwhelmed by noise and variability effects. Any one non-dominant sideband can be useful for planet-gear shift detection only after its magnitude has overcome the mean of the noise or variability effects at the corresponding frequency, or else noise must first be removed, and the variability compensated, by some means.

The theory set forth in section 3.4.3 suggests that, in general, because the sensitivity of the phase of a single-planet-gear sideband is for the most part proportional to the tooth meshing harmonic number *m* at which it is located (as expressed by Equation 3.16), it may be possible to detect smaller single-planet-gear shifts by observing changes

in the sidebands of the overall system vibration at higher harmonics. However, if multiple planet gears shift in comparative amounts, the complex interaction of the individual planet-gear sidebands is likely to repeal the proportionality between the sensitivity of the overall system sidebands and m. In addition, although higher tooth meshing harmonics with larger m values can be more sensitive to planet-gear shifting, they can be as well more sensitive to noise and variability effects, because larger frequencies are likely to have smaller values of β_m, which generate shorter sidebands.

Hence, there a tradeoff ensues when selecting sidebands of different frequencies for their sensitivity to planet-gear shifts. Sidebands at higher harmonics respond more to smaller planet-gear shifts, but the shorter sidebands of these high frequency regions of the spectrum first have to overcome the noise to be useful for shift detection, and this may be impossible sometimes, due to the small values of β_m. Conversely, lower harmonics might have a better chance to show sideband magnitudes well above the noise mean, but their ability to detect small shifts is quickly compromised by the variability effects. These situations are illustrated in Figure 5.30.

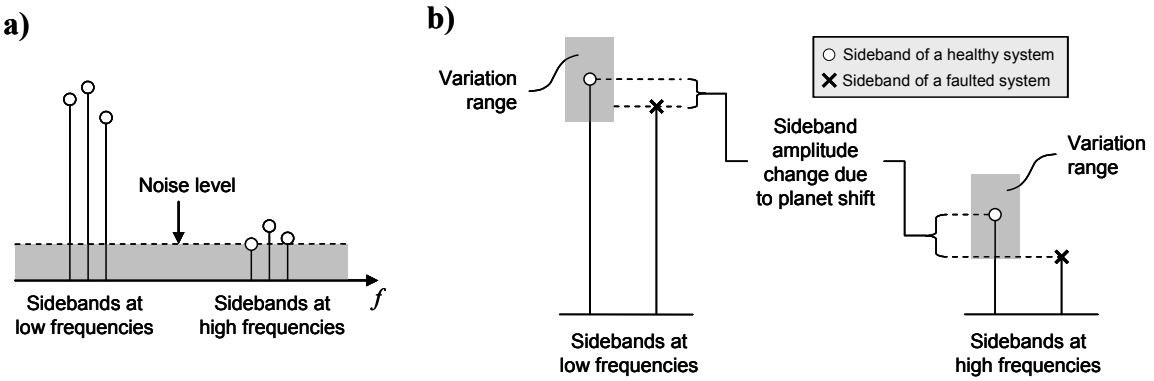

Figure 5.30. Effect of noise and variability levels on the sideband magnitudes at different frequency regions; a) spectrum representation of several sidebands as compared to some level of noise; b) the effect of variability. Note in (b) that detecting a planet-gear shift may be challenging because the faulted system's sideband is within the variation range of the healthy system's sideband

Thus, the selection of the harmonic frequency range on which to work when analyzing the system sideband magnitudes and spectral shape can play an important role in successfully assessing the condition of a planetary gear system. Even further, different fault conditions may require that different harmonic regions be considered.

5.5.3. Suggested condition indicators

We are now interested in developing condition indicators that involve the use of sideband magnitudes to detect the angular shifting of planet gears. We mentioned in section 5.5.1 that some condition indicators have a weakness in the sense that, even under similar operating conditions, they can vary from system to system. This variation occurs because the values of the condition indicators depend on parameters that change between systems and between data acquisition setups. We are here proposing the use of relative measurements of the sideband amplitudes to compensate for this weakness.

5.5.3.1. Suggested condition indicator 1: relative sideband index

Taking as a reference the sideband index feature of Equation 5.8, let us define the relative sideband index as

$$\text{relSI} = \frac{SB_{1,d-1} + SB_{1,d+1}}{2SB_{1,d}}. \tag{5.11}$$

This condition indicator differs from the SI indicator because it is now evaluated as a ratio with respect to the amplitude of the dominant sideband. relSI has the advantage that it may be able to mitigate the effects of varying scales in sideband levels across systems caused, for example, by differences in transducer gains.

5.5.3.2. Suggested condition indicator 2: sized relative harmonic sideband index

The sideband index and relative sideband index indicators consider only two sidebands of the first tooth meshing harmonic region. If, instead, we wish to consider other sidebands, we may do so by defining

$$\text{relHSI}(m, K) = \frac{\sum_{k=1}^{K} \left(SB_{m,d-k} + SB_{m,d+k} \right)}{2 \cdot K \cdot SB_{m,d}}. \tag{5.12}$$

Under this definition, the relSI condition indicator is modified to allow for evaluations at different tooth meshing harmonic regions (m), and to use more than the two adjacent sidebands of the dominant, depending on the value of the "size" parameter K. Provisions can be taken to avoid the use of the apparent sidebands in the numerator of the right-hand side of Equation 5.12.

5.5.3.3. General form of suggested relative metrics

From the theory presented in section 3.3.2, we know that for every group of N_p adjacent sidebands, one of them is dominant or apparent, while the other N_p–1 are non-dominant. Since in a system with more than two planet gears we will always have more non-dominant than dominant and apparent sidebands, we can try to combine information from their magnitudes to mitigate the effect of noise (e.g., average their magnitudes). In addition, because the dominant and apparent sidebands have a lesser relative variation, we can use these as a reference value to measure the change in nearby non-dominant sidebands. In this way, the amplitude of dominant and apparent sidebands can work as a reference to the average amplitude of nearby non-dominant sidebands. A straightforward way to implement this idea for measuring changes in the amplitude of sidebands is to define a metric that provides a ratio of the amplitudes on non-dominant sidebands to dominant and apparent sidebands, calculated as

$$\begin{matrix}\text{Basic form of ratio metrics} \\ \text{in a harmonic region}\end{matrix} = \frac{\sum \text{non-dominant magnitudes}}{\sum \text{dominant and apparent magnitudes}}. \qquad (5.13)$$

This inviting measure, however, is based on quantities that change rapidly with respect to the shift of a planet gear. It may prove useful to define a metric that measures a ratio with respect to a quantity with "lesser variability". Hence a slight variation to Equation 5.13 is proposed as follows:

$$\begin{matrix}\text{Compensated} \\ \text{ratio metrics in} \\ \text{a harmonic region}\end{matrix} = \frac{\sum \text{non-dominant magnitudes}}{(\sum \text{dominant and apparent}) + (\text{non-dominant compensation})}. \qquad (5.14)$$

The behavior of the terms involved in the two previous equations is shown in Figure 5.31. Note that adding the dominant and non-dominant curves produces a curve (represented by a dashed line) that is less variable, which may provide a good reference for relative metrics with the form of Equation 5.14. The example shown in the graph considers unit-magnitude, single-planet-gear sidebands for reasons of simplicity. Under this assumption, the curve corresponding to an apparent sideband would be the same as that of the dominant sideband shown.

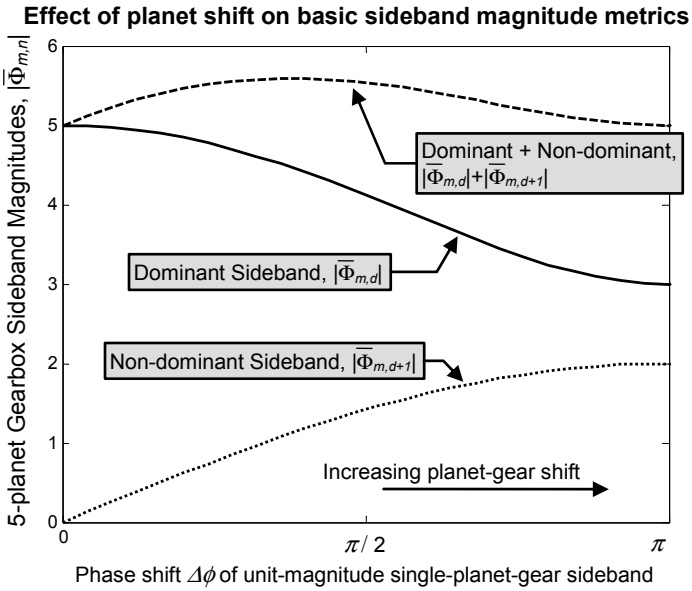

Figure 5.31. Effect of single-planet-gear shift on basic sideband magnitude metrics. The planet-gear shifts considered are "small", i.e., $\Delta\varphi < \pi$ for all cases shown (compare to Figure 3.17)

5.5.3.4. Definition of N_p-sideband groups and basic group metrics

We may also generate metrics by considering the spectrum shape. Since one apparent or dominant sideband appears in the spectrum every total of N_p adjacent

sidebands, it is convenient to define the "N_p-sideband groups". An N_p-sideband group includes a total of N_p adjacent sidebands, one of which is dominant or apparent, and is centered among the others, as illustrated in Figure 5.32. If the number of planet gears in the system is even, then the dominant or apparent sideband can be in either of the two available central positions. Because the sidebands in each group are adjacent, their magnitudes are similar and may provide a sound basis for comparison.

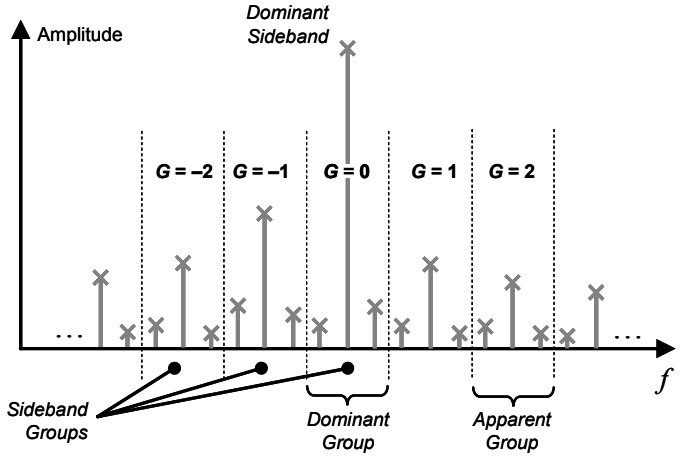

Figure 5.32. Definition of N_p-sideband groups. Sideband groups are integrated by N_p sidebands, with an apparent or dominant sideband centered within the group. The illustration represents a system with $N_p = 3$ planet gears. Sideband groups are identified by a number G, with $G = 0$ corresponding to the group with the dominant sideband, $G < 0$ for groups to the left of this one, and $G > 0$ to the right

At each specific meshing harmonic region (m), groups can be identified with a number G that describes their position. $G = 0$ corresponds to the group that includes the dominant sideband (referred to as the "dominant group") at the corresponding harmonic region, $G = -1$ for the group to the left of this one, $G = -2$ for the next group to the left and so on. Similarly, $G = 1$ for the first group to the right of the dominant group, G=2 for the next group to the right and so on.

We also suggest the evaluation of the average size of the non-dominant sidebands in a specific N_p-sideband group. This value can be calculated by adding the magnitudes of all the non-dominant sidebands in a group and dividing by (N_p – 1). In equation form, the average size of non-dominant sidebands in a group be described as

$$avgND(m,G)=\begin{cases}\dfrac{\left(\sum_{k=-(Np-1)/2}^{-1} SB_{m,d+k+Np\cdot G}\right)+\left(\sum_{k=1}^{(Np-1)/2} SB_{m,d+k+Np\cdot G}\right)}{N_p-1}, & \text{for } N_p \text{ odd} \\ \dfrac{\left(\sum_{k=-Np/2}^{-1} SB_{m,d+k+Np\cdot G}\right)+\left(\sum_{k=1}^{(Np/2)-1} SB_{m,d+k+Np\cdot G}\right)}{N_p-1}, & \text{for } N_p \text{ even}\end{cases}. \quad (5.15)$$

Condition indicators can be defined based on measurements of relative sideband sizes in N_p-sideband groups, evaluating a ratio of the amplitudes of non-dominant versus dominant or apparent sidebands, as shown below.

5.5.3.5. Condition indicators 3 and 4: relative size of sidebands in an N_p-sideband group

The next two condition indicators suggested are the "basic relative size of sidebands in an N_p-sideband group," defined as

$$\text{BrelSG}(m,G)=\frac{avgND(m,G)}{SB_{m,d+Np\cdot G}}, \quad (5.16)$$

and the "compensated relative size of sidebands in an N_p-sideband group," defined as

$$\text{relSG}(m,G)=\frac{avgND(m,G)}{SB_{m,d+Np\cdot G}+(N_p-1)\cdot avgND(m,G)}. \quad (5.17)$$

These two condition indicators follow the patterns of Equations 5.13 and 5.14, respectively. However, we are proposing that the average magnitude of non-dominant sidebands be used instead of the simple summation of non-dominant sideband magnitudes. This provides for a metric that *may be more comparable across varying gearbox geometries*, *regardless of the number of planet gears*. If the non-dominant sideband magnitudes were not averaged, systems with more planet gears would tend to provide larger values for the metric. Because the dominant group ($G = 0$) is expectedly the one with the largest magnitudes[15], such a group will most likely have the largest signal-to-noise ratio and may be the best in which to evaluate this condition indicator.

5.5.3.6. Condition indicators 5 and 6: group averaging of relative sideband sizes

The next two condition indicators suggested are the "basic group averaging of relative sideband sizes," defined as

$$\mathrm{BrelSX}(m, X) = \frac{\sum_{g=-X}^{X} \mathrm{BrelSX}(m, g)}{2X + 1}, \tag{5.18}$$

and the "compensated group averaging of relative sideband sizes," defined as

$$\mathrm{relSX}(m, X) = \frac{\sum_{g=-X}^{X} \mathrm{relSG}(m, g)}{2X + 1}. \tag{5.19}$$

These two condition indicators average several evaluations (groups) of the BrelSG and relSG indicators respectively. The groups averaged include the dominant group and its adjacent groups. The quantity X refers to the number of adjacent groups

[15] The reason for this is the effect considered in Figure 3.9; see section 3.3.2.

taken in the average at both sides of the dominant group. Although the equations initially appear to be involved, especially because of their dependence on relSG and *avgND* quantities, it is worthwhile to remember that the calculation is, in general, simple. The following expressions show the simple pattern of these equations:

$$\mathrm{BrelSX}(m,X) = \frac{\sum \frac{\text{avg(non-dominant)}}{\text{apparent}} \text{ in an } N_p \text{ group}}{\text{number of groups taken}}; \tag{5.20}$$

$$\mathrm{relSX}(m,X) = \frac{\sum \frac{\text{avg(non-dominant)}}{\text{non-dominant} + \text{apparent}} \text{ in an } N_p \text{ group}}{\text{number of groups taken}}. \tag{5.21}$$

The term "apparent" in the two previous equations refers in general to the magnitude of the apparent sideband in an apparent group ($G \neq 0$) or to the dominant sideband in a dominant group ($G = 0$).

5.5.3.7. Condition indicator enhancement: harmonic averaging of relative condition indicators

To further mitigate the effects of noise in the sidebands of gearbox vibration spectra, we may average results of any of the condition indicators suggested above across tooth meshing harmonics, i.e., across values of m from 1 to M, where M is the desired number of harmonics to consider. The operation is performed as

$$relS_{HA}(M,X) = \frac{\sum_{m=1}^{M} relS(m,X)}{M}. \tag{5.22}$$

The *relS* symbol refers here to the use of any of the preceding condition indicators, like relHSI, relSG, relSX, etc, and the *HA* subscript indicates the harmonic averaging operation. The idea behind this definition is to try to combine the information provided by a condition indicator at different harmonics (i.e., evaluated at different values of *m*) into a single useful quantity. Simulation analysis of this kind of operation suggests that it allows for a high sensitivity of small planet-gear shifts. The averaging operation may be able to offer, in general, an improvement in the signal-to-noise ratio of the condition indicators.

5.6. Noise calibration for the simulations of gearbox vibration

5.6.1. Justification of the need for noise calibration

5.6.1.1. Explanation of the procedure followed to show the importance of noise calibration

With the developments of sections 5.2 through 5.5, above, we are now in a position to utilize the vibration model of a planetary gearbox to generate an initial set of simulated vibration signals. However, as described in section 5.2.4, before data from the vibration model can be used to characterize the gearbox experiments, noise calibration of the simulation architecture must be performed. To show why noise calibration is important, and how it can be done, we will now implement the model-based diagnostic technique of Figure 5.3 to generate simulated vibration signals of the planetary gear assembly of the helicopter's main transmission for different carrier-plate crack lengths and different values of operating torque. The simulated signals will be processed to

provide three examples that should justify the importance of noise calibration. In the three examples, we would have liked to follow the next procedure:

1) Run an experiment with a healthy gearbox and extract vibration data.
2) Extract model parameters from the experimental data of the healthy gearbox.
3) Induce a fault (crack) in the gearbox to and measure vibration.
4) Simulate the same fault with the model, still using the parameters of the healthy gearbox, and generate simulated vibration.
5) Compare the characteristics of the vibrations of steps (3) and (4), i.e., between the model of a faulted gearbox and a faulted gearbox.

Unfortunately, we do not have experimental data that were obtained at both healthy and faulty states from the same gearbox, as the above procedure requires. The experimental data that we have is either (1) healthy from one gearbox and faulty from different gearboxes, or (2) all from a faulty gearbox with a growing crack. Therefore, we need a way to make a reasonable comparison of simulated vibration with experimental vibration, for which we have two options.

On the one hand, we can use a healthy gearbox to obtain model parameters, then simulate a fault with the model and finally compare the vibration characteristics of the simulation with experimental data from a faulted gearbox. This procedure will be used by the first and third or our examples. On the other hand, we can use the same gearbox to extract model parameters and make vibration comparisons, but the model parameters are not extracted from a healthy (zero crack length) gearbox. Instead, the model parameters

are extracted from vibration data with the shortest possible crack length. Simulations of a longer crack in the model are then compared to vibration data corresponding to this longer crack length. This procedure will be used by the second of our examples.

The first two of our examples will shown the effect of noise on vibration spectra, particularly on the amplitude of non-dominant sidebands. The focus is on non-dominant sidebands because noise and sideband magnitude variability tend to increase noticeably their magnitude, as explained in section 5.5.2. This increase is beyond that caused by planet shifting. In the third and last of our examples, representative feature values will be extracted from the simulated vibration signals using one of the condition indicators or vibratory features previously presented in section 5.5. The characteristics of the three examples used are summarized in Table 5.5.

Table 5.5. Characteristics of the examples used to show that adding noise to the gearbox vibration model improves the replication of vibration characteristics of experimental data

Example characteristics	Example 1	Example 2	Example 3
Tool used for comparisons	non-dominant sidebands	non-dominant sidebands	feature values
Healthy (zero crack length) gearbox used to extract model parameters	yes	no	yes
Same gearbox used for deriving model parameters is used for comparison to experimental data	no	yes	no
Scaling of sidebands required to make valid comparisons	yes	no	no (relative features used)
Crack length of gearbox used to extract model parameters (inches)	0	1.34	0
Crack length at which comparisons take place between the model and experiment (inches)	2	2	1.34 to 7.7 aprox. (growing crack)
Comparison results shown in	Figure 5.33	Figure 5.34	Figure 5.34

5.6.1.2. Example 1, using non-dominant sidebands

Figure 5.33 shows three different superimposed spectra. The first spectrum is that of experimental vibration data corresponding to the helicopter gearbox with a crack of about 2 inches in the carrier plate. The second spectrum corresponds to the sidebands from the vibration model, corresponding to a healthy carrier plate at 40% of nominal torque. Here, no crack is simulated, and the α_n and β_m parameters used in the model have been extracted from experimental data corresponding to a healthy transmission, but at 50% of nominal torque, because healthy system data at 40% were not available. We are assuming that the effect of the difference in torque is small enough to be negligible. The third spectrum corresponds to the vibration characterization proposed by the model when a 2-inch crack is present in the carrier plate. This characterization is derived from the healthy model but adding the planet-gear shifts caused by the 2-inch crack, as determined from finite element analysis.

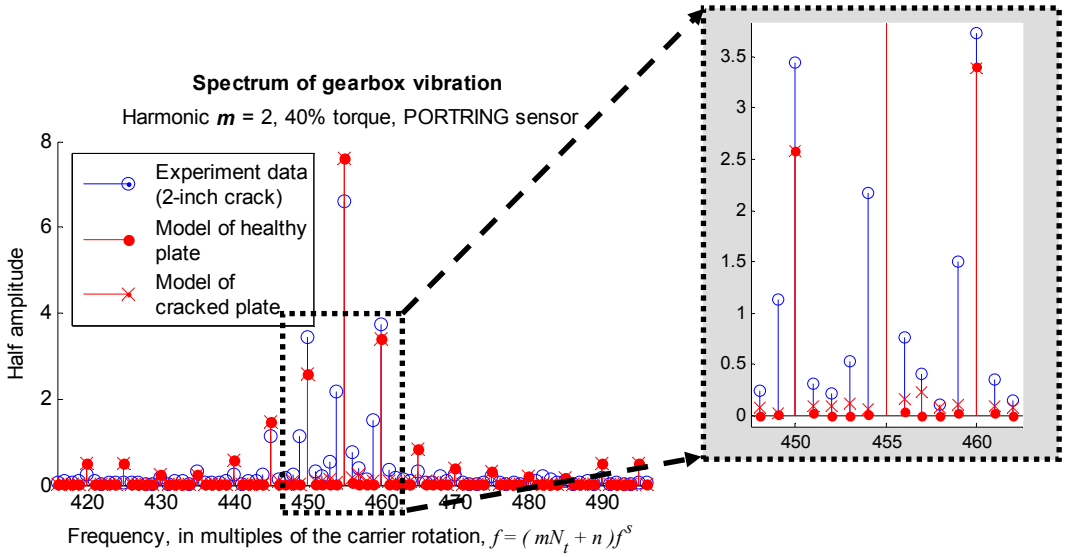

Figure 5.33. Illustration of the difference in the levels of non-dominant sidebands between a noiseless model and experimental data. Model parameters were extracted from a different system than the one providing the experimental data shown. Thus, the model spectra have been scaled to match the RMS of the experimental spectrum

The experiment-data spectrum of Figure 5.33 corresponds to vibration data obtained from the experiment with a growing crack, but the vibration data used to derive the model parameters is from an experiment without a crack, which involves a different system setup. Data from two different setups had to be used in this example because the experiment with a growing crack did not provide vibration data of a healthy (zero crack length) carrier plate (refer to Table 5.5). The two setups provided data with different amplitude scales in the vibration signals. Therefore, to show comparable spectra in the figure, the two spectra corresponding to the model had to be scaled to match the sideband levels observed in the spectrum of the growing-crack experiment. The scaling factor used is the ratio of the RMS of the frequency response coefficients shown.

5.6.1.3. Example 2, using non-dominant sidebands

Figure 5.34 shows spectra without the sideband-scaling artifact that was needed in Figure 5.33. For Figure 5.34, the same system provided the data for the experiment spectrum shown and for deriving the model parameters used in the two model spectra of the graph. However, the system was run starting with a 1.3-inch crack, so we have no "healthy" vibration reference. Nevertheless, we are assuming that the 1.3-inch crack is small enough to allow the system to behave as if it had no crack, and the model parameters used in the model spectra are derived from data corresponding to this crack length. The experiment spectrum corresponds to a 2-inch crack.

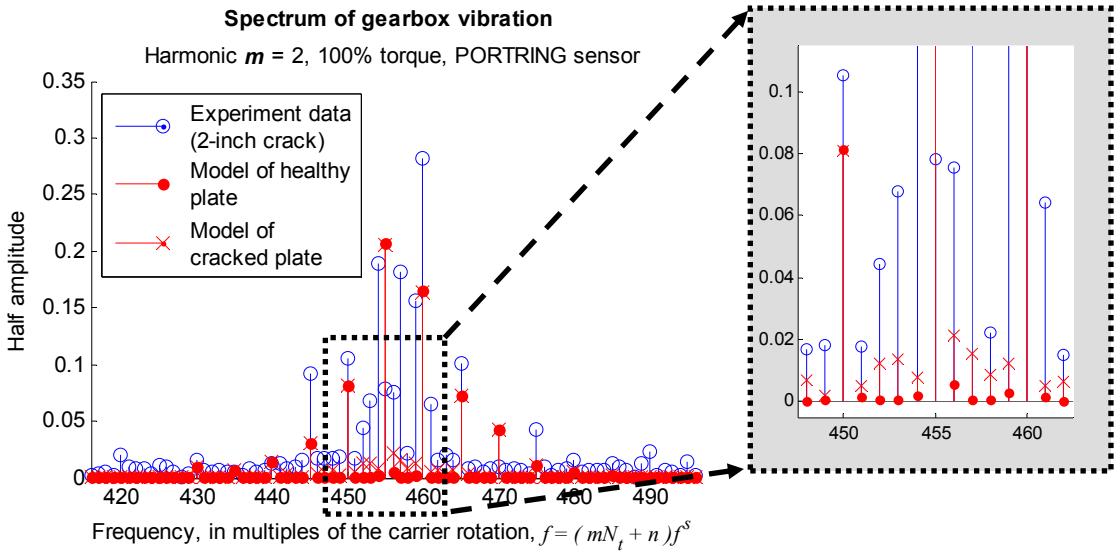

Figure 5.34. Illustration of the difference in the levels of non-dominant sidebands between a noiseless model and experimental data. Model parameters were extracted from the same system than the one providing the experimental data shown. However, the model parameters were extracted from data corresponding to a shorter crack length (1.34 inches) in an attempt to approximate the behavior of the system without the crack

5.6.1.4. Example 3, using feature values

Figure 5.33 and Figure 5.34, above, showed that, when the planet-gear shift angles are input to the vibration model, and before noise is added, the model is not able to show non-dominant sidebands with magnitudes comparable to those observed in experimental data. We attribute this deficiency to the lack of noise in the simulated vibration signal, thus suggesting that noise must be added modeled vibration signals to replicate better the experimental vibration. The need to add noise is now made more evident through Figure 5.35, below, by using feature values. Here, we see that the feature curve for the noiseless model is quite different from that of the experimental data. When "appropriate" levels of noise (discussed in the next section) are added to the model, the model feature curve approximates the experiment feature curve much closer.

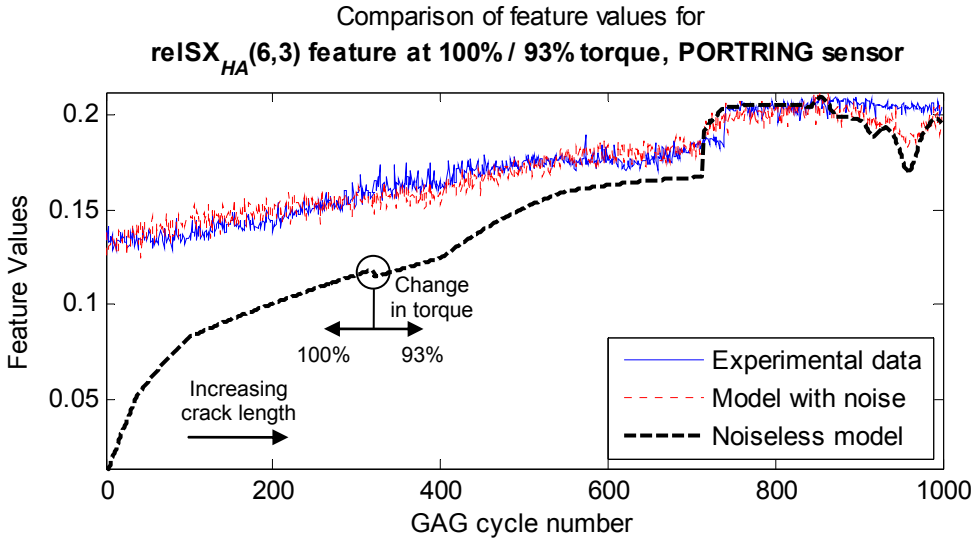

Figure 5.35. Illustration of the effect of noise in the feature values calculated from simulated vibration signals of the helicopter planetary gearbox. Observe how, when noise is added to the model vibration, the model feature values approximate the features values observed in experimental vibration data

5.6.2. Two variants of a possible technique for calibrating the noise levels

In this section, we discuss two techniques with which an appropriate level of noise might be added to modeled vibration signals. It is worthwhile to note that these techniques are rather simple, and more advanced options are available. For example, the application of a more advanced technique for characterizing noise in the planetary gear transmission is treated by Zhang et al. (2007, to appear).

We consider the addition of noise to the model vibration in the frequency domain. We believe the complexity of the mechanical system is sufficient to require the consideration of noise in different frequency bands. Furthermore, the gearbox vibration simulation has been designed to model spectrum sidebands, and it is reasonable to focus on how the noise affects them, as discussed in section 5.5.2.

To simulate noise, we can add a random variation to the sideband magnitudes. Thus, we generate values for random variables that can be characterized with normal probability distributions. The normal distribution is selected because of empirical considerations. The random variables describe our simulated noise, and their values are added to the sidebands of the noiseless simulated vibration to generate noisy simulated vibration. Thus, individual sidebands are modified with individual random values. This can be expressed as

$$SB_{m,n}^{\text{noisy}} = \left| SB_{m,n}^{\text{noiseless}} + \eta \right|, \tag{5.23}$$

where each $SB_{m,n}$ represent the half amplitude (a real value) of sideband (m, n), and η is a normally distributed random variable with mean μ and variance σ^2, i.e.,

$$\eta \sim (\mu, \sigma^2) . \tag{5.24}$$

To calibrate the noise levels in the sidebands we adjust the parameters of the distributions corresponding to individual random variables used with individual sidebands. The parameters are chosen depending on how well feature values from the model approximate feature values of the experimental data. However, we are wary not to over-fit the model, because this would nullify the model validation process. To validate the model, we want to calibrate the noise at specific, "reference" operating conditions and see if the model is able to replicate changes in the gearbox vibration when operating conditions of the system change. We assume that the noise we are characterizing remains unchanged, because changes in the system behavior are characterized by the model, not by the noise.

Since we will be validating the model by comparing feature values of the model against feature values of data from the crack-length progression experiment, as will be seen in section 5.7, we will calibrate the noise levels observing their effect on feature values. There are many ways to characterize the parameters of the noise distribution described. We test two variants here.

In the first noise-calibration variant, we characterize the noise as a normal distribution with zero mean affecting all the sidebands in a tooth meshing harmonic region equally. Our selected reference operating conditions in this variant come from the short vibration experiment with a healthy planetary carrier plate.

The second noise-calibration variant characterizes the noise as a series of normal distributions with non-zero mean affecting sidebands individually. Our selected reference operating conditions for this variant come from the initial part of the crack-progression experiment (initial 15 GAG cycles). Although the gearbox already has a crack, its behavior in the initial part of the experiment is assumed comparable to that of a gearbox without a crack. This assumption is reasonable because the crack is short.

5.6.2.1. Noise-calibration variant 1

In this subsection, we characterize gearbox vibration noise as a normal distribution with zero-mean affecting all the sidebands in a tooth meshing harmonic region equally. To arrive at the characterization of this distribution and test the approach, we use data from the short vibration experiments with a healthy planetary carrier plate. We appoint these data as a description of our reference operating conditions.

Following the nomenclature of Equations 5.23 and 5.24, the addition of noise to the model sidebands is done as

$$SB_{m,n}^{\text{noisy}} = \left| SB_{m,n}^{\text{noiseless}} + \eta_m \right|, \tag{5.25}$$

where

$$\eta_m \sim (0, \sigma_m^2), \tag{5.26}$$

and σ_m^2 is the variance that is added to simulated sidebands within a tooth meshing harmonic region m. The same value of variance is used in all the sidebands that have a common m value.

The value of the variance σ_m^2 is selected so that feature values calculated from the spectrum of the simulated gearbox vibration approximate the corresponding feature values extracted from experimental gearbox vibration. The procedure is illustrated in Figure 5.36.

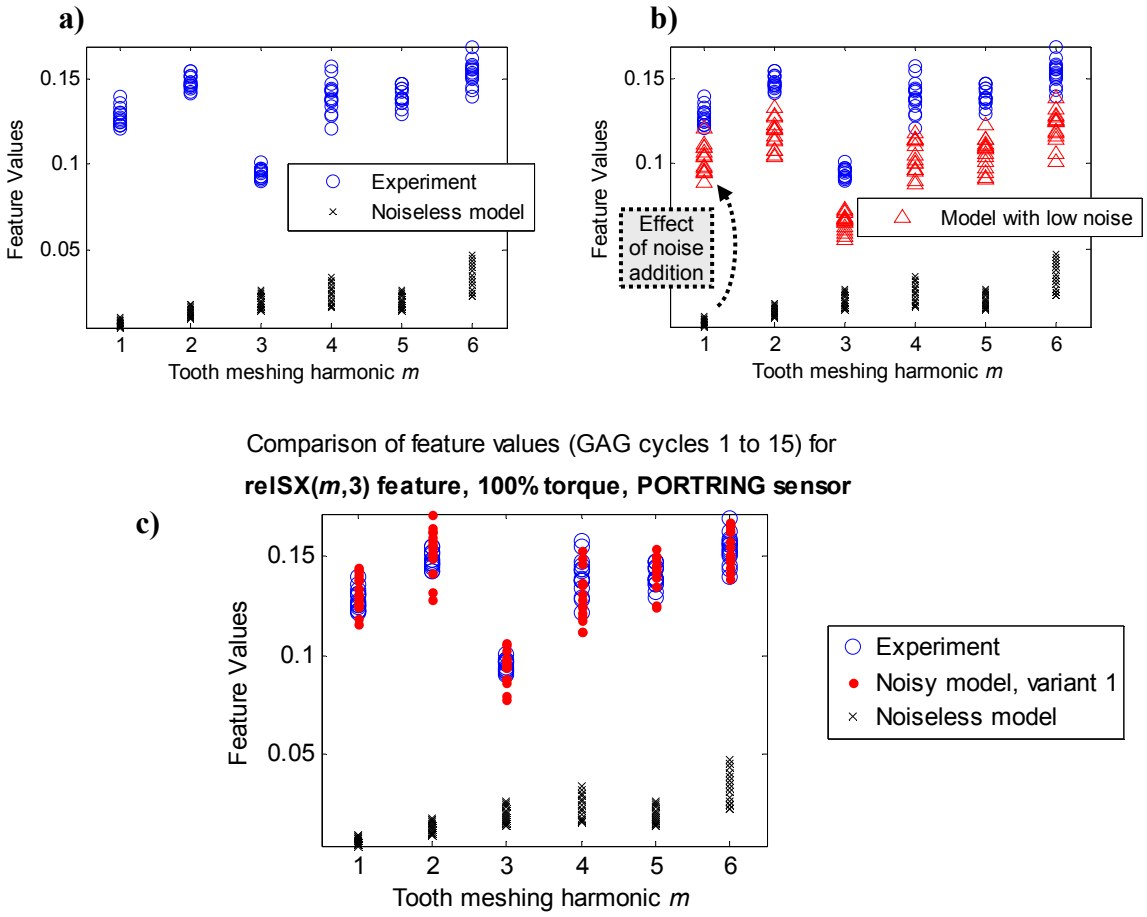

Figure 5.36. Illustration of the procedure followed to perform calibration of the noise levels in modeled gearbox vibration sidebands. a) The noiseless model feature values are calculated and compared to the experiment's features. b) Noise levels (σ_m^2) added to the sidebands of the simulated vibration spectrum are gradually increased; this raises the feature values. c) When appropriate noise levels are reached, the feature values of the model are comparable to the feature values of the experiment; results of noise calibration using the calibration procedure variant number 1 at 100% of nominal engine torque are shown

Figure 5.36(c) shows the results of performing noise calibration under the procedure discussed above at 100% of engine torque. Figure 5.37 shows the corresponding results at 40% engine torque.

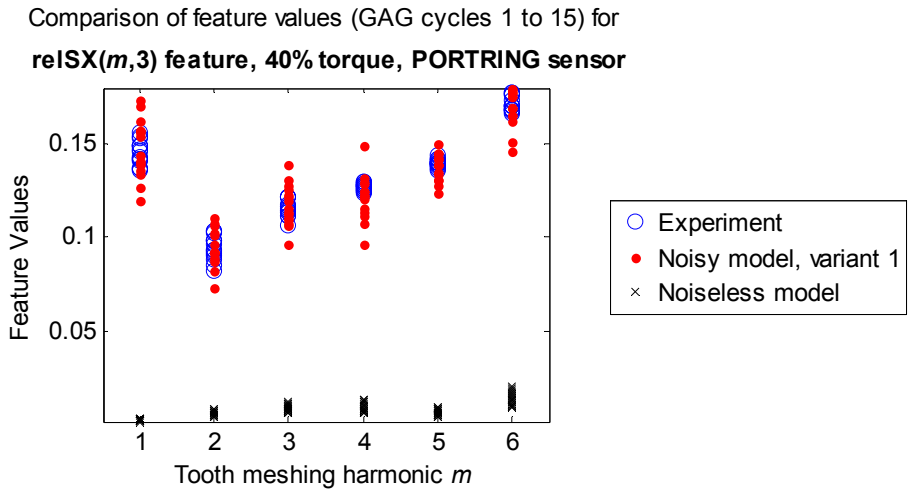

Figure 5.37. Results of noise calibration using the calibration procedure variant number 1 at 40% of nominal engine torque

5.6.2.2. Noise-calibration variant 2

In this subsection, we characterize gearbox vibration noise as a series of normal distributions with non-zero means, each affecting an individual sideband of the gearbox vibration spectrum. To arrive at the characterization of this distribution and test the approach, we use data from the initial part of the crack-progression experiment (initial 15 GAG cycles), which, although having a crack, is assumed to behave as a system without a crack. This assumption is reasonable because the crack is short. We appoint these data as a description of our reference operating conditions.

Following the nomenclature of Equations 5.23 and 5.24, the addition of noise to the model sidebands is done as

$$SB_{m,n}^{\text{noisy}} = \left| SB_{m,n}^{\text{noiseless}} + \eta_{m,n} \right|, \tag{5.27}$$

where

$$\eta_{m,n} \sim (\mu_{m,n}, \sigma_{m,n}^2); \tag{5.28}$$

$\mu_{m,n}$ is the mean of the distribution of the random variable $\eta_{m,n}$ and is approximately equal to the mean value of $SB_{m,n}^{\text{experim}}$ in noisy experimental gearbox vibration from the reference operating conditions; and $\sigma_{m,n}^2$ is the variance of $\eta_{m,n}$ and is approximately equal to the variance of $SB_{m,n}^{\text{experim}}$.

Individual values of $\eta_{m,n}$ with their own individual distributions are added to simulated sidebands at particular (m, n) locations. Thus, each of the $SB_{m,n}^{\text{noiseless}}$ sidebands is affected by its unique $\mu_{m,n}$ and $\sigma_{m,n}^2$ parameters. The values of the mean $\mu_{m,n}$ and the variance $\sigma_{m,n}^2$ are selected so that feature values calculated from the spectrum of the simulated gearbox vibration approximate the corresponding feature values of experimental gearbox vibration. Figure 5.36 shows the results of performing noise calibration under the procedure discussed in this section at 100% of engine torque. Figure 5.37 shows the corresponding results at 40% engine torque. We are thus treating the noise parameters as torque-dependent.

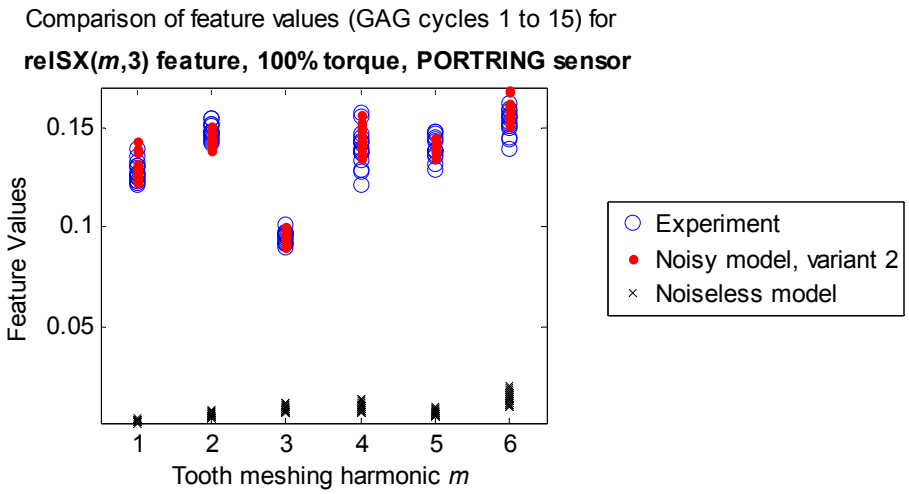

Figure 5.38. Results of noise calibration using the calibration procedure variant number 2 at 100% of nominal engine torque

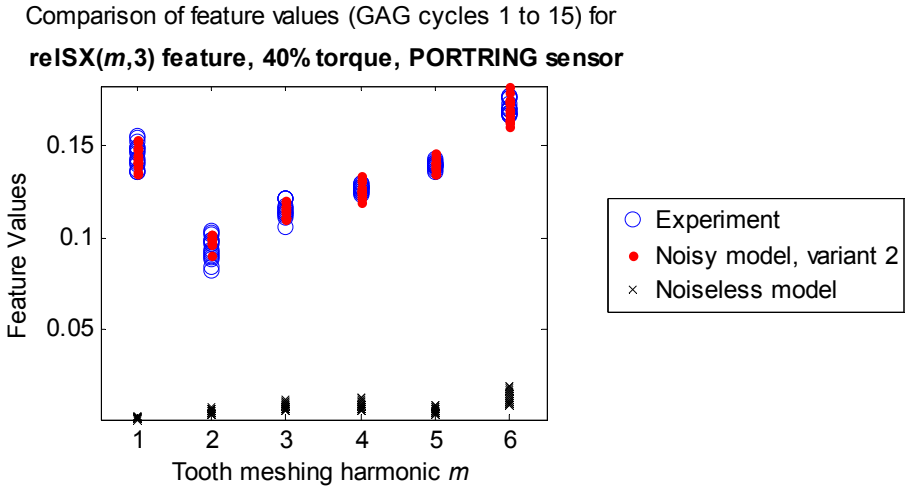

Figure 5.39. Results of noise calibration using the calibration procedure variant number 2 at 40% of nominal engine torque

5.7. Validation and performance of the vibration model

The vibration model of the planetary gearbox discussed in section 5.2 is able to incorporate the results of the frequency response analysis of section 5.3 (fault-insensitive parameters) and the planet-gear shift angles obtained from the finite element simulations

of section 5.4 (fault-sensitive parameters). The model can generate a simulated vibration signal that is similar in certain characteristics to the vibration observed in the planetary gear assembly of the helicopter's main transmission. Simulated vibration signals can be generated for different crack lengths present in the carrier plate, and for a variety of values of the operating torque. Representative feature values can be extracted from both a simulated vibration signal and the experimental vibration signal of an actual gearbox. The feature values can be calculated using the condition indicators presented in section 5.5.

The intent in this section is to validate the comprehensive implementation of the vibration model as described in the paragraph above. We validate the vibration model of planetary gearboxes using one of two sets of experimental data (refer to section 3.2). First, we use data either from the short vibration test with a healthy planetary carrier plate or from the initial part of the experiment with a growing crack, to determine the values of the fault-insensitive parameters for the model. The choice of data depends on which of the two noise-calibration variants presented in section 5.6.2 is used. Then, we consider data from the crack-length progression test to compare the model vibration to the experimental vibration at different crack lengths. This particular experiment is well suited to validate the simulated vibration because it provides a series of points to make comparisons.

It is possible to utilize the two different experiments for a single set of simulations with the model because both experiments had a similar setup, as they were both carried out in a test cell with the same gearbox configuration. We also exploit the abilities of the

“relative” features presented in section 5.5.3, since they have been designed precisely in an attempt to mitigate the effects of system-to-system, or setup-to-setup variations.

Figure 5.40 through Figure 5.47, below, illustrate the effectiveness of the planetary gearbox vibration model. Results presented in the graphs involve the implementation of the model with the fault-insensitive parameters discussed in section 5.3, the fault-sensitive parameters presented in section 5.4, and the noise calibration procedure described in section 5.6.

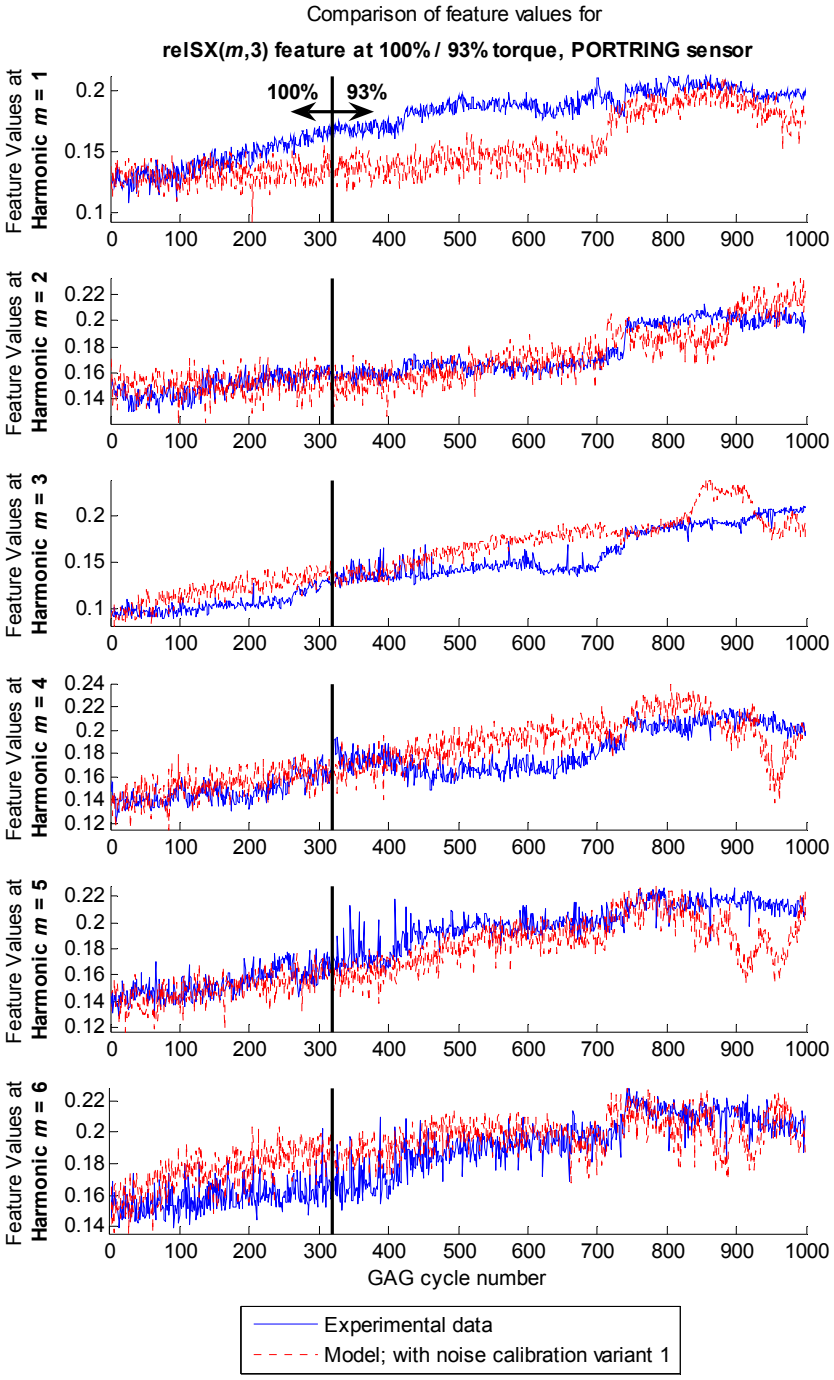

Figure 5.40. Comparison of feature values extracted from the helicopter transmission vibration and features extracted from the vibration produced by simulations with the planetary gear vibration model. The horizontal axis corresponds to the count of load cycles and is related to the crack growth in time. The model uses the noise-calibration procedure variant number 1. Torque is 100% or 93% (as indicated)

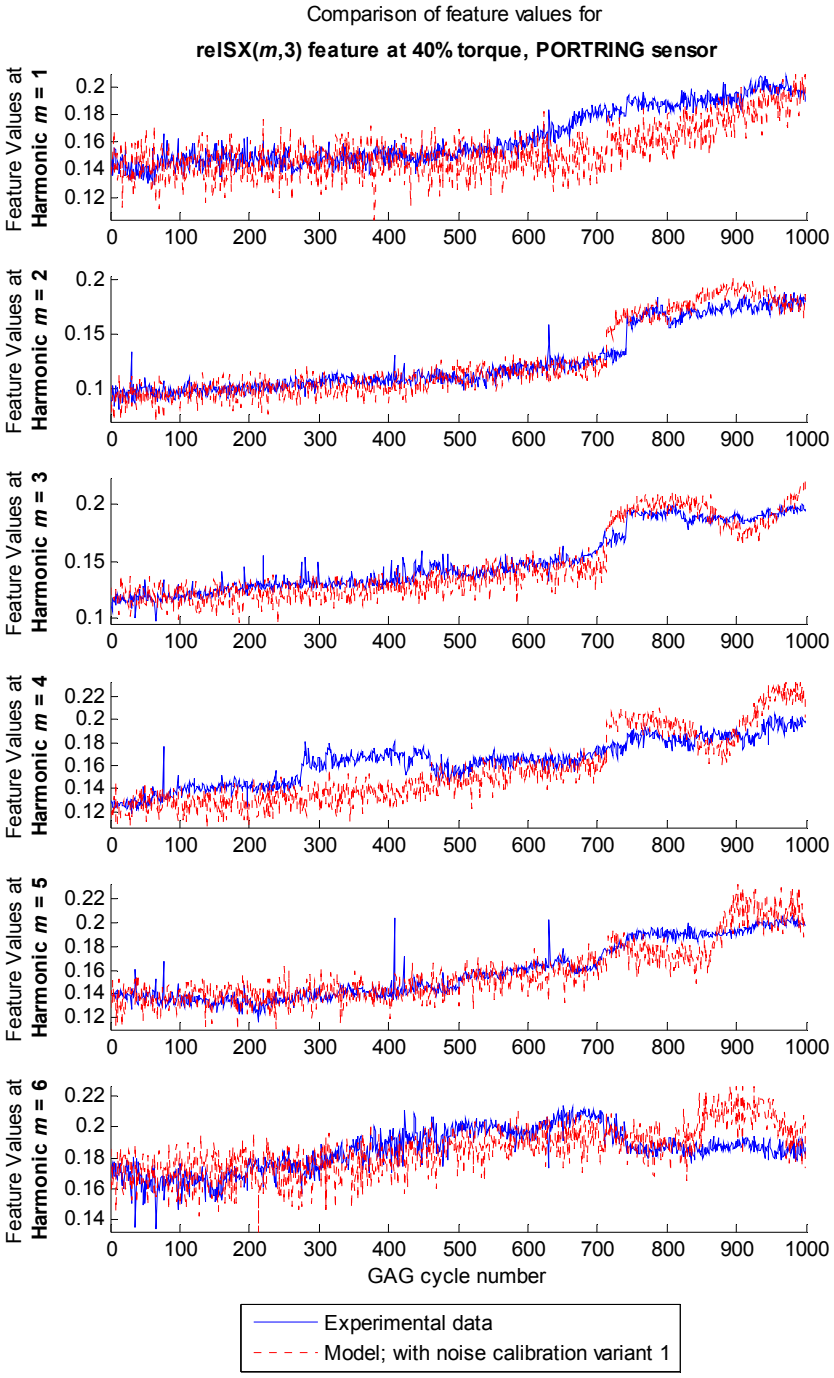

Figure 5.41. Comparison of feature values extracted from the helicopter transmission vibration and features extracted from the vibration produced by simulations with the planetary gear vibration model. The horizontal axis corresponds to the count of load cycles and is related to the crack growth in time. The model uses the noise-calibration procedure variant number 1. Torque is 40%

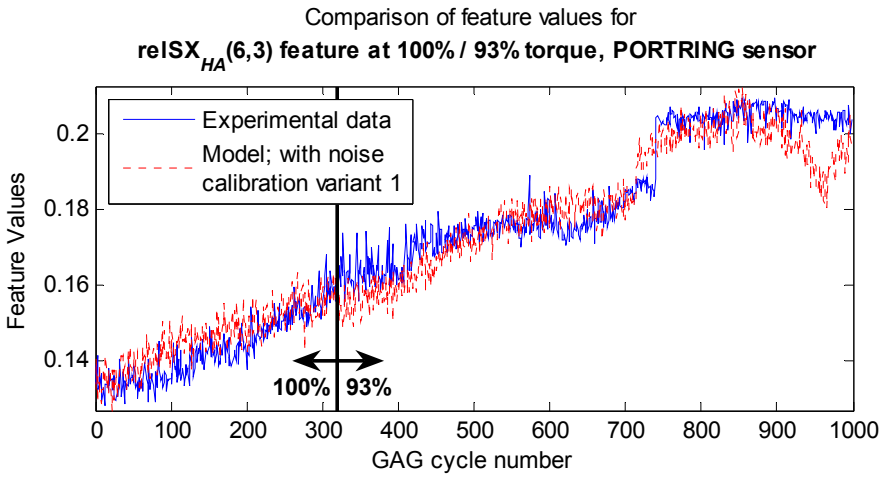

Figure 5.42. Comparison of values for the feature of Figure 5.40 in its harmonically averaged form

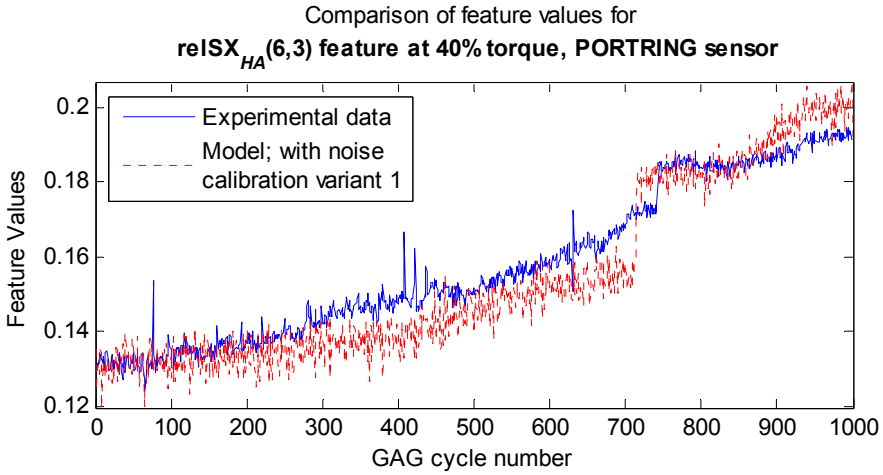

Figure 5.43. Comparison of values for the feature of Figure 5.41 in its harmonically averaged form

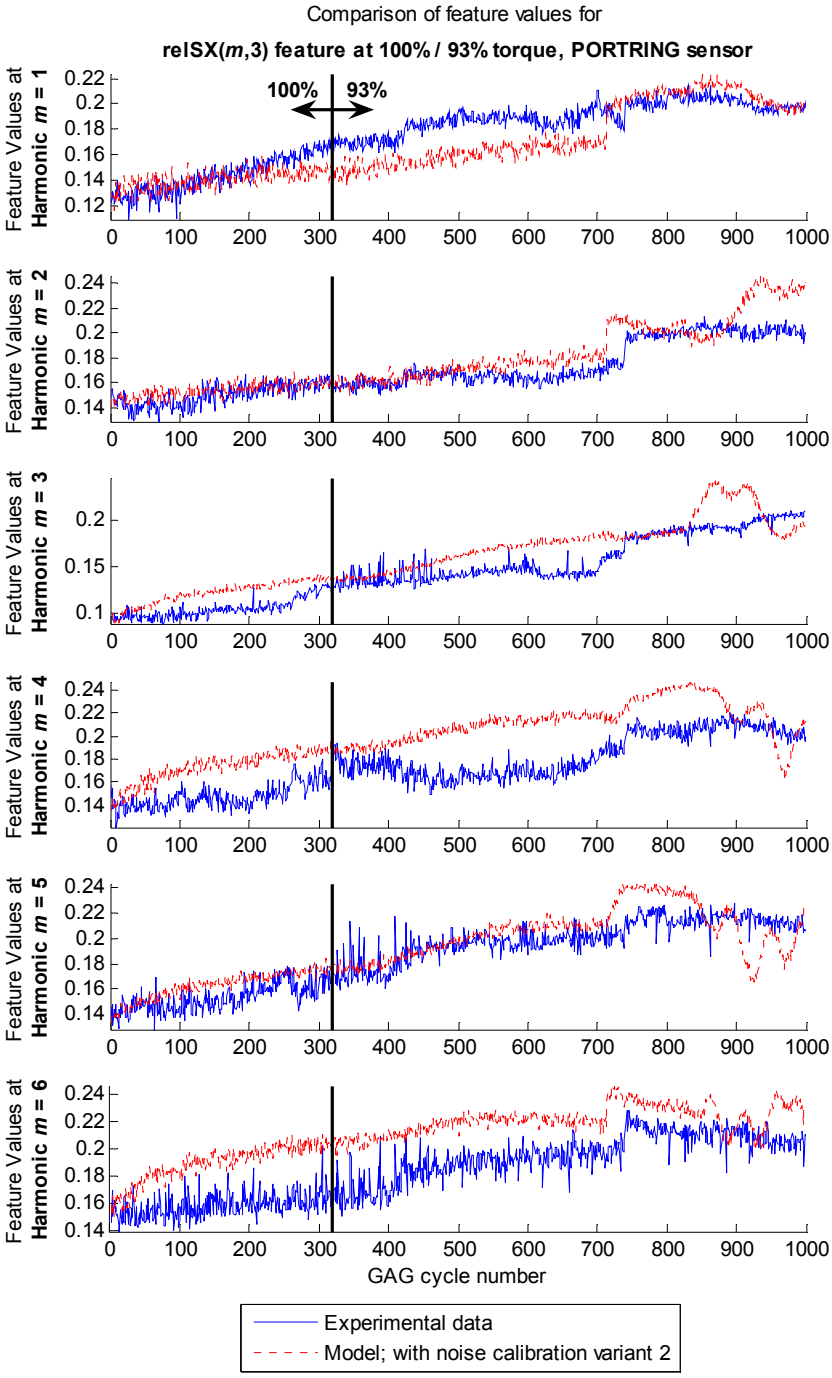

Figure 5.44. Comparison of feature values extracted from the helicopter transmission vibration and features extracted from the vibration produced by simulations with the planetary gear vibration model. The horizontal axis corresponds to the count of load cycles and is related to the crack growth in time. The model uses the noise-calibration procedure variant number 2. Torque is 100% or 93% (as indicated)

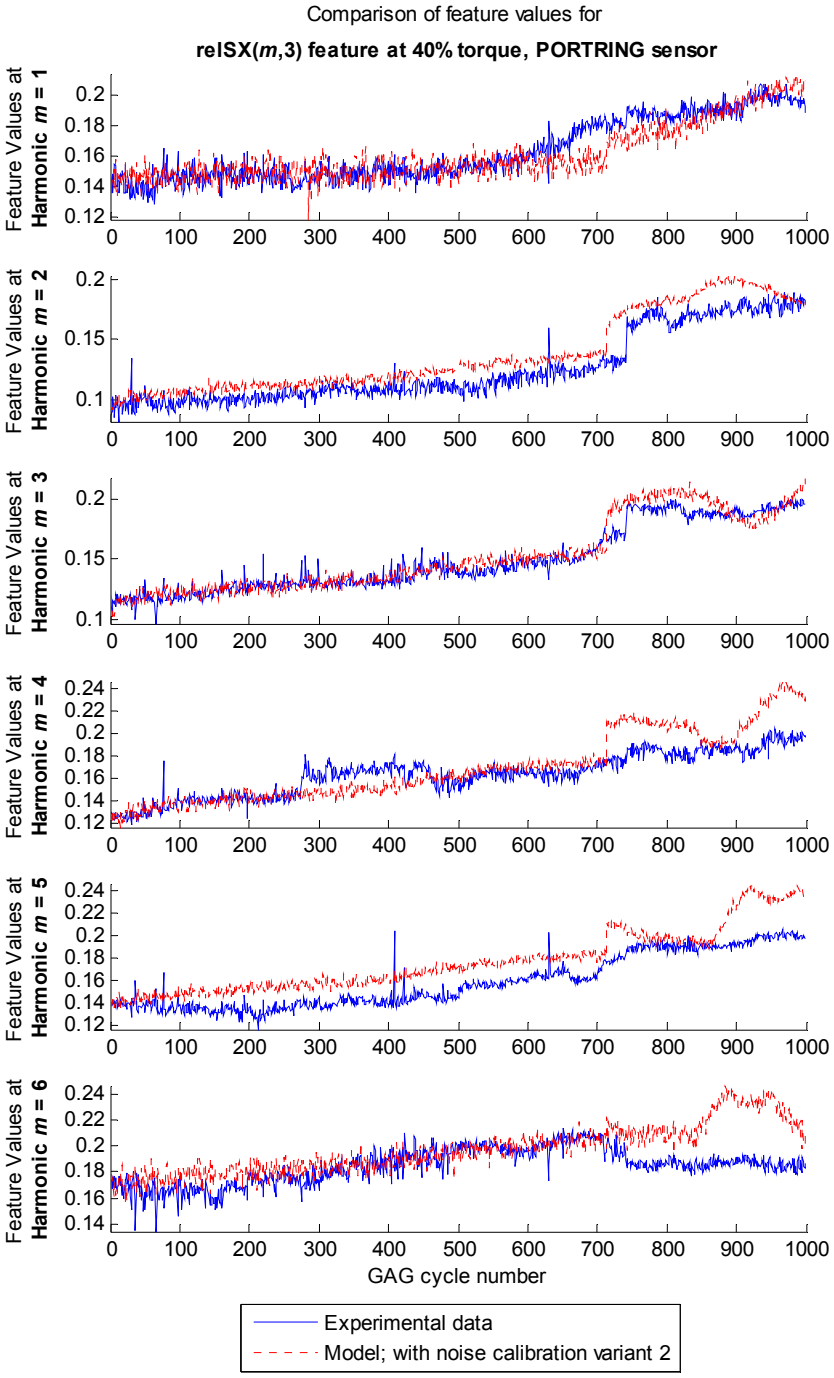

Figure 5.45. Comparison of feature values extracted from the helicopter transmission vibration and features extracted from the vibration produced by simulations with the planetary gear vibration model. The horizontal axis corresponds to the count of load cycles and is related to the crack growth in time. The model uses the noise-calibration procedure variant number 2. Torque is 40%

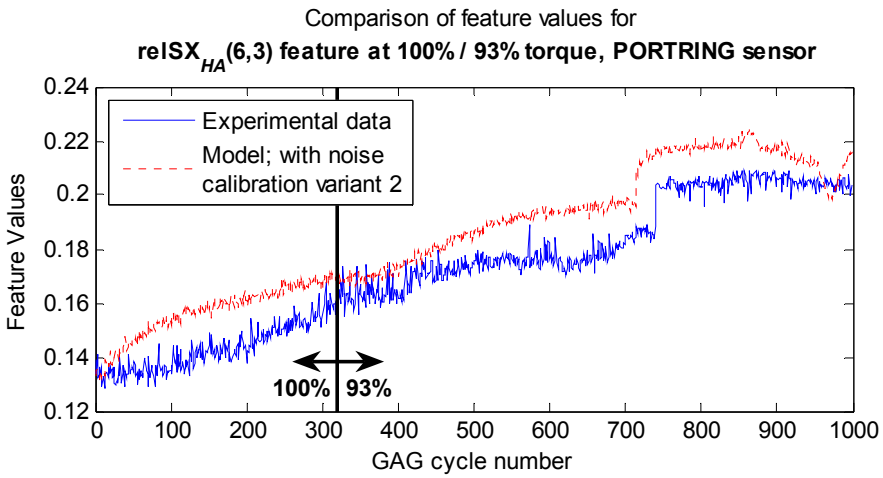

Figure 5.46. Comparison of values for the feature of Figure 5.44 in its harmonically averaged form

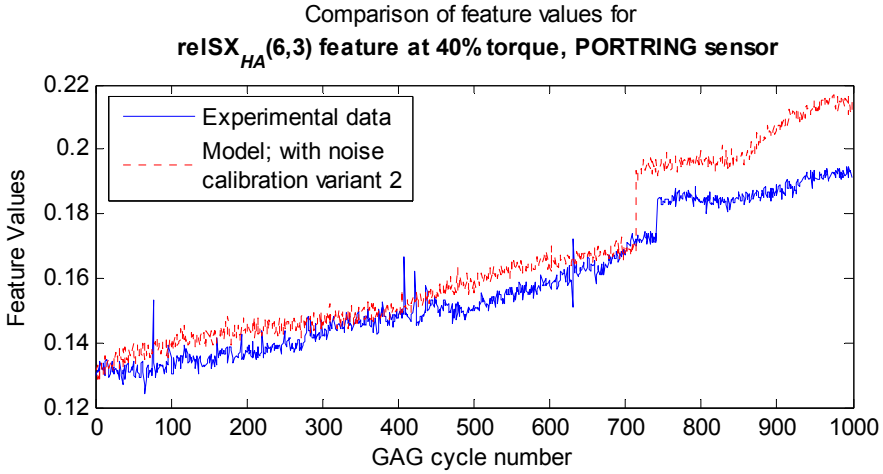

Figure 5.47. Comparison of values for the feature of Figure 5.45 in its harmonically averaged form

Obviously, to obtain the results presented, a series of simulations was run with the model, each instance corresponding to a specific crack length comparable to the crack length present in the gearbox at a given GAG cycle number, i.e., the model used the lengths of the crack as measured from the experiment. As explained in section 3.4.5.2, the crack lengths in the crack-progression experiment are known at different GAG cycles

from related instrumentation (ground truth points). Before features were extracted, the experimental vibration data were pre-processed by applying time synchronous averaging, or TSA (refer to section 3.4.5). Vibration of about 21 or 22 revolutions (depending on the availability of experimental data) of the planetary carrier plate was averaged at each GAG cycle.

Two important observations must be made about the results presented in the graphs within this section. First, the fault-insensitive parameters used in the model with the noise-calibration procedure variant number 1, correspond to a different experiment than the one being characterized. The parameters were obtained from a healthy gearbox, while the characterizations seen in Figure 5.40 through Figure 5.43 address the crack progression test. Second, noise calibration of the vibration simulations for Figure 5.40 through Figure 5.47 was performed by comparing the level and dispersion of the feature values within the span of only the first 15 GAG cycles. After this, no other form of calibration, or any model adaptation was performed.

Validation of the planetary gearbox vibration model is primarily given by the results presented in the graphs within this section. However, validation is also enhanced by the fact that, even in the presence of the two observations described in the preceding paragraph, the characterizations of the model appear to be quite adequate and repeatable, even for a mechanical system of such complexity as the helicopter transmission gearbox.

5.8. Application of the reverse engineering technique for identifying a crack in the helicopter transmission

It has been shown that the diagnosis model allows us to calculate the vibration feature values that a helicopter gearbox will exhibit when a crack is present in the planetary carrier plate. This calculation is able to consider a specific crack length and the torque at which the gearbox operates. We now discuss how we can use the model to diagnose a helicopter gearbox with such a crack.

To find whether a helicopter gearbox has a crack present or not (i.e., to perform fault *detection*), we use standard detection techniques that check on the statistical separation[16] of two sets of data: feature values extracted from the vibration of the helicopter gearbox to diagnose, and feature values descriptive of normal operating conditions. This is the first step in diagnosis.

The following step in diagnosing the gearbox is the *identification* of the fault, i.e., assessing the length of the crack. This is where the ability of the vibration model to produce feature values for different crack lengths is crucial. We exploit this ability by comparing the feature values extracted from the helicopter gearbox at fault against the feature values of model simulations with different crack lengths. Finding a match between the gearbox and one of the model simulations will provide information about the crack length present in the gearbox. This procedure is the reverse engineering technique

[16] Detection and feature separation techniques are beyond the particular subject of interest in this thesis. Literature on the subject is abundant. For a good modern summary refer to Vachtsevanos et al. (2006).

covered in section 4.2.2. To diagnose the helicopter gearbox, we adapt the reverse engineering technique presented earlier in Figure 4.3 as illustrated in Figure 5.48, below.

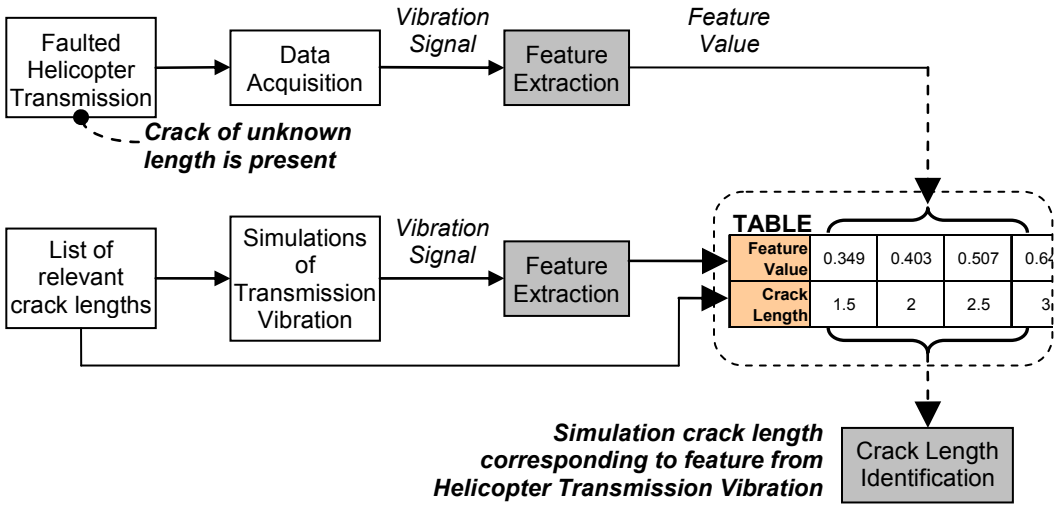

Figure 5.48. Application of the "reverse engineering" approach for performing model-based fault diagnostics with the helicopter transmission problem

An example of how to apply this technique is the following. We obtained vibration signals from the planetary gearbox experiment with a growing crack. We extracted features from it, and Figure 5.42 in section 5.7 showed what one of those particular features looks like. The figure also showed the corresponding feature values from the vibration model. If we wanted to perform fault identification with those feature values exclusively, we would try to match the feature values of the gearbox to the feature values of the model to arrive at an estimate of the crack length. Using the same data of that figure, we now plot the feature values of the model against crack lengths, as shown in Figure 5.49. We can approximate the crack length present in the gearbox from

matching the gearbox feature values to the model feature values and determining the crack length from the model.

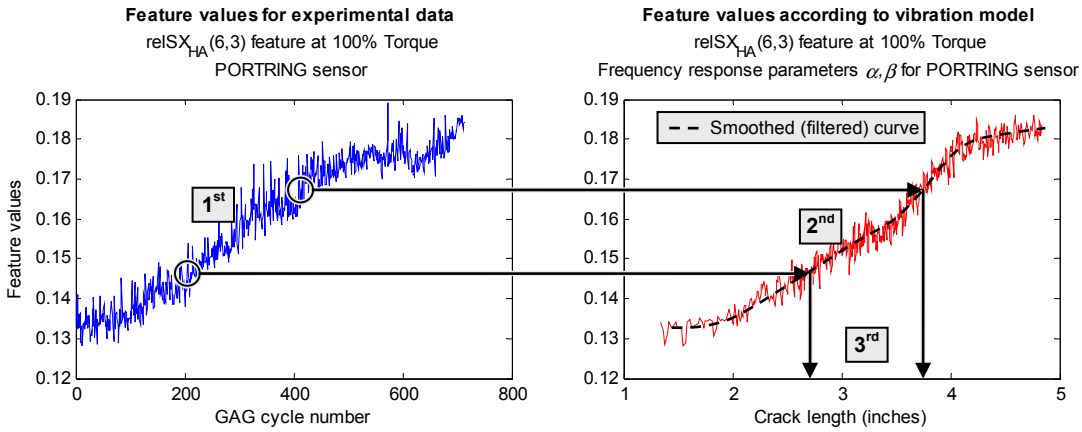

Figure 5.49. Illustration of the procedure followed to match experimental feature values to model feature data to perform crack length identification; first, feature values in the experiment are assessed; second, comparative feature values are sought in the model data; third, crack length in the experiment is assessed by the corresponding crack length in the model. Data seen here corresponds to data from Figure 5.42

Notice, however, that using this technique, there will be a difference between the crack lengths observed in the experiment and those obtained from the characterizations of the model, because the feature values of the model are slightly different from the feature values of the gearbox for known crack sizes. The difference is made obvious when plotting, once again, some data from Figure 5.42 in terms of ground-truth crack lengths instead of cycles. Such plot is shown in Figure 5.50, below. The crack lengths corresponding to the experimental data are known from instrumentation used for measuring the crack progression throughout the experiment. The difference in feature values will obviously affect the quality of our diagnosis.

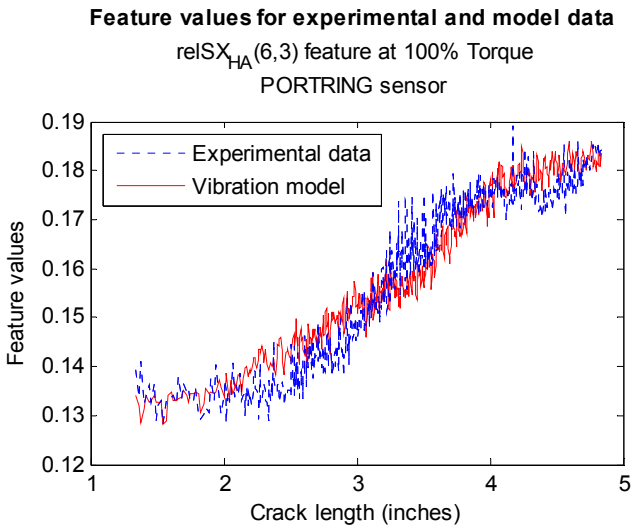

Figure 5.50. Example vibratory feature value data as a function of crack length for experimental data and model data

Thus, in general, we need to qualify and interpret the feature-matching algorithm results for several reasons. First, noise is present, both in the gearbox vibration and in the model. Second, the model is only an *approximation* to the gearbox behaviors. Third, we may want to combine the information from several features.

The implementation of a diagnostic algorithm should consider these elements before providing an estimate of the crack length. We will want such an algorithm to use filtering and, possibly, state estimation techniques to improve matching and arrive at a more confident estimate of the fault. This subject is also relevant for prognosis, so it is further discussed in chapter 6.

6. A MODEL-BASED PROGNOSIS ARCHITECTURE

6.1. Objectives

The goal of this chapter is to suggest a methodology for designing a model-based prognostic architecture that can (1) establish the foundation for performing model-based prognosis in a class of dynamic systems, (2) integrate results from anteceding diagnostic activities, like those presented in chapter 4, and (3) be applied to prognosticate a crack in the planetary carrier plate of a helicopter transmission such as the one described in section 3.1.

As with the diagnostic architecture discussed in chapter 4, the prognostic architecture suggested in the present chapter integrates modeling, simulation, and experimental data. The class of dynamic systems to which it can be applied will fit the descriptions presented in sections 6.2 and 6.3, and the assumptions set forth earlier in section 4.2.1. Focus is still placed on models that characterize the physics-of-failure mechanisms of faulted systems, referred to as *physics-based models* in the engineering diagnostics and prognostics literature. However, the methodology suggested might be applicable to other kinds of models by appropriately adapting its constituent modules.

The architecture is immediately applicable to prognosticate the growth of the crack in the helicopter transmission using a fracture mechanics model. Such application, discussed in detail in chapter 7, will validate and demonstrate the use of the methodology suggested in the present chapter.

6.2. A generic approach to model-based prognosis for a class of dynamic mechanical systems

Figure 6.1 shows a generic method for designing model-based prognostic architectures with focus on systems that require anteceding diagnostic activities. We refer to prognostic activities as those whose objective is to determine the remaining useful life (RUL) or the time to failure (TTF) of damaged components. Furthermore, we take on this topic with interest in applying the understanding of the physics-of-failure mechanisms of a system in the design of the model-based prognostic architecture.

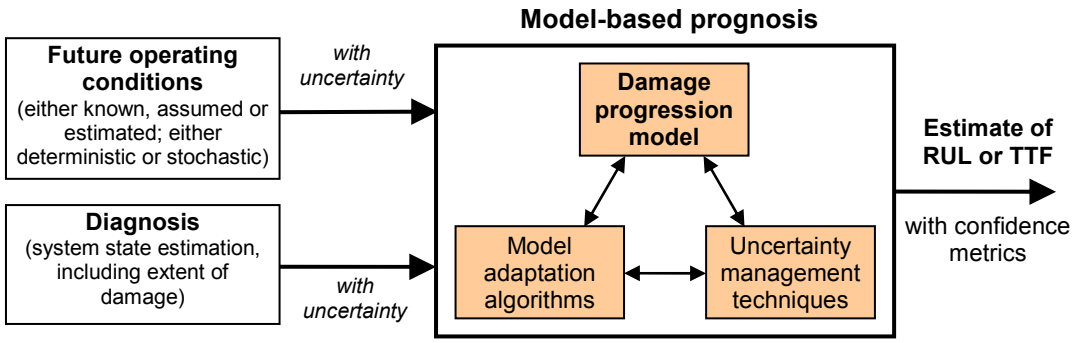

Figure 6.1. A generic approach to model-based prognostics

The method proposed is to provide functionality to the distinct blocks represented in Figure 6.1. Such a modular approach is *applicable to many kinds of systems* and models. Implementing a prognostic architecture with this method in a complex system will typically involve the participation of a team of experts in the different aspects and disciplines involved. That is why, although we will now be describing the basic functions of each block, this thesis does not cover them all in detail. The thesis focuses only on the *diagnosis* and *damage progression model* blocks from a model-based perspective.

The *future operating conditions* block refers to the determination of the expected usage pattern of a system. The way in which damage progresses in a system depends on how the system is used. Hence, to make a prognosis of a system, we need information about the expected usage pattern of a system, which is also referred to as the *loading profile*. The loading profile should be time-series data providing specific information of how and what loads will be successively applied to the system. Depending on the system and type of fault, the order in which varying loads are applied may also be critical information. One of the promises of prognostics is precisely their ability to offer information about how a system will behave under different loading profiles. This is important for system operators because, as they are in control of the loading profile, they can make a decision to change it if it serves a purpose, like extending the life of a system. The subject of loading profiles is discussed further in section 6.3.2.

The *diagnosis* block provides diagnostic functions, such as those provided by the architecture discussed in chapter 4. It must be noted that, although the diagram of Figure 6.1 suggests that diagnostics be performed before prognostics, the method is also applicable to systems that do not require diagnostic updates, such as systems where the life expectancy of a system is used, regardless of any possible diagnosis (see section 6.3.1).

Both the diagnosis and future operation conditions blocks provide information needed by the *model-based prognosis* block. This information is used to assess the future development of damage in the modeled plant or system. To arrive at a prognosis, the

dynamic behavior of the plant and its damage must be simulated. Three different interrelated critical aspects of this simulation are represented inside the block.

The first aspect is a *damage progression model* that characterizes the development of the fault dynamically. One architecture to accomplish this function is presented in section 6.3. To deal with the uncertainty present in the diagnosis and the expected future operating conditions, the damage progression model can simulate multiple scenarios of fault development, each corresponding to a different variant in the uncertain information provided.

The second aspect is the utilization of *model adaptation algorithms*. Adaptation algorithms abound in the literature. Techniques such as these will allow the damage progression model to be dynamically updated to replicate the plant behaviors more accurately. When on-line data is available to update the dynamic models, it is convenient to represent the problem as one of *state estimation*. Several approaches can be applied to solve the state estimation problem. When the system is linear, and the noise present is assumed Gaussian, Kalman filtering gives the optimal solution. Many cases, though, cannot be represented with a linear realization. For these, more complex estimation algorithms need to be used, such as extended Kalman filtering, grid-based methods, and particle filtering (see Arulampalam, 2002). However, this subject is outside the scope of this thesis.

The third aspect is the implementation of *uncertainty management techniques*. These will offer a variety of functions, among which we find:

(1) the adequate interpretation and mitigation of the uncertainty in the diagnosis and operating conditions,

(2) the determination, supervision, and control of the multiple scenarios that the damage progression model simulates,

(3) the execution of state estimation algorithms to support the operation of the damage progression model and the model adaptation algorithms to increase their accuracies, and

(4) the collection and interpretation of the results provided by the multiple-scenario simulations of the damage progression model to provide reliable estimates of the RUL or TTF with *confidence metrics*.

Confidence metrics provide a measurement of the certainty in the results offered by the prognostic algorithm. These metrics will typically exhibit characteristics of the probability distribution describing the chances of failure of the system at a given time or condition.

The subject of uncertainty management is, again, beyond the scope of this thesis. A good overview of the subject is provided by Vachtsevanos et al. (2006) and an application of uncertainty management techniques to the helicopter transmission problem described in chapter 3 is studied by Orchard (to be published).

6.3. The damage progression model

In general, a plant model used in the task of diagnosing a system will not likely be the same as the model used in prognostics. This is because models usually replicate a predetermined set of system characteristics while assuming that others are constant, and the two sets generally differ in diagnoses and prognoses. This assumption allows models to be kept as simple as our tolerances require. Naturally, unnecessary model complexity is avoided, because a model that simulates unneeded and negligible conditions typically requires excessive amounts of work, solution time, and computing power. Additionally, there is the danger of unaccounted-for behaviors, unexplained deviations, and perhaps counter-intuitively, even loss of accuracy, since the expanded set of parameters (away from those of interest) may not be as well known.

Take, for example, the case of the helicopter transmission problem described in chapter 3. The so-called physics-based diagnostic model attempts to reproduce the vibrations corresponding to specific crack lengths on the planetary carrier plate of the transmission, one crack length at a time. Information about the crack growth rate is irrelevant for this model, and the only reason the model requires "time" as an independent variable is because vibration signals are involved, not because damage is progressing. This progression is not considered. In fact, the damage is considered static in every diagnosis simulation using the model. This is a fair and valid assumption as long as the damage progression timescale is different from the vibration timescale, which is the case for the fracture fault considered.

For prognosticating the fault in the helicopter transmission, in contrast, we need a different kind of model. This model must provide information about how the crack length progresses in time. Damage is not static anymore, and vibration changes need not even be considered here, since they are an *a posteriori* effect of the crack length, and not the focus of the progression study, which concerns only *a priori* causes. The prognostic model should be able to simulate the progression of the crack length while considering the degradation of the system and the variations in the loads applied to the gearbox (i.e., its usage patterns). Furthermore, these system conditions, each of which is now referred to as a *state*, may not be accurately known. Even after diagnosing the system, we can only approximate the crack length at any given instant, and the load *to be experienced* by the cracked component will be an estimate too, better expressed stochastically. Both of these states will be most properly described with *probability distributions*. Thus, we may require that our *fault progression model* provide probabilistic results as well.

Thus, in general, a model used in the prognosis of a dynamic system must integrate a damage progression model with information from the diagnosis of the fault, the expected loads to be applied to the system, and the parameters or states describing the system and its changing conditions. Following the train of thought of section 4.2.1, a model with these characteristics may be represented with the block diagram of Figure 6.2.

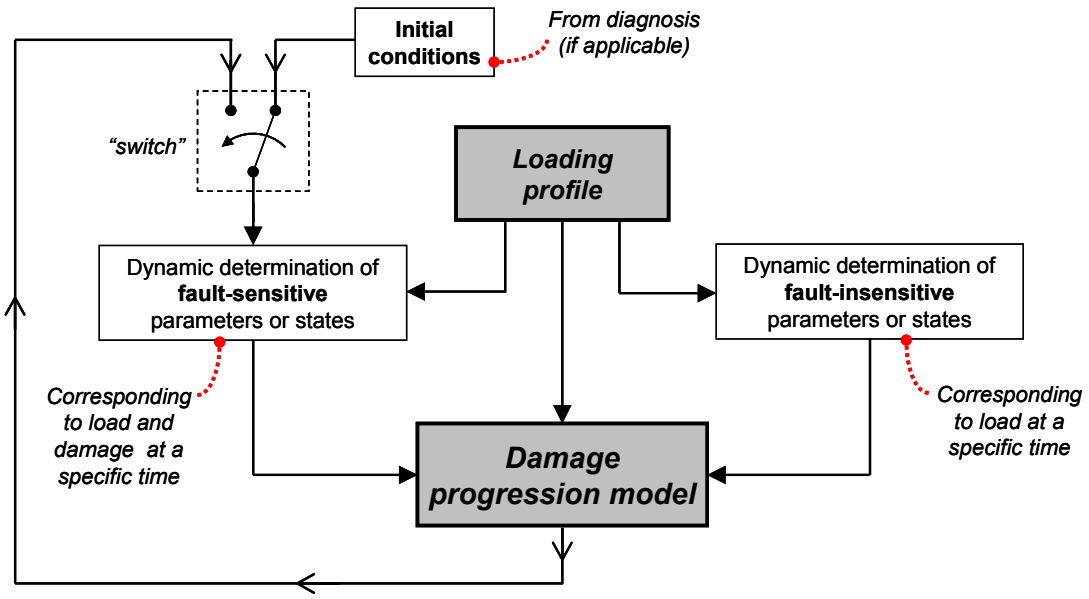

Figure 6.2. Suggested architecture for performing model-based simulation of systems with a dynamic fault

It is illuminating to compare the diagram of Figure 6.2, above, with that of Figure 4.1 presented earlier, in section 4.2.1. The two approaches are similar in several ways. First, they both classify parameters into fault-sensitive or fault-insensitive. The fault-insensitive parameters can be in both cases determined from experimental data, and both architectures provide the ability to consider different operating conditions and loads.

However, in addition to the obvious differences, there are some non-obvious. One of the most important non-obvious differences is that all the blocks in the diagnostic architecture of Figure 4.1 are *static* with respect to the fault. With the exception of the initial conditions, the blocks in the prognostic architecture of Figure 6.2, above, are *dynamic*. By this terminology, we mean that a dynamic realization must consider changes in the fault under some description, which is typically the passing of time, although other descriptions are possible. In contrast, a static description considers an unchanging fault.

One of the important visible differences is that in Figure 6.2 there is now a closed loop connecting the model block with the block of fault-sensitive parameters. The loop is suggestive of the dynamic conditions and the dependence in time of the prognostic architecture.

The simulation architecture proposed here can be applied by following the steps described in sections 6.3.1 through 6.3.5, below.

6.3.1. Initial conditions for the prognostic model: the integration with diagnostics

As stated above, a damage progression simulation is always dynamic, i.e., it is dependent on some description of time. Thus, a pre-requisite for running such a simulation is to establish the initial conditions of the system. Since we are concerned with prognosticating a system failure, our initial conditions must be indicative of either the existence of a fault or, at least, the possibility that the system will degrade in a certain way as damage progresses. An example of the first situation would be an initial crack length in a system that, when used, will experience fracture growth. For the second case, our initial conditions could be the readiness or configuration of a system. For example, we may want to prognosticate the failure of a battery depending of how much charge it had initially, or the failure of a light bulb depending on the alloy used in the filament.

To have the initial conditions indicate the existence of a fault in a working system, we will typically use diagnosis. This is because a diagnostic system will detect, locate and assess the size of an incipient fault, and the size of the fault is the most

important initial condition for prognosticating a system with an incipient fault. Such is the case in the helicopter application studied in this thesis. It is precisely at the stage of initial conditions assessment that the diagnostic and prognostic tasks integrate.

The initial conditions block of the architecture shown in Figure 6.2 is static with respect to the fault. This means that the initial conditions are used at the beginning of a damage progression simulation, and represent only the initial state of the system, not the dynamic behavior of the damage or degradation. This is the reason why a "switch" is illustrated in the diagram. Once the initial conditions are used to determine for the first time the fault-sensitive parameters or states, the position of the switch is changed. The initial conditions are not used anymore, and the dynamics of the modeled fault are used instead.

6.3.2. The loading profile

As discussed in section 6.2, to arrive at a prognosis of a system, we need information about the future usage pattern of a system, also known as the *loading profile*. The ability to vary the loading profile in a damage progression simulation is a desirable characteristic in a prognostic architecture, because it can provide information that aids operators in making decisions when a fault appears on a system. An example of how changes in the load profile can be applied to the architecture suggested by Figure 6.2, above, is illustrated by Figure 6.3, below. The illustration represents the idea that three different possible loading profiles can be simulated separately. These correspond to simulating that (1) the load profile that the system has been experiencing for some time

while operating is to remain; (2) the load profile can be estimated from past experience; and (3) the load profile will be as the operator is deeming and describing before the simulation is started. It should be clear that the three loading profiles could be of interest to an operator in charge of deciding how to continue to operate a system with an incipient fault.

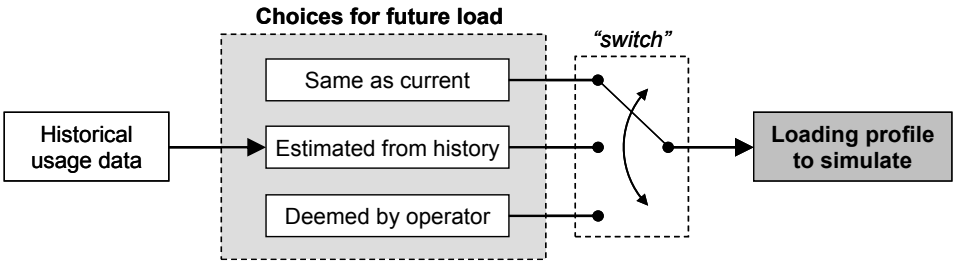

Figure 6.3. Illustration of how different loading profiles can be selected for simulating the progression of damage in a system

Any prognosis is an estimate of future conditions, and as such, it is uncertain and probabilistic in nature. In making a prognosis of a specific condition, operational conditions play a crucial role, because the progression of damage depends upon usage of the system. For some systems, future operational conditions are well known, but for most systems, these will be continually adapted to meet specific requirements at different points in time. When a particular prognosis is made, this fact should have been recognized and the prognosis should be accompanied by a specification of validity under specific operational conditions. The uncertainty in the loading profile can be reduced by enhancing communication between the operator of the system (who is in control of the loading profile), by improving our estimation techniques, or by both.

6.3.3. The fault-insensitive parameters or states

The *fault-insensitive parameters and states* describing the system are determined from design information, by experimental data, or by any other means. In addition to model-and system-specific descriptions, these parameters can include material properties, physical constants, and the like. In this aspect, the determination of fault-insensitive parameters and states for prognosis is similar to that of diagnosis (see section 4.2.1.1). However, there are important differences and additions.

Although the fault-insensitive parameters and states have no correlation with changes in the fault by definition, some are likely to be dynamically dependent upon the operating conditions of the system. Take, for example, the stress in a mechanical component that is not affected by the fault considered in a system, but that is an important element in the model of the system. As a state in the model description, the stress depends upon the load applied. However, the load applied to the system may vary throughout operation, and hence the "stress state" considered depends upon the load conditions. This is why the loading profile block is connected to the block with the fault-insensitive states in Figure 6.2, and why we identify this block as a dynamic block.

Since the fault-insensitive parameters and states are dynamic, i.e., changing, we need different sets of them. Each set corresponds to different operating conditions. Thus, the damage progression model will need to use different sets at each step or iteration of the damage progression simulation, according to the changes in load prescribed by the loading profile.

There are two possible approaches to determining the different sets of fault-insensitive parameters and states dynamically. We can try to do it on-line or off-line. The two approaches are discussed in more detail in section 6.3.4, below, because the fault-sensitive parameters and states considered there also share this characteristic.

6.3.4. The fault-sensitive parameters or states

In this step, the operating conditions and an instantaneous amount of damage are used to analyze the response of different components or subsystems of the plant to the presence of the fault of the instantaneous size considered. The objective of this analysis is to determine the values of the *fault-sensitive parameters and states*. This process is somewhat similar to the one discussed for the diagnostic modeling architecture in section 4.2.1.3. It is particular to the plant and it may require support from a variety of engineering disciplines. However, it must be noted once again that, for prognosis, the model is dynamic. Thus, multiple fault sizes must be considered in succession. The succession is given by some consideration of time and the corresponding dynamic characteristics of the loading profile.

When the damage progression simulation starts, determining the fault-sensitive parameters and states requires the consideration of initial conditions, as described in section 6.3.1. After this, when the simulation is running, new values of the fault-sensitive parameters and states are determined successively. The determination of these values is done utilizing the progression of damage that the simulation is characterizing. The

parameters and states recalculated each time reflect the change in the fault size. The recalculation process is continuous and runs along with the simulation, iteratively.

As with the fault-insensitive parameters discussed above in section 6.3.3, there are two possible approaches to determining, dynamically, the fault-sensitive parameters and states. We can try to do it on-line or off-line. The on-line approach uses information from the plant while it is operating. This requires that the analysis or simulations that determine the parameters or states be executed in parallel with the machine operation. It also requires that the analysis or simulations be carried out timely, which is not always possible, especially with complex systems, because some simulations may take hours to derive useful results, as will be seen with an example, further below.

In contrast, the off-line approach executes these analyses or simulations beforehand. The results of the simulations for different operating conditions can be stored in a database. When the plant is operating, the stored parameters corresponding to the operating conditions of the plant can be retrieved from the database and used for the prognosis.

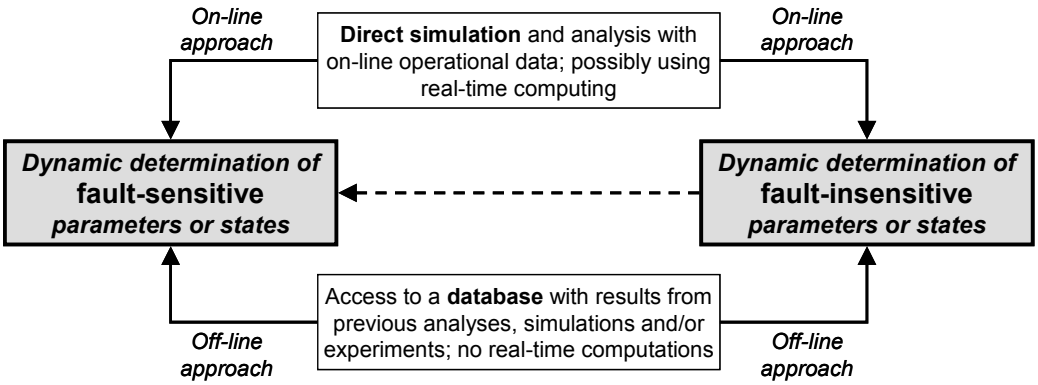

Figure 6.4. The on-line and off-line approaches to the dynamic determination of parameters and states of a prognostic model. The diagram illustrates the idea that parameters and states can be determined using a combination of on-line and off-line activities. The dotted arrow represents the idea that the fault-sensitive block may require information from the fault-insensitive block

Take, for example, the case of the helicopter transmission of focus in this thesis. The crack tip stress, which is an important parameter that is used to determine the crack growth rate, is calculated from a finite element analysis or FEA (see chapter 7). Crack tip stresses are dependent upon the crack length. Thus, crack tip stresses must be determined for different crack lengths. Each FEA simulation for determining a crack tip stress may take hours to complete. Needing multiple crack tip stresses could mean, therefore, that we must run FEA simulations for days before we can make a prognosis. This is completely unacceptable in system that can fail within the span of minutes. Therefore, the crack tip stresses corresponding to different crack lengths and different loads must be determined by this technique beforehand and kept stored for their use when required by a prognosis system.

6.3.5. The damage progression model

To arrive at a prognosis, we must run a simulation with the damage progression model to observe how the fault will evolve. The simulation can consider the damage progression as a series of steps. At each step, the model uses specific values of (1) the fault-sensitive parameters and states, (2) the fault-insensitive parameters and states, and (3) the operating conditions prescribed by the loading profile. Since the fault is dynamic, all three sets of values can change from one step to the next. Thus, the three sets of values must be determined at each step of the simulation.

The change in operating conditions at each step of the simulation is determined from the loading profile, in accordance with the descriptions of section 6.3.2. If applicable, the change in the fault-insensitive parameters and states is also determined considering the loading profile, because, as explained in section 6.3.3 they can have a dependency on it. In the first step of the simulation, the fault-sensitive parameters and states are determined from the initial conditions discussed in section 6.3.1. The operating conditions prescribed by the loading profile are also important here. For the following steps, the initial conditions are not needed, and instead, the results of the damage progression simulation from previous steps are used, as described in section 6.3.4.

7. PROGNOSIS OF THE HELICOPTER TRANSMISSION

In this chapter, we briefly exemplify how the helicopter transmission problem described in section 3.1 might be prognosticated using *model-based prognostics* and applying the concepts and methods discussed in chapter 6. Our prognosis of the helicopter transmission problem will predict how the crack in the planetary carrier plate will grow given a specific load profile and thus have an opportunity to estimate when the component will fail.

In the following sections, we first discuss briefly how the generic approach to model-based prognosis of section 6.2 might be used to design a prognostic system for the fracture problem of the helicopter transmission. However, we do not address this subject in detail, because such a task is beyond the reach of this thesis, and, as explained in that section, implementing the entire methodology for model-based prognostics is a complex task that requires the participation of a team of experts. To exemplify the use of the model-based prognostic approach, we assume that diagnostic activities precede the prognostic operation. In a real world implementation, diagnosis might be performed as discussed in chapter 5, but other techniques could be used as well.

After establishing an approach to prognosis of the fracture problem, this chapter exemplifies how to use the modeling architecture of section 6.3 with a fracture mechanics model for characterizing the growth of the crack. This example uses a simplified model whose intent is only to illustrate the methodology. We finally run simulations of the crack progression and validate the results with experimental data.

7.1. Model-based prognosis of the helicopter transmission fault

The ultimate objective of an engineering prognosis is to provide information about the remaining useful life or the expected time-to-failure of a system in operation. A prognosis of the helicopter transmission problem discussed in chapter 3 would be no different from this. The Georgia Institute of Technology and Impact Technologies LLC have worked in conjunction to realize a working demonstration of a prognostic system for experimental damage progression tests with the helicopter transmission (see Patrick et al., submitted for review). Because the task is so complex, it has been carried out by a team of researchers, with different aspects requiring the participation of specialists in the corresponding disciplines. This team activity is used here to provide validation and a means of refinement to the model-based prognostic architecture discussed in chapter 6. Figure 7.1 illustrates how the effort was implemented, and highlights the critical functional components of the prognosis task:

- Loading Profile
- Diagnosis
- Crack Growth Model
- Particle Filtering

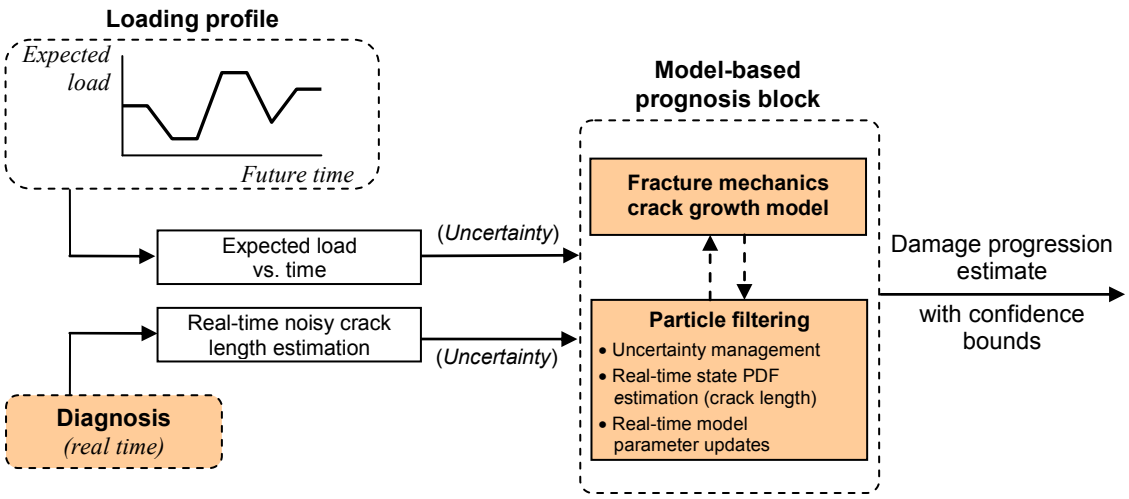

Figure 7.1. Application of the technique of Figure 6.1 for performing model-based prognostics to the helicopter transmission problem

Observe that Figure 7.1 is an adaptation of the technique proposed by Figure 6.1 in section 6.2. The diagnosis block of the diagram shown in Figure 7.1, above, was implemented as discussed in chapter 5. It provides information about the estimated crack length at a given point in time as evaluated from feature values. The feature values can be extracted from gearbox vibration signals in real time and be provided to a particle-filtering algorithm for improving the state estimation task and updating parameters of the crack growth model.

The particle-filtering algorithm is a state-of-the-art estimation technique used for a variety of activities. The particle-filtering technique has the ability to provide an estimate not just of the system state values characterized by the model, but also of the probability distribution, or probability density function (PDF) for these states (see, for example, Orchard et al., 2005, and Abbas et al., 2007). This distribution allows for performing uncertainty management and model adaptation simultaneously. The model

adaptation is carried out by updating, dynamically, the model parameters characterizing the fault progression. Projecting the PDF estimate in time, via simulations with the loading profile and the damage progression model, provides a means to make estimates of the RUL or TTF of the helicopter transmission component at fault. Implementation of the particle-filtering technique is outside the scope of this thesis. Its use with the helicopter transmission problem is studied by Orchard (to be published) and described in Patrick et al. (submitted for review).

Using the predetermined loading profile, the crack-growth model block provides information about the progression of the fault. These two blocks are discussed in more detail in the following sections.

7.2. Damage progression model of the planetary carrier crack

This section illustrates how the model-based prognostic simulation methodology proposed in section 6.3 can be used for characterizing the growth of the crack in the planetary carrier plate of the helicopter transmission. The first step is to apply the diagram of Figure 6.2 to the crack problem. An adaptation of this architecture is suggested in Figure 7.2.

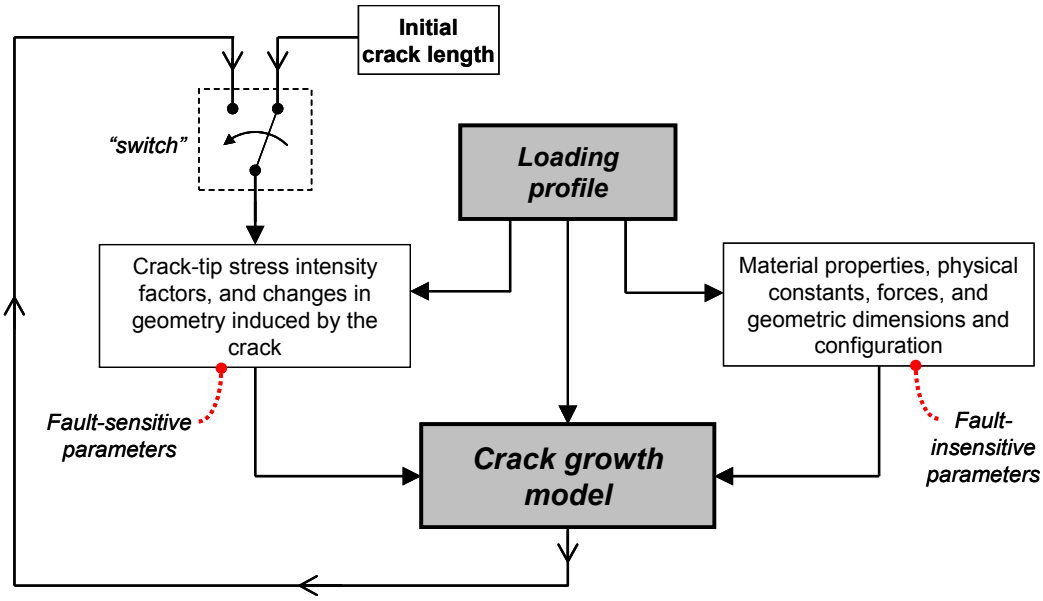

Figure 7.2. Application of the technique of Figure 6.2 for performing model-based simulation of the damage progression in the planetary carrier plate

To exemplify and validate this approach, we utilize data from the helicopter transmission experiments with a growing crack (see section 3.2). Let us now consider each of the blocks present in the diagram of Figure 7.2.

7.2.1. Initial conditions: the starting crack length

As described in section 3.2, the experiment of focus tested a planetary carrier plate with a seeded fracture. The experiment was able to measure the growth of the crack caused by the operational loads of the functioning planetary gear transmission. The initial crack length was 1.34 inches long. The crack did not grow at the same rate in all of the directions of the crack front, including the length or depth. As will be seen, the fact that the crack grew at different rates in the inboard and outboard directions is of particular importance. These directions of growth are represented in Figure 7.3. The crack reached

the outer edge of the circumference of the plate at a total length of about 4.8 inches, at which point the planetary carrier plate started to experience increased deformations.

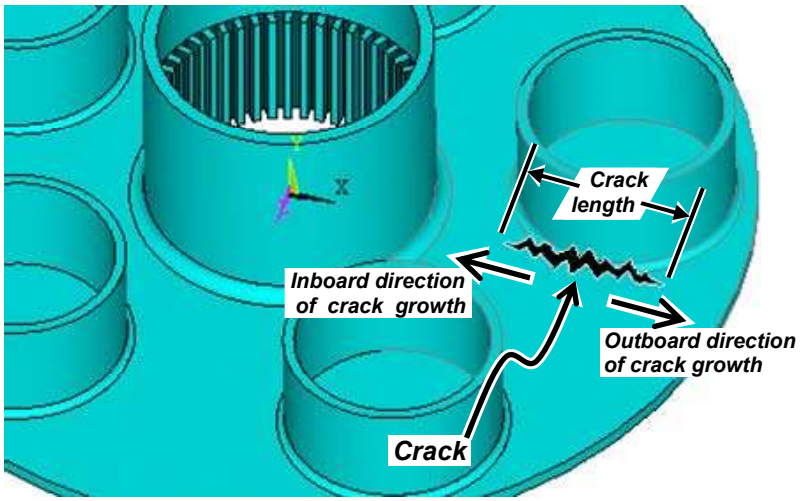

Figure 7.3. Definition of the crack length and the inboard and outboard directions of crack growth on the planetary carrier plate

7.2.2. Loading profile

The crack growth experiment applied load cycles by varying the engine torque continuously to make the crack grow. These cycles were designed by the technical leaders of the experiment to resemble a helicopter taking off the ground, hovering for some time and then landing, in what is called a ground-air-ground (GAG) cycle. GAG cycles are comprised of a succession of increasing and decreasing engine torques with short "dwelling" periods maintaining constant torque levels. An illustration of an approximate succession of typical GAG cycles is shown in Figure 7.4.

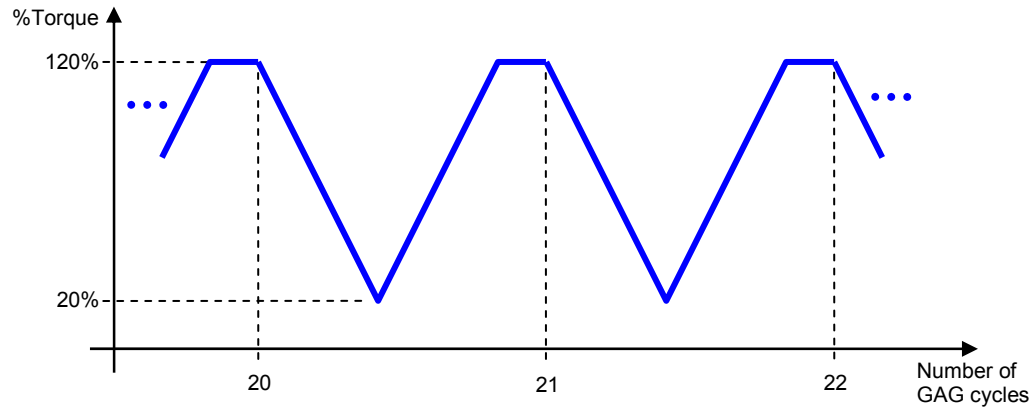

Figure 7.4. Illustration of the application of ground-air-ground (GAG) cycles in the operation of the helicopter transmission during the crack progression experiment

The experiment was run for more than 1000 GAG cycles, but we focus here only on a subset of these. GAG cycles were applied at a rate of about 25 cycles per hour, and most of them had similar patterns, except for a few initial GAG cycles that were used for calibration and baseline data retrieval. The first 320 GAG cycles varied the torque from about 20% of nominal engine torque to 120%. The next GAG cycles up to number 1000 varied the torque from about 20% to 93%. In this work, we assume that GAG cycles have the patterns illustrated in Figure 7.5, and that nominal engine torque is 54,000 lb·ft.

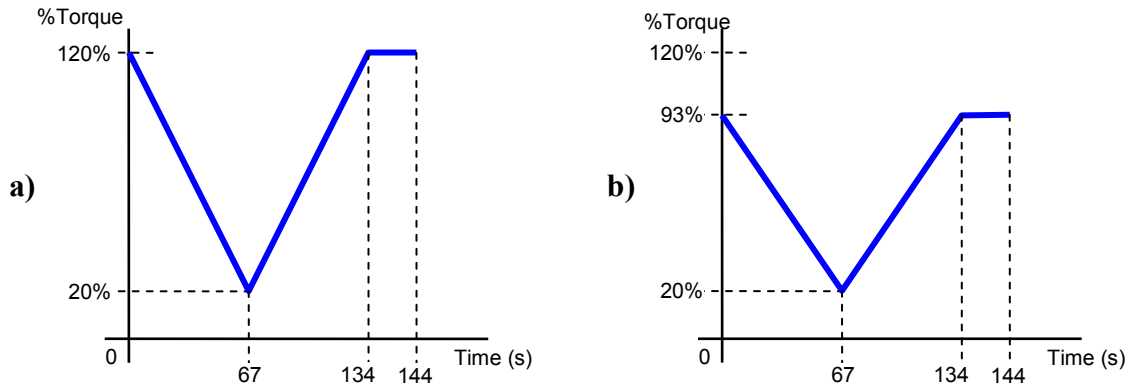

Figure 7.5. Approximate pattern of individual GAG cycles used in the crack progression experiments. a) Pattern assumed used in GAG cycles 1 through 320. b) Pattern assumed used in GAG cycles beyond 320

GAG cycles are comprised of a series of load sub-cycles corresponding to different operating mechanisms in the gearbox. Sahrmann (2004) characterized the three most significant series of sub-cycles as follows:

1) a cyclic load with an amplitude of about $A_1 = 10\%$ of nominal engine torque occurring at a rate of one cycle per revolution of the planetary carrier plate, i.e., with a frequency of about $f_1 = 4.3$ Hz;
2) a cyclic load with an amplitude of about $A_2 = 5\%$ of nominal engine torque occurring at a rate of four cycles per revolution of the planetary carrier plate, i.e., with a frequency of about $f_2 = 17.2$ Hz; and
3) a cyclic load with an amplitude of about $A_3 = 2\%$ of nominal engine torque occurring at the planetary gear tooth meshing frequency, i.e., with a frequency of about $f_3 = 980.4$ Hz.

The addition of these loads produces a more complex loading profile than is evidenced by the GAG cycle shapes discussed above. The effect of these sub-cycles is illustrated in Figure 7.6.

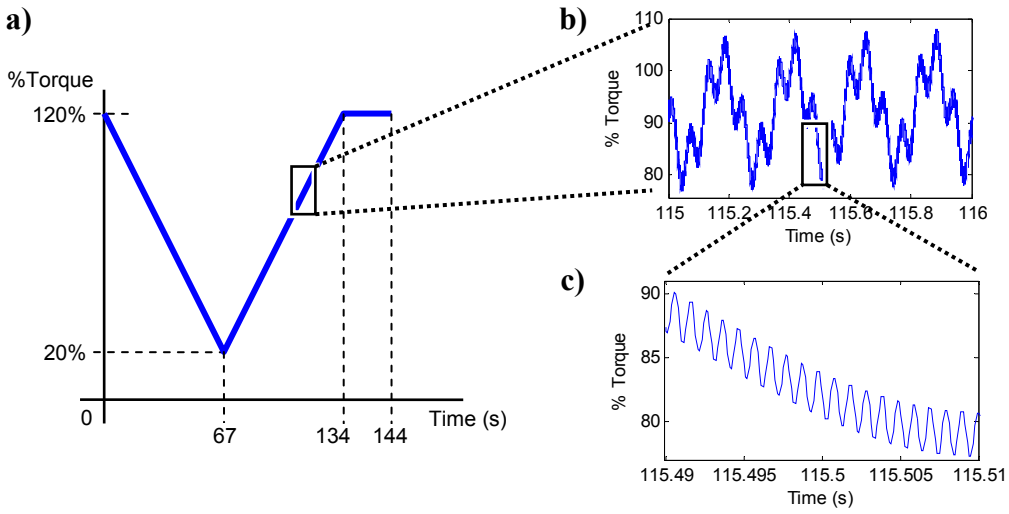

Figure 7.6. Assumed composite loading of the planetary gearbox; a) the engine torque load of a single GAG cycle; b) the effect of the cyclic loads present once and four times per revolution of the planetary carrier plate; c) the load effect of the gear meshing action

7.2.3. The fault-insensitive parameters

Some examples of the fault insensitive parameters of the damage progression model are basic geometrical dimensions of the planetary carrier plate, the forces acting on the plate and material properties. The major geometrical dimensions of the plate are an obvious set of fault-insensitive parameters. Conversely, dimensions of the crack are not.

The forces acting on the planetary carrier plate resulting from the application of the loading profile are taken as fault-insensitive, i.e., we are assuming that the load will

not vary significantly with the crack growth. The load is applied as described in section 5.4.1. The damage progression model uses some common material properties, such as the density, Poisson's ratio, and the Young modulus of the plate alloy, and some not so common, such as certain fracture parameters. These latter will be discussed in subsequent sections.

7.2.4. The fault-sensitive parameters

There are two sets of fault-sensitive parameters in the damage progression model of the planetary carrier plate. The first set contains the geometric dimensions of the crack, i.e., the length of the crack and its inboard and outboard increments, and crack depth. The second set contains the geometric crack-tip stress intensity factors, which are parameters that characterize the physical mechanisms driving the crack growth. These are discussed in more detail in sections 7.3 and 7.4, further below.

7.2.5. The crack growth model

To simulate the growth of the crack, it is necessary to rely on a mathematical description of the crack growth (i.e., a crack growth equation) in conjunction with a means to consider the changes in the geometry of the plate caused by the growth of the crack. The crack growth equation used is a basic characterization. Although representations that are more accurate exist, we select this one for reasons of simplicity. Details on the crack growth equation are presented in section 7.3.

The effect of the crack geometry is determined using finite element analysis. ANSYS (see section 5.4) was again used, but in a different operating mode than in chapter 5. Instead of the deformation analysis carried out for diagnosing the crack, we execute a crack-tip stress analysis. As will be seen in section 7.3, the crack-tip stresses are critical parameters driving the crack growth. The use of ANSYS for this task is described in section 7.4.

Results from the finite element analysis are input into the crack growth equation to determine the crack progression curve. This defines our crack growth model. The approach is illustrated in Figure 7.7.

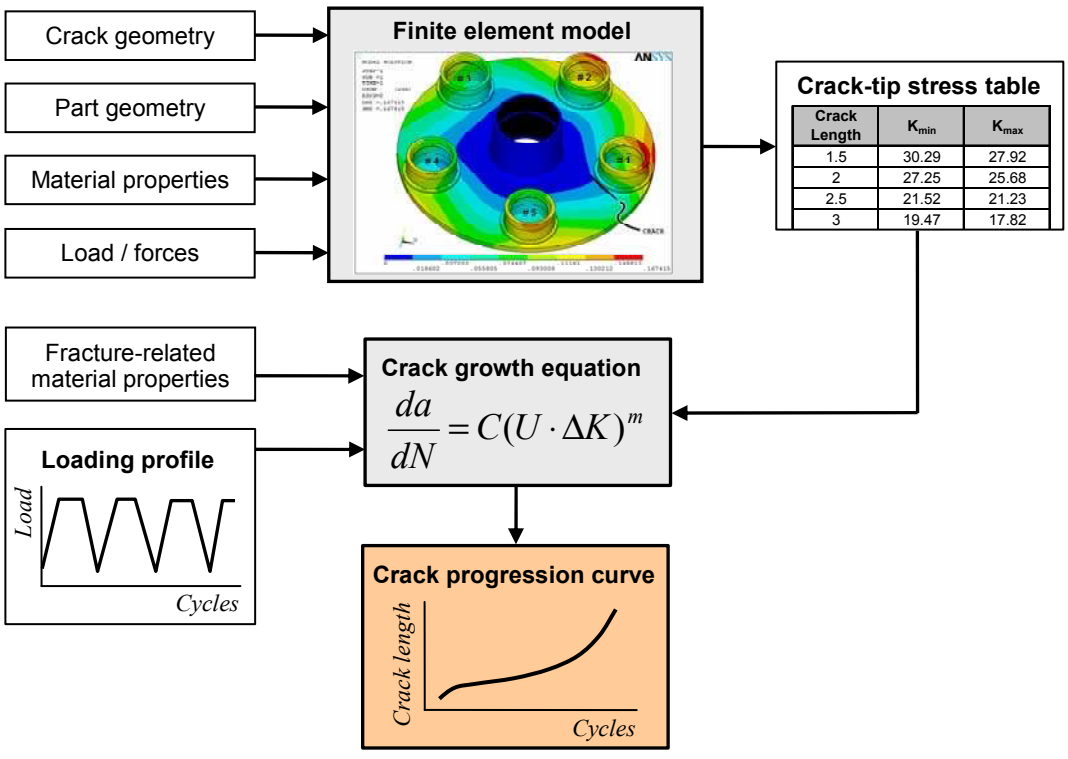

Figure 7.7. Crack growth model used in the helicopter transmission problem

7.3. The crack growth equation used

7.3.1. The perspective of linear elastic fracture mechanics

One of the most important areas of research in the field of fracture mechanics is the area of fatigue crack growth. This discipline studies the propagation of cracks in materials resulting from the application of cyclic loads. For materials with linear behavior, and whose basic properties are constant in time, the field of linear elastic fracture mechanics (LEFM) provides adequate characterizations of the behaviors of fracture and crack growth. Of particular importance to this thesis is the ability of LEFM to characterize crack growth under fatiguing loads.

There are two mainstream perspectives for studying fatigue crack growth phenomena. One considers the stress fields around cracks and its initial focus is on the crack tip regions, later to consider, indirectly, the geometric properties of the cracked bodies. See Figure 7.8. The other approach focuses on the body as a whole and uses energy considerations to arrive at a description of failure in the body. In this case, the stress fields near the crack tips are indirectly considered (see Sanford, 2003, chapter 7). Our focus here is on the first approach.

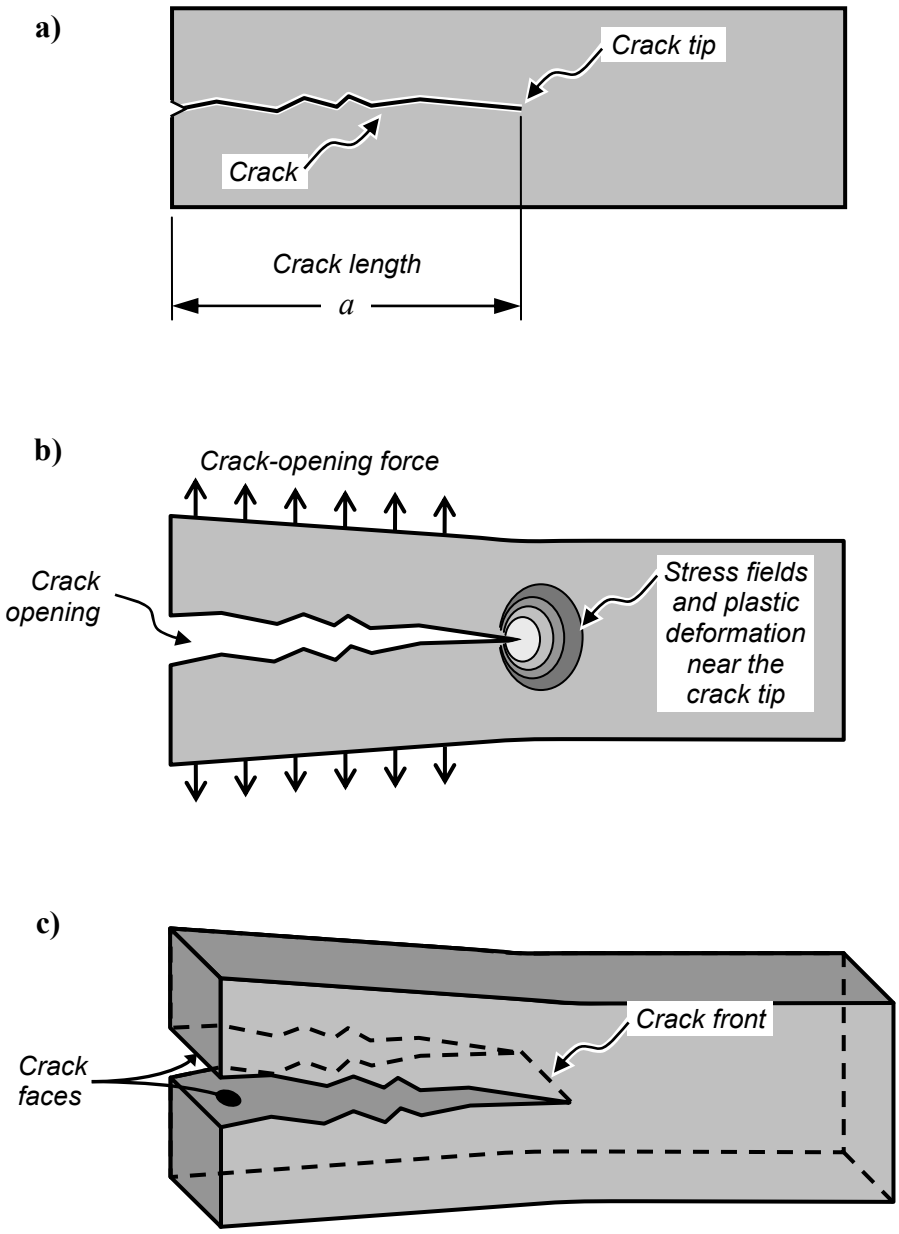

Figure 7.8. Basic geometric definitions in fracture studies. a) Illustration of a solid body with an edge crack; the crack length *a* is measured from the edge of the body to the crack tip. b) Illustration of the stress fields appearing when the crack opens in response to the application of forces. c) The three-dimensional consideration of a crack tip is referred to as the crack front

7.3.2. Geometric crack-tip stress intensity factors

As described below, we consider fracture mechanisms involving the stress fields around crack tips or crack fronts. The description of stress fields involves the determination of the directional components of the stresses present in specific spatial locations of a body. The theory of LEFM suggests that, in general, the stresses near a crack tip behave linearly along specific directions, and can be represented by scaling some function of the spatial location considered, and of the configuration (or *mode*) of the load applied to the body, i.e.,

$$\sigma = K \cdot f(r, \theta, \text{load configuration}), \tag{7.1}$$

where σ is a directional component of the stress at the location described by the polar coordinates (r,θ), and K is a constant scale factor providing linearity.

The scale factor K in Equation 7.1 is an important parameter characterizing the stress fields near a crack tip, and is known as the *geometric stress intensity factor*. An important property of K is that it is also able to relate the geometric properties of the cracked body and the geometry of the crack to the load applied to the body. LEFM generally characterizes this relationship in the form

$$K = \mathrm{S}\sqrt{\pi \cdot a} \cdot f(\text{body geometry}, \text{crack shape}), \tag{7.2}$$

where S is a remote load applied to the body and a is the crack length. Equations 7.1 and 7.2 show that the geometric stress intensity factor K offers a means to relate the stresses near the crack tip, which ultimately drive crack growth, with the geometric parameters

describing the cracked body, including the shape and length of the crack. For this reason, its significance in the study of fractures is enormous.

7.3.3. The limiting cases of plane stress and plane strain

To simplify the analysis, many problems in fracture mechanics, although spatial, are reduced to a two-dimensional state of stress. This assumption is sometimes valid and provides a good approximation to the actual three-dimensional stresses occurring in solid bodies. The problem reduction assumes that either *plane strain conditions* or *plane stress conditions* govern near the crack tip (see Anderson, 1995, p. 82). Neither of the two cases occurs in general, but the conditions are limiting cases and can provide information of extreme values. The actual conditions of the material near a crack tip is thus somewhere in between the two cases, although it is generally acknowledged that plane strain conditions are a closer approximation, except for thin plates with cracks spanning the entire width.

Therefore, as we model the crack, we can use these limiting cases to determine bounds for our model estimates of the crack-tip stress intensity factors. We thus know that the actual conditions occurring in the plate can be described with a value of stress intensity K that is between the values of $K_{p\varepsilon}$ at plane strain conditions and $K_{p\sigma}$ at plane stress conditions, i.e.,

$$K_{p\varepsilon} > K > K_{p\sigma} . \tag{7.3}$$

7.3.4. Paris Law and Elber's crack closure model

In the early 1960s, Paris and Erdogan (1963) proposed that fatigue crack growth could be generally characterized with an equation of the form

$$\frac{da}{dN} = C(\Delta K)^m, \tag{7.4}$$

where da/dN is the increase in the crack length a per each cycle number N of applied load; C and m are material constants determined empirically; and the term ΔK, referred to as the *stress intensity range* describes the change in applied stresses at the crack tip.

Equation 7.4 has become widely known as the *Paris Law* of crack growth. The values of the constants C and m can be related to the crack growth-rate curve of a given material. The crack growth rate is generally an exponential function that, in a log-log plot is approximately linear in certain regions for most metallic materials. The constants describe the geometry of such a linear relation, as illustrated in Figure 7.9. The models in this thesis used $C = 7.7331\times10^{-10}\ \frac{\text{ksi}}{\text{in}^{1/2}}$ and $m = 3.5074$.

Although Paris' relation holds approximately true for most metallic materials under specific cyclic loading conditions, it typically needs adaptations to reproduce a variety of effects and growth mechanisms. For example, the relation focuses on the stress intensity range

$$\Delta K = K_{\max} - K_{\min} \tag{7.5}$$

while discarding the possible effects of the mean level of the stress intensity, illustrated in Figure 7.10, which has been widely accepted to be an important parameter affecting the

crack growth rate. K_{max} and K_{min} are the maximum and minimum values of the cyclic geometric crack-tip stress intensity factors. The basic properties of stress intensity factors were described in section 7.3.2.

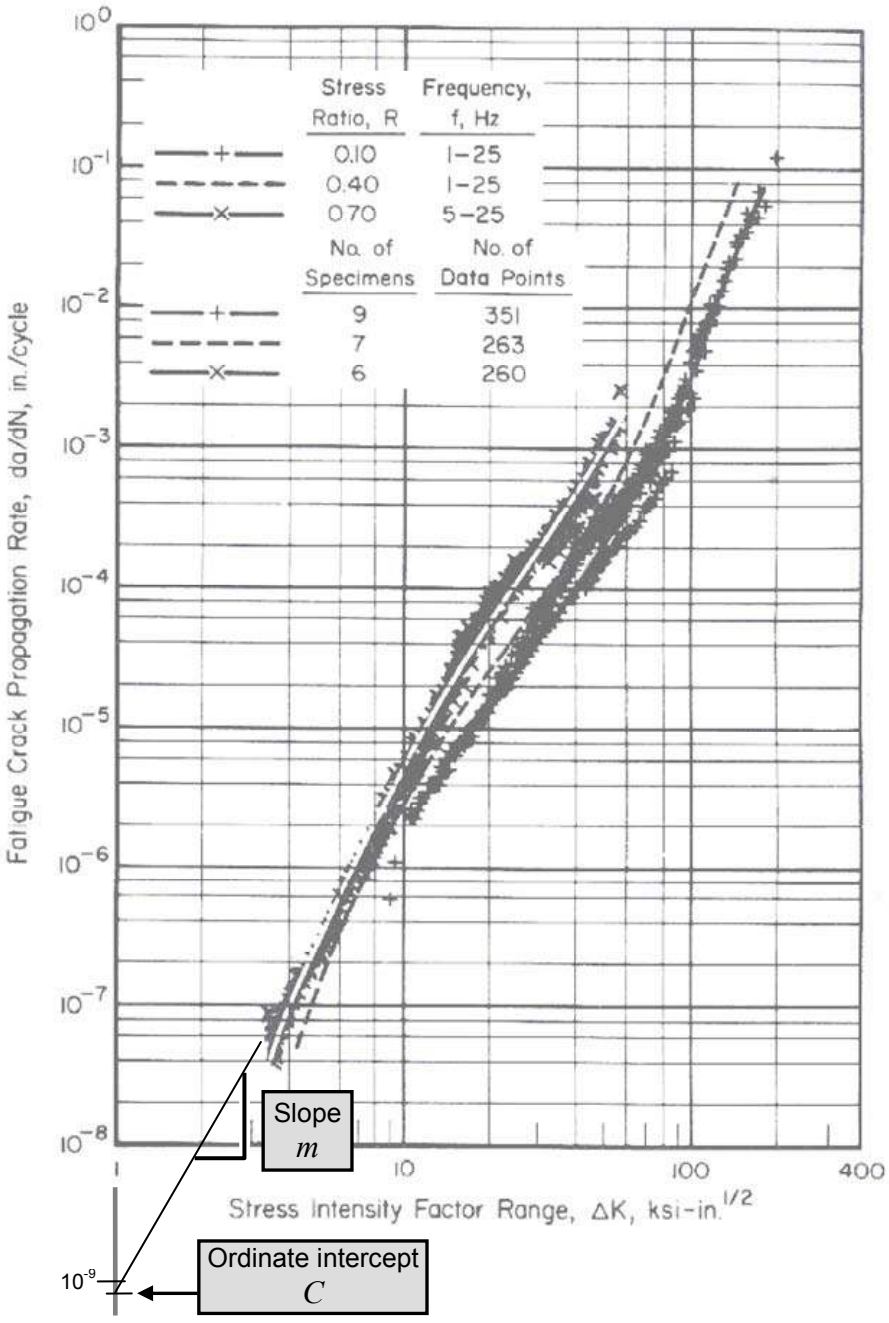

Figure 7.9. Fatigue-crack-propagation data for Ti-6Al-4V titanium alloy. Relationship to the values of the constants C and m of Paris Law is illustrated. Adapted from Rice et al. (2003)

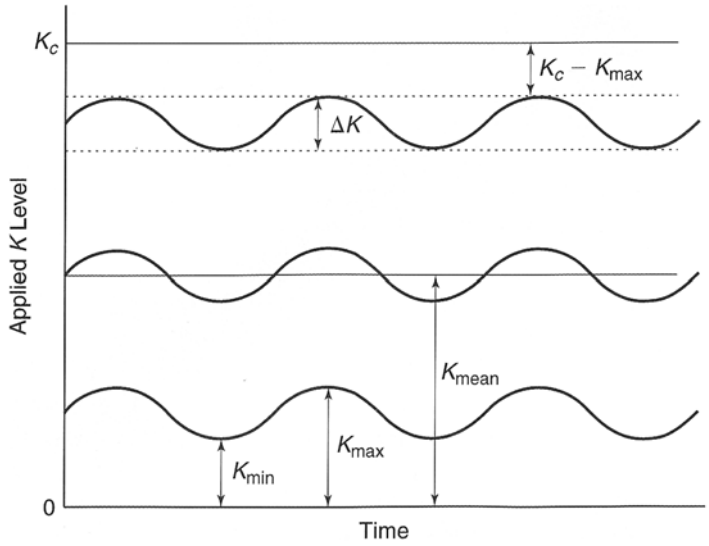

Figure 7.10. Illustration of constant-amplitude load cycles at different mean levels of the stress intensity. Reproduced from Sanford (2003), p. 292

Another shortcoming of Equation 7.4 is that it does not take into account the important effect of *plasticity-induced crack closure*. This mechanism, which in general causes retardation of the crack growth, will be explained in section 7.5.

Thus, in order to approximate better the growth pattern of the crack in the planetary carrier plate of the helicopter transmission, an adaptation of Paris Law proposed by Elber (1971) is used. Elber suggested an empirical correction for Paris's crack growth model that takes into account both of the effects mentioned before. His model characterizes the crack growth rate as

$$\frac{da}{dN} = C(\Delta K_{eff})^m, \tag{7.6}$$

where

$$\Delta K_{eff} = U \cdot \Delta K \tag{7.7}$$

is known as the *effective* stress intensity range. U is a correction factor that allows for the consideration of both the mean level of the stress intensity and the retardation effects of crack closure.

Katcher and Kaplan (1974) determined that the value of U for Ti-6Al-4V, the material of the carrier plate (see Sahrmann, 2004), is approximated by the relation

$$U = 0.73 + 0.82R\,, \tag{7.8}$$

where R is the ratio of $K_{\min}$ to $K_{\max}$ for an individual cycle of load, i.e.,

$$R = \frac{K_{\min}}{K_{\max}}\,. \tag{7.9}$$

$K_{\min}$ and $K_{\max}$ are as defined by Figure 7.10. However, Equation 7.8 is valid for cycles exhibiting constant amplitude. If variable-amplitude loading is to be applied, the equation must be appropriately interpreted on a cycle-by-cycle basis. This subject will be considered in more detail in section 7.5.

Knowing the values of $K_{\min}$ and $K_{\max}$ for each load cycle and the loading profile makes it possible to integrate (numerically) the crack growth relation prescribed by Equation 7.6 and estimate the crack growth pattern. We will approximate the values of $K_{\min}$ and $K_{\max}$ from finite element analysis as discussed in section 7.4.

It is worthwhile to note that the crack growth description suggested here is used with the intention to approximate roughly the progression of the crack length. The purpose here is only to illustrate the model-based prognostic architecture proposed in

chapter 6. More information on the principles of crack growth modeling can be found in Sanford (2003), Anderson (1995) and Dowling (1999).

7.4. Determination of the static crack-tip stress intensity factors through FEA

7.4.1. Preliminary considerations

A commercial software package for Finite Element Analysis, or FEA, known as ANSYS (see section 5.4), was used to determine the crack-tip stress intensity factors *K* of different crack sizes. It is necessary to determine the stress intensity factors at different crack lengths because, as shown in Equation 7.3, they are dependent on the crack length and shape. Nevertheless, it is not necessary to determine the stress intensity factors for different values of the load applied, and a static-load realization can suffice, because, as Equation 7.3 once again shows, the intensity factors for linear materials such as the one under consideration typically vary linearly with the value of the load S applied. To determine the values of *K* for different loads can be done by scaling the value of *K* for a particular instance of static load.

7.4.2. Determination of the static crack-tip stress intensity factors as a function of crack length and shape

Finite element modeling of cracks requires special modeling considerations, including *node duplication* inside the crack faces (explained earlier in section 5.4.2), and the use of *collapsed elements* (also called *singular*, or *degenerate* elements) around the crack tip. Collapsed elements provide a good approximation of the stress field gradients

on the crack tip neighborhood using few finite elements. Furthermore, there are mathematical relations tying node displacements to the value of the corresponding stress intensity factor K at the crack tip (see Sanford, 2003, chapter 4). Element collapsing is illustrated in Figure 7.11.

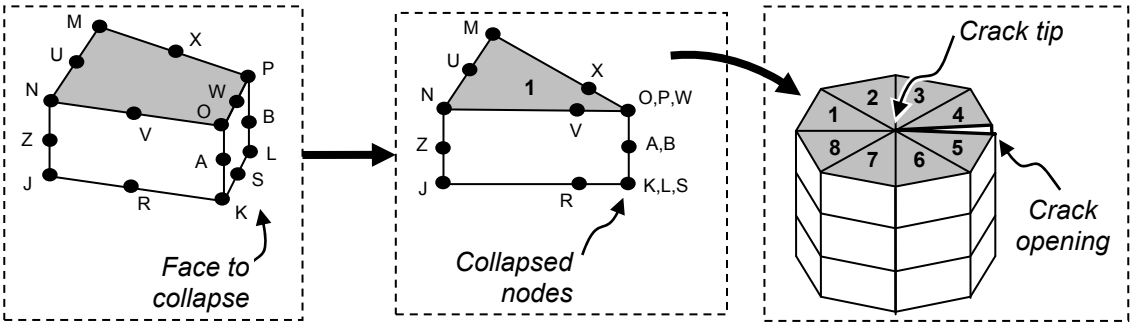

Figure 7.11. Collapsing of the side of a finite element to be used for modeling and simulating crack tip stresses and displacements

Using these considerations, it is possible to approximate the values of the stress intensity factor K for different crack lengths and at different locations along the crack front. See, for example, Figure 7.12.

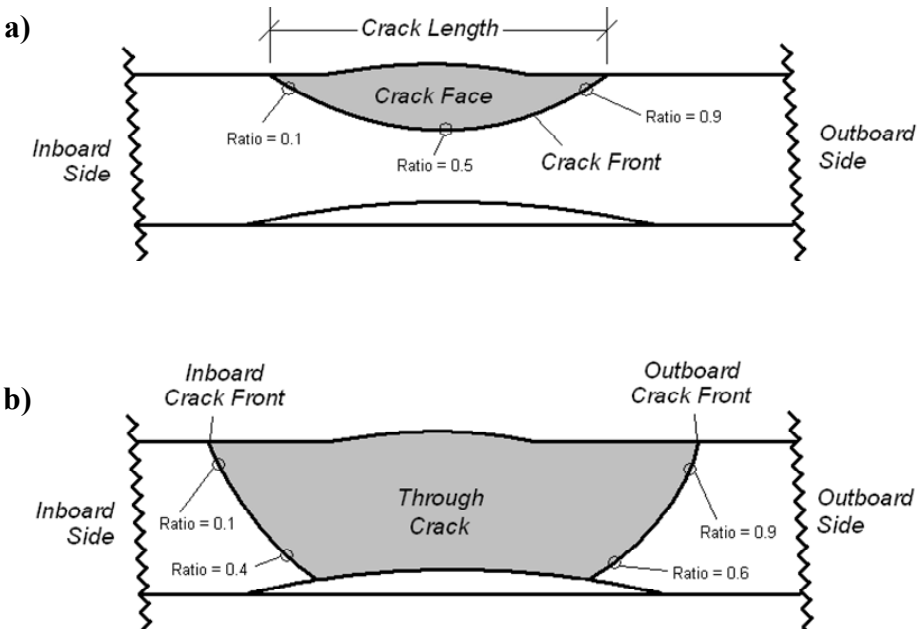

Figure 7.12. Illustration of how crack-tip stress intensity factors can be determined for different lengths and at different locations along the crack front. Different locations are here identified with a "ratio" dimension particular to different crack lengths and shapes

Figure 7.13 illustrates the planetary carrier plate model used for analyzing crack-tip stresses. It is worthwhile to note that the plate design is simpler than that used in chapter 5. More emphasis was placed on the design of the crack shape in this model than in geometric details of the plate.

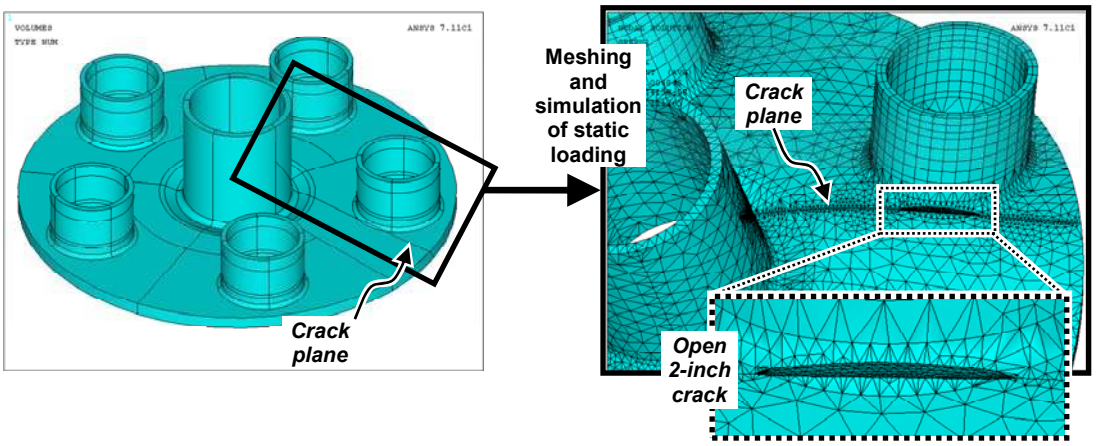

Figure 7.13. Three-dimensional computer model of the planetary carrier plate as used for crack-tip stress studies. Plate deformation shown is exaggerated for illustrative purposes

Figure 7.14 illustrates how some of the concepts discussed above were applied to the finite element model.

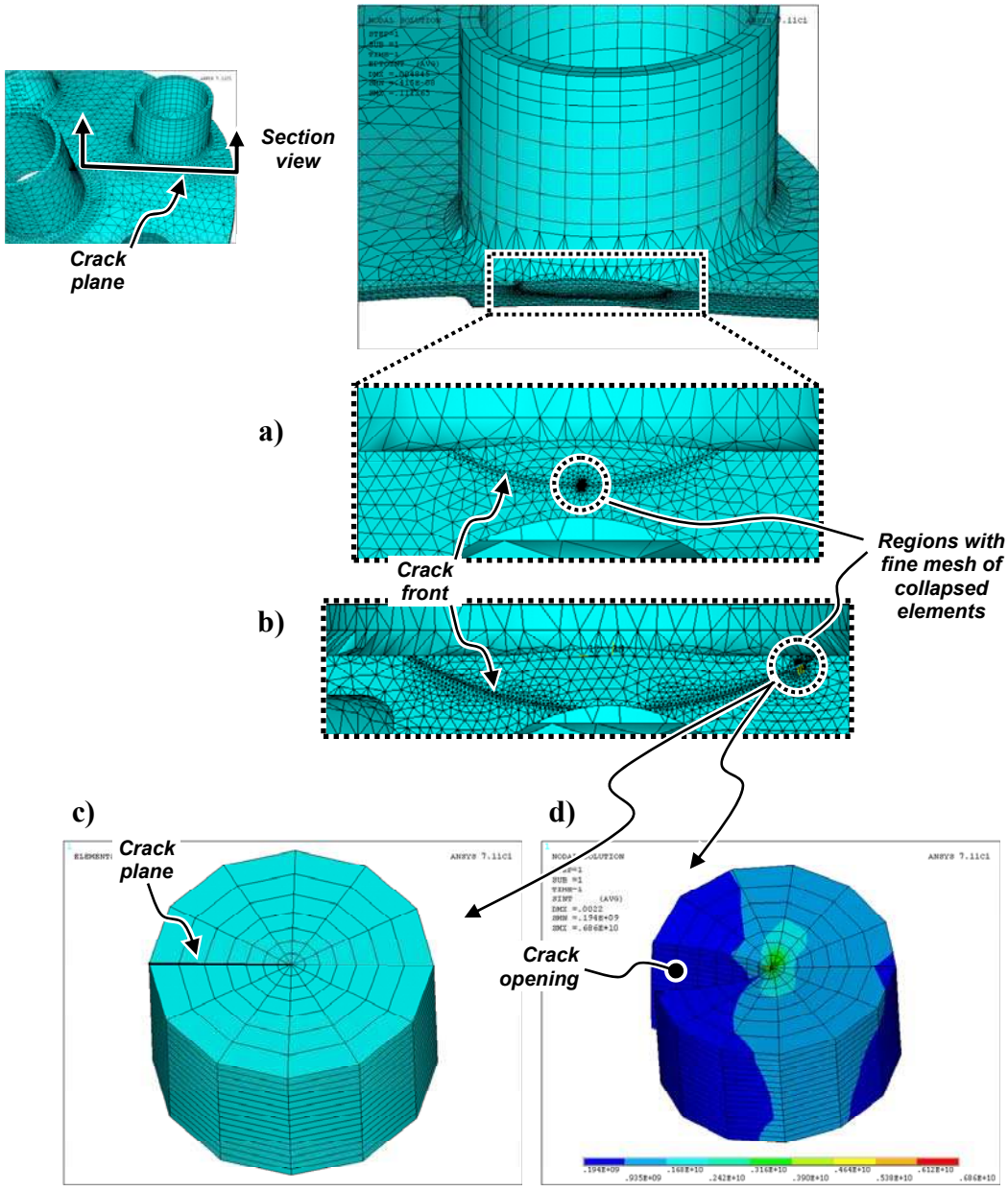

Figure 7.14. Details on the finite element modeling of crack tips. a) 1.5-inch-long crack. b) 3-inch-long crack. c) View of the design of collapsed elements located on a region of the crack front. d) Deformation of collapsed elements and corresponding opening of the crack caused by the application of load; ranges of stress intensity are also shown, in Pa. Amount of deformation shown is exaggerated for illustrative purposes

Using this modeling technique, crack lengths ranging from 1.5 to 4.5 inches were simulated for locations near the top of the plate on both the inboard and outboard sides of the crack tips, i.e., at location ratios corresponding to about 0.05 and 0.95 of those illustrated in Figure 7.12. ANSYS provided the crack-tip stress intensity factors shown in Table 7.1 at 100% (i.e., 54,000 lb·ft) of nominal engine torque.

Table 7.1. Crack-tip stress intensity factors obtained from ANSYS. The simulations were run using the same half-lengths in the inboard and outboard sides of the crack, i.e., inboard length = outboard length = (total length / 2)

Total Crack Length (inches)	**Inboard***		**Outboard***	
	K plane strain	*K* plane stress	*K* plane strain	*K* plane stress
1.5	57.39	51.13	73.58	65.56
2	58.03	51.71	67.97	60.56
2.5	52.67	46.94	56.42	50.28
3	51.03	45.48	54.12	48.24
3.5	56.27	50.13	70.56	62.88
4	69.90	62.30	64.60	57.57
4.5	71.32	63.55	72.25	64.38

K* units are **ksi / in$^{1/2}$

7.4.3. Determination of crack-tip stress intensity factors as a function of applied load (torque)

All the values of *K* presented in section 7.4.2, above, were obtained from simulations with a static torque corresponding to 100% of nominal engine torque (54,000 lb·ft). However, the value of *K* is expected to vary linearly with the load application. Hence, for the variations in the load prescribed by the loading profile discussed in section 7.2.2, instantaneous values of *K* corresponding to instantaneous values of load can be

estimated proportionally from the static values provided by Table 7.1. The operation is performed as

$$K_{\text{Load}} = \frac{\%\,\text{Load}}{100} \cdot K_{100} = \text{S}^{\%} \cdot K_{100}\,, \tag{7.10}$$

where K_{Load} is the expected value of K at some specific "% Load" and K_{100} corresponds to the values shown in the table; $\text{S}^{\%}$ represents the proportion of the load applied to the plate with respect to the application of 100% of nominal engine torque. For example, the instantaneous value of the crack tip stress intensity factor of a 2-inch crack near the inboard-side crack tip (location ratio = 0.05) at 80% of nominal engine torque, assuming that plane stress conditions are present, is approximately equal to

$$K_{80} = \frac{80}{100} \cdot (51.71) = 41.37\ \tfrac{\text{ksi}}{\text{in}^{1/2}}\,. \tag{7.11}$$

7.5. Application of the loading profile in the crack growth model

7.5.1. Preliminary considerations

As expressed in section 7.3, progression of the crack length on the planetary carrier plate can be approximately described by numerical integration of Equation 7.6. However, to obtain a numerical description of the increase in crack length as a function of the load cycles applied, we must first determine the values of the effective crack-tip stress intensity range ΔK_{eff} at each load cycle.

In section 7.4 we derived a way to approximate, through modeling, instantaneous values of K within the loading profile. However, according to Equation 7.6, to characterize crack growth, we must approximate the values of ΔK_{eff} corresponding to individual cycles with particular values of K_{max} and K_{min}. Furthermore, the values of ΔK_{eff} must be determined considering the cycle shapes prescribed by the loading profile and the effect of crack closure. The following sections illustrate how this can be done.

7.5.2. Plasticity-induced crack closure

Let us describe the maximum and minimum values of the cyclic load applied to a material by S_{max} and S_{min} respectively. The load is assumed applied far from the crack region, i.e., it is a *remote load*. When S_{max} is applied, the corresponding large values of stress σ near the crack tip cause *plastic deformation*[17] of the material around the crack tip. The value of the stress determines the amount of deformation. After the maximum load S_{max} is reached, load diminishes in the cycle until it reaches the minimum load value S_{min}. Although stresses near the crack tip also diminish, the plastic deformation causes the appearance of *residual compressive stresses* behind the crack tip (i.e., in the region where material has just separated). These compressive stresses are illustrated by negative values of the vertical stress σ in Figure 7.15. The compressive stresses have a tendency to close the crack opening behind the crack tip, so that, when the stress is diminishing in the cycle, once the crack closes, further reductions in the stress do not influence the crack growth, as the crack tip has become "shut" inside the deformed material.

[17] *Plastic deformation* is irreversible deformation experienced by the material, and is as opposed to *elastic deformation*, which is temporary and recovered by the material when the stresses are removed.

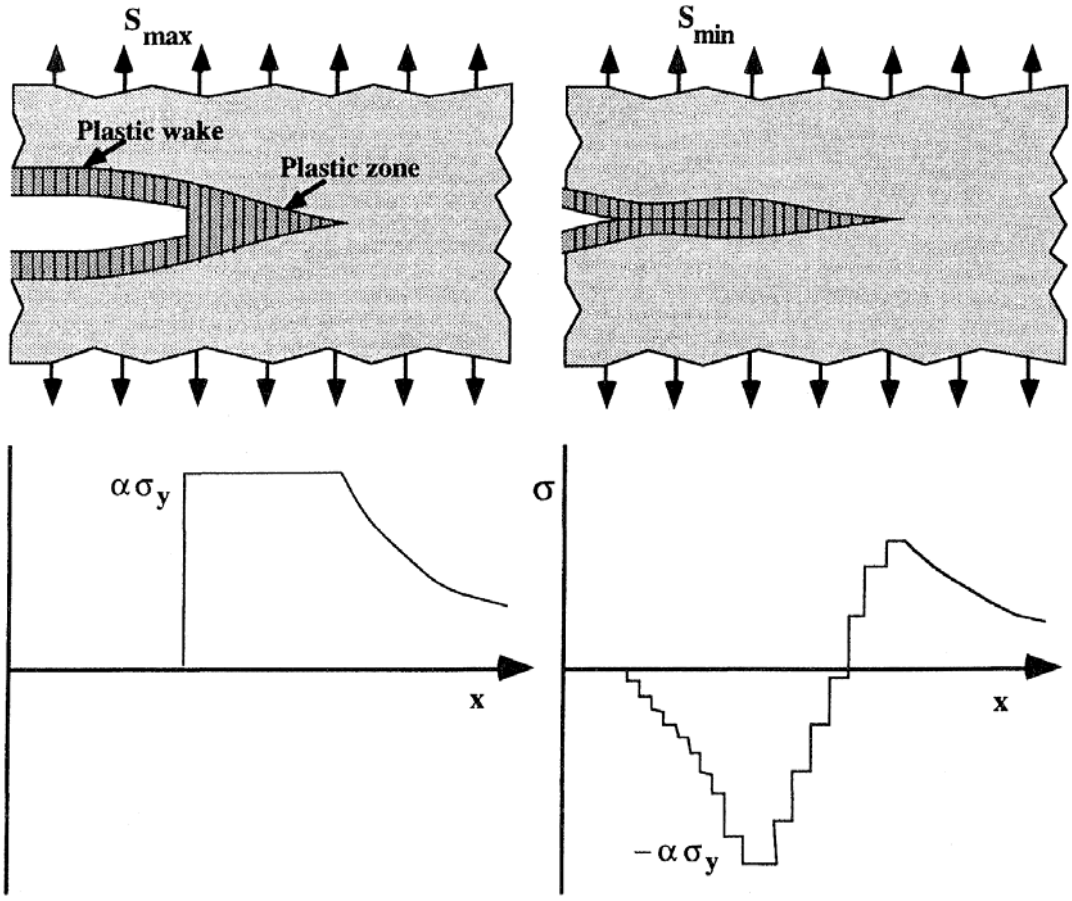

Figure 7.15. Illustration of the stresses appearing in the material around the crack tip in the wake of plasticity-induced crack closure. The illustration represents a discretized description, along the direction of crack growth (**x**), of the local vertical stresses σ resulting from the application of a remote cyclic load with maximum and minimum values of S_{max} and S_{min}, respectively. This description is used by Newman (1995) to model fatigue crack-growth under the presence of crack closure. Parameters α and σ_y are known as the constraint factor and the flow stress, respectively, and are used to characterize plasticity. Reproduced from Anderson (1995), p. 540

Similarly, when the applied load starts to increase following the reaching of S_{min}, the load will not effect crack growth until the compressive stresses are overcome and the crack re-opens. The value of local stress needed to re-open the crack is known as the *crack-opening stress*, and is denoted by σ_{op}.

7.5.3. Effective crack-tip stress intensity range

Let us denote by K_{op} the crack-tip stress intensity factor corresponding to the presence of local stresses given by σ_{op}, i.e., K_{op} is the instantaneous value of K when $\sigma = \sigma_{op}$.

Elber (1971) suggested that once crack closure appears, all the cycles reaching values of K_{min} below that of K_{op} should be regarded as cycles with $K_{min}=K_{op}$. The reason for this is that, once the crack closes, the remaining part of the load cycle below K_{op} does not effect crack growth. See Figure 7.16. Thus, ΔK_{eff} is calculated from all the cycles having K_{max} above K_{op} as

$$\Delta K_{eff} = K_{max} - K_{op} . \tag{7.12}$$

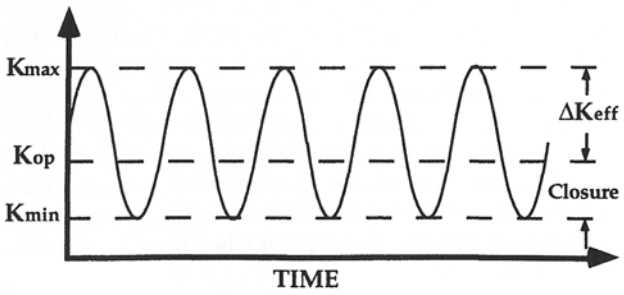

Figure 7.16. Definition of the effective crack-tip stress intensity range.
Reproduced from Anderson (1995), p. 521

Although the validity of Elber's results and characterizations has been sometimes questioned (see, for example Shih and Wei, 1974), it is generally acknowledged that Elber's relation has considerable merit, and has thus been used and referenced widely by the literature. Here, we regard Elber's characterization as a good approximation for our modeling purposes.

By considering individual load cycles, each with a local maximum and local minimum of load S, we can estimate the values of K_{max} and K_{min} for each cycle. The cycles are determined from the patterns described in section 7.2.2. The corresponding values of ΔK at each load cycle can be determined from Equation 7.5. The value of ΔK_{eff} can be determined by considering the loading profile cycle patterns and applying the relations provided by Equations 7.7, 7.8 and 7.9 to find K_{op} and thus characterize crack closure. The application of the loading cycle patterns is done under the consideration of *variable-amplitude loading*, i.e., where the cycles are considered individually because the loads change from one cycle to the next. This procedure is described in the section following.

It should be noted that there are multiple techniques available to model the growth of cracks under variable-amplitude loading, and there can be effects beyond plasticity-induced crack closure influencing the crack growth rate. For example, a variety of load *interaction* effects can be considered, for which strip-yield models or yield-zone models, such as that of Willenborg, can be useful (see Sander, 2004). This thesis uses a crack closure model with an analysis that approximates a cycle-by-cycle consideration because of its simplicity, the ties of the present work to that of other researchers involved with the helicopter problem under consideration, and the availability of empirical data for the material under consideration.

More details on the mechanism of plasticity-induced crack closure can be found in Sanford (2003). Summaries on techniques for modeling crack growth with variable-amplitude loading are offered by Dowling (1999) and Murthy et al. (2004). Important advances in applied modeling of fatigue crack growth with the consideration of crack closure are attributable to Newman (1995, 1984), who also developed a computer program to simulate and analyze fatigue crack growth (see Newman, 1992).

7.5.4. Application of variable-amplitude loading

We now proceed to the determination of the values of ΔK_{eff} for individual load cycles in the loading profile of the planetary carrier plate. To this effect, we must characterize the value of K_{op} at which crack closure occurs.

First, observing the form of Equation 7.7 we note that U must be restricted to lie in the range $0 < U \leq 1$ because the crack growth rate is only slowed by the effect of crack closure, and not sped up. From Equation 7.8, this means that, for Ti-6Al-4V, the value of R must be smaller than 0.33 if crack closure is to affect the crack growth behavior.

From the consideration of the cycle patterns of the loading profile (see section 7.2.2), we observe that only the engine torque cycling of each GAG cycle is capable of reaching the ratio of R<0.33. None of the sub-cycles of load is capable of causing crack closure on their own, since their R ratio is too large.

We have two different patterns for the GAG cycles, so their patterns of crack closure are different. Let us consider them separately.

7.5.4.1. GAG cycles varying the load from 20% to 120% of nominal engine torque

Since we have assumed that the values of K vary linearly with load applied (see section 7.4.3), we can use Equation 7.8 to estimate R from

$$R = \frac{K_{\min}}{K_{\max}} = \frac{S_{\min}}{S_{\max}} = \frac{S^{\%}_{\min}}{S^{\%}_{\max}}, \tag{7.13}$$

where

$$S^{\%}_{\min} = \frac{S_{\min}}{S \text{ at } 100\% \text{ of nominal engine torque}}, \tag{7.14}$$

$$S^{\%}_{\max} = \frac{S_{\max}}{S \text{ at } 100\% \text{ of nominal engine torque}}. \tag{7.15}$$

Using $S^{\%}_{min}$ = 20% and $S^{\%}_{max}$ = 120% we have that R=16.7%. In this way, from Equation 7.7, we obtain U=0.867.

Using the relations provided by Equations 7.5, 7.7 and 7.12 we arrive at

$$K_{op} = K_{max} - U(K_{max} - K_{min}). \tag{7.16}$$

Once again, using the linear relationship that exists between the applied load and K, it can be shown that

$$S_{op} = S_{max} - U(S_{max} - S_{min}), \tag{7.17}$$

from which it follows that

$$S^{\%}_{op} = S^{\%}_{max} - U(S^{\%}_{max} - S^{\%}_{min}), \tag{7.18}$$

where

$$S^{\%}_{op} = \frac{S_{op}}{S \text{ at } 100\% \text{ of nominal engine torque}}. \tag{7.19}$$

With this relation, we proceed to estimate the value of engine torque at which K_{op} must occur. Substituting values for $S^{\%}_{min}$, $S^{\%}_{max}$ and U in Equation 7.18 we find that $S^{\%}_{op}$ = 33.3%. See Figure 7.17.

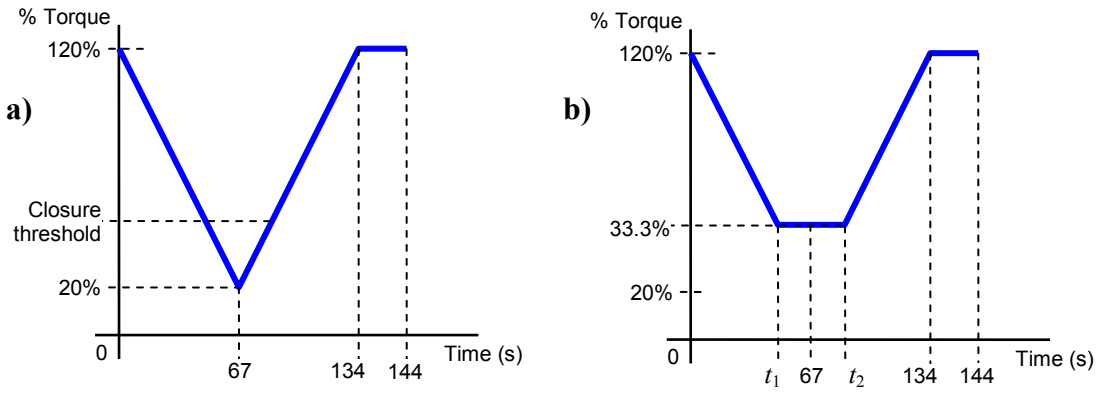

Figure 7.17. Illustration of the crack closure threshold for GAG cycles 1 through 320. a) The crack closure threshold location is illustrated over the pattern of a GAG cycle; compare to Figure 7.5a. b) The "effective" portion of a GAG cycle causing crack growth

Thus, ΔK_{eff} occurs only within the range of applied engine torque going from 33.3% to 120%. Furthermore, following Elber's criterion, none of the sub-cycles below 33.3% of engine torque grow the crack, because both their K_{max} and K_{min} values are below K_{op}.

We can use the time axis of Figure 7.17(b) to estimate how many of the sub-cycles are effective at growing the crack. The amount of time during which the load in a GAG cycle is below the closure threshold is the time interval between t_1 and t_2. Only the sub-cycles outside this interval are effective at growing the crack. Such effective sub-cycles occur in (134 s × 0.867 + 10 s) = 126.18 s, corresponding to about 87.6% of the total number of sub-cycles. This result characterizes ΔK_{eff}, and allows the use of Equation 7.6 to determine the growth pattern of the crack in GAG cycles 1 through 320.

7.5.4.2. GAG cycles varying the load from 20% to 93% of nominal engine torque

The procedure followed in this section is virtually identical to that of section 7.5.4.1. Only the numerical values change. Thus, we only present the results and not the entire process.

Since $S_{max}^{\%}$ is now 93%, Equations 7.13 and 7.7 yield, respectively, R = 21.5% and U = 0.906.

From Equation 7.18, we find $S_{op}^{\%}$ = 26.86%, and thus only about 91.25% of the sub-cycles are effective at growing the crack. This result characterizes ΔK_{eff} for GAG cycles 321 and beyond.

7.5.4.3. Application of load cycles

We would now like to apply Equation 7.6 to determine the effect of the individual load cycles within the loading profile on the crack growth pattern. In the ideal case, we would want to consider the cycle shapes in the loading profile and apply these to the crack growth equation to determine the individual crack progression increments da/dN. Such procedure, known as *cycle counting*, is a standard procedure followed in studies and modeling of crack propagation. The cycle shapes must be considered individually to determine when a specific load cycles is complete and what its amplitude is, as illustrated in Figure 7.18.

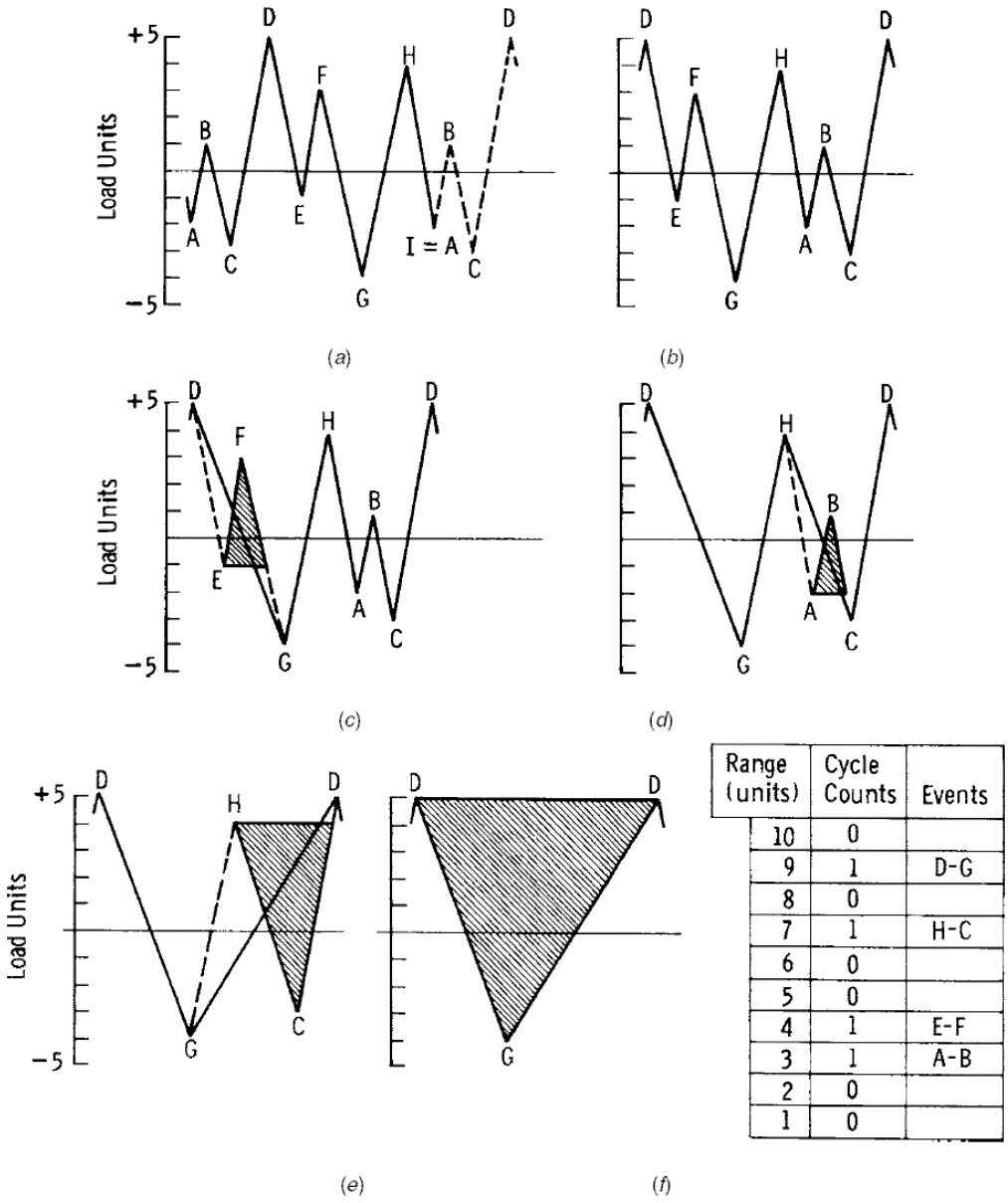

Range (units)	Cycle Counts	Events
10	0	
9	1	D-G
8	0	
7	1	H-C
6	0	
5	0	
4	1	E-F
3	1	A-B
2	0	
1	0	

Figure 7.18. Example of simplified rainflow cycle counting. Reproduced from ASTM (2005)

There exist a variety cycle counting techniques, including level-crossing counting, peak counting, "rainflow" counting, etc. See, for example, ASTM (2005). Here, however, we exploit the regular pattern of our loading profile to simplify the analysis and approximate a solution to cycle counting.

We can calculate the values of ΔK_{eff} for each particular load cycle of the loading profile. We determine individual load cycles considering the torque cycle and all the sub-cycle series described in section 7.2.2. The torque cycle is fully characterized by the variation of load between S_{op} and S_{max}, so that, substituting Equation 7.10 for each of these two parameters in 7.12, we have

$$\Delta K_{eff,\,\text{torque cycle}} = K_{100} \cdot S^{\%}_{max} - K_{100} \cdot S^{\%}_{op} . \tag{7.20}$$

The sub-cycles are characterized by loads with varying amplitudes as prescribed by the loading profile. We can represent the load variation of sub-cycles with values of $S^{\%}_{max}$ and $S^{\%}_{min}$ that are particular to each individual sub-cycle within each sub-cycle series. These values are calculated considering the load effect of the torque cycle and the additional load contributed by a sub-cycle series. For the case $S^{\%}_{max}$ we have

$$\underbrace{S^{\%}_{max,\,\text{sub-cycle}}}_{\substack{\text{For a particular}\\ \text{load sub-cycle}}} = \underbrace{S^{\%}}_{\substack{\text{Contribution from}\\ \text{the torque cycle}}} + \underbrace{S^{\%} A_n}_{\substack{\text{Contirbution from}\\ \text{the sub-cycle series}}} . \tag{7.21}$$

Similarly, for $S^{\%}_{min}$ we have

$$S^{\%}_{min,\,\text{sub-cycle}} = S^{\%} - S^{\%} A_n . \tag{7.22}$$

The values of $S^{\%}$ used in Equations 7.21 and 7.22 correspond to instantaneous values of the load caused by the torque cycle, so that $S^{\%}$ can take on any value corresponding to engine torques between 20% and 120% of the nominal. It is clear that all of the individual sub-cycles, which are more than a hundred thousand within each GAG cycle, have unique values of $S^{\%}_{\text{max, sub-cycle}}$ and $S^{\%}_{\text{min, sub-cycle}}$. Therefore, to simplify the calculation of the effect of individual sub-cycles, we will now assume that the effect of all of the sub-cycles within a sub-cycle series can be approximated by the effect of one "average" sub-cycle. Thus, instead of considering the variation range of $S^{\%}$, we focus on the mean value of the effective load within the torque cycle, i.e.,

$$S^{\%}_{\text{max},n} = S^{\%}_{\text{mean},eff} + S^{\%}_{\text{mean},eff} A_n \,, \tag{7.23}$$

and

$$S^{\%}_{\text{min},n} = S^{\%}_{\text{mean},eff} - S^{\%}_{\text{mean},eff} A_n \,, \tag{7.24}$$

where $S^{\%}_{\text{max},n}$ and $S^{\%}_{\text{min},n}$ characterize the effective load of all the sub-cycles within each sub-cycle series n, for n = 1 to 3, and $S^{\%}_{\text{mean},eff}$ characterizes the mean effective load applied to the average sub-cycle.

The value of ΔK_{eff} driving crack growth from particular series of sub-cycles can now be approximated substituting the values of $S^{\%}_{\text{max},n}$ and $S^{\%}_{\text{min},n}$ in Equation 7.10 and then again in Equation 7.5 to obtain

$$\Delta K_{eff,n} = K_{100} \cdot S^{\%}_{\text{max},n} - K_{100} \cdot S^{\%}_{\text{min},n} \,. \tag{7.25}$$

Substituting Equations 7.23 and 7.24 in Equation 7.25, we find that we can approximate the value of ΔK_{eff} for the sub-cycle series as

$$\Delta K_{eff,n} = 2A_n \cdot K_{100} \cdot \mathrm{S}^{\%}_{\mathrm{mean},eff} \,. \tag{7.26}$$

Equations 7.20 and 7.26 characterize the values of ΔK_{eff} for the four different cycle patterns involved in a GAG cycle, which ultimately drive crack growth. To approximate the crack growth progression pattern we can substitute these values in Equation 7.6 to determine the contributions of each of the four cycle series to the crack development. Thus, we write

$$\underbrace{\frac{da}{dN}}_{\substack{\text{Crack growth increment}\\ \text{per GAG cycle}}} = \underbrace{C(\Delta K_{eff,\,\text{torque cycle}})^m}_{\substack{\text{Contribution of}\\ \text{torque (GAG) cycle}}} + \underbrace{\sum_{n=1}^{3} C(\Delta K_{eff,n})^m}_{\substack{\text{Contribution of each}\\ \text{sub-cycle series}}} \,. \tag{7.27}$$

Equation 2.27 approximately models the crack growth progression in the planetary carrier plate providing crack length increments for each complete GAG cycle. To approximate better the crack progression, Equation 2.27 should be applied separately for the inboard and outboard directions of crack growth. The application of the equation should also be done using the stress intensity factors obtained in section 7.4.2 and summarized earlier in Table 7.1, and with the loading profile parameters obtained in sections 7.5.4.1 and 7.5.4.2, which are summarized in Table 7.2, below.

Table 7.2. Summary of assumed loading profile parameters for the crack growth experiment with the helicopter transmission planetary carrier plate

	Parameter	GAG cycles 1 to 320	GAG cycles beyond 320
Torque (GAG) cycle	$S^{\%}_{min}$	20%	20%
	$S^{\%}_{max}$	120%	93%
	Effective time fraction	87.6%	91.25%
	$S^{\%}_{op}$	33.3%	26.86%
	$S^{\%}_{mean,eff}$ (*)	74.30%	59.33%
Sub-cycle series 1	Amplitude, A_1	10%	
	Frequency, f_1	4.3Hz	
	Cycles per GAG cycle	619.2	
	Effective cycles per GAG cycle, $N_{1,eff}$	524.4	565.0
Sub-cycle series 2	Amplitude, A_2	5.22%	
	Frequency, f_2	17.2 Hz	
	Total cycles per GAG cycle	2,477	
	Effective cycles per GAG cycle, $N_{2,eff}$	2,169.9	2260.3
Sub-cycle series 3	Amplitude, A_3	2%	
	Frequency, f_3	980.4 Hz	
	Total cycles per GAG cycle	141,178	
	Effective cycles per GAG cycle, $N_{3,eff}$	123,671.9	128,824.9

(*) Note that $S^{\%}_{mean,eff} \neq \frac{S^{\%}_{max} + S^{\%}_{op}}{2}$ because the torque cycle remains at S_{max} and S_{op} for different amounts of time (see Figure 7.17)

7.6. Simulation of damage progression and model validation

The crack growth model described in this chapter has been implemented with the approach to model-based prognosis proposed in section 6.2, and the model-based damage-progression simulation architecture of section 6.3. The result of this effort has been an adequate characterization of the growth of the crack in the planetary carrier plate.

To verify the effectiveness of the model, we use experimental data from the damage-progression tests (experiments with a growing crack) carried out with a planetary carrier plate (see section 3.2).

Crack length measurements were obtained throughout the experiment using crack length gages. Crack length gages are standard instrumentation devices that detect discrete increments in the length of fractures. Crack gages are adhered to the surface that the crack is expected to cross when growing. Each gage is installed making sure that a series of parallel delicate electrical connection lines inside the gage are perpendicular to the direction of crack growth. As the crack progresses, the connection lines are broken, thus providing information of the crack reach. Crack gages are shown in Figure 7.19. Each discrete crack length measurement obtained is referred to as a "ground truth" point. By interpolating the ground truth crack lengths with respect to the GAG cycle numbers, it is possible to characterize the progression of the crack length.

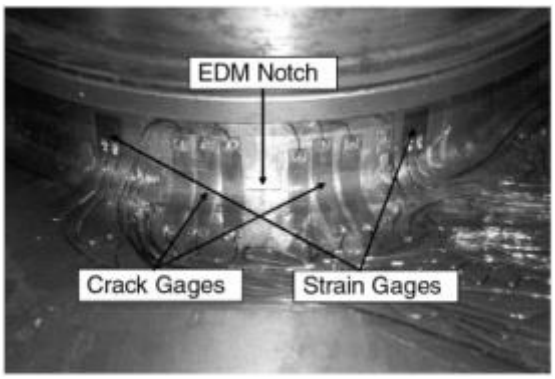

Figure 7.19. Instrumentation for measuring the progression in length of a crack and certain localized strains on the root of a planet gear mounting post of a planetary carrier plate with a seeded fracture. The fracture "seed" is a small notch generated through electrical discharge machining (EDM). Reproduced from Vachtsevanos et al. (2006)

The experiment was run with a slight modification to the mechanical configuration of the gearbox. The intention of this modification was to increase the stresses in the carrier plate and increase the crack growth rate. The modification was deemed to increase the stresses of the plate by about 5%. Thus, the model presented in section 7.5 and characterized by Equations 7.27, 7.26 and 7.20 was modified to run simulations using a similar increase in the values of S_{max} and all $S^{\%}_{max,n}$, i.e., they were scaled with a factor of 1.05. Figure 7.20 shows a comparison between the results of the crack-growth model simulations and the ground truth points.

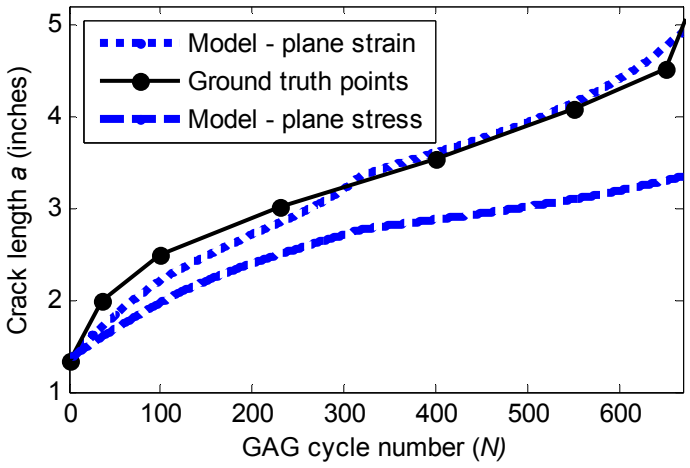

Figure 7.20. Comparison of crack growth model of the planetary carrier plate and experimental crack growth data

The results presented in Figure 7.20 demonstrate that it is possible to implement a damage progression model using the architecture proposed in section 6.3. With the availability of such a damage progression model, it is possible to implement a model-based prognostic architecture for the planetary carrier plate that utilizes model adaptation algorithms and uncertainty management techniques in the spirit of the methodology proposed in section 6.2. Such an effort is beyond the scope of this thesis, but has actually been carried out in a team effort. The description of such work is presented in Patrick et al. (submitted for review) and Orchard (to be published).

8. CONCLUSIONS AND FUTURE WORK

A generic approach to designing model-based engineering diagnostic and prognostic systems has been presented in this thesis. The methodology has been successfully tested and partially validated by applying it to the case of diagnosing a fracture fault in a helicopter transmission gearbox and characterizing its progression. Further validation is, nevertheless, possible, and this remains as an area of future work. Such additional validation can be provided by more experimentation with the helicopter transmission of consideration, as discussed below, and by the employing of the modular methodologies proposed in this thesis with other engineering applications and systems.

The modeling approaches for both diagnosis and prognosis presented in this thesis were set up in analogous ways. Both modeling techniques consider how to adapt and implement a model to achieve their respective objectives. For the case of diagnostics, such consideration is the use of what has been designated a "reverse engineering approach". This approach allows for the use of a model in the problems of fault detection and identification. For the case of prognostics, the model is used as part of a "generic" approach to model-based prognostics. This generic approach enables the use of information from a variety of sources to arrive at reliable prognoses of the remaining life of engineering system components, including diagnosis, usage patterns, uncertainty management techniques, model adaptation algorithms, and the aforementioned damage progression model.

Another, more important, analogy between the model-based approaches to diagnosis and prognosis is the procedure presented to adapt and implement models for their respective uses. Although in general a model used in the task of diagnosing a system is not likely to be the same as that of prognosis, the two approaches follow a comparable treatment of the model parameters, starting by classifying them as either fault-sensitive or fault-insensitive. Both approaches also provide an opportunity to use experimental data to calibrate the model and consider different operating conditions to enhance the replication of the behaviors observed in the modeled systems when a fault is present.

Analogies cannot go very far here, however. There are important fundamental differences in the use that diagnostics and prognostics make of models, one of which being that, for diagnostics, it is possible to consider a fault as a static event, whereas for prognostics, the definition of the fault must be dynamic. The approach presented takes into consideration several aspects such as this.

It was mentioned in the thesis that one of the most important disadvantages of the model-based approach to diagnostics and prognostics is that modeling can be a complex and involved task. Even for the illustrative purposes of the present work, such task was no exception. The models required for both diagnosis and prognosis required much consideration and careful adaptations to enable their practical implementation. It follows thus that an area of future work related to this thesis involves the development of techniques for simplifying modeling efforts.

This difficulty notwithstanding, the modular methodology for designing model-based diagnostic and prognostic architectures presented in this thesis proved immensely helpful in addressing the multiple modeling aspects that required consideration, and was verified to be a valuable guide for directing and focusing invested efforts.

Similarly, the approach to combine the use of parameters that are determined on-line with parameters that are determined off-line, suggested by this thesis, proved advantageous as well. The utility of such technique was not only in assisting analysis, but also in facilitating the running of simulations of damage progression in the helicopter transmission. This was important because some of the models required considerable amounts of computing resources to derive useful results, more than what could be considered "practical" for a working implementation of a diagnosis or prognosis system of an engineering system in operation. This tool has almost certainly brought the applied architecture a step closer to becoming a suitable candidate for a working implementation of a health management system for the helicopter transmission.

Related to this is the fact that team members of the structural integrity prognosis system (SIPS) program sponsored by DARPA are expected to complete another round of testing of helicopter transmissions with damage progression tests. These tests will continue to offer a chance to validate diagnosis and prognosis techniques such as those presented in this thesis. The experiments also intend to offer an opportunity to develop an integrated health management system that will be able to detect a crack in the planetary carrier plate of the main transmission gearbox, assess its length and prognosticate its growth. This task shares a few common characteristics with this thesis. Both intend not

only to increase safety on the thousands of helicopters in operation with a potential to develop this kind of fault, but also to offer advances in the state-of-the-art in applied diagnosis and prognosis of engineering systems, and validation for the still-emergent discipline of engineering prognostics.

REFERENCES

Abbas, M., A. A. Ferri, M. E. Orchard and G. Vachtsevanos (2007). An intelligent diagnostic/prognostic framework for automotive electrical system. IEEE Intelligent Vehicles Symposium, June 13-15, 2007, Istanbul, Turkey.

Ambarisha, V. K. and R. G. Parker (2006). "Suppression of planet mode response in planetary gear dynamics through mesh phasing." Journal of Vibration and Acoustics, Transactions of the ASME **128**(2): 133-142.

Anderson, T. L. (1995). Fracture Mechanics. Fundamentals and Applications. Boca Raton, FL, CRC Press.

Arulampalam, M. S., S. Maskell, N. Gordon and T. Clapp (2002). "A tutorial on particle filters for online nonlinear/non-Gaussian Bayesian tracking." IEEE Transactions on Signal Processing **50**(2): 174-188.

ASTM (2005). Annual Book of ASTM Standards, American Society for Testing and Materials. West Conshohocken, PA. **E1049-85(1997)**: Standard Practices for Cycle Counting in Fatigue Analysis: Vol 03.01.

Barlas, I., G. Zhang, N. Propes and G. Vachtsevanos (2003). Confidence Metrics and Uncertainty Management in Prognosis. MARCON, Knoxville, TN, U.S.A., May.

Bilosova, A., J. Ondrouch and J. Bilos (2002). Changes in modal parameters during fatigue tests of turbine blades. Proceedings of the 2002 International Conference on Noise and Vibration Engineering, ISMA, Sep 16-18 2002, Leuven, Belgium, Katholieke Universiteit Leuven, Heverlee, B-3001, Belgium.

Blunt, D. M. and J. A. Keller (2006). "Detection of a fatigue crack in a UH-60A planet gear carrier using vibration analysis." Mechanical Systems and Signal Processing **20**(8): 2095-2111.

Bodas, A. and A. Kahraman (2004). "Influence of carrier and gear manufacturing errors on the static load sharing behavior of planetary gear sets." JSME International Journal, Series C (Mechanical Systems, Machine Elements and Manufacturing) **47**(3): 908-15.

Botman, M. (1975). "Epicyclic gear vibrations." American Society of Mechanical Engineers (Paper)(75-DET-14): 5.

Botman, M. (1980). "Vibration measurements on planetary gears of aircraft turbine engines." Journal of Aircraft **17**(5): 351-357.

Byington, C. S., M. J. Roemer and T. Galie (2002). Prognostic Enhancements to Diagnostic Systems for Improved Condition-Based Maintenance. IEEE Aerospace Conference Proceedings, Big Sky, MT, USA, IEEE.

Byington, C. S. and P. Stoelting (2004). A Model-based Approach to Prognostics and Health Management for Flight Control Actuators. IEEE Aerospace Conference Proceedings, 6-13 March 2004, Big Sky, MT, U.S.A., IEEE.

Chaari, F., T. Fakhfakh and M. Haddar (2006). "Analytical investigation on the effect of gear teeth faults on the dynamic response of a planetary gear set." Noise and Vibration Worldwide **37**(8): 9-15.

Chen, J. and R. J. Patton (1999). Robust Model-Based Fault Diagnosis for Dynamic Systems. Boston, MA, U.S.A., Kluwer Academic Publishers.

Chow, E. Y. and A. S. Willsky (1980). Issues in the Development of a General Algorithm for Reliable Failure Detection. Proceedings of the 19th Conference on Decision and Control, Albuquerque, NM.

Clough, R. W. (1960). The Finite Element Method in Plane Stress Analysis. Proceedings of ASCE Conf. Electron Computat., Pittsburg, PA, U.S.A.

Cornell Fracture Group, Ed. (2003). FRANC3D Concepts and Users Guide. Version 2.6. Ithaca, NY: Cornell Fracture Group, Cornell University.

Courant, R. (1943). "Variational methods for the solution of problems of equilibrium and vibrations." Bulletin of the American Mathematical Society **49**: 1-23.

Dowling, N. E. (1999). Mechanical Behavior of Materials. Upper Saddle River, NJ, Prentice-Hall Inc.

Elber, W. (1971). The Significance of Crack Closure. Damage Tolerance in Aircraft Structures, ASTM STP 486, Philadelphia, PA, American Society for Testing and Materials.

Engel, S. J., B. J. Gilmartin, K. Bongort and A. Hess (2000). Prognostics, the real issues involved with predicting life remaining. 2000 IEEE Aerospace Conference, Mar 18-25 2000, Big Sky, MT.

Favaloro, S. C. (1985). A preliminary evaluation of some gear diagnostics using vibration analysis. Report Number AD-A161939; ARL-AERO-RPOP-TM-427; Available from NTIS HC A03/MF A01, Accession Number N86-23942 (AH) Aeronautical Research Labs., Melbourne (Australia).

Federal Standard 1037C (1996). Telecommunications: Glossary of Telecommunication Terms., U.S. General Services Administration.

Garga, A. K., K. T. McClintic, R. L. Campbell, C.-C. Yang, M. S. Lebold, T. A. Hay and C. S. Byington (2001). Hybrid reasoning for prognostic learning in CBM systems. 2001 IEEE Aerospace Conference, Mar 10-17 2001, Big Sky, MT.

Gelman, L. and S. Gorpinich (2000). "Non-linear vibroacoustical free oscillation method for crack detection and evaluation." Mechanical Systems and Signal Processing **14**(3): 343-51.

Gertler, J. J. (1998). Fault Detection and Diagnosis in Engineering Systems. New York, Marcel Dekker, Inc.

Giurgiutiu, V. (2002). Current issues in vibration-based fault diagnostics and prognostics. Smart Nondestructive Evaluation for Health Monitoring of Structural and Biological Systems, Mar 18-19 2002, San Diego, CA, United States, The International Society for Optical Engineering.

Hess, A. (2002). Prognostics, from the need to reality-from the fleet users and PHM system designer/developers perspectives. 2002 IEEE Aerospace Conference Proceedings, 9-16 March, Big Sky, MT, USA, IEEE.

Hess, A. and W. Hardman (2002). Seeded fault testing in support of mechanical systems prognostic development. 2002 IEEE Aerospace Conference Proceedings, 9-16 March, Big Sky, MT, USA, IEEE.

Hines, J. A., D. S. Muench, J. A. Keller and A. K. Garga (2005). Effects of time-synchronous averaging implementations on HUMS features for UH-60A planetary carrier cracking, Grapevine, TX, United States, American Helicopter Society, Alexandria, VA 22314-2538, United States.

Inman, D. J., C. R. Farrar, V. L. Junior and V. S. Junior, Eds. (2005). Damage Prognosis : For Aerospace, Civil and Mechanical Systems, John Wiley and Sons.

Jarrell, D., D. Sisk and L. Bond (2002). Prognostics and Condition Based Maintenance (CBM) - A Scientific Crystal Ball, Pacific Northwest National Laboratory, Richland, Washington; Report PNNL-SA-36771.

Jaw, L. and W. Wang (2004). A run-time test system for maturing intelligent system/vehicle capabilities - SIDAL. 2004 IEEE Aerospace Conference Proceedings, 6-13 March 2004, Big Sky, MT, USA, IEEE.

Jaw, L. C. (1999). Neural networks for model-based prognostics. Proceedings of the 1999 IEEE Aerospace Conference, Mar 6-13, 1999, Snowmass at Aspen, CO, USA, IEEE, Los Alamitos, CA, USA.

Kacprzynski, G. J., M. J. Roemer, G. Modgil, A. Palladino and K. Maynard (2002). Enhancement of physics-of-failure prognostic models with system level features. 2002 IEEE Aerospace Conference Proceedings, 9-16 March 2002, Big Sky, MT, USA, IEEE.

Kacprzynski, G. J., A. Sarlashkar, M. J. Roemer, A. Hess and W. Hardman (2004). "Predicting remaining life by fusing the physics of failure modeling with diagnostics." JOM **56**(3): 29-35.

Kahraman, A. (2001). "Free torsional vibration characteristics of compound planetary gear sets." Mechanism and Machine Theory **36**(8): 953-971.

Kahraman, A. (1994a). "Natural modes of planetary gear trains." Journal of Sound and Vibration **173**(1): 125-130.

Kahraman, A. (1994b). "Planetary gear train dynamics." Journal of Mechanical Design, Transactions of the ASME **116**(3): 713-720.

Katcher, M. R. and M. Kaplan (1974). Effect of R-Factor and Crack Closure on Fatigue Crack Growth for Aluminum and Titanium Alloys. ASTM STP 559, Philadelphia, PA, American Society for Testing and Materials.

Keller, J. and P. Grabill (2003). Vibration Monitoring of a UH-60A Main Transmission Planetary Carrier Fault. The American Helicopter Society 59th Annual Forum, Phoenix, AZ, May 6-8, 2003.

Khiripet, N. (2001). An architecture for intelligent time series prediction with causal information. Electrical and Computer Engineering Theses. Atlanta, GA, U.S.A., Georgia Institute of Technology.

Larsen, J. M. and L. Christodoulou (2004). "Integrating damage state awareness and mechanism-based prediction." JOM **56**(3): 14.

Lin, J. and R. G. Parker (1999). "Analytical characterization of the unique properties of planetary gear free vibration." Journal of Vibration and Acoustics, Transactions of the ASME **121**(3): 316-321.

Lin, J. and R. G. Parker (2002). "Planetary gear parametric instability caused by mesh stiffness variation." Journal of Sound and Vibration **249**(1): 129-145.

Luo, J., M. Namburu, K. Pattipati, L. Qiao, M. Kawamoto and S. Chigusa (2003). Model-based Prognostic Techniques. IEEE Systems Readiness Technology Conference (AUTOTESTCON 2003), Sep 22-25 2003, Anaheim, CA, United States, Institute of Electrical and Electronics Engineers Inc.

Mathur, A., K. F. Cavanaugh, K. R. Pattipati, P. K. Willett and T. R. Galie (2001). Reasoning and modeling systems in diagnosis and prognosis. Component and Systems Diagnostics, Prognosis, and Health Management, Apr 16-17 2001, Orlando, FL, Society of Photo-Optical Instrumentation Engineers.

McFadden, P. D. and J. D. Smith (1985). "An Explanation for the Asymmetry of the Modulation Sidebands about the Tooth Meshing Frequency in Epicyclic Gear Vibration." Proceedings of the Institution of Mechanical Engineers, Part C: Mechanical Engineering Science **199**(1): 65-70.

McInerny, S. A., B. Hardman, J. A. Keller and R. Bednarczyk (2003). Detection of a cracked-planet carrier. Proceedings of the Tenth International Congress on Sound and Vibration, Stockholm, Sweden, Institute of Acoustics.

McNames, J. (2002). "Fourier series analysis of epicyclic gearbox vibration." Transactions of the ASME, Journal of Vibration and Acoustics **124**(1): 150-3.

Mi, B., J. E. Michaels and T. E. Michaels (2006). "An ultrasonic method for dynamic monitoring of fatigue crack initiation and growth." Journal of the Acoustical Society of America **119**(1): 74-85.

Michaels, J. E. and T. E. Michaels (2005). "Detection of structural damage from the local temporal coherence of diffuse ultrasonic signals." IEEE Transactions on Ultrasonics, Ferroelectrics and Frequency Control **52**(10): 1769-82.

Moaveni, S. (2003). Finite Element Analysis: Theory and Application with ANSYS. Upper Saddle River, NJ, U.S.A., Prentice Hall.

Murthy, A. R. C., G. S. Palani and N. R. Iyer (2004). "State-of-the-art review on fatigue crack growth analysis under variable amplitude loading." Journal of the Institution of Engineers, Calcutta, India **85**(August): 118-29.

Newman, J. C., Jr. (1984). "A crack opening stress equation for fatigue crack growth." International Journal of Fracture **24**(4): 131-5.

Newman, J. C. (1992). FASTRAN-II - A Fatigue Crack Growth Structural Analysis Program. February 1992 Revised Copy. Langley, VA, U.S.A., NASA Technical Memorandum 104159.

Newman, J. C., Jr. (1995). "Fatigue-life prediction methodology using a crack-closure model." Transactions of the ASME. Journal of Engineering Materials and Technology **117**(4): 433-9.

Orchard, M. E. (to be published). A Particle-Filtering-Based Framework for On-line Fault Diagnosis and Failure Prognosis. Ph.D. Thesis. Electrical and Computer Engineering, Georgia Insititute of Technology, Atlanta.

Orchard, M. E., B. Wu and G. Vachtsevanos (2005). A Particle Filtering Framework for Failure Prognosis. Proceedings of WTC2005 World Tribology Congress III September 12-16, Washington, D.C., USA.

Padula, S. L. and R. K. Kincaid (1999). Optimization Strategies for Sensor and Actuator Placement. NASA Langley Research Center. Langley, VA, NASA Report no. 19990036166; NASA/TM-1999-209126; L-17839; NAS.

Paris, P. C. and F. Erdogan (1963). "A Critical Analysis of Crack Propagation Laws." Journal of Basic Engineering **85**(4): 528-534.

Park, H. G., S. Chien, M. Zak, M. James, R. Mackey and F. Fisher (2003). Active State Model for Autonomous Systems, NASA Jet Propulsion Laboratory, Report NPO21243, Sept. 2003.

Park, H. G. and M. Zak (2003). "Gray-box approach for fault detection of dynamical systems." Transactions of the ASME. Journal of Dynamic Systems, Measurement and Control **125**(3): 451-4.

Parker, R. G. (2000). "A physical explanation for the effectiveness of planet phasing to suppress planetary gear vibration." Journal of Sound and Vibration **236**(4): 561-573.

Parker, R. G. and J. Lin (2004). "Mesh phasing relationships in planetary and epicyclic gears." Journal of Mechanical Design, Transactions of the ASME **126**(2): 365-370.

Patrick, R., M. E. Orchard, B. Zhang, G. J. Kacprzynski, M. Koelemay, A. A. Ferri and G. Vachtsevanos (submitted for review). An integrated approach to helicopter planetary gear fault diagnosis and failure prognosis. AUTOTESTCON 2007, Sept 17-20 2007, Baltimore, MD, Institute of Electrical and Electronics Engineers Inc.

Patton, R. J., P. M. Frank and P. M. Clark, Eds. (2000). Issues in Fault Diagnosis for Dynamic Systems. London, Springer-Verlag.

Powrie, H. E. G. and C. E. Fisher (1999). Engine health monitoring: Towards total prognostics. 1999 IEEE Aerospace Conference. Proceedings, 6-13 March 1999, Snowmass at Aspen, CO, USA, IEEE.

Rao, S. S. (1990). Mechanical Vibrations. Reading, MA, U.S.A., Addison-Wesley.

Rice, R. C., J. L. Jackson, J. Bakuckas and S. Thompson (2003). Metallic Materials Properties Development and Standardization (MMPDS). Report DOT/FAA/AR-MMPDS-01; NTIS PB2003106632. Washington, D.C., U.S. Department of Transportation, Federal Aviation Administration**:** 1728.

Roemer, M. J., G. J. Kacprzynski and R. F. Orsagh (2001). Assessment of data and knowledge fusion strategies for prognostics and health management. 2001 IEEE Aerospace Conference, Mar 10-17 2001, Big Sky, MT.

Sahrmann, G. J. (2004). Determination of the crack propagation life of a planetary gear carrier. 60th Annual Forum Proceedings, Baltimore, MD, Jun. 7-10 2004, American Helicopter Society.

Samuel, P. D. (2003). Helicopter Transmission Diagnostics using Constrained Adaptive Lifting. Ph.D. Thesis. Aerospace Engineering, University of Maryland, College Park.

Sander, M. (2004). Comparison of fatigue crack growth concepts with respect to interaction effects. Proceedings of ECF 15, Stockholm, Sweden.

Sanford, R. J. (2003). Principles of Fracture Mechanics. Upper Saddle River, NJ, Pearson Education, Inc., Prentice Hall.

Shih, T. T. and R. P. Wei (1974). "A study of crack closure in fatigue." Engineering Fracture Mechanics **6**(1): 19-32.

Stewart, R. M. (1977). Some Useful Data Analysis Techniques for Gearbox Diagnostics. Report MHM/R/10/77, Machine Health Monitoring Group, Institute of Sound and Vibration Research, University of Southampton; July, 1977.

Strang, G. and G. J. Fix (1973). An Analysis of the Finite Element Method. Englewood-Cliffs, NJ, U.S.A., Prentice-Hall.

Strass, M. (2002). Transmission Crack Grounds Two-Thirds of Army Black Hawk Fleet. Defense Daily. **214(25)**.

Swanson, D. C. (2001). A general prognostic tracking algorithm for predictive maintenance. 2001 IEEE Aerospace Conference, Mar 10-17 2001, Big Sky, MT.

Swansson, N. S. (1980). Application of Vibration Signal Analysis Techniques to Condition Monitoring, Melbourne, Aust, Inst of Eng, Aust, Barton.

Szczepanik, A. (1989). "Time synchronous averaging of ball mill vibrations." Mechanical Systems and Signal Processing **3**(1): 99-107.

Toda, A. and M. Botman (1979). "Planet indexing in planetary gears for minimum vibration." American Society of Mechanical Engineers (Paper)(79-DET-73): 6.

Turner, M. J., R. W. Clough, H. C. Martin and L. J. Topp (1956). "Stiffness and deflection analysis of complex structures." Journal of the Aeronautical Sciences **23**(9): 805-823.

Vachtsevanos, G. (2003). Performance Metrics for Fault Prognosis of Complex Systems. IEEE Systems Readiness Technology Conference (AUTOTESTCON 2003), Sep 22-25 2003, Anaheim, CA, United States, Institute of Electrical and Electronics Engineers Inc.

Vachtsevanos, G., F. L. Lewis, M. J. Roemer, A. Hess and B. Wu (2006). Intelligent Fault Diagnosis and Prognosis for Engineering Systems. Hoboken, NJ, John Wiley and Sons

Vachtsevanos, G. and P. Wang (2001). Fault prognosis using dynamic wavelet neural networks. AUTOTESTCON 2001, Aug 20-23 2001, Valley Forge, PA, Institute of Electrical and Electronics Engineers Inc.

Vosilla, J. A. (2003). Northrop Grumman to Help DARPA Predict Aircraft Structural Health and Readiness. PrimeZone Media Network. Business Contracts Wire News; November 4, 2003.

Vosilla, J. A. (2006). Northrop Grumman Awarded Follow-on Contract for System That Predicts Structure Failures. PrimeZone Media Network. Business Contracts Wire News, Northrop Grumman Company Announcement; February 21, 2006.

Willsky, A. S. (1976). "A Survey of Design Methods for Failure Detection in Dynamic Systems." Automatica **12**: 601-611.

Wu, B., A. Saxena, T. S. Khawaja, R. Patrick, G. Vachtsevanos and P. Sparis (2004). An approach to fault diagnosis of helicopter planetary gears. Proceedings of AUTOTESTCON 2004, San Antonio, TX, Institute of Electrical and Electronics Engineers Inc., Piscataway, NJ 08855-1331, United States.

Yang, Q. (2004). Model-Based and Data Driven Fault Diagnosis Methods with Applications to Process Monitoring. Electrical Engineering and Computer Sciences Theses. Cleveland, OH, Case Western Reserve University**:** 203.

Yuksel, C. and A. Kahraman (2004). "Dynamic tooth loads of planetary gear sets having tooth profile wear." Mechanism and Machine Theory **39**(7): 695-715.

Zhang, B., T. S. Khawaja, R. Patrick and G. Vachtsevanos (2007, to appear). Deconvolution De-noising for Helicopter Vibration Data. Proceedings of the 2007 American Control Conference, July 11-13, 2007, New York City, USA

Zhang, G. (2005). Optimum Sensor Localization/Selection in a Diagnostic/Prognostic Architecture. Electrical and Computer Engineering Theses. Atlanta, GA, U.S.A., Georgia Institute of Technology.